UNIVERSITA' DEGLI STUDI DI SASSARI

DIPARTIMENTO DI ARCHITETTURA, DESIGN E URBANISTICA

Corso di Dottorato di ricerca in Architettura e Ambiente

XXXVI ciclo

Luminescence Dating and Sedimentary Evolution of Martian Analog Environments

Dottoranda: Myriam Francesca Stelletti

Tutor: Prof Vincenzo Pascucci

A mia madre e mia sorella,

i miei fari nelle notti più buie,

i miei porti sicuri,

la brezza che gonfia le mie vele,

la mia Orsa Maggiore,

la mia Orsa Minore

Thesis Contents

Abstract

The present thesis is part of the *IN-TIME project* (*In-Situ Instrument for Mars and Earth Dating Applications*), funded under the European Union H2020-MSCA-RISE-2018 research program (G.A. n. 823934). The project involves a consortium of seven European organizations and industries from Italy (Università degli Studi di Sassari - UNISS; Università degli Studi 'G. d'Annunzio' Chieti – Pescara - UNICH), Spain (Universidad Complutense de Madrid - UCM; Sensia Solutions - SL), and Cyprus (Cyprus Space Exploration Organisation - CSEO; Space System Solutions -S3- LTD), coordinated by ALMA Sistemi SRL, with the University of Texas as an associated US partner to the project.

The primary objective of the IN-TIME project is to develop a miniaturized instrument capable of dating Martian geological deposits in-situ through the Luminescence technique. This innovative technology has applications not only in planetary exploration but also in Earth's field, serving as a light and portable dating instrument in geology and archaeology. Additionally, it acts as a risk assessment tool for accident and emergency dosimetry and nuclear mass-casualty events. The second objective of the project is to test on Mars analogue the possibility to date basalt derived sedimentary deposits.

Accurate estimation of absolute ages on Mars is crucial for understanding its surface and atmosphere on going evolutionary processes. Knowledge of the occurrence and time-frequency of such processes allows for hazard evaluation, essential for future deployments, missions, and, eventually, human presence on Mars. However, the chronology of recent events on Mars poses challenges due to uncertainties associated with the current methodology (crater counting), which are comparable to the younger ages obtained (approximately 1 Ma).

While a return sample mission (Mars Sample Return) is planned for 2030 by NASA and ESA, the timeline for obtaining detailed information from the returned samples is uncertain. In the meantime, pursuing in-situ dating of deposits emerges as a more economically viable approach, considering the potential delays in the comprehensive analysis of samples brought back to Earth.

The aim of this thesis aligns with the second objective of the IN-TIME project, which includes:

- Identification and validation of the most suitable protocol for dating Martian analogue sediments, with a focus on deposits derived from basalt, using luminescence.
- Reconstruction of late Quaternary depositional environments and the paleoclimatic evolution of a Martian analogue.

To achieve these goals, this research focused on studying the sedimentary processes of the El Jable plain and Famara cliffs on Lanzarote, a terrestrial analog to Martian environments. Through detailed sedimentological analysis and luminescence dating, the research reconstructs the depositional history of these sites, emphasizing their relevance to understanding climatic fluctuations on both Earth and Mars. The study draws significant parallels between the geomorphological features of Famara barrancos and Martian gullies, particularly in their formation mechanisms and depositional structures, with transient flows shaping steep terrain on both planets—water on Earth and carbon dioxide sublimation on Mars.

The successful application of the pIRIR$_{200}$ luminescence protocol allowed for the detailed dating of sedimentary sequences in Lanzarote, revealing alternating periods of fluvial and aeolian activity. These findings provide important insights into the paleoclimatic oscillations of Lanzarote during the Late Quaternary, which serve as a model for interpreting similar climatic events on Mars. This research not only advances our understanding of planetary science but also offers valuable insights for future Martian missions and human exploration, by providing a framework for interpreting the planet's geological and climatic history through in-situ dating techniques.

Introduction

Determining the age of Martian geological formations is pivotal for understanding the planet's evolution, providing essential insights into its geological history, and potentially influencing the planning and execution of future human missions to Mars. Various techniques, such as crater counting, rover-based radiometric analysis, orbital exploration, and mineralogical studies, provide valuable interpretations into Mars temporal history. However, these approaches come with inherent disadvantages. Crater counting, while reliable, offers only relative ages and faces challenges with overlapping craters and calibration limitations. Rover-based radiometric analyses are sophisticated but time-consuming and provide predominantly relative or approximate ages. Satellite images, crucial for orbital exploration, can be influenced by atmospheric conditions, impacting image clarity, and dating precision. Mineralogical studies, while informative, demand a profound understanding of past environmental conditions, and variations can result from multiple factors. Despite notable advancements, these techniques require careful consideration and mitigation of their respective limitations to ensure accurate interpretations of Mars' temporal history.

Luminescence dating emerges as a promising method for Martian geochronology, offering absolute age estimates and addressing limitations associated with other techniques. Unlike crater counting, it provides more precise dating without the challenges of overlapping craters and calibration issues. Additionally, it presents a less time-consuming alternative to rover-based radiometric analyses, offering a comprehensive and reliable approach for unraveling the temporal history of Mars. The technique can be valuable for upcoming missions, both robotic and human.

Despite the promising features of luminescence dating, it is important to note that this technique has a temporal limitation. Luminescence dating allows the analysis of materials dating back no more than one million years. Therefore, the focus of the technique is directed towards recent or active Martian deposits, representing a crucial consideration for its applicability.

Previous studies have highlighted additional challenges associated with the use of luminescence on Martian analogue sediments (Lepper et al., 2000; Doran et al., 2004; Jain et al., 2006; Kalchgruber et al., 2007; Detschel et al., 2009). The primary challenges involve rapid anomalous fading, resource-

intensive experiments for efficiency-depth profiles, and the need for burial models to mitigate age determination errors. Lower natural dose rates on Mars, coupled with higher cosmic ray fluxes, may limit age bounds for shallow deposits. Rapidly buried deposits face dominantly decay-induced irradiation, potentially increasing the maximum age limit. However, successful luminescence dating on Mars requires understanding Martian-specific factors and addressing uncertainties related to burial and erosion rates. Additionally, OSL (Optically Stimulated Luminescence) measurements on Martian analogues reveal substantial variability, emphasizing the need for further experimental work. The limited representation of feldspar, constituting only 20% of primary silicate minerals, may impact the generalizability of luminescence characteristics derived from Earth-based studies.

Building upon the challenges and considerations highlighted, the central inquiry of this thesis is to explore the feasibility of using in-situ luminescence instrumentation for dating Martian analogue basalt-derived deposits. By addressing the limitations and complexities associated with luminescence dating on Mars, this research aims to contribute valuable insights and methodologies that can enhance our understanding of the temporal aspects of Martian geological formations.

Initially, the research concentrated on Lanzarote, one of the Canary Islands, due to its geological and morphological features that could potentially resemble those on Mars. After a careful selection of areas potentially suitable for dating, sediments from colluvial, alluvial, dune, and braided deposits were subjected to tests to assess their response to the Infrared Stimulated Luminescence protocol. The protocol was designed with a Martian perspective in mind, employing a workflow that prioritizes speed and an ease use of a miniaturized instrument installed on a rover. Therefore, the decision was made to work on fine-grained rather than coarse-grained sediments, as the steps involved to obtain this size are fewer and simpler. Additionally, the decision to work with k-feldspar (rather than, for example, quartz) was made because addressed to purely basaltic derived sediment. Observed that the chosen protocol was effective based on the results obtained during the experimental phase, the research progressed to date the Martian analogue material and subsequently compared the obtained ages with those of radiocarbon dating (^{14}C) from organic material samples.

Following that, the research progressed to the next stage, focusing on luminescence studies in specific Martian analogue environments, located within the sedimentary basin of El Jable (Lanzarote, Canary Island, SP). The aim was to explore the possibility of establishing the late Quaternary depositional history of this basin using the "Martian" protocol. The sedimentary basin

of El Jable, being the remnant of a caldera, exhibits intriguing parallels with Martian geological formations, such as meteoritic impact craters. The eroded flanks of the Famara volcano's caldera, forming extensive alluvial fan systems, are linked to the inner rim of a meteorite-induced crater on Mars. This connection extends to Martian gullies, resembling channel formations observed in the Famara fans (*barrancos* in Spanish). Additionally, the dune system in El Jable interbedding with the alluvial fans, exhibits similarities with dune systems in certain Martian craters. This interplay deepens our understanding of Martian analogue environments, shedding light on potential depositional histories of meteoritic impact craters filled with recent deposits and other geological on-going processes on the Red Planet. To investigate the evolutionary depositional history of the El Jable sedimentary basin, 13 samples were collected from *Barranco Las Piletas* and dated with luminescence. Subsequently, the obtained ages were compared with 31 organic samples, dated with radiocarbon, originating from both the alluvial fans and dune system.

From this thesis, two types of conclusions have emerged: one related to the selected luminescence methodology for dating Martian analogue material and another addressing the evolutionary dynamics of the sedimentary basin in Lanzarote.

Regarding luminescence, the protocol pIRIR$_{200}$ applied to fine-grained polymineral k-feldspar minerals yielded excellent results, particularly in aeolian environments. However, certain samples from slackwater deposit returned discreet results. Attempts were made to enhance outcomes by altering the protocol, specifically by reducing the temperature. Despite these adjustments, the results did not significantly improve, indicating incomplete sediment bleaching for these samples. Therefore, for a future perspective on the use of luminescence on Mars, it would be advisable to work on aeolian environments.

From a sedimentary perspective, this study successfully reconstructed the evolution of the El Jable basin from the late Marine Isotope Stage (MIS) 6 to the Holocene. This reconstruction enabled the correlation of deposits with different climatic periods, distinguishing between dry and humid conditions. However, it was not possible to delve into the details of the MIS using luminescence dating.

Overall, this work contributes valuable insights into Martian analogue dating methodologies and sedimentary basin evolution, setting the stage for future advancements in Martian geochronology.

Chapter 1

Mars

1.1 Introduction

Mars show a remarkably rich and complex geological record which unlikely those on Earth is well preserved due to the absence of crustal recycling operated by Plate Tectonics. Since the 1960s, over 40 missions, whether orbiting, landing, or conducting surface exploration with rovers, have significantly advanced and broadened our comprehension of the celestial body's geological, climatic evolution, and potential for habitability (Fig. 1). Enormous progress has been reached in the field of hyperspectral analysis and identification of local mineralogy from orbit (Christensen et al., 2001, 2003; Murchie et al., 2007; Rossi and Gasselt, 2010) and, therefore of the rock's composition present on the planet surface.
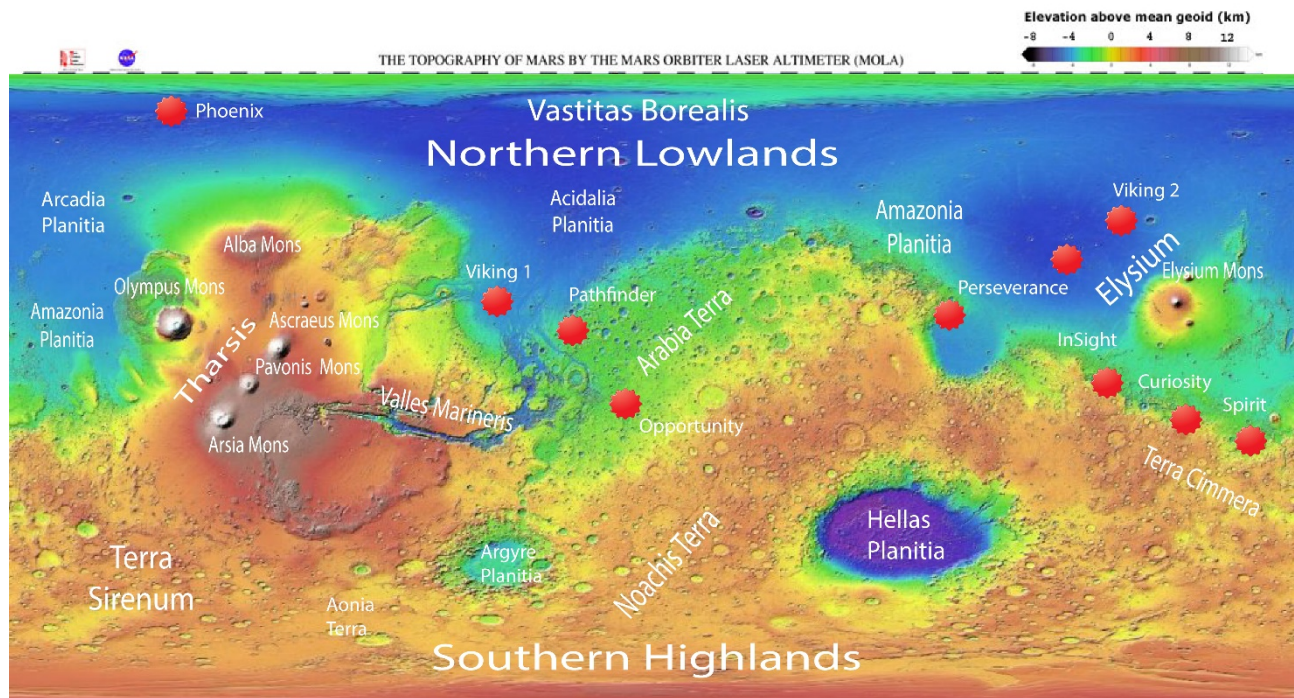
Figure 1. Maps of Mars' global topography (MOLA dataset), captured by HiRes, showing landing site (red dots) and elevation contrast between northern and southern hemispheres. The Tharsis volcano-tectonic province is situated near the equator within the longitude range 220° E to 300° E, featuring the expansive Valles Marineris canyon system and significant volcanic shields, including Olympus Mons (18° N, 225° E), Alba Patera (42° N, 252° E), Ascraeus Mons (12° N, 248° E), Pavonis Mons (0°, 247° E), and Arsia Mons (9° S, 239° E). Prominent impact basins include Hellas (45° S, 70° E), Argyre (50° S, 320° E), Isidis (12° N, 88° E), and Utopia (45° N, 110° E). Tharsis and Elysium Regions, with major volcanoes are also highlighted.

Geological processes are the key driving forces that shape the surfaces, crusts, and lithospheres of planets. These processes are closely connected with interactions in the atmosphere, encompassing aeolian and polar phenomena, activities in the hydrosphere like fluvial and lacustrine processes, and events in the cryosphere, involving glacial and periglacial occurrences. Additionally, internal planetary processes such as tectonism and volcanism contribute to these dynamics. External influences from the planetary environment, demonstrated by impact cratering processes, further contribute to these transformative forces. The resulting sedimentary features on Mars lead us to hypothesize that the planet may not have always been as inactive as it appears today. Approximately 3 billion years ago, the Red Planet seemingly deviated from its current cold, dry, and inhospitable state. Geochemical data and models support the notion that the early atmosphere was denser and composed of different elements. Consequently, surface heat retention was higher, and temperatures elevated. The increased atmospheric pressure likely facilitated the existence of liquid water. Several discoveries provide evidence for a different early climate on Mars, such as the glauconitic-like clay minerals discovered in Gale Crater in 2016 by the Curiosity Rover. Their

formation required specific stable conditions over thousands of years, including temperatures between -3 and 15 °C and a neutral pH of the water (Losa-Adams et al., 2021). In Gale Crater, the hydrated calcium sulfate veins detected by the ChemCam of Curiosity "may indicate a prolonged activity of aqueous processes in relatively nonacidic conditions and under limited temperatures and lithostatic pressures" (Nachon et al., 2014). The potential presence of liquid water in the past is further supported by numerous geological structures on the Martian surface, such as deltas, valley networks, and open-basin lakes.

While progress has been made in answering to many questions, numerous aspects remain unresolved. In the context of planetary exploration and the concept of habitability on other planets, comprehending the geological processes and climatic cycles becomes essential. This understanding is crucial for assessing both the negative and positive impacts on potential future human missions to Mars.

1.2 Physical and Chemical Characteristics

Mars diameter is a little over half that of Earth with an equatorial axis of about 3397 km, and a polar axis of about 3376 km. The surface area of Mars is 149×106 km² which roughly corresponds to the surface area covered by land masses on the Earth. Mars' surface gravity has a value of 3.711 m/s² and is thus in between that of Earth (9.81 m/s²) and Earth's moon (1.63 m/s²).

Mars atmosphere is less than 1% as dense as Earth and is made up of carbon dioxide (95%), nitrogen (3%), argon (1.6%), with traces of oxygen and water (Mahaffy et al., 2013). The pressure at the surface ranges from 6.9 to 9 mbar with peak values of 14 mbar at the deepest elevation and 0.7 mbar at the top of Olympus Mons. Surface pressure vary considerably due to seasonal condensation of CO_2 at the poles where up to 25% of the atmosphere sublimates. Due to the thin atmosphere, the Red Planet is incapable of holding heat, therefore the temperature varies between 20°C and -153°C (Kieffer et al., 1977). At these temperature and surface pressure ranges, liquid CO_2 cannot be stable therefore during the Martian summer carbon dioxide ice sublimes from the pole and redeposited during the winter. At least 12-16 % of the atmosphere is deposited and removed each Martian year which process generates a great pressure change and strong wind (Genova et al., 2016).

Mars is a rock planet composed of minerals containing silicon and oxygen, metals, and other elements. Similarly, to other rock planets, Mars interior is differentiated into crust, mantle, and core. The crust is probably largely of basaltic composition (although some crustal rocks, especially in the northern hemisphere, might be made of andesite) with a variable thickness of 30-100 km, greater in the southern hemisphere (Jacqué, 2006; Wieczorek and Zuber, 2004; Goossens et al., 2017). The crust is considered to be a one-plate planet showing no indication of plate tectonics. The mantle chemical composition is probably like Earth, but it is still unknown whether the discontinuity between the upper and lower mantle exists (Dreibus and Wanke, 1985; Zuber, 2001). The metallic core is considered to have a radius of roughly 1300-1500 km (Schubert and Spohn, 1990; Stevenson, 2001; Rivoldini et al., 2011). The absence of a magnetic field leads to the conclusion that Mars core is mainly solid today (Connerney et al., 1999, 2001; Solomon et al., 2005) even though a fossil magnetization discovered in the rock from the southern hemisphere dated billion years, makes us speculate that Mars must have had a magnetic field. The magnetic field could have prevented the ablation of the old atmosphere by the charged particles of the solar wind and thus established the climatic conditions.

1.3 Geology and Geochronology

Topographically, Mars shows a wide height range from -7550 m at the deepest point located in the Hellas Planitia impact basin in the eastern hemisphere to 22640 m at the top of Olympus Mons, the highest volcano in the solar system (Hartmann, 2003). Due to the absence of sea level, these elevation values referred to the equipotential surface of aeroid with a radius of 3396 km (Smith et al., 1999), in which zero altitude was defined by the height at which atmospheric pressure is 610.5 Pa corresponding to the triple point of water (Zeitler et al., 2000).

A marked visible feature of the Red Planet is its dichotomy boundary evidenced by an escarpment located in mid-longitude which divides the northern hemisphere from the southern one. The northern one shows lower altitudes while the southern one presents higher altitudes and more impact craters with basins (Rossi and Gasselt, 2010) (Fig. 1). Two-thirds of the Martian surface is heavily cratered like the surface of the highlands on the Moon. The surface has clearly survived the period of the Late Heavy Bombardment (LHB) that all the planetary bodies in the inner Solar System experienced prior to around 3.7 Ga.

The knowledge of Martian geological history and its graphic representation in a map is a result of many observations started in the 70s on Viking and Mariner 9 missions' images together with topographic data. Stratigraphic relations, lithologic properties, and changing features are useful geomorphic characteristics of geologic mapping.

Soderblom et al. (1974) first recognized four stratigraphic sections: ancient-eroded uplands, cratered plains, Elysium volcanic rocks, Tharsis volcanic rocks. The concept of ancient is based on the simple fact that the more a unit is cratered, the more was exposed to the impact flux, and, thus, it is the older. Neukum and Wise (1976) developed a cratering chronological model calibrated and scaled to the lunar cratering rate providing the basis for a Martian time scale.

The first global geological map of Mars was established by Scott and Carr (1978) representing a time-stratigraphic classification with three different periods (Noachian, Hesperian, Amazonian). Subsequently Tanaka (1986) divided these periods into eight epochs (Early Noachian, Middle Noachian, Late Noachian, Early Hesperian, Late Hesperian, Early Amazonian, Middle Amazonian, Late Amazonian, see next paragraph) which were dated by the chronology function of Hartmann and Neukum (2001) based on the Ivanov (2001) crater production function. The Crater Size-Frequency Distributions (CSFDs) is a time-dependent tool used to date Martian units, and it is based on the correlation between crater diameters with specific terrain units subsequently fitted to an impact cratering rates model based on Earth and Moon cratering rate history. Nevertheless, the dating method has a poor temporal resolution. The lunar crater record itself presents an uncertainty of approximately a billion years during the Hesperian. Additionally, the Martian impact flux might have varied, ranging from being equivalent to the Moon to up to five times higher. Moreover, fluvial and aeolian weathering on Mars's surface has changed the shape of impact craters, therefore their preservation is compromised. As a consequence, the accurate ages of Martian surface units are ambiguous, with potential variations of two or more times on older terrains. Furthermore, disagreements may extend to an order of magnitude or more on younger surfaces with fewer craters (Cohen et al., 2019).

The most detailed and updated geological map of Mars was produced by Tanaka et al. (2014), through Mars Global Surveyor Mars Orbital Laser Altimeter (MOLA) topographic reconstructions and Mars Odyssey Thermal Emission Imaging System (THEMIS) infrared image mosaics. The map is a result of a correlation between age, and eight geologic unit groups (polar, impact, volcanic, apron, basin, lowland, highland, and transition) (Fig. 2). The result is a very detailed map consisting of 44

different units.
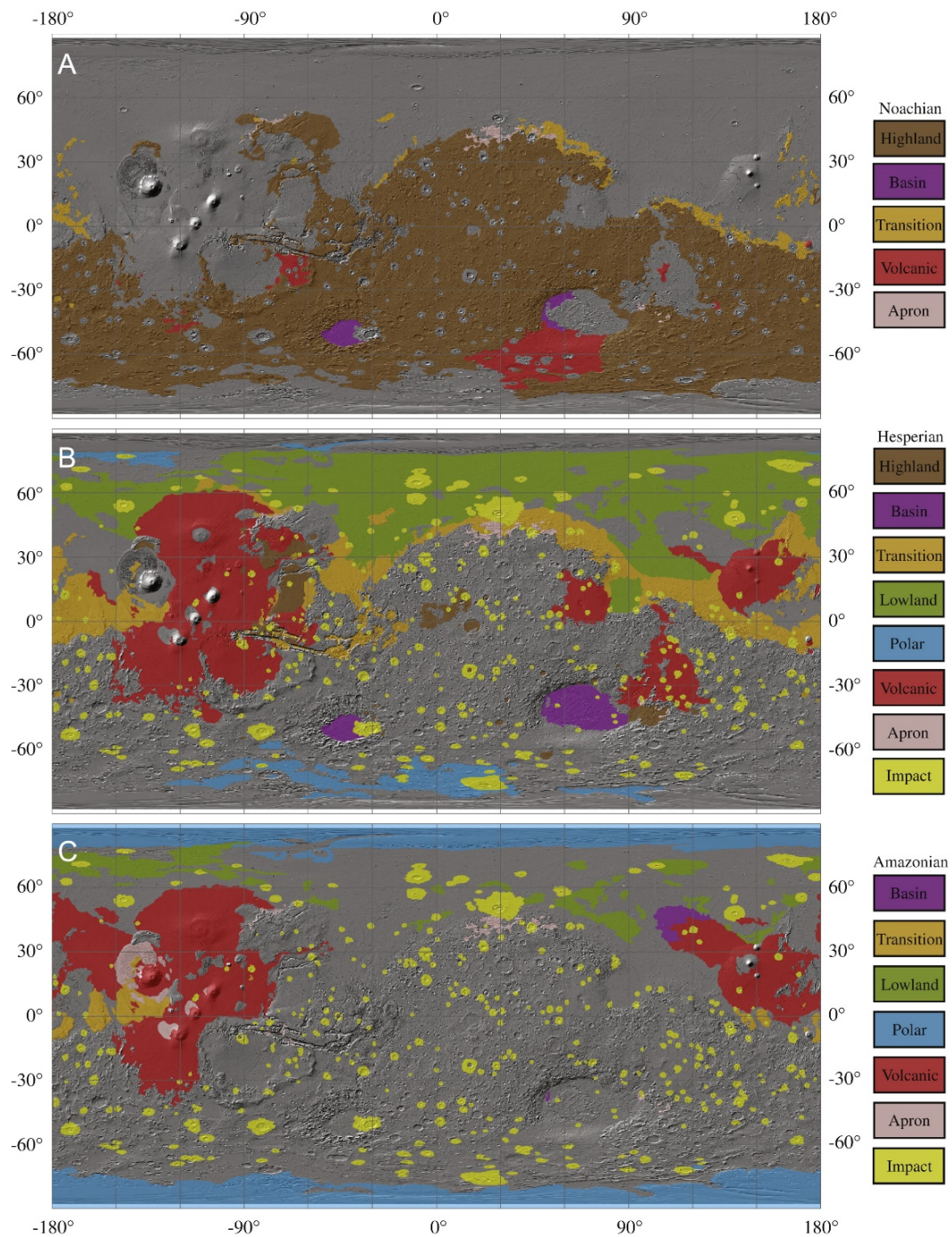
Figure 2. Martian unit groups organized by geological periods: (A) Noachian, (B) Hesperian, and (C) Amazonian. The Noachian map (A) highlights ancient highland dominance with minimal volcanic influence, while the Hesperian rocks (B) reveal northern lowland infilling, impact basins, polar deposits, and Tharsis and Elysium volcanic growth. The Amazonian map (C) depicts ongoing Tharsis and Elysium volcanism, local mass wasting, sediment accumulation in highland-lowland transitions, and sedimentary apron formation around Olympus Mons. Scattered Hesperian and Amazonian impact craters mark the highland landscape (B and C) (Tanaka et al., 2014).

1.3.1 Noachian Period

Named after Noachis Terra this period include the oldest units: Early Noachian (4.08 - 3.96 Ga), Middle Noachian (3.96 - 3.85 Ga), Late Noachian (3.85 - 3.57 Ga) (Werner and Tanaka, 2011), predominantly located in the highland's terrains of the southern hemisphere. The informal pre-Noachian represents the interval of the accretion and differentiation of the planet started about 4.6 Ga. To this epoch belongs the buried or inferred large impact basins: Utopia, Acidalia, Chryse, and it is likely that the magnetic field was active. In fact, the most ancient terrains (>3.9 Ga) which include Terra Sirenum, Arabia Terra, and Terra Cimmeria, display magnetic anomalies together with relatively large tectonic structures such as extensional and compressional faults, structurally controlled basins, mountain ranges, and ridges.

Most of the geologic record of this interval has been erased by the intense impact bombardment occurred from the Early to Late Noachian Epochs. The surviving geological units can be ascribed to the largest impact basins (Hellas, Isidis, Argyre) and probably to the low elevation of the northern lands that generated the crustal dichotomy. Noachian highland and volcanic edifices are fewer in the Middle Noachian than in the Early Noachian. The Tharsis bulge is thought to have formed during the Noachian as well as the numerous valley networks widespread in the southern highlands. Several authors attribute the origin of the valley network to water in liquid state. This presence in later periods is rare, and valleys might be witnesses of warmer and wetter climatic condition in the early planet's history (Squyres and Kasting, 1994; Clifford and Parker, 2001; Salese et al., 2016). Many fluvial and lacustrine deposits dated to Noachian have been discovered and studied (Pondrelli et al., 2005; Mangold and Ansan, 2006; Fassett and Head, 2008; Di Achille and Hynek, 2010; Goudge et al., 2012). Numerous craters show channels entering from one side, depositing material originating delta fan-like morphologies and spilling out on the other side of the crater. One of the most famous is the Jezero crater in Isidis Planitia, the landing site of the Perseverance rover. Several sedimentary structures discovered within craters appear to have formed from ponding of water and lake formation. A theory of a primordial ocean was also suggested (Clifford and Parker, 2001; Di Achille and Hynek, 2010). At the end of the Noachian most hydrologic activity at the surface and large floods ceased (Fassett and Head, 2008). Phyllosilicates (clay) were discovered in the Arabia Terra, Terra Meridiani, Syrtis Major, Nili Fossae, and Mawrth Vallis regions. These minerals usually derive from alteration products of igneous minerals (found in magma) due to long-term contact with water. This could be another confirmation of a moist environment present during the

Noachian.

1.3.2 Hesperian Period

The Hesperian Period (named after Hesperia Planum) was less subject to impact cratering therefore the geological units are better preserved. The Period comprised two Epochs: Early Hesperian (3.57– 3.40 Ga) and Late Hesperian (3.40- 3.00 Ga) (Werner and Tanaka, 2011). The transition from Late Noachian to Early Hesperian is marked by the change in climate from warmer, wetter to colder, dryer conditions (Hartmann and Neukum, 2001). Consequently, the landform morphology, mineralogy, erosion, and weathering rates changed drastically. As a result of higher evaporation and aeolian activity, sulfate-rich deposits became more evident. The presence of sulfate is an indication of how the environment has changed from being moist in the Noachian to acidic in the Hesperian. Ephemeral lakes or seas may have formed just in the northern lowlands.

The crustal contraction during the Early Hesperian, perhaps linked to planetary cooling, generated tectonic structures related to moderate- to high-relief wrinkle ridges. The perpendicular orientation of Valles Marineris to the wrinkle ridges could be related to its tensional origin started during this Epoch (Fig. 1).

The Hesperian was dominated by extensive vulcanism in the form of ridged plains and shield-like central edifices known as paterae (such as Apollonaris, Alba, Peneus, Hadriaca, Amphitrites); the widespread highland valley of the Noachian cease to form, and extensive lava plains developed forming Hesperia Planum, Syrtis Major Planum, Malea Planum and much of the floor of Hellas (Carr, 2007).

During Late Hesperian, volcanism became concentrated within the Tharsis (including Ascraeus, Pavonis, and Arsis Montes) and Elysium (including Elysium Mons) provinces. Adjacent to these major volcanic provinces, catastrophic releases of ground water carved extensive outflow channels.

During Hesperian, in the southern circumpolar several units associated to ice interactions deposits shaped the Dorsa Argentea Formation (esker-like ridges, marginal pits, a candidate marginal lake deposit, several major valleys).

1.3.3 Amazonian Period

Named after Amazonis Planitia the Amazonian Period comprises the Early Amazonian (3.00- 0.88 Ga), Middle Amazonian (0.88- 0.235 Ga) and Late Amazonian Epochs (0.235 Ga – present) (Werner and Tanaka, 2011). Low rates of meteorite impacts, cold and hyper arid conditions, aeolian processes and oxidizing environments are the main characters of this Period. Sporadic and more regionally concentrated is the volcanic and glacial/periglacial activity. The volcanic activity prevailed during Middle Amazonian Epoch in the Tharsis and Elysium regions forming the largest shield volcanoes: Olympus, Alba, Ascraeus, Pavonis, and Arsia Montes. Small basaltic shields, fissure vents, and lava flows occur during the Late Amazonian Epoch. The Amazonian lowlands cover much of the northern hemisphere and are interpreted to be characterized by both volcanic and outflow channel flooding material. The northern Middle Amazonian lowland cover part of the Vastitas Borealis where the most extensive accumulations of dune sands surround the Planum Boreum.

The Amazonian cryosphere, thick up to ca 9 km at the equator to ca 10-12 km at the poles, have generated many geological units such as ice-cemented dust, fretted terrain, terrain softening, Lobate debris aprons and glaciers (Carr, 2007). During the Late Amazonian the Polar caps developed on the Planum Boreum and Planum Australe plateaus, consisting of carbon dioxide ice overlying water ice (Byrne, 2009) with evidence of melting ice.

Surface alteration by the formation of anhydrous ferric oxides led to the planet's characteristic red color (Fig. 3).
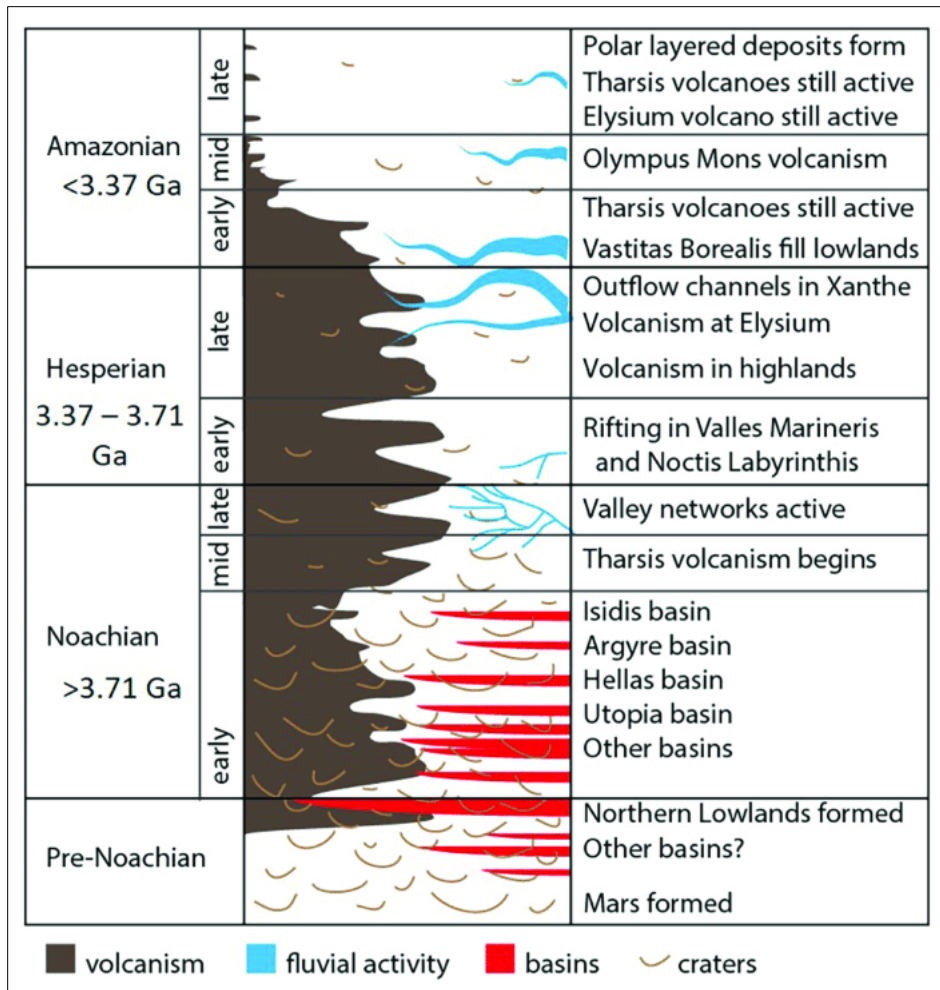
Figure 3. A simplified geologic time scale of Mars, highlighting key geological events according to Howari et al. (2021).

1.4 Mineralogy

Remote sensing data from the Mars Global Surveyor Thermal Emission Spectrometer (TES), the visible/near-infrared (IR) spectroscopy from spacecraft-based and Earth-based telescopes and X-rays diffraction analysis have revealed the type of volcanic products and their mineralogic composition. Mars' surface is predominantly composed of mafic materials, with basalt being the dominant fine-grained magmatic rock, featuring high-Ca clinopyroxene and plagioclase feldspar (Fig. 4). While exhibiting typical basaltic characteristics, certain regions display a higher silica content, resembling andesitic rocks on Earth or even silica glass. Regions of low albedo show concentrations of plagioclase feldspar, with northern low albedo regions displaying higher than normal concentrations of sheet silicates and high-silicon glass. Hematite is consistently identified, while the

detection of carbonates and sulfates lacks robustness. Olivine is found in isolated regions, albeit below the limits of detection (Bandfield, 2002). Much of the surface is deeply covered by finely grained iron (III) oxide dust (Christensen et al., 2003; Golombek, 2003). While quartz hasn't been globally detected, specific areas, such as the northern flank of the Syrtis Major volcanic construct, reveal quartz-bearing granitoid rocks (Christensen et al. 2005). The Martian landscape also hosts clay minerals and sulfate deposits, adding significant layers to its geological history. Clays, associated with aqueous alteration, have been discovered by rovers like Curiosity, particularly in Gale Crater, indicating Mars' watery past. Sulfate deposits, found in regions like Meridiani Planum, point to a history of acidic water, as extensively studied by the Opportunity rover.
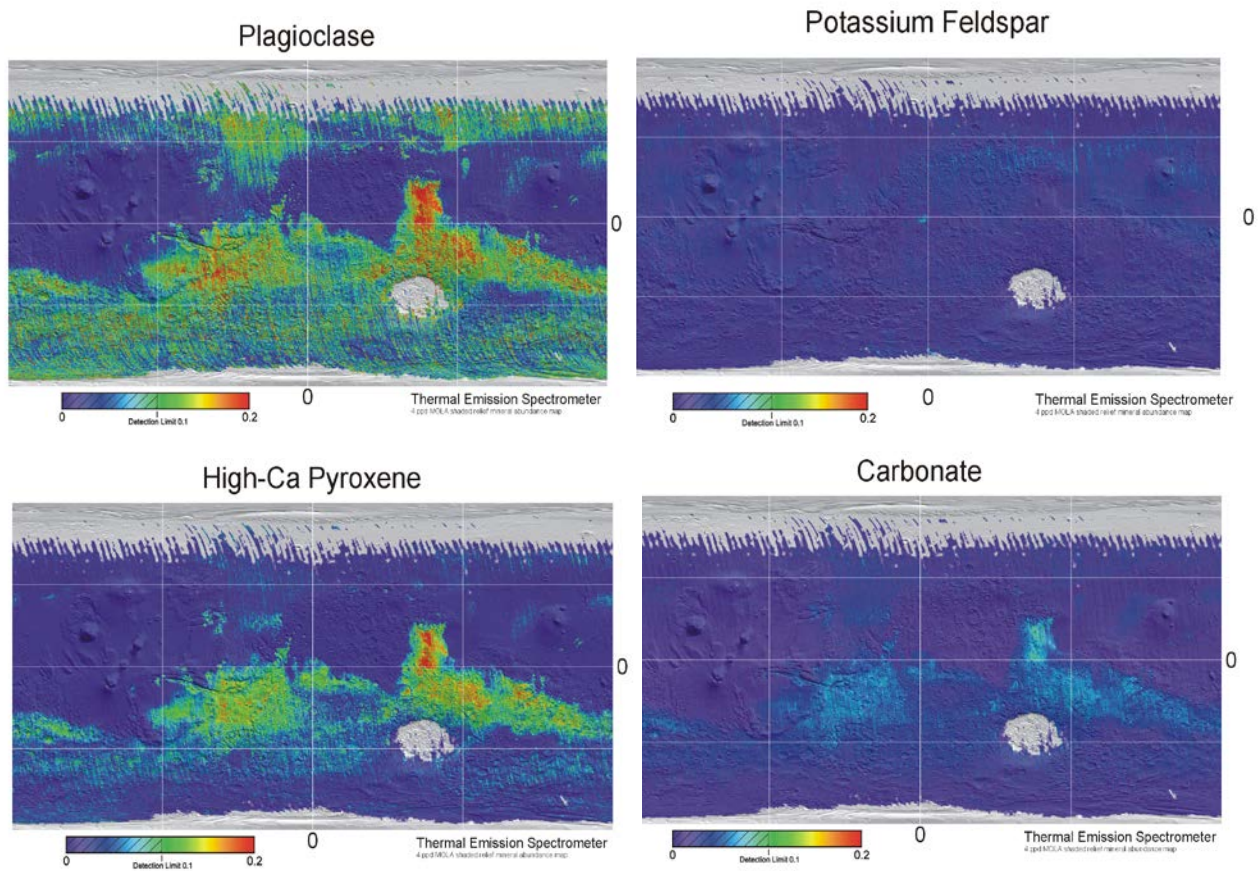

Figure 4. Global-scale spectral remote sensing of Mars using the Thermal Emission Spectrometer (TES). Concentration maps of plagioclase, potassium feldspar, high-calcium pyroxene, and carbonate (Bandfield, 2002).

1.5 Endogenetic processes

From a geological point of view, the endogenetic processes are those phenomena that originate within the lithosphere. The processes are related to a re-establishment of internal thermal equilibrium and are associated with those structures that generate heat to maintain their body temperature. The achievement of equilibrium is expressed by geological structures such as volcanoes, tectonic movements, and seismic phenomena, which continuously redefine the surface shapes, creating depressions, reliefs, and deformation in the rock layers and new crust.

1.5.1 Volcanism and Tectonic

Volcanism is recorded from the early history of Mars to the Late Amazonian Epoch, but it is not uniformly distributed. Two topographically dominating and morphologically distinct volcanic provinces are recognized: the Tharsis and Elysium regions. Their morphologies are strongly analogous to terrestrial basaltic volcanic landforms. Both are situated close to the equator on the dichotomy boundary between the cratered (older) highlands and the northern lowlands (Fig. 1).

Several volcanic landforms are observed based on the different eruption styles: central volcanoes, tholi, paterae, and small domes, as well as vast volcanic plains.

The Tharsis region is the most dominating feature of the Martian topography and shows numerous volcanic edifices of different ages and morphology which have originated multiple lobate flows of lava. The region hosts the largest volcanoes of the Solar System (Olympus Mons, Ascraeus Mons, Pavonis Mons, and Arsia Mons) which share many characteristics with Hawaiian basaltic shield volcanoes. The main differences between the Martian and Terrestrial volcanos are the greater sizes and lengths of the Martian ones, due mostly to the lower gravity and higher eruption rates. Their eruption style appears effusive and relatively non-explosive in nature, although there are indications of composite volcano construction (Werner, 2009). Another distinction is the Martian volcanos lifetime which is much longer than the Terrestrial ones: Tharsis volcanoes took billions of years to reach today's morphologies.

The Elysium is the second-largest volcanic province on Mars and includes three volcanos: Hecates Tholus, Elysium Mons, and Albor Tholus. The domes volcanos emitted effusive lava flows considered to be more viscous than ordinary basalts (Werner, 2009) (Fig. 1).

Nowadays there are no ongoing tectonics activities such as volcanism and mountain-building processes. However, a variety of tectonic structures are observed, both compressional (wrinkle ridges, lobate scarps, fold belts) and extensional (simple graben, complex graben, rifts, tension cracks, troughs, and polygonal troughs). The features could be evidence that tectonic activities such as convection or subduction mechanisms, were active up to a certain point. An ancient phase of plate-tectonic could justify the magnetic anomalies in the cratered highlands (Rossi and Gasselt, 2010).

1.6 Exogenic processes

Exogenic processes have shaped (and some of these still do) the Martian surface, generating unique scenarios in the Solar System. Many Martian landforms and deposits resemble Terrestrial counterparts, although their scale is much greater.

Erosion and deposition processes have led to the formation of, fluvial landforms, lake and ocean-related landforms, and polar, circumpolar, periglacial, glacial, and mass-wasting landforms such as aeolian landforms. Only a few of these processes are still active.

Evidence for locally effective agents moving materials, including modem observations of dust storms and surface albedo changes, is juxtaposed with the preservation of many landforms billions of years old.

1.6.1 Impact Crater Landforms

The Late Heavy Bombardment (LHB) between 4 Ga and 3.8 Ga significantly shaped the planets of the Solar System, leaving visible impact signs on Mars and Mercury. Major Martian basins, such as Hellas, Argyre, Isidis, and Utopia, likely originated from this event and contributed to the planet's hemispheric dichotomy. The bombardment, coupled with solar wind erosion, may have led to the erosion of Mars' primordial thicker atmosphere. Mars exhibits over 42,000 cataloged impact craters ≥ 5 km in diameter, influencing various geological units. In older units like the Noachian uplands, impacts define the terrain and create topographic roughness. Fluvio-lacustrine systems identified in 179 craters from the Middle or Late Noachian formed through water and sediment influx from valley networks and channels (Cabrol & Grin, 1999).

The study of undersurface crustal material involves analysing ejecta deposits formed during impact, providing insights into cratering processes, gravity conditions, atmospheric presence, and icy substrates (Fig. 5). Older impact craters offer clues to modification processes and stages, including volcanic, fluvial, glacial, periglacial, and aeolian forces.

Impact craters play a crucial role in geochronology studies, helping reconstruct planetary surface stratigraphy through crater size-frequency distribution analyses. This method, associated with crater density and radiometric ages, contributes valuable information derived from Moon's samples (Ivanov and Head; 2001).

Figure 5. Image taken from HiRISE showing a new Mars crater, 8 meters wide, formed explosively with a blast zone extending over a kilometer. Materials near the crater display yellowish and lighter grey hues, while ejected materials further away vary from dark brown to bright bluish in enhanced-color view, indicating impacts on different geological layers (ESP_048456_1640; NASA/JPL-Caltech/UArizona).

1.6.2 Water-related Morphologies

According to many authors the climate during the Noachian was warmer and wetter, significantly different from the present hyper arid cold desert environment (Squyres & Kasting 1994; Cabrol & Grin 1999; Bishop et al., 2018; Palumbo & Head, 2018). Denser atmosphere, higher pressure, moist

climatic regimes might have allowed the formation of water in the liquid state which probably survived for long periods eventually outgassing at the end of Noachian.

With the present conditions (mean atmospheric pressure of 6 mbar; mean diurnal temperatures ranging from – 120 °C at the pole to – 50 °C at low latitude) liquid water is unstable on Mars surface. Water intended as a molecule of hydrogen and oxygen was detected on surface in various forms: as a sequence of ice-rich layers, and as mantles of snow in the northern polar ice caps and at mid-latitudes (Christensen, 2006); as water vapor showing seasonal, vertical, and latitudinal variations in the atmosphere (Fouchet et al., 2007; Fedorova et al., 2018); as liquid spheroids interpreted as brines on ground ice on Mars Arctic (Rennó et al., 2009). Evidence of past water on Mars is also provided by the numerous hydrated minerals detected by the Spectro-imaging instrument (OMEGA) on Mars Express. Phyllosilicates (clay) which derived from alteration products of igneous minerals (found in magma) due to long-term contact with water were discovered in the Arabia Terra, Terra Meridiani, Syrtis Major, Nili Fossae, and Mawrth Vallis region; hydrated sulphates formed through interaction with acid water, were detected in layered deposit in Valles Marineris, Terra Meridiani and within dark dunes in the northern polar cap.

By the analyses of the low-frequency radar profiles acquired from Mars Express spacecraft, a stable body of salty liquid water was discovered at about 1.5 km below the ice of the South Polar Layered Deposits (Orosei et al. 2018).

Although today water in liquid form on the Martian surface has not been found, evident superficial erosion-geological features that resemble those water-related on Earth are widespread.

The most impressive are the **Valley networks** which reminds the terrestrial river drainage systems. These features are concentrations of widespread giant dendritic channels that might have formed by surface runoff following rainfall or as result of groundwater discharge (Fasset and Head, 2008). The average length is around 200 m, but some can reach over thousands of kilometres (e.g., the Naktong Vallis/Scamander Vallis/Mamers Vallis system), the maximum width is of several hundred meters and average depth around 80 meters. Valley networks occur predominantly in Noachian cratered highland terrain but also on mid-to-higher latitudes, dissecting volcanic edifices, and crater walls (Fig 6). Although they resemble terrestrial stream valleys, the Martian valleys are far less complex: fewer branches, steep walls, flat floors, and a cross sectional shapes varying from V-shaped in the upper reaches to U-shaped in the lower reaches. Low tributaries constituted a

moderately lower drainage density than those on Earth. The networks themselves are spaced apart, indicating that low competition was present between adjacent drainage basins (Chapman, 2007).
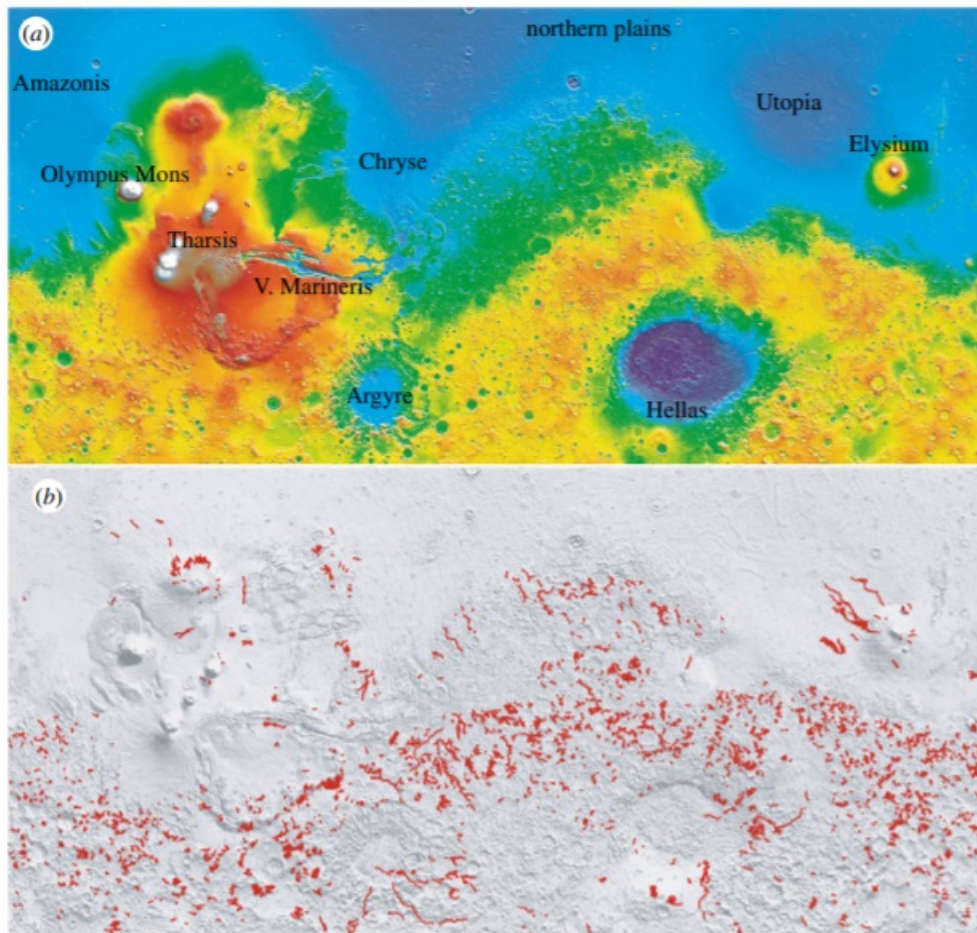

Figure 6. Above: Global topography; Below: the distribution of the larger valley networks (Carr 2012).

The category of fluvial features also includes **outflow channels** which are channels of thousands of km long, tens of km wide, showing low sinuosity, rare tributaries, common branching downstream resulting in an anastomosing pattern of channels (Fig. 7). They have been interpreted to be the result of some sort of catastrophic fluid release (most likely water), about two orders of magnitude larger than the largest known flood events on Earth but a certain role of ice in channel formation and modification has been proposed too (Chapman, 2007). The outflow channels typically postdate the valley networks, although most are still very ancient. They seem to have formed at a time when climatic conditions were like those of today, during the Late Hesperian Epoch. Tributaries are rare, but branching downstream is common, resulting in an anastomosing pattern of channels.

The distribution of outflow channels is limited to four main areas: Chryse-Acidalia basin, west of the Elysium volcano complex in Elysium Planitia, the eastern part of Hellas basin, along the western and southern border of Amazonis Planitia.

Figure 7. Kasei Vallis (25◦ N, 300◦ E), the largest outflow channel on Mars, emerges from a shallow north-south canyon extending to the eastern northern plains (Carr 2012). Flow was from the bottom left to right.

Together with the valley networks and outflow channels, **lake basins** were part of the Martian hydrological system. According to Fasset and Head (2008), they were fed by precipitation and runoff, forming a sort of lake-chain system. Groundwater as well was an important net source for the preservation of the largest lakes, more widespread in the lowlands. Numerous lake basins were common in impact craters in Terra Sirenum, Argyre basin, Hellas basin, Valles Marineris and Parana Crater, fed by both Valley Networks and Outflow channels, among which many of them consist of both inlet and outlet valleys. Deposits of probable ancient lake in the Gusev Crater have been closely photographed by Curiosity Rover. The most famous picture (Fig. 8) shows fine-grained, horizontally layered, easily erodible sediments which resemble a paleolake environment where water persisted in a stable environment for long time. Curiosity not only photographed but also took soil samples to be analysed with X-ray diffraction. The Windjana sample, which represents the Dillinger Unit, is interpreted as an aeolian sand unit among fluvial deposits, and it is mainly composed of alkali

feldspar (microcline, orthoclase and sanidine), plagioclase feldspar (andesine), mafic silicates (augite, pigeonite), and iron oxide spinel (magnetite) (Treiman et al., 2016).

Figure 8. Picture of the Kimberley formation made by Curiosity rover. Indications of a possible ancient lake in Mount Sharp are evident, as the layers in the foreground incline towards the base, suggesting the flow of water toward a pre-existing basin. The strata further reveal that water flowed towards the basin before the larger bulk of the mountain's main structure formed (www.nasa.gov).

Several **deltas** have been identified mostly located in the paleo lake within craters or over a narrow elevation range along the dichotomy boundary, interpreted as outflow into a northern ocean. The deltas typically are fan shaped, outlined by an outward-facing scarp, and have distributary channels on their upper surfaces. Two particularly striking deltas are in the craters Eberswalde and Jezero (Fig 9). In Eberswalde Crater, river meanders grew and cut off their loops (as on Earth), then the wind slowly blown away the floodplain sediments, leaving the channel beds behind as ridges. The information detected by the Compact Reconnaissance Imaging Spectrometer for Mars and the Context Camera positioned on NASA's Mars Reconnaissance Orbiter has revealed that the delta in Jezero crater constituted of phyllosilicates and carbonates (magnesite) deposits, indicating a probable past aqueous environment. It is no coincidence that Jezero was chosen as the landing site of Perseverance rover in 2021 to better analyse the origin of these deposits and seeking proof of ancestral form of life. In fact, on Earth carbonates support the preservation of micro and macro life forms as rocks and fossils. The sedimentological analysis performed on the images made by Perseverance, reveal presence of cobbles and boulders in steep foresets which on Earth indicate a

delta progradation into a deep lake. Multiple flood episodes where of variable intensities as indicated by the shape of some boulder conglomerates lying on delta deposits (Mangold et al., 2021). The lack of deep incision of the deltas as the lake levels declined suggests that the fluvial activity declined abruptly (Carr, 2012).
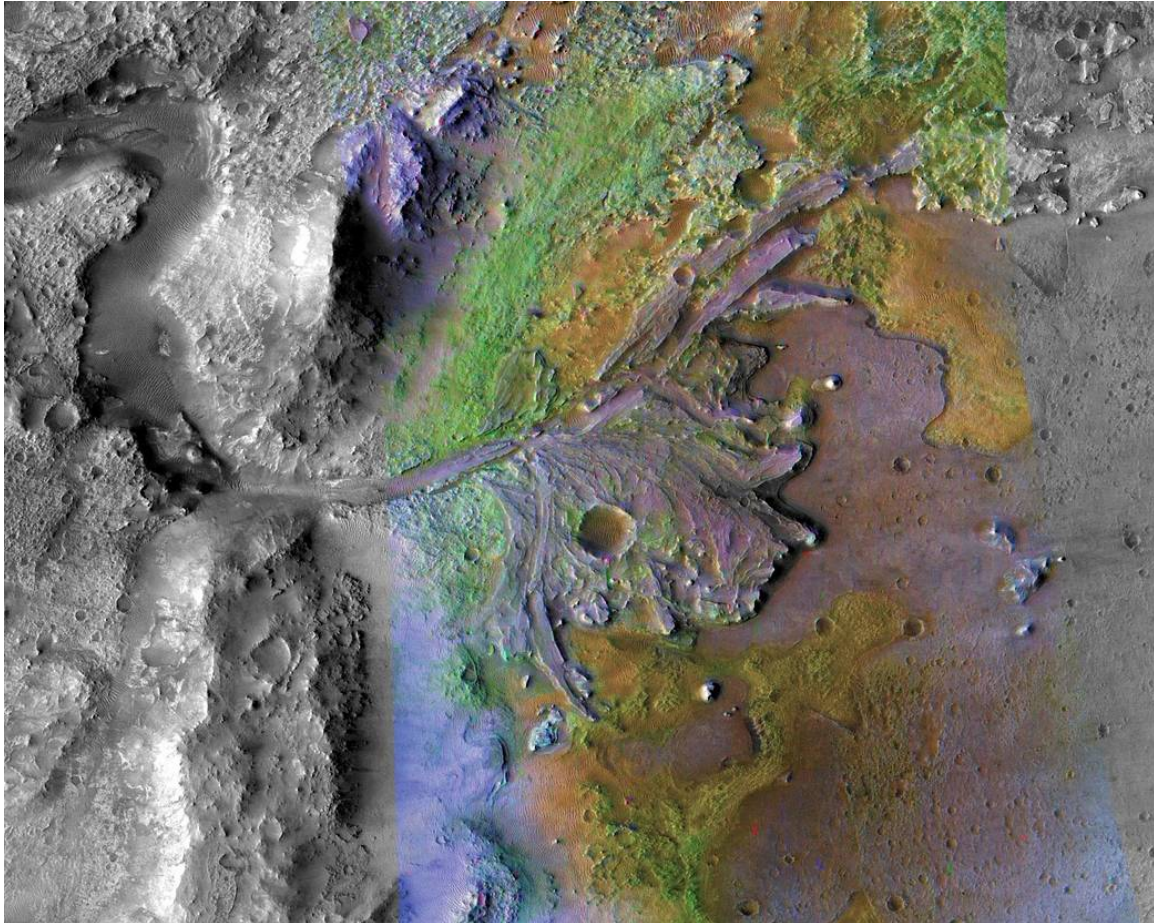

Figure 9. Image of the delta in Jezero Crater, the landing site of Perseverance rover. The green color represents carbonates, the orange represents olivine sand eroding out of carbonate-containing rocks (NASA/JPL-Caltech/MSSS/JHU-APL).

Within some meteoritic impact craters, not only deltas but also **alluvial fans** morphologically like fluvial fans on Earth have been identified. Even thought they might remind other radial deposits (deltas or distributive fluvial system) the alluvial fans are strictly related to the type of deposits which are transported by sporadic, high energy, surface flow events interspersed with long periods of dry inactivity. As on Earth, alluvial fan formation is highly linked to climate, so their study allows us to better understand climate evolution. Martian fans are widespread within craters in Noachian highland mostly between 39°N and 50°S, although the majority are between n 10°S and 30°S. Some of these are very well preserved, thus the measurement of the fans, catchment area and basin reliefs can be easily performed by analysing data acquired by infrared THEMIS images and Mars

Orbiter Laser Altimeter (MOLA). Martian fans could be relatively large (up to 150 km in diameter), long (up to 40 km), showing low gradients, and slightly concave surfaces. Studies suggest that fans formed episodically during the Late Hesperian to Early Amazonian from snowmelt events (Wilson et al., 2021) (Fig. 10).

Figure 10. Perspective view of large alluvial fan deposit in Aurorae Chaos/Ganges Chasma. This region is thought to have played a pivotal role in channeling water into the northern plains during Mars' early history, estimated to be active within the first 1–2 billion years (ESA).

Chaotic terrains, associated with Mars' outflow channels, exhibit a unique morphology characterized by irregular arrays of fractured and tilted blocks, resembling terrestrial mesas or blocky terrains (Fig. 11). Typically found in the Martian highlands at low latitudes along the dichotomy boundary, these terrains span tens of kilometres and extend hundreds of meters deep. They are linked to abrupt water loss events, and various models propose their formation, yet uncertainties persist in the mechanism and evolution. Proposed formation mechanisms include pressurized water release from aquifers or subsurface cavernous systems destabilized by magmatic intrusions, dissolution of sub-cryospheric aquifers due to magma impact, release of CO_2 or gas-water mixtures from decomposed gas hydrates, and shallow subsidence of plateau regions resulting in fractured mesas (Rodriguez et al., 2005; Meresse et al., 2008; Zegers et al., 2010).
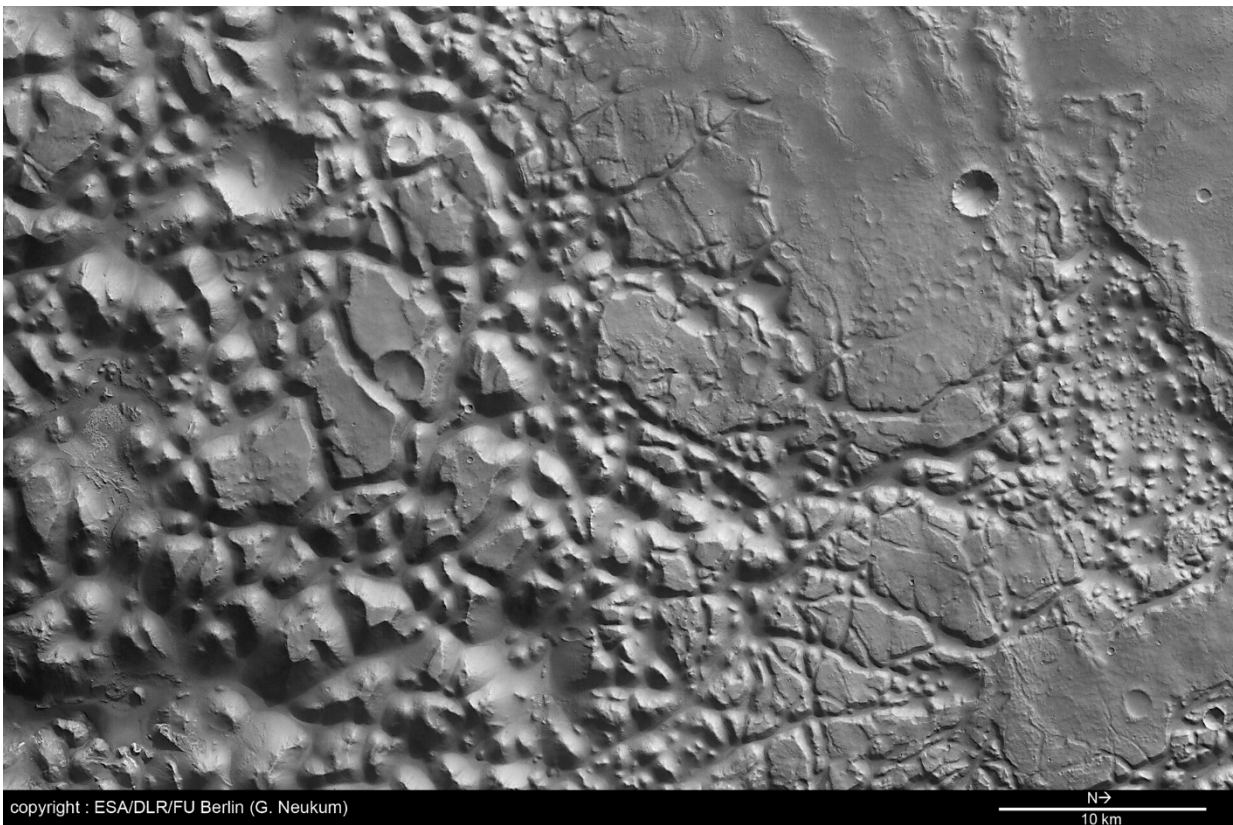

Figure 11. Chaotic terrain in Iani Chaos (www.esa.int)

The theory of a post Noachian-Hesperian **ocean** is supported by many authors (Baker et al., 1991; Parker et al., 1993; Head et al., 1999, Clifford & Parker, 2001; Carr &Head, 2003; Xiao et al., 2023). The Vastitas Borealis basin might have hosted a liquid water ocean which covered almost a third of Mars 'surface, known as Oceanus Borealis. Two possible paleoshorelines were recognised: the Arabia shoreline that roughly follows the topographic dichotomy, associated to the Late-Noachian Valley Networks and the Deuteronilus shoreline which largely follows the southern boundary of the Hesperian-aged Vastitas Borealis, associated to the Late Hesperian outflow channels (Fig. 12). Deuteronilus line elevation is supposed to be lower than Arabia, but different elevations and lengths for both have been proposed (Sholes et al., 2021). The theory of an ancient ocean is also supported by the discovery of deposits and landscapes related to mega tsunami events, such as boulder lobes extended to hundreds of kilometres as well as backwash channels (Rodriguez et al., 2016; Costard et al., 2017).
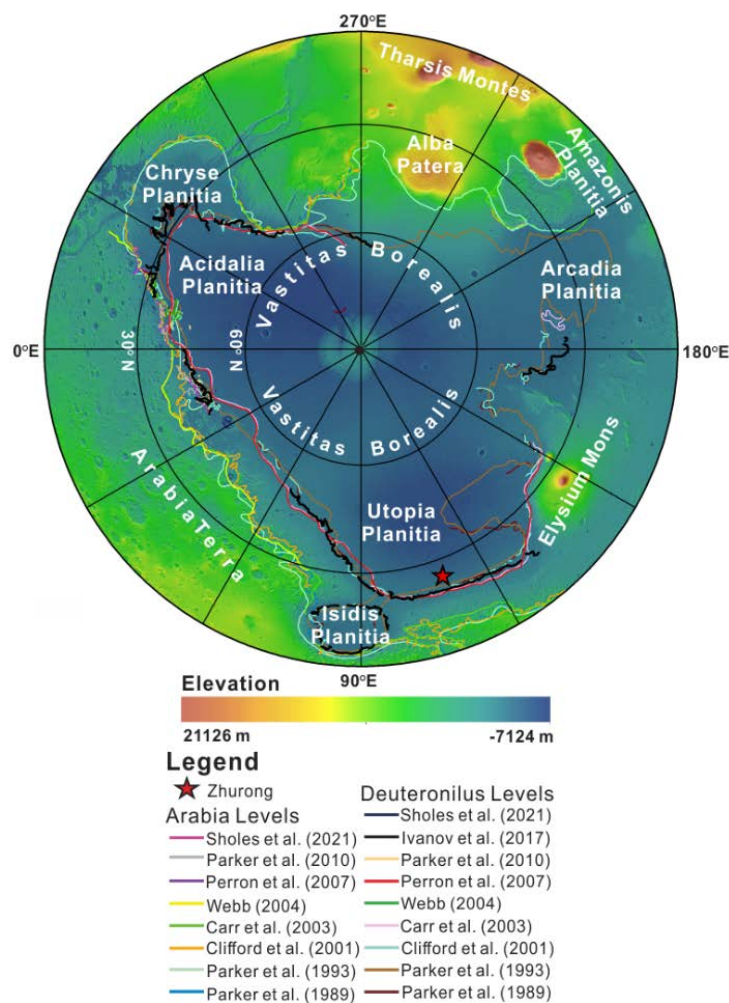

Figure 12. The Topographic map of Mars's northern hemisphere shows previously proposed shorelines related to Arabia and Deuteronilus. The red star denotes the location of the landing site of the Zhurong rover (Xiao et al., 2023).

1.6.3 Mass Wasting Landform

Mass wasting is a significant process contributing to the degradation of landforms on Mars. The absence of an atmosphere allows these structures to endure alterations for longer periods compared to Earth. Terrestrial landslides are swiftly erased by erosion, plant growth, and geological activity. Mass wasting landforms are observed at various scales, ranging from giant rock avalanches to small slumps. Some notable examples of large-scale mass wasting can be seen around the margins of Olympus Mons and on the floor of Valles Marineris.

Typically, mass wasting occurs at the base of bedrock escarpments in impact craters, outflow channels, chasms (canyons), and fossae (grabens). These features are widespread across the Martian surface, with a concentration at intermediate southern latitudes during the Amazonian Period, approximately 1.8 billion years ago. The morphologies of mass wasting vary depending on the deposits produced, and some of these forms remain active on Mars today (Fig. 13). These processes are primarily associated with the arid climate, influenced by frost and gravity. However, certain slope features are also linked to aqueous flows, or the seasonal sublimation of CO_2 mixed with ice.
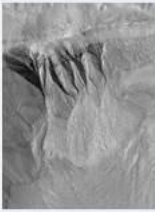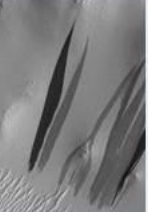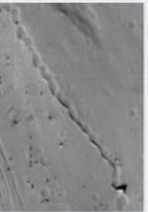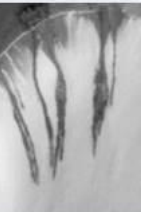
	I. Landslides	II. (Alcove-Channel-Apron) Gullies	III. Slope Streaks	IV. Linear gullies	V. Recurring Slope Lineae (RSL)	VI. Boulder tracks	VII. Dark (frost/flow) streaks
Typical width x length in meters (yards)	1,000 x 5,000	200 x 1000	20 x 500 (typical size decreases) →	5 x 1000	2 x 100	2 x 100	2 x 50
Example							
General shape/ characteristics	Alcove due to ridge failure. Debris apron, can be long or chunky	Triangular alcove. Often has a v-shaped channel. Triangular deposit/ apron	Apex/Initiation point (e.g., impact crater). May contain ridges or ripples, bifurcating downslope. Digitate ends	Small alcove or converging troughs. Can be sinuous, often have levees. Abrupt end or terminal pit(s)	Starts in rocky material. Narrow, follows topography	Track, may be segmented or continuous. Terminal boulder, of same width	Can extend from dark spots, bright haloes. Mostly linear, sometimes braided. Digitate ends
Where found	Large, steep, slopes	Moderate to steep slopes	Bright, dusty steep slopes	sandy, pole-facing slopes	Steep, rocky, slopes in dark regions	steep, rocky areas	frost-covered dune slopes
When active?	All seasons	Late winter-early spring	All seasons	Early spring	Only season with warmest temperatures	All seasons	Winter-early spring

Figure 13. Seven distinct types of Martian slope features believed to be the outcome of material flowing, sliding, or rolling down slopes (NASA/JPL-Caltech/ASA/MSSS/UA).

Gullies on Mars are frequent forms of the mid to high latitudes at average elevation, developing on rocky slopes in meteor crater wall, and on sandy dune slopes. They are another well-studied landform as their morphology resembles water-formed features on Earth. Gullies are categorized into classic (Malin and Edgett, 2000; Treiman, 2003;) and linear (Coles et al., 2019): the classic shows three physiographic elements, an alcove (a steep scarp), a debris apron (cone-shaped site of deposition), and channel which connect the alcove and apron; in linear gullies the apron is missing, and they only develop on sandy bottom (Fig. 14).

Not only liquid water but also a combination of processes has been proposed for their formation: sublimation of seasonal carbon dioxide frost, frosted granular flow, dry granular flow, released of groundwater from shallow or deep aquifers, melting of shallow permafrost (Coles et al., 2019). Image analysis from High Resolution Imaging Science Experiment (HiRISE) show that new mass movements are present in Martian gully landforms especially in the southern hemisphere during the late winter or spring (Dundas et al., 2019).
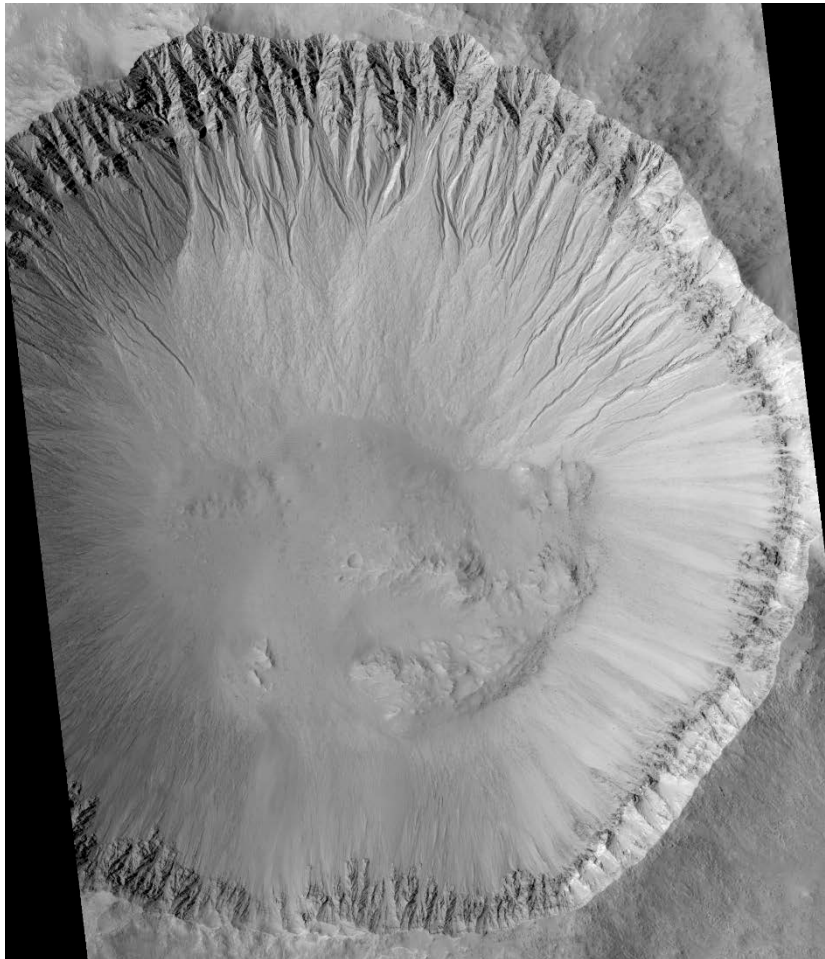
Figure 14. Classic Gullies in Galap Crater; Lat -37.660° Long 192.932° (NASA/JPL-Caltech/UArizona; image ID: ESP_048693_1420)

Slope streaks, prominent in equatorial dusty regions on Mars, are easily recognizable mass movement features. These dark or occasionally bright streaks align along crater rims and escarpments, resembling granular flows or thin dust avalanches. Key characteristics include their thinness, initiation at a point, downhill propagation, a characteristic opening angle, and variability in the opening angle with slope character. They may be straight, curved, or sigmoid, with widths ranging from 20 to 200 m and lengths from hundreds of meters to over 1000 m. These streaks are still active, and their formation is commonly associated with the CO_2 frost cycle, involving the sublimation of dry ice buildup overnight. (Fig. 15).
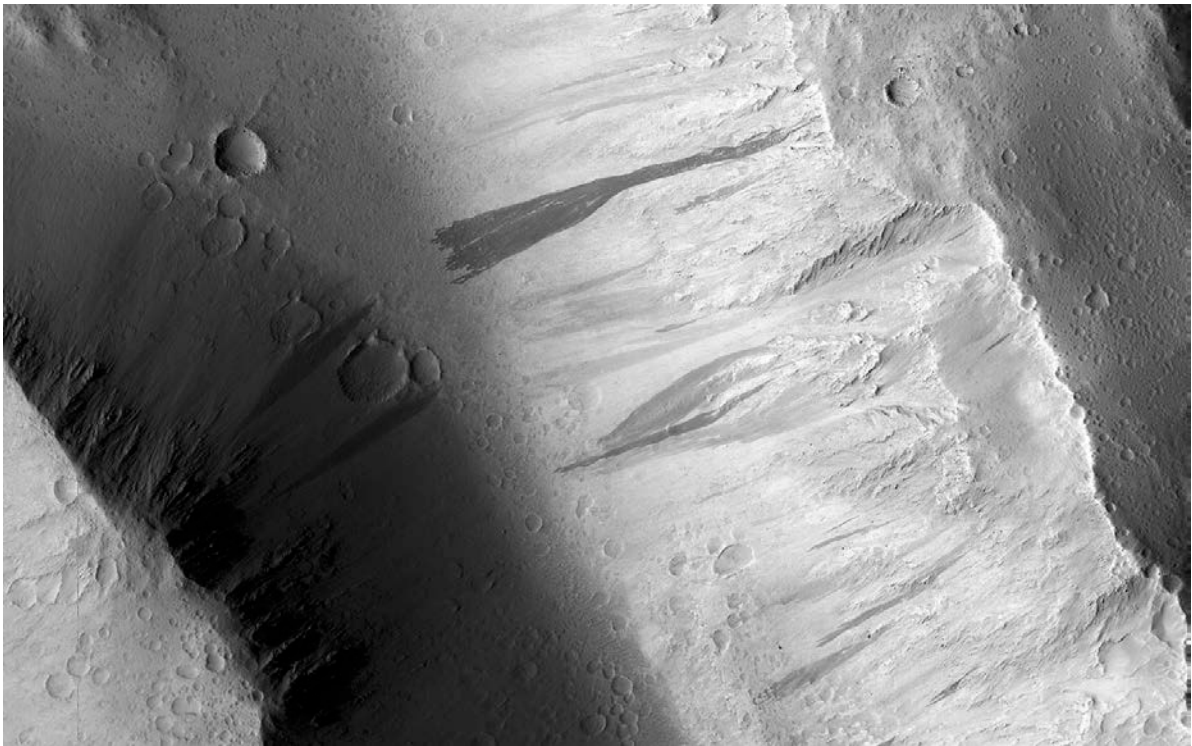
Figure 15. Dark slope streaks, Lat 15.232°Long 214.930° (NASA/JPL-Caltech/UArizona)

The **Recurring slope lineae** (**RSL**) are dark streaks as well but unlike the slope streaks, they are an order of magnitude thinner (1-20 m wide), developing mostly on steep (25°-40°) equator-facing rocky slopes during warm seasons, in the southern middle latitudes (-60° to -30° latitude), especially within the deep canyons of Valles Marineris. The formation of RSL is debated. As the soil temperature is relatively high (from ~250 to 300 K), CO_2 frost cycle is excluded. Some authors propose the presence of water as flowing or seeping or derived from atmosphere or from melting shallow ice (McEwen et al., 2014), while other associate them as granular flows (Dundas et al., 2017).

Dust avalanches are very similar to slope streaks but with a greater depth scale reaching hundreds of meters of length (Gerstell et al., 2004). They are basically dense clouds of reddish air-lofted material fall from steep slopes (> 50°) of south and southwest-facing NPLD marginal scarps with heavily fractured walls. (Sullivan et al., 2001) (Fig. 16). This process is very widespread on Mars, probably triggered by high wind, impact cratering, rockfalls or dust evils.
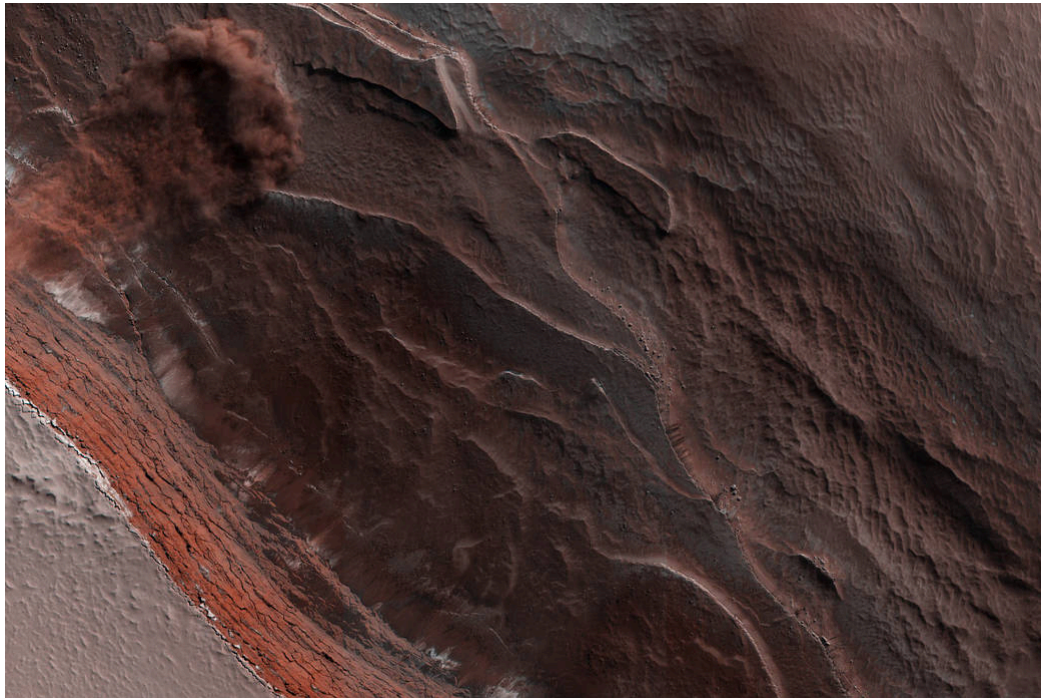
Figure 16. Dust avalanches, top left a cloud of saltating particles at the North Pole of Mars
(www.nasa.gov)

Lobate debris aprons (LDAs) form a distinct landscape in the midlatitude regions of Mars, acting as geomorphic indicators of ice-ground processes alongside lineated valley fill (LVF) and concentric crater fill (CCF) (Fig. 17). Created by the flow of rock and ice mixtures from massifs, mesas, canyon walls, and crater rims, these wedge-shaped deposits exhibit concave to planar surfaces. LDAs can exist individually or overlap, forming complex aprons. Their thickness ranges from tens to hundreds of meters, with lengths varying from a few meters to hundreds of kilometres. Merged LDAs from different directions display ridges, indicative of compressional deformation resembling glaciers.

Surface textures result from ground ice sublimation, possibly influenced by wind and viscous ice creep. Glacial activity is suggested to be associated with the Amazonian Period (Berman et al., 2015).

Figure 17. Mesas, lobate debris aprons, and lineated valley fill in Fretted Terrain, 50.5E, 42.316 (NASA/JPL/Arizona State University; image ID: SP254302).

1.6.4 Aeolian Landforms

The aeolian landforms are very-well developed on Martian surface. Unlike on Earth where sand composition is dominated by resistant quartz eroded from continental crust, the sand on Mars is mainly composed of basalt, reflecting the dominant rock type and low chemical degradation rates on the planet (Fig. 18). Martian aeolian bedforms can be broadly divided into three categories based on size and albedo: **dunes**, **ripples**, and **transverse aeolian ridges** (**TARs**).
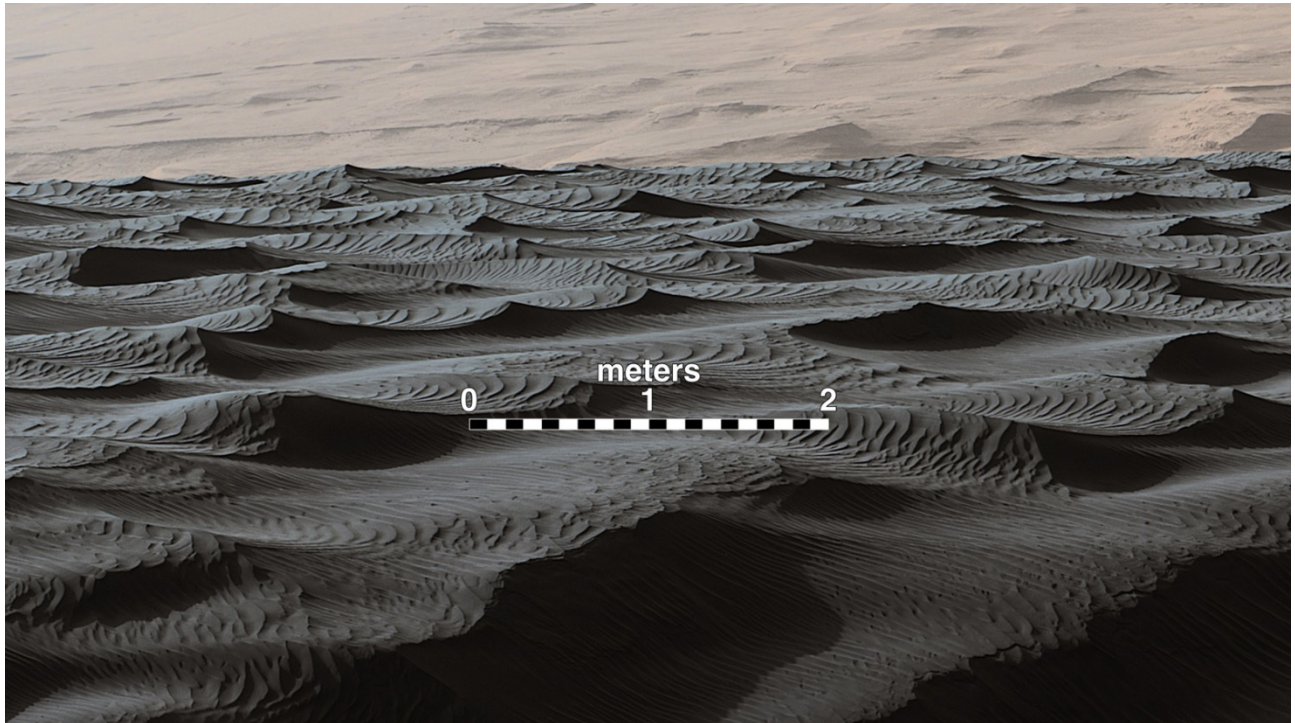
Figure 18. Dunes and ripples at "Bagnold Dunes" on the northwestern flank of Mars' Mount Sharp (www.jpl.nasa.gov).

The **large dark dunes** are among the most widespread aeolian features and are now known to be made up of actively saltating sand grains mostly basaltic in composition. Sand **dunes** are a unique indicator of the interaction between the atmosphere and surface: their morphology is sensitive to subtle shifts in wind circulation patterns and strengths, providing insights on the seasonal variability and changes in Martian orbital parameters. Dunes are widespread over a wide range of elevations and terrain types; mostly present in low plains, they are also evident in craters (Fig. 19), canyons, intermontane depressions, and impact basins.

The largest continuous dune field, Olympia Undae, extends for 470.000 km ^{2} in the northern hemisphere, surrounding the polar ice sheet. Many dune fields are visible in the southern hemisphere over the highland's terrain, showing a progressive increase in the number, area and

volume of dunes, as well as complexity of morphology, from the equator to the south pole, probably linked to a greater sand supply (Hayward et al., 2007). Dunes of Mars and Earth present almost the same morphology (barchan, barchanoid, transverse, dome, linear, star, sand sheet), even if there are several dune forms which are not present in the terrestrial classification system such as the
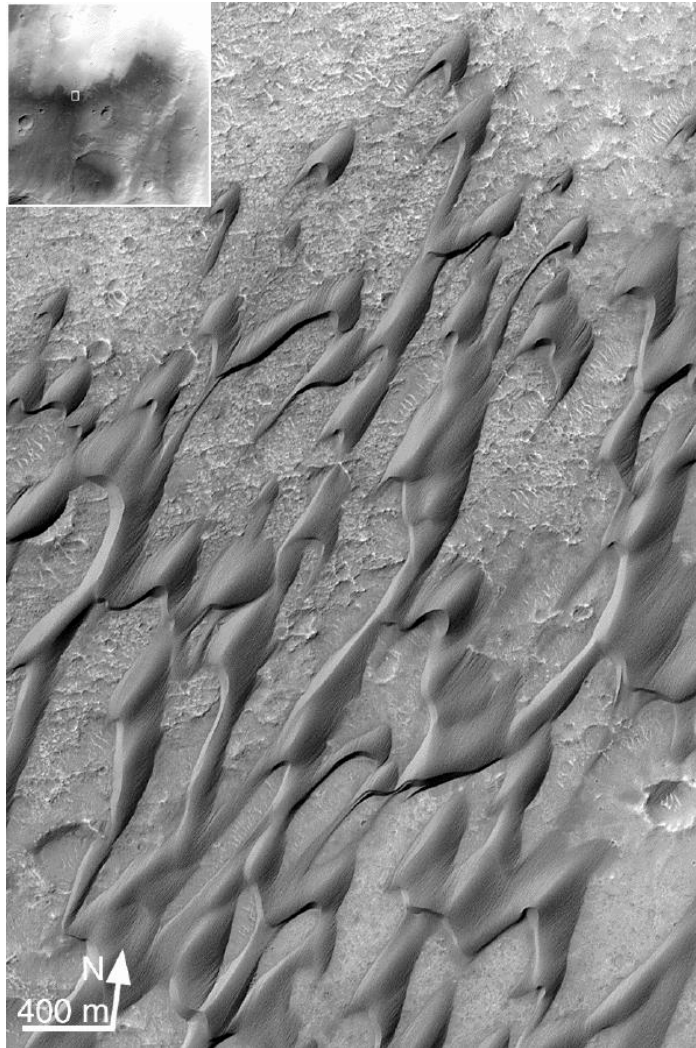
Figure 19. Erosional streaks on dunes in Herschel Crater suggest cementation, as depicted in this MGS MOC (Mars Global Surveyor Mars Orbiter Camera) image (NASA/JPL/MSSS).

circular dune (Fig. 20). The presence of a large percentage of transverse dunes indicates that unidirectional winds are the most common. Another difference is the height since the Martian dunes show great variability reaching up to ~ 300 m (Fenton et al., 2003; Bourke et al., 2006).

Martian **ripples'** form in fine sand on small and large scale, made of sediments of similar size. Small ripples are referred as impact ripples, formed by a particle impact-driven instability, and coexists with larger ripples of wavelengths of 1-3 m and heights exceeding 1 dm. Large ripples structures show similarity with fluid-drag ripples and have been interpreted as analogous to terrestrial

subaqueous ripples, formed by higher kinematic viscosity of the low-density atmosphere of Mars (Sullivan et al., 2008; Lapôtre et al., 2016).
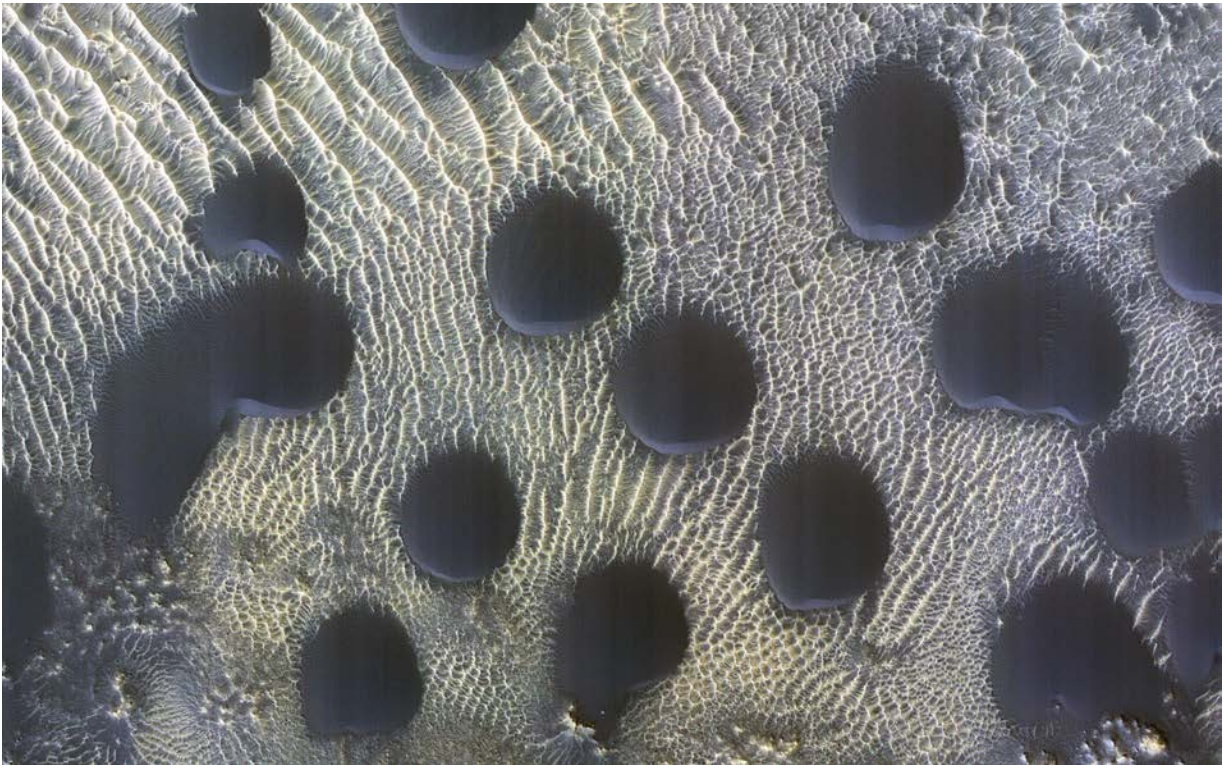
Figure 20. Circular dune with steep slip faces on the south ends, Lat 42.505° Long 67.076 ° (NASA/JPL-Caltech/University of Arizona; image ID ESP_076510_2230).

Contrary to dunes and ripples, the **Transverse Aeolian ridges** (**TARs**) are not active in the present-day Mars. TARs are bright windblown deposits, of smaller particle size, mid-way in height between dunes and ripples (10–100 m wavelength, 1–14 m tall), narrow transverse dimensions, and elongate simple form. They are generally older than large dark dunes, lacking any clear evidence of recent activity (Fig. 21). TARs are concentrated in the Martian tropics, largely absent from latitudes north of +35° and south of -55°, frequently located in topographic lows such as crater interiors and channels, above friable or to proximal friable terrain. The origin of these features remains mysterious more than 20 years after their discovery on Mars. Geissler (2014) hypothesizes that TARs could be constituted of dust blown by the wind in the past in a similar way as the terrestrial antidunes, which over time indurated and eroded to their current states.

Hugenholtz and Barchyn (2017) assume that TARs are part of a continuum of megaripples; similarly, Silvestro et al. (2020) reported movement of some brighter bedforms described as megaripples or small TARs.
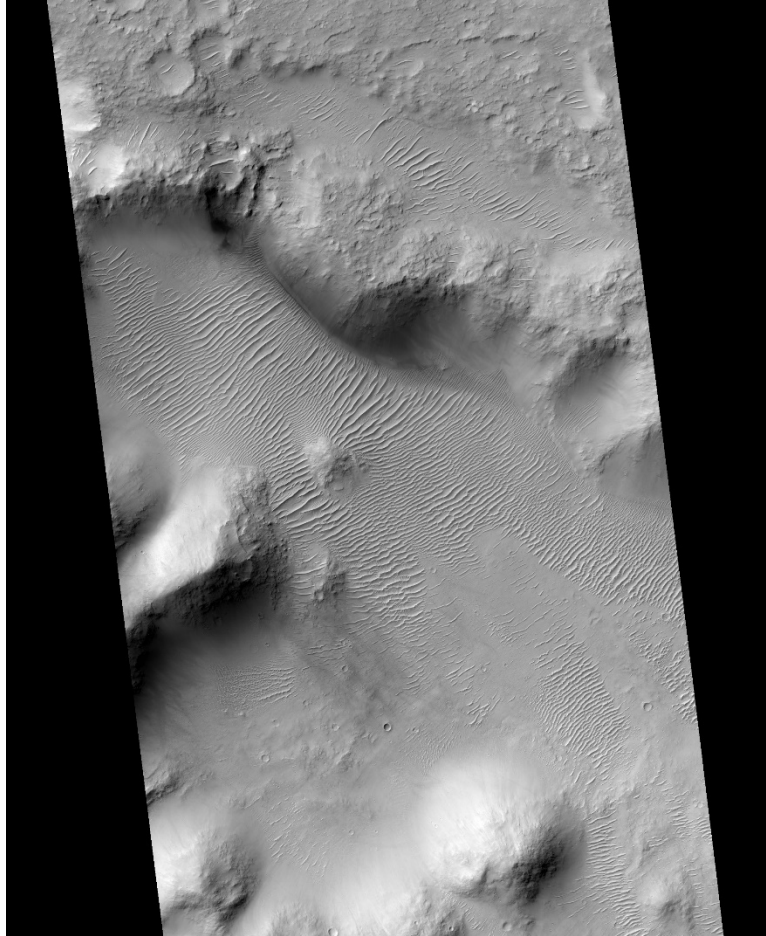
Figure 21. Transverse Aeolian ridges (TARs) Bedforms in Viking 763A11, Lat -14.246° Long 170.158° (NASA/JPL-Caltech/University of Arizona; image ID ESP_016875_1655)

Wind streaks are aeolian features that are formed when the wind that is carrying dust, encounters a raised feature; the direction of the streaks gives us an understanding of where the wind was blowing from. Wind streaks can show bright or dark patterns: bright streaks (Fig. 22) are commonly produced by the deposition of bright dust on dark soil, while dark streaks are formed by the exposure of dark rock surface from a vortex or by basaltic sand blown away from a crater. Wind streaks occur in several area on Mars, although giant dark streaks extending more than 150 km in length are located northern Meridiani Planum and nearby Oxia Palus (Geissler et al., 2008).

Figure 22. Bright streaks of dust collect downwind of craters and other obstacles in Syrtis Major Planum (NASA/JPL-Caltech/Arizona State University)

Dust devil tracks (**DDTs**) are dark (some time bright) erosional surface lineaments left by passages of wind vortices, showing straight, curvilinear, or meandered morphologies (Fig. 23). Similarly on Earth, the tracks sizes reflect the width and duration of vortex: widths can range between ~ 1 m and 1 km while lengths can reach up to several kilometres (Reiss et al., 2016).

The mechanism includes a dust erosion by dust devils which exposes coarser grained substrate consisting of coarse sand particles (0.5 < particle diameter < 2mm), which changes the photometric properties of the surface and leads to low albedo track areas in contrast to the undisturbed surroundings. Not just the grain size but also the roughness, porosity, and compaction of the soil might affect the albedo. The deflation thickness layer has been measured <~2 μm with a dust grain density of 3000 kg m^{-3} (Reiss et al., 2014). DDTS are found at almost all latitude and all elevations except in the polar ice regions.
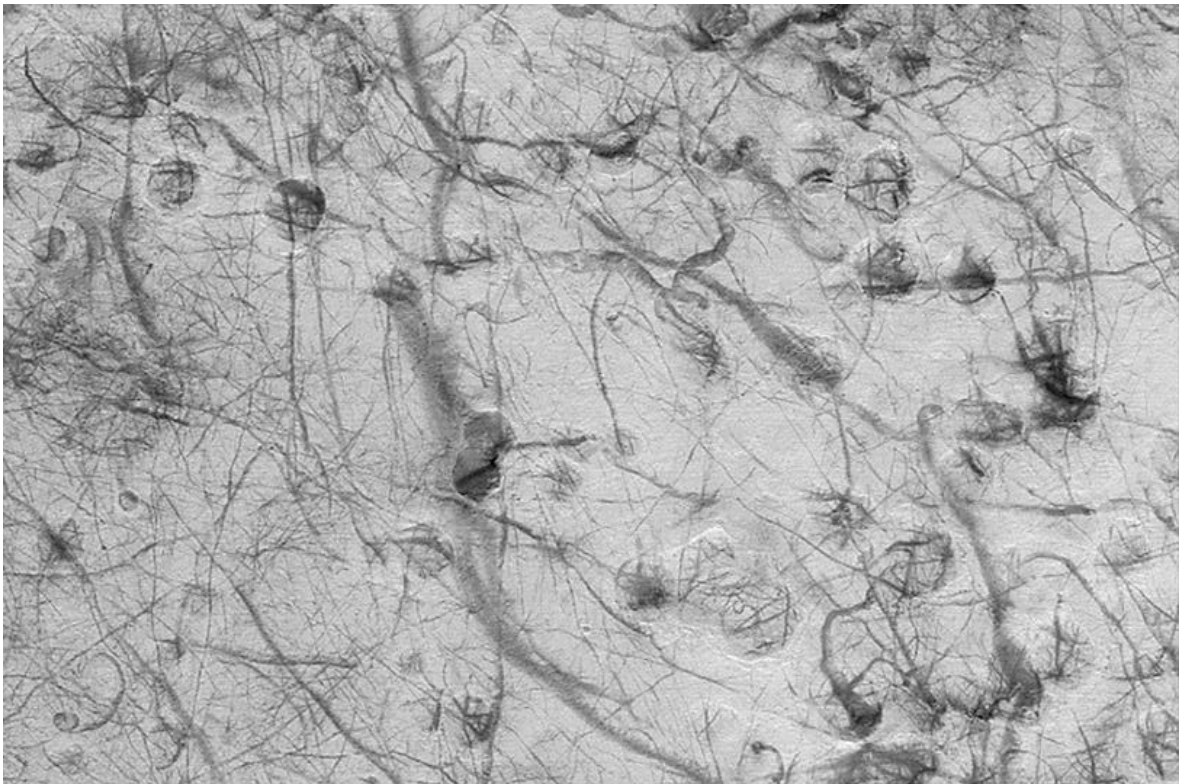
Figure 23. Dust devil tracks during early summer in the Martian southern hemisphere, near 40.2°S, 237.7°W The picture covers an area of about 3 km (www.jpl.nasa.gov)

1.6.5 Sedimentary processes

Layered deposits are high-priority targets for exploration since they not only preserved long sequences of the stratigraphic record of Mars, but also exhibit evidence for hydrous mineral phases that indicates aqueous activity. Depending on their location, deposits are distinguished into **Equatorial Layered Deposits** (**ELDs**) and **Polar Layered Deposits** (**PLDs**) (Fig. 24).

The ELDs are related to light-toned, fine-grained weakly lithifies layers located in various geological contexts, of probable Noachian to Hesperian age. The diversity of their characteristics implies that several mechanisms were involved in their formation and different hypothesis have been proposed related to pyroclastic deposits, lacustrine and aeolian environments, groundwater emplacement and fluctuations (Pondrelli et al., 2015; Di Pietro et al., 2023).

PLDs are subdivided into **North Polar Layered Deposits** (**NPLD**) and **South Polar Layered Deposits** (**SPLD**) constituting spiralling troughs made of an alternation of dark and bright horizontal and sub horizontal layers of a probable mix of ice and dust/sand accumulated at poles of Mars. Once the dust storms reach the polar region, the condensation of water and dioxide accelerate the fall of the dust to the surface, contributing to the formation of the carbon dioxide cap. These deposits might preserve a record of the seasonal and climatic cycling of atmospheric CO_2, H_2O, and dust over millions of years (Zurek, 1999).
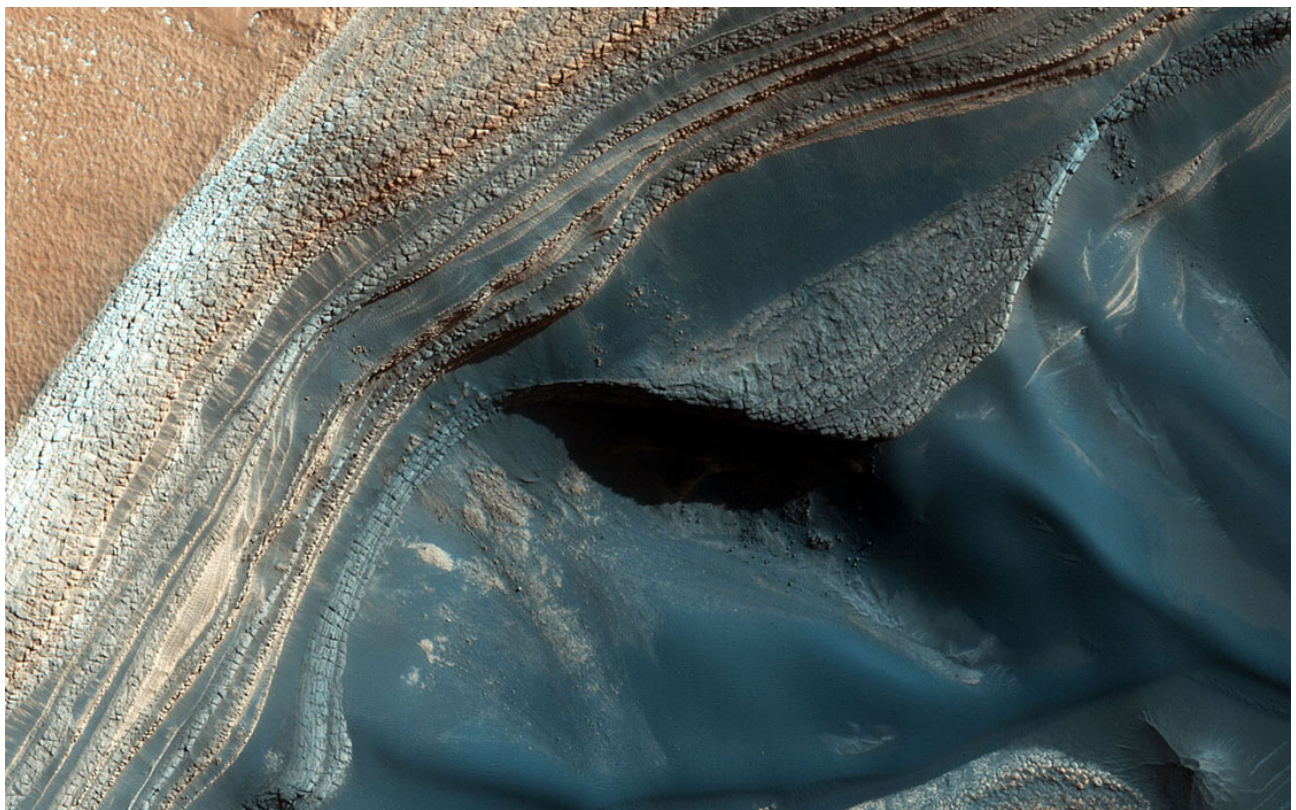
Figure 24. The North Polar layered deposits Photographed via the HiRISE camera on NASA's Mars Reconnaissance Orbiter (NASA/JPL-Caltech/Univ. of Arizona).

1.6 Active processes

Although Mars may appear to be a dead planet, there are several active processes alteration the Martian surface and predominantly attributable to exogenous dynamics. It is still unclear whether endogenous processes are active since plate tectonics would seem to have lacked the ideal conditions to evolve, and volcanic activity would appear to have stopped millions of years ago. Nevertheless, on May 4, 2022, NASA's InSight mission recorded a marsquake of magnitude 4.7 ± 0.2 just north of the dichotomy boundary, of probably subsurface tectonic source (Fernando et al., 2023) (Fig. 25). It is therefore possible that the Red planet has not yet reached the ultimate level of its evolution. On the contrary, if we focus on the exogenous processes, Mars seems to be a very dynamic planet.
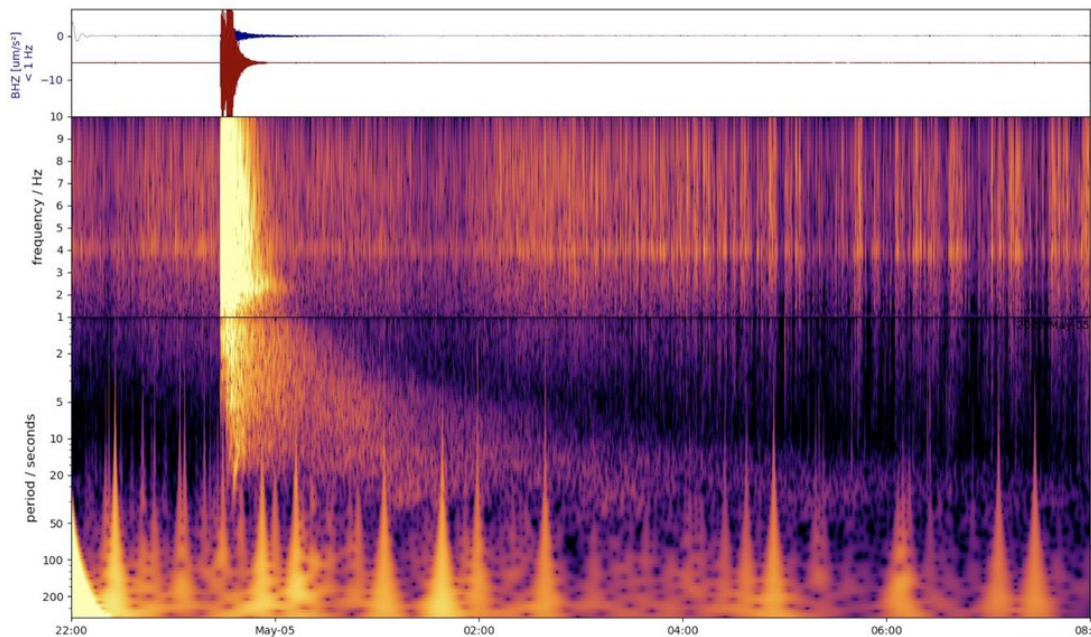
Figure 25. The most significant seismic event ever recorded on another planet, estimated at magnitude 4.7 ± 0.2, identified by NASA's InSight lander. Image credit: NASA/JPL-Caltech/ETH Zurich.

Meteoritic impact is a major component of Martian geomorphology by shaping the surface in the past and still in the present day. New impact cratering formed on Dec. 24, 2021, was detected by the Context Camera aboard NASA's Mars Reconnaissance Orbiter in the Amazonis Planitia region, about 150 meters across. According to Daubar et al. (2013), present-day meter- to decametre-sized craters are currently forming at a measurable rate: 1.65×10^{-6} craters/km^2/yr for >3.9 m effective diameter.

Processes that are clearly active on Mars are related to aeolian activity and mass wasting. Wind is the most active surface agent: large dust storms occur locally and regionally especially during summertime in the southern hemisphere, when the higher surface temperature warms the air that becomes lighter. As the air rises into the atmosphere, it brings with it dust, forming convection cells like those on Earth. Clouds of red dust containing iron oxides can be blown all over the planet by strong winds which can reach maximum about 100 kilometres per hour, less than half the speed of some hurricane-force winds on Earth. Overall, the amount of dust during a single global storm is estimated to be 4.3 x 10^{11} kg (Martin, 1995).
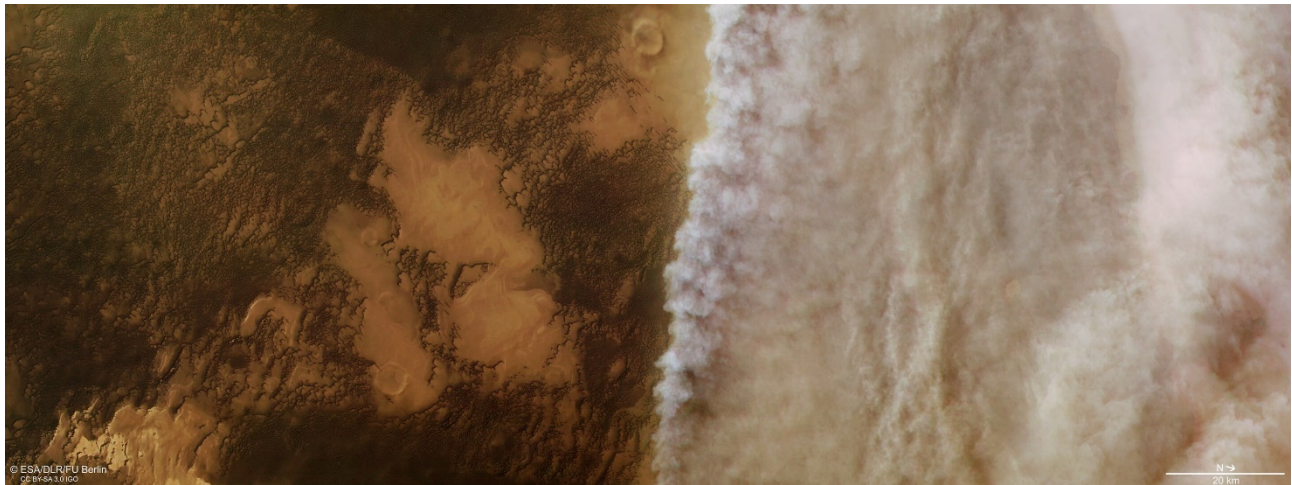
Figure 26. In April 2018, ESA's Mars Express spacecraft, equipped with a high-resolution stereo camera, captured a striking upwelling front of dust clouds near the north polar ice cap of Mars.

As mentioned previously wind can generate several bedform which many of them show earth-like morphologies. The most spectacular active aeolian features are the dust devil tracks (DDTs), dune, small and large ripples. DDTs contribute significantly to the lifting of dust into the Martian atmosphere, estimated to be 2.3 ± 1 x 10^{11} kg each year, mostly from Lat 60°N during spring and from Lat 60°S during summer (Whelley et al., 2008). Aeolian bedforms such as dunes and ripples are very actively migrating and evolving within the present-day climate: changing slipface streaks, shrinking and disappearance of decametres-scale dome dunes, migration of decimetre-scale ripples, seasonal variations in sand flux, alcoves formation were reported in several areas (Fenton, 2006; Bourke et al., 2008; Silvestro et al., 2010; Hansen et al., 2011; Bridges et al., 2012; Ayoub et al., 2014). As examined by Chojnacki et al. (2019) the average migration rate for barchan and barchanoid dunes (~2–120 m tall) and sub-meter-tall ripples (~40 cm height) is ~0.5 ± 0.4 m/yr (1σ). The most active dune region on Mars occurs within the expansive north circumpolar ergs of Olympia

and Abalos Undae; here the dune movement is not just triggered by the wind but also by CO_2 ice sublimation during summer, and condensation of seasonal ice.

With regards to mass wasting the most remarkable morphologic changes have been observed on gullies both on impact crater walls and on sand, even though those on sand appear to be much more dynamic. Gullies in the southern hemisphere show more alteration in morphologies than those in the south. The channel structure can vary considerably when large flows occur, showing new incisions, extension of channel mouths, and boulder transport. Flows appear nearly every Mars year as a single event or as multiple events in a single gully during a few Mars years, but some gullies might show a flow of orders of magnitude less frequently (Conway et al., 2019). Combined observations of outcrop sedimentology and surface morphology suggest that most gully fans on Mars are formed by debris-flow deposition which subsequentially were modified or erased by post-depositional processes (de Haas et al., 2015).

Generally, as on Earth, rockfalls, impact craters, dust devil, CO_2 seasonality, and thermal stress trigger visible tracks on steep slopes surface. For instance, Recurring Slope Lineae are generally more active in slopes that receive more direct sunlight, and immediately after a global dust storm; they grow for several months during warm seasons and fade during winter reappearing annually mostly in the same locations (McEwen et al., 2014). Slope streaks contrary to RSL are not seasonal and persist for
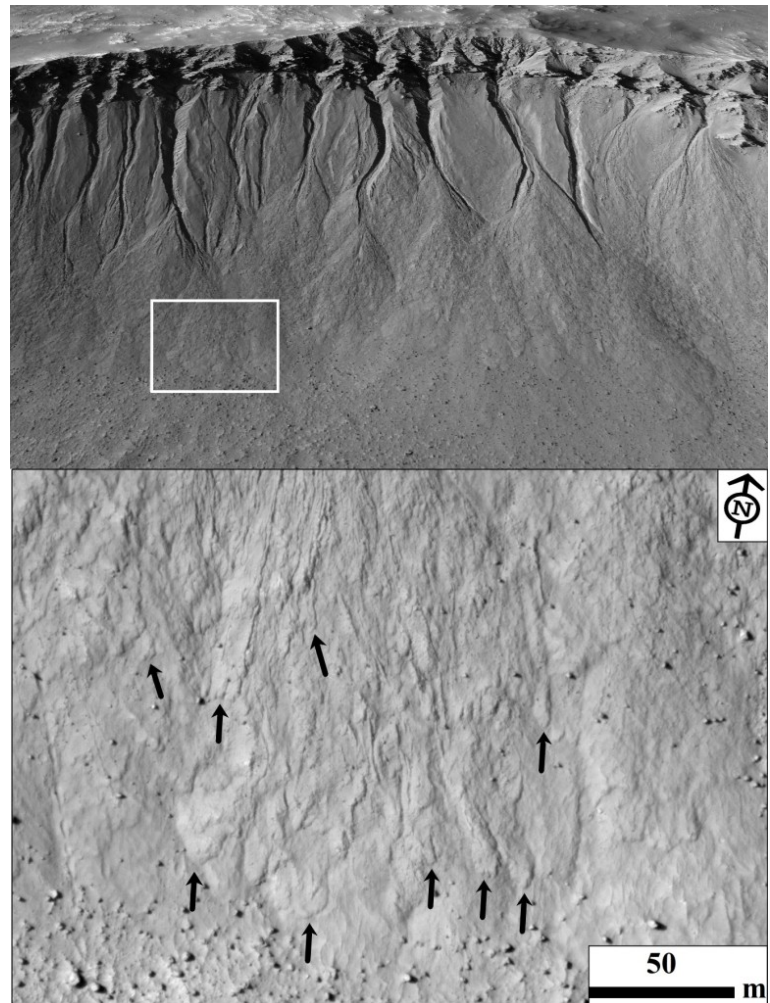
Figure 27. Top: A three-dimensional view depicting gullies on the pole-facing wall of Los crater (~8 km in diameter) on Mars. The HiRISE image (ESP_020774_1445) with a resolution of 0.25 m/pixel is draped over a 1 m/pix HiRISE elevation model. The crater floor, located approximately 1 km below the crater rim, is visible (bottom panel's box indicates its location). Bottom: gully fan surface, featuring overlapping lobate deposits with convex-up and tongue-shaped terminal lobes, accompanied by lateral levees, showing that a debris-flow like process may be responsible for gully formation (Sinha et al., 2020). Image credits: NASA/JPL/University of Arizona.

many years; their flow is superficial and are probably constituted of soil enriched with low-albedo ferric oxides which make them darker than their surroundings. Mass wasting processes such as avalanches and block falls are widespread on poles; dust avalanches are common in North Polar Layered Deposits (NPLD) coinciding with the seasonal sublimation of CO_2 ice, and thermal stress in scarp walls subsurface due to solar heating (Byrne t al., 2017). Sublimation and defrosting are the basis of many processes in Polar regions: during spring solid ice sublimes due to the greenhouse effect, resulting in the buildup of pressure gas which lately escapes generating the displacement of loose grains, cracks, and a variety of periglacial landforms as the curious "Swiss Cheese" terrain (Mangold, 2011).

1.7 Mars habitability

The missions initiated in the 1960s with the goal of exploring the Red Planet have unveiled that Mars differs from the 18th-century community's imaginative depiction. Contrary to the earlier belief that Mars was inhabited by aggressive extraterrestrial beings commonly referred to as "Martians" or highly intelligent human-like creatures, the reality is quite different. The Soviet Union started missions to Mars in 1960, marking the beginning of Mars exploration endeavours. Over the years, multiple countries, including the United States, Europe, and India, have conducted missions to Mars. To present, a cumulative total of 46 missions have been undertaken, with 19 achieving success. One of the first successful missions was carried out in 1964 by NASA under the name of *Mariner 4*: the flyby provided the first images of the surface (Fig. 28) together with data about surface atmospheric pressure, daytime temperatures, magnetic field, and

Figure 28. The first close-up image of Mars, taken by Mariner 4 spacecraft, near the boundary of Elysium Planitia to the west and Arcadia Planitia to the east. The resolution of this image is roughly 5 km and north is up (Mariner 4, frame 01D, https://nssdc.gsfc.nasa.gov).

radiation. The many missions that have subsequently taken place (and are taking place) have

markedly improved our knowledge of Mars to such an extent that we classify it as Earth's little sibling due to the similarities they have in common. Through the *Viking program* which launched two orbiters and two landers (*Viking 1* and *Viking 2)* in 1975, we obtained the first photograph ever taken from the surface of Mars and from the spacecraft we discovered carved deep valleys, eroded grooves into bedrock, and branched streams extended for kilometres. Mar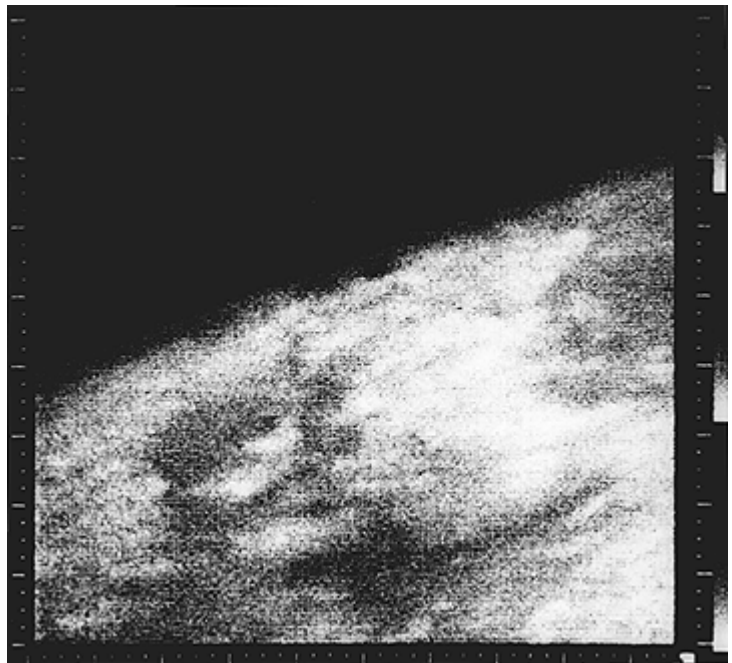s began to reveal its first secrets, and scientists started to speculate about the possible presence of water and thus perhaps life on the planet. *Mars Pathfinder* spacecraft first landed a wheeled robotic rover equipped with wheels named *Sojourner* in 1997 which first analysed in-situ the composition of rocks and soil. In the same year a space probe was sent into orbit with the mission *Mars Global Surveyor* (*MGS*) which studied and mapped the entire Martian surface, analysed the thermal structure of the atmosphere, and established the nature of the magnetic field. The mission returned more data than all previous ones combined: we have discovered gullies, debris flow, massive flow features, and we developed the first high-resolution topographic map based on a laser altimeter. The *Mars Odyssey* mission detected large amounts of hydrogen with the spectrometers, indicating the presence of water in the ice layers confirmed subsequentially by the spacecraft *Orbiter* from mission *Mars Express.* Two more rovers landed on Mars in 2004 in two different locations through the mission *Mars Exploration Rover*: *Spirit* and *Opportunity rovers* obtained a large quantity of information about the composition and chemistry of minerals and rocks. The *Mars Reconnaissance Orbiter* is a spacecraft equipped with instruments that we still exploit today such as the HiRISE camera, CTX camera, CRISM, and SHARAD. Another renowned rover launched as part of the *Mars Science Laboratory* (MSL) mission is *Curiosity*. It landed on Mars in 2012 with the primary objectives of investigating Mars past and present potential to support microbial life, assessing the planet's geology and climate, and exploring its habitability. The rover is equipped with a suite of scientific instruments, including cameras, spectrometers, a laser for vaporizing rocks, and a drill for collecting samples. The Chemistry and Camera (*ChemCam*) instrument can analyse the composition of rocks and soil from a distance using a laser. Originally designed for a two-year mission, Curiosity has significantly surpassed expectations and continues to operate on Mars. The interior of Mars was first investigated by the mission *InSight (Interior Exploration using Seismic Investigations, Geodesy and Heat Transport),* landed in 2018 which aims to measure seismic activity (Marsquakes), heat flow from the planet's interior, and the wobble of Mars' axis of rotation exploiting *Seismic Experiment for Interior Structure* (*SEIS*) that detects ground motion from seismic waves, and *Heat Flow and Physical Properties Probe* (*HP3*) which measure the heat flow from the interior of Mars. In 2020, multiple nations achieved

49

significant milestones in Mars exploration. The Hope Probe, part of the Hope Mars Mission, was launched by the United Arab Emirates (UAE) to study the Martian atmosphere and climate. China's Tianwen-1 mission, an ambitious endeavour comprising an orbiter, lander, and rover (Zhurong), is aimed at exploring the Martian surface. NASA Mars 2020 mission, designed with a primary focus on astrobiology, includes the search for signs of past microbial life and the collection and preservation of rock and regolithic samples for potential return to Earth. The Perseverance rover, a key component of the Mars 2020 mission, is assigned to explore the Jezero Crater, a site on Mars believed to have once hosted a lake and river delta, making it a compelling location for the search for signs of past life.

The future of Mars exploration is marked by a mix of robotic missions, sample return efforts, technological innovations, and the pursuit of human exploration. These activities aim not only to answer scientific questions about Mars but also to pave the way for potential human settlement.

Key components of the upcoming Mars exploration initiatives encompass various aspects.

- *Sample Return Missions*: NASA's *Perseverance* rover, having landed on Mars in 2021, is equipped to gather and store Martian rock and soil samples. Future collaborative missions with the European Space Agency (ESA) aim to retrieve and bring these samples back to Earth for comprehensive analysis.

- *Ingenuity and Aerial Exploration*: the *Ingenuity* helicopter, a component of the *Perseverance mission*, showcased the feasibility of powered, controlled flight in Mars' thin atmosphere. Subsequent missions may integrate aerial vehicles to enhance exploration and reconnaissance capabilities.

- *Human Exploration*: ambitious plans for human Mars exploration are under discussion by space agencies, notably NASA's *Artemis program*. This program seeks to establish a sustainable human presence on the Moon, serving as a crucial precursor for future Mars missions.

- International Collaboration between global space agencies remains a prominent feature in Mars exploration. The participation of diverse nations brings varied expertise and resources to effectively address the challenges associated with exploring Mars.

- New Orbital and Surface Missions: Planned orbiter missions, such as the *European Space Agency's ExoMars Trace Gas Orbiter* and NASA's *MAVEN* (*Mars Atmosphere and Volatile Evolution*) mission, will persist in examining the Martian atmosphere. Concurrently, surface missions will concentrate on exploring specific regions of interest.

- Technological Advancements encompassing AI and autonomous systems, will play a pivotal role in enhancing the capabilities of future Mars missions. This involves the refinement of rovers, landers, and instruments for more intricate scientific investigations.
- Private Sector Involvement such as SpaceX, actively engage in Mars exploration initiatives. SpaceX's Starship, designed as a fully reusable spacecraft, holds a strategic role in potential crewed missions to Mars.

The exploration of Mars has become synonymous with the search for conditions that could support life, past or present, and the evaluation of factors influencing the planet's suitability for human habitation. This pursuit, known as "*Mars Habitability*," delves into the intricate interplay of geological, atmospheric, and astrobiological factors, unravelling the mysteries of Mars to uncover clues about the potential existence of life beyond Earth and lay the groundwork for future human exploration.

Residing on Mars necessitates the ability to create essential products using local resources found on the planet. One critical aspect is the synthesis of vital chemicals, particularly oxygen, essential for survival. Scientists (Jiang et al., 2023) have developed an autonomous AI-Chemist, operated by robotics, that can synthesize and optimize oxygen evolution reaction catalysts from materials sourced from Martian meteorites. The entire process, including pre-treating Martian ore, synthesizing, and characterizing the catalyst, and determining the optimal formula, was conducted without human intervention. Utilizing a machine learning model based on both first-principles data and experimental measurements, the AI-Chemist efficiently identified the optimal synthetic formula from a pool of over 3 million potential compositions. This groundbreaking development showcases the capability of the robotic AI-Chemist to autonomously produce chemicals and materials for Mars exploration.

In the pursuit of expanding the horizons of human exploration and pushing the boundaries of our reach into the cosmos, the concept of "*Mars Architecture*" has emerged as a visionary blueprint. This concept includes the collective strategies, designs, and technologies aimed at making human exploration and potential habitation of the Red Planet a reality. This architectural framework encompasses a multifaceted approach, involving spacecraft design, innovative life support systems, and the establishment of habitats capable of sustaining human life in the challenging environment of the Red Planet. Various space agencies, private companies, and researchers have proposed

ambitious plans and cutting-edge technologies to facilitate human missions to Mars, envisioning a future where Mars becomes a tangible frontier for human habitation.

Some key aspects that often come under consideration in discussions related to Mars architecture a rein relation to:

- Designs and plans for spacecraft capable of carrying humans and cargo to Mars.
- Habitats and Life Support Systems: Architectural designs for habitats that can provide a safe and habitable environment for humans on Mars (Fig. 29).
- Life support systems that address the challenges of sustaining life in the Martian atmosphere.
- Sustainability and Resource Utilization: Strategies for utilizing local Martian resources, such as regolith, to create building materials and support life.
- Technologies for recycling and reusing resources to ensure long-term sustainability.
- Power Generation: Development of power systems, such as solar panels or nuclear reactors, to meet the energy needs of habitats and equipment on Mars.
- Robotic Exploration: Deployment of robotic missions for advanced reconnaissance, resource identification, and preparation of the Martian surface before human missions.
- International Collaboration: Considerations for global collaboration, involving multiple countries and organizations, to pool resources, expertise, and technology for Mars exploration.
- Private Sector Initiatives: Involvement of private companies, such as SpaceX, in developing and implementing plans for Mars exploration and potential colonization.
- Risk Mitigation and Contingency Planning: Strategies for mitigating risks associated with long-duration space travel and habitation on Mars. Contingency plans for emergency situations and the health and safety of astronauts.

In essence, Mars Architecture embodies the collective ingenuity, collaboration, and determination of humanity to venture into the cosmos, extending our reach to the enigmatic and promising landscapes of Mars. As of 2023, ongoing developments may reshape and refine this architectural vision, making it imperative to stay abreast of the latest advancements in Mars exploration (Fallacara & Netti, 2023).
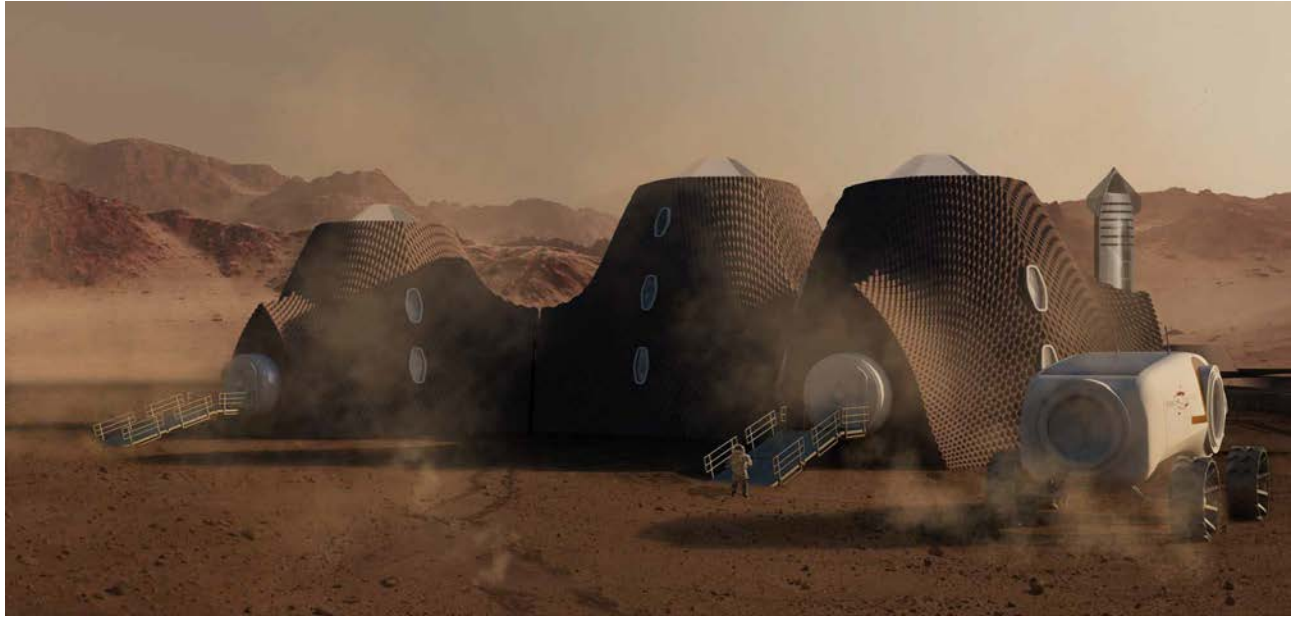
Figure 29. The Polytechnic University of Bari's Architectural Design Thesis Laboratory, known as archi.mars, researched and designed "HiveMars," a permanent and self-sufficient settlement. The concept integrates ISRU (In-Situ Resource Utilization)-enabled and prefabricated structures to establish a scalable infrastructure supporting human life on the Martian surface (Vlahovljak et al., 2021).

Chapter 2

Martian analogue: Lanzarote

2.1 Introduction

Currently, human exploration of Mars for in-situ investigations remains beyond our reach, with the inaugural mission to retrieve Martian samples scheduled for 2027 through the "Mars Sample Return" Program. This ambitious initiative aims to bring back samples collected by the Perseverance rover in Jezero Crater, with an anticipated return to Earth in 2033 (NASA, 2024).

During this interim period, achieving a comprehensive understanding of Mars' evolution necessitates focused research in Earth locations that replicate the physical, chemical, geological, and climatic conditions found on Mars. Terrestrial analogues, meticulously selected based on specific physical and chemical conditions, serve as invaluable reference points for interpreting data collected from Mars. These analogues play a pivotal role in bridging the gap between our current understanding and the wealth of knowledge anticipated from future Martian missions.

Martian analogues are indispensable tools for testing, learning, and refining the technologies and systems that constitute Mars architecture. They provide a bridge between theoretical planning and the practical challenges of exploring and potentially colonizing the Red Planet. The significance of Martian analogues lies in their multifaceted roles: 1. Technology Testing: analogues serve as testing grounds for Mars mission technologies, including rovers, life support systems, and communication devices; 2. Human Adaptation Studies: Understanding how humans adapt to challenges on Mars, such as isolation and limited resources, is crucial for designing effective habitats and support systems; 3. Operational Planning: Analogues contribute to the development and refinement of operational procedures for Mars missions, addressing potential challenges in exploration, resource utilization, and habitat maintenance; 4. Scientific Research: Opportunities for scientific research in analogues contribute to our understanding of Mars and its potential habitability, allowing researchers to study geological, environmental, and biological aspects; 5. Training Astronauts: Analogues serve as essential training grounds for astronauts, allowing them to experience and adapt

to Mars-like conditions before actual missions; 6. Mission Contingency Planning: Insights gained from analogues contribute to mission planning by identifying and addressing potential challenges, aiding in the development of contingency plans; 7. Understanding Planetary Evolution: Studying analogous environments on Earth helps researchers draw parallels to Mars, contributing to our understanding of planetary evolution and the factors influencing diverse planetary states.

Multiples are the Martian analogues on Earth:

- Iceland: studied for its volcanic activity, Fe-rich lavas, interaction between fire and ice, and hydrothermal systems (El-Maarry et al., 2017). Also selected as a testing zone for spacesuits and off-world vehicles.

- Atacama Desert (Chile): the chemistry and mineralogy (sulfate, chloride, and nitrate) associated with the hyper-dry climate indicate a past climatic fluctuation considered similar to that on early Mars (Sutter et al., 2007). The desert hosts microbial communities that could provide important information about possible Martian biosignatures (Warren et al., 2019).

- Antarctic Dry Valleys: characterized by a hyper-arid polar desert environment, above 1500 m elevation, with temperatures that do not exceed 0 °C. The hydrologic cycle is dominated by ice and vapor phase processes such as sublimation. Here, periglacial processes, geomorphic features, and sediment alteration are studied (Gibson et al., 1983; Dickinson et al., 2003).

- Hawaii: a great analogue for the study of shield volcanoes constituting the geology of Mars. Weathering of the very recent basaltic flows improves knowledge in understanding the primary composition and geochemical processes of the Martian surface (Seelos et al., 2010). Habitability is also investigated (Hughes et al., 2019). In 2020, the first all-woman crew of the HI-SEAS (Hawaii Space Exploration Analog and Simulation) mission was established here.

- Devon Island (Canadian Arctic): located at 75°N latitude, provides solar radiance similar to the Martian Equator. Studied for similarities related to periglacial, fluvial, paleolacustrine, and regolithic features (Lee et al., 1998).

- Desert of Utah, near Hanksville: The Mars Desert Research Station (MDRS) provides accommodation for different crews, and various activities are carried out, such as astrobiology field research (Roman et al., 2015; Thiel et al., 2011).

- White Sands National Park (USA): the white gypsum sand dunes at White Sands resemble certain Martian terrains, providing a unique setting for studying aeolian processes and the interactions between wind and surface materials (Fenton et al., 2017).

- Rio Tinto (Spain): an analogue of the Noachian sulfate deposit in the Meridiani Planum, in which jarosite has been discovered. Here, the weathering of sulfide-rich minerals, iron and sulphur geochemistry, and biological conditions are studied (Amils et al., 2014; Fernández-Remolar et al., 2008).
- Lanzarote (Canary Islands, Spain): this volcanic island offers Mars-like lava fields and rocky terrains. It has been used for testing robotic instruments and studying extremophiles in volcanic environments, providing insights into potential Martian habitats (Martínez-Frías et al., 2017; Miller et al., 2018; Sauro et al., 2023).

Lanzarote Island not only exhibits geological and volcanic features reminiscent of Mars but also offers a unique advantage in studying recent and active geological processes, which are similarly present on the Martian surface. The island's volcanic origins and arid climate, make it an ideal natural laboratory for exploring depositional and geomorphological processes similar to those that shaped Mars. By investigating the sedimentary sequences and depositional environments on Lanzarote, we can draw meaningful parallels with Martian terrains, enhancing our understanding of the Red Planet's geological history, particularly during its wetter and more dynamic phases.

2.2 Lanzarote geological overview

Lanzarote is the easternmost island in the Canary Islands archipelago, only 100 km away from the African coast (Fig. 30).
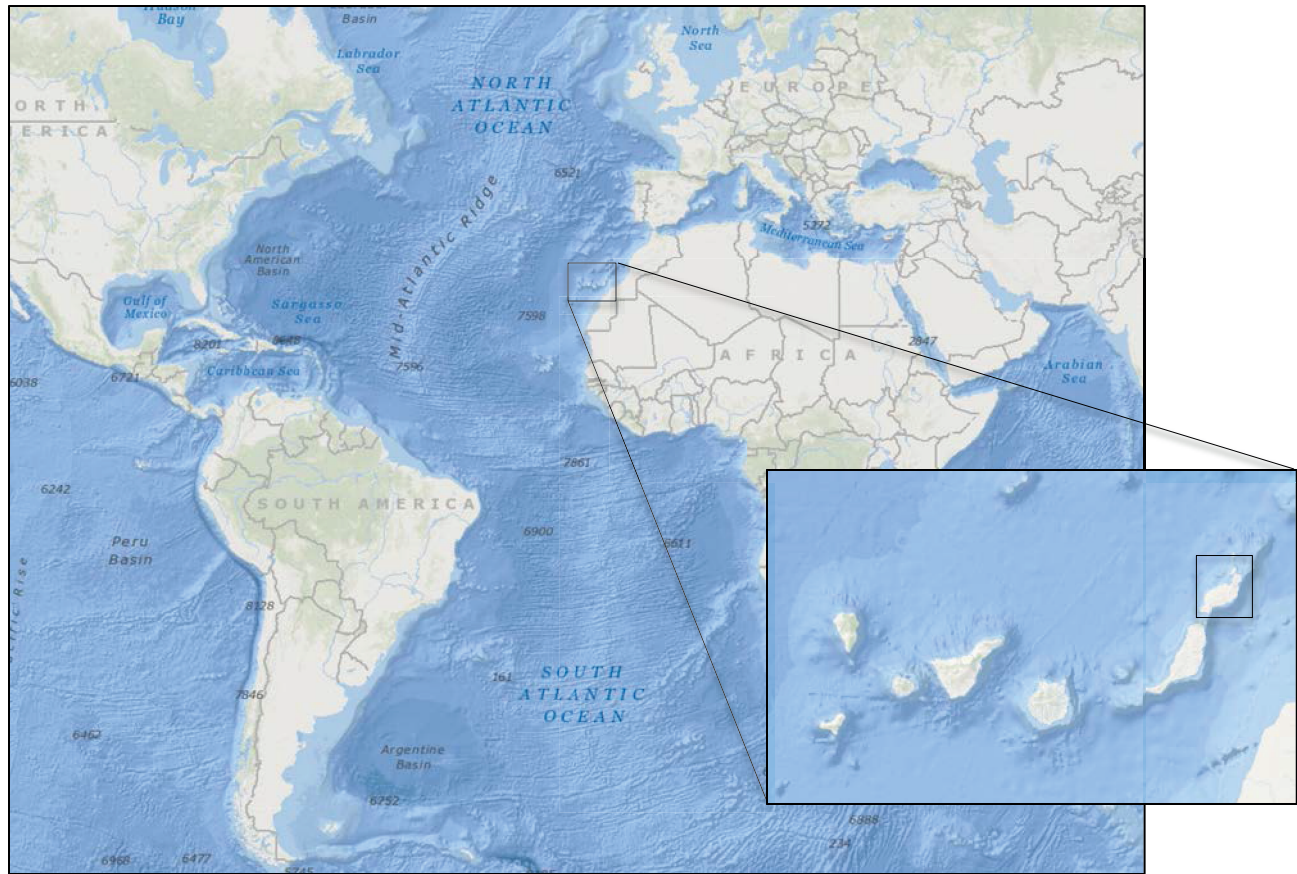
Figure 30. Lanzarote and the Canary island in the world.

As the other islands, Lanzarote underwent successive phases of volcanic construction, with its formation occurring predominantly during three distinct periods: an underwater phase and two subaerial phases (Pre-erosional or Shield stage and Post-erosional or Differentiate stage). The underwater phase started during the Mid-Oligocene (35- 28 Ma) through submarine emissions of pyroclasts and lavas (pillow-lavas and hyaloclastites), constituting the basement of the island. While this geological unit remains concealed in outcrops on Lanzarote, its existence is substantiated by a geothermal study conducted in the vicinity of the Timanfaya National Park (Sánchez Guzmán and Abad, 1986). The survey, penetrating the crust to a depth of 2.702 m, revealed that the oldest materials consist of sediments such as clays and clayey marls, showcasing abundant marine microfauna dating back to the Middle-Upper Palaeocene (65-55 Ma).

The Pre-erosional or Shield stage began in the Mid-Miocene, spanning approximately 15.6 to 14 Ma (Coello et al., 1992). During this phase, a significant volcanic activity unfolded, characterized by the emission of substantial volumes of basaltic lava and pyroclastic flows originating from Los Ajaches,

a shield-type volcanic edifice situated in the southern region. The massif extends its reach from Femés to Punta Papagajo, reaching its highest point at 560 meters, and westward from Yaiza to Salinas del Janubio, where it has undergone more pronounced erosion (Fig. 31).

This edifice exhibits a noteworthy compositional diversity in the lava, emitted over a relatively brief timeframe. The lava types include alkali basalt with a prevalence of basanite, which is widespread across the entire island, along with picro-basalt, trachy-basalt, and trachyte, the latter being exclusive to this particular area (Carracedo and Badiola, 1993).
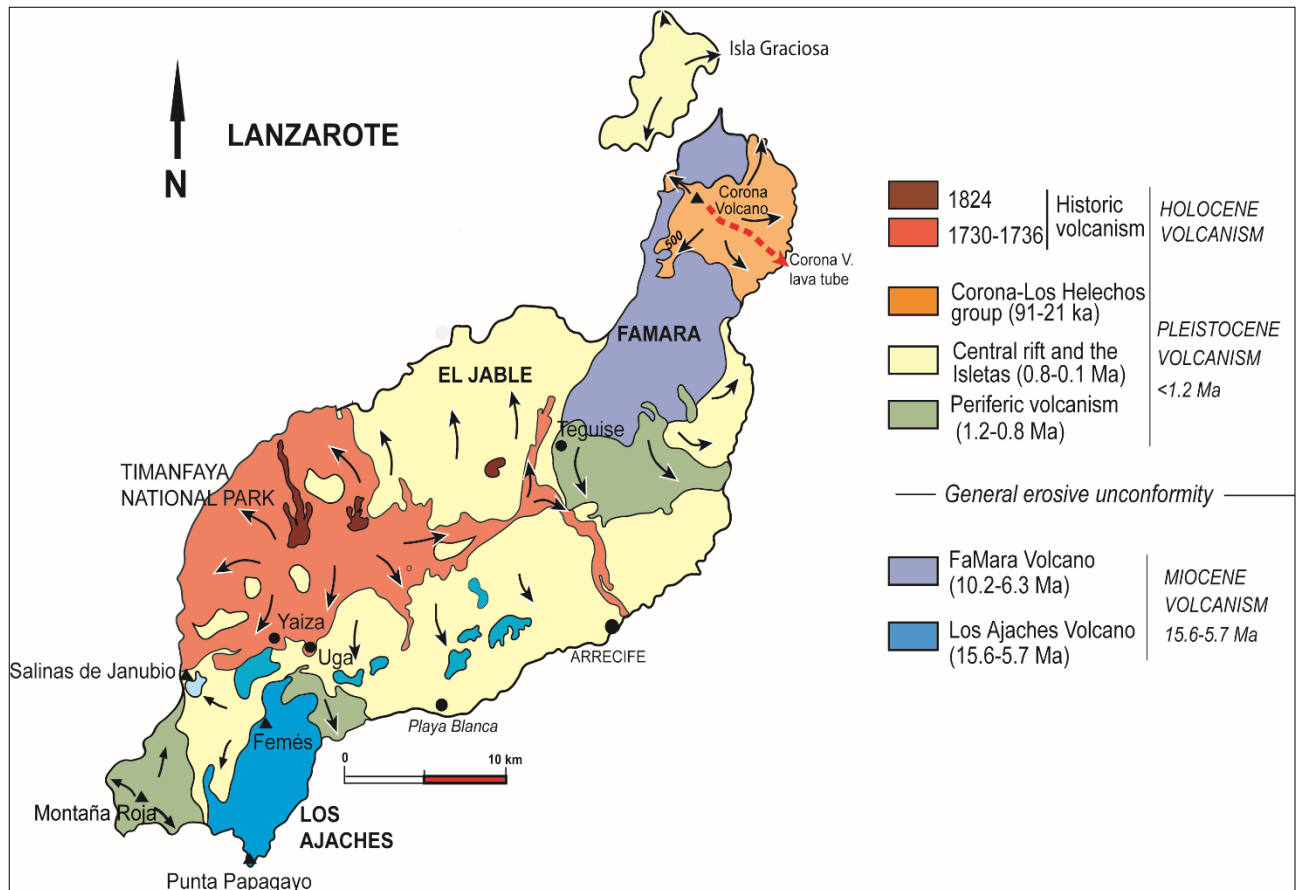
Figure 31. Simplified geological map of the of the geological evolution of Lanzarote. Modified from Hoernle and Carracedo (2009).

After approximately three million years of volcanic dormancy, the once-primitive island underwent extensive erosion. Resuming activity in the Upper Miocene, a new, independent volcano emerged in the northeastern part of the island, now forming the Famara massif. The Famara volcanic structure exhibits distinct characteristics, marked by a sequence of sub-horizontal basaltic lavas generated in three successive stages, each separated by unconformities. The lower unit, which

appears at the base of the western escarpment of the massif and in the bottoms of certain *barrancos* (Spanish toponymy for gully) in the eastern sector, consists predominantly of basaltic lavas, pyroclastic materials, and dikes formed between 10.2 and 8.3 Ma. The intermediate unit, visible up to 20 meters, is characterized by basaltic lava flows, frequent cones and pyroclastic mantles ejected between 6.7 and 5.3 Ma. The upper unit, emitted from 3.9 to 3.8 Ma, primarily comprises powerful basalt extrusions that fill erosive channels formed during periods of eruptive quiescence (Carracedo and Badiola, 1993; Coello et al., 1992).

Simultaneously with the intermediate stage of Famara around 6.6 Ma, volcanic activity manifested in the region that now encompasses the village of Tias, situated in the central part of the island. Massive basaltic lavas, characterized by columnar jointing and interspersed pyroclastic materials, were emitted until approximately 6.1 Ma. This activity gave rise to a flattened relief, with a thickness ranging from 10 to 20 meters, visible today in sporadic outcrops along the road from Arrecife to Uga. The resulting volcanic edifices formed a land bridge, connecting Los Ajaches to Famara (Fig. 31).

Following a significant temporal hiatus of 2.5 Ma marked by volcanic inactivity, the initiation of the Post-erosional or Differentiate stage signifies a pivotal transition from the Miocene series to the Pliocene-Quaternary volcanoes. During this period, the volcanic massifs underwent substantial erosion, with Famara experiencing a swift reduction in size due to lateral collapse on its western flank. This hypothesis is supported by the presence of a substantial Pleistocene-Holocene marine abrasion platform, as indicated in studies by Coello et al. (1992), Páez et al. (2000), and Troll & Carracedo (2016). This platform is situated in the vicinity of the narrow El Rio strait, which separates the main island from La Graciosa (Fig. 31).

The Pliocene-Quaternary activities are distinguished by the emission of extensive lava fields that overlaid materials from the preceding period, featuring eruptive rates notably lower than those observed in the Miocene. Emission centres were positioned in proximity to Los Ajaches, Montaña Roja, and the Caldera Riscada volcano group, emerging to the south of Famara within the Teguise volcano group. Commencing approximately 0.7 Ma, volcanism assumed a fissural character, with emission centres aligning NE-SW. This period includes sub-historic eruptions from the La Quemada-Los Helechos-Corona group and historic eruptions such as those in 1730 to 1736 and 1824, contributing to the formation of the region now recognized as Timanfaya (Fig. 31 and 32).
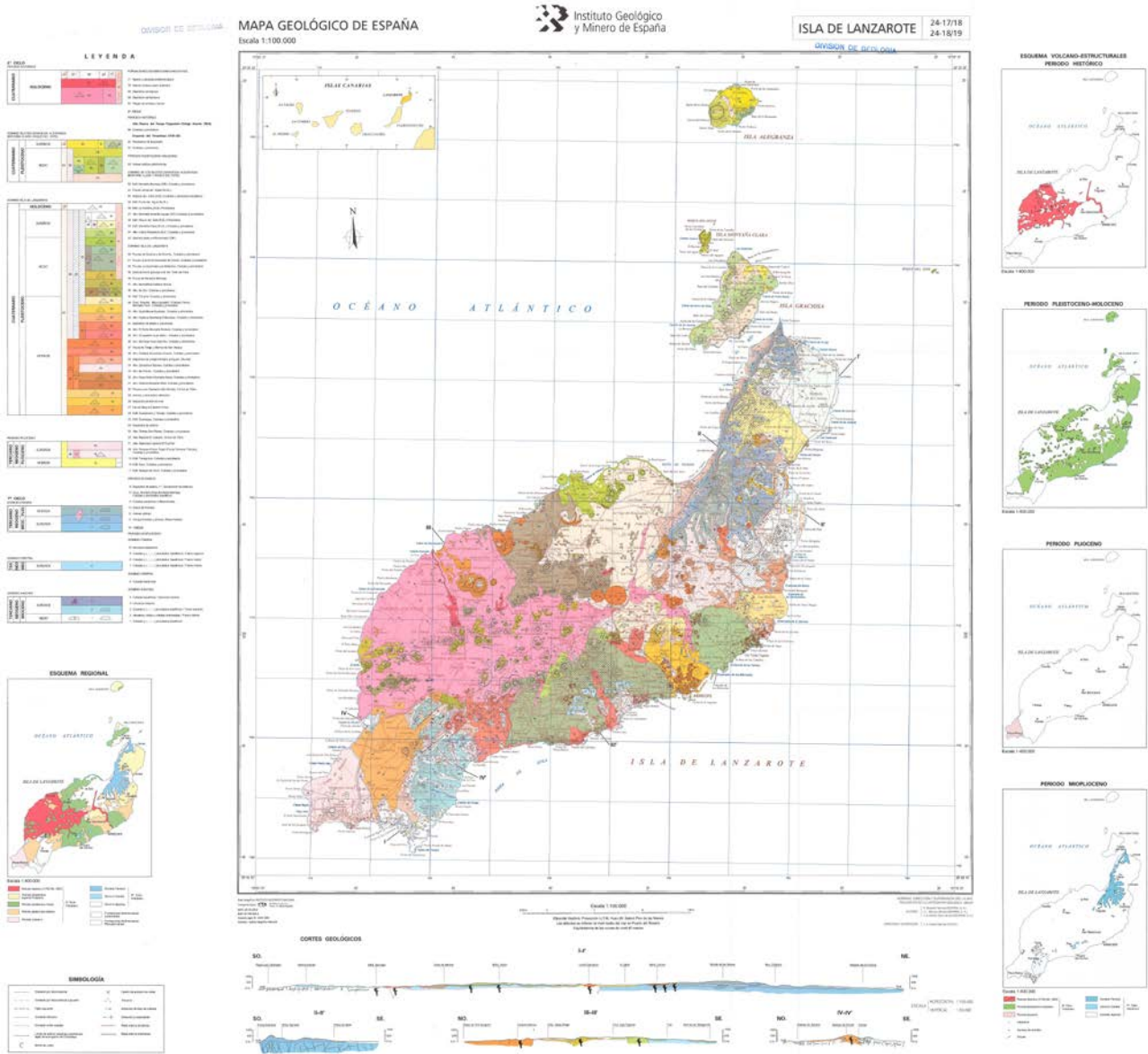
Figure 32. Lanzarote geologic map (Instituto Geológico y Minero de España).

2.3 Lanzarote as Martian analogue

Both Lanzarote and Mars exhibit fascinating geological similarities, particularly in their volcanic terrains. Lanzarote, shaped by shield and cinder cone volcanoes, boasts predominantly basaltic landscapes (Fig. 33). Similarly, Mars features numerous volcanoes emitting mainly basaltic lava, as mentioned in the Mars Chapter.

Figure 33. In the captivating basalt landscape of Lanzarote, a white bus provides scale.

While the mechanisms governing the formation of **calderas** and **meteoritic craters** differ significantly, their morphologies exhibit striking similarities. Emphasis is placed on the concept that calderas and meteoritic craters can be considered as analogues. Beyond their shared circular or nearly circular shapes, both features can display central peaks, rims, and inner structures (Fig. 34). These similarities extend to hydrological features, such as channels and valleys within the confines

of their rims, suggesting that similar erosional and depositional processes shaped these structures despite their distinct origins.
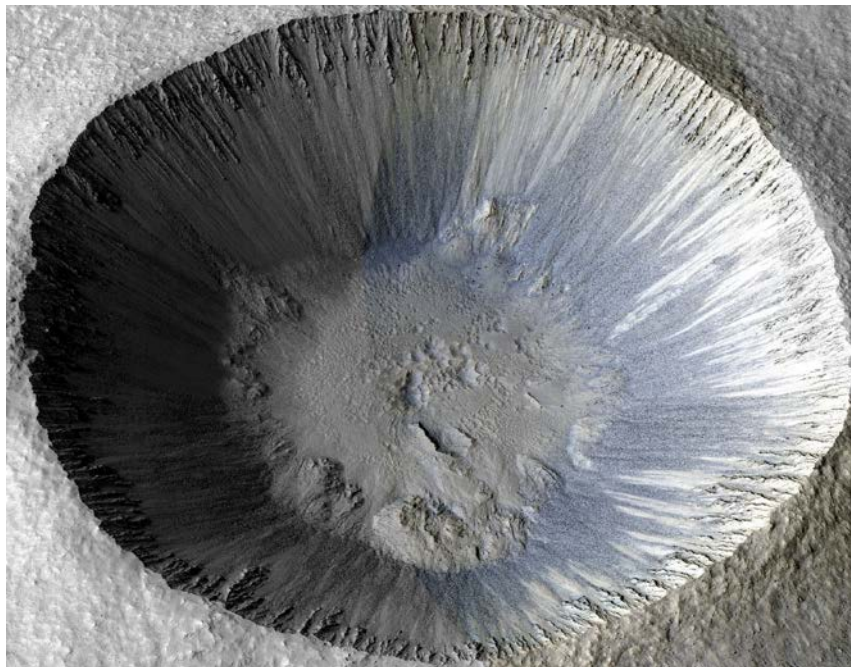
Figure 34. Above the expansive Caldera Blanca on Lanzarote; below the youthful Zumba crater on Mars (PSP_003608_1510; NASA/JPL-Caltech/UArizona).

Lanzarote's **lava tube** formations, such as the renowned Corona lava tube, also offer valuable analogues for Martian environments. Lava tubes on Mars, formed by basaltic flows, resemble those found on Lanzarote, providing insights into the subsurface dynamics of both planets (Fig. 35). These formations are crucial for understanding how lava interacts with subsurface environments in low-atmosphere conditions, which may provide clues for the presence of past or present subsurface water reservoirs on Mars.

Figure 35. Above: Volcanic Tube of La Corona. Lanzarote (picture from geotourismroute.eu); Below:
Probable lava tube in Pavonis Mons, Tharsis Montes (ESA/DLR/FU Berlin, CC BY-SA 3.0 IGO).

The **climatic conditions** of Lanzarote and Mars further enhance their similarity. Lanzarote's dry, arid climate—with sparse vegetation and an annual rainfall of around 250 mm—closely parallels the hyper-arid conditions of modern Mars. However, both Lanzarote and Mars have undergone significant climatic fluctuations in the past. Evidence of wetter climates on Mars, such as the mud cracks and stratigraphy of Mount Sharp in Gale Crater, suggests that the planet once supported liquid water, contributing to the formation of fluvio-lacustrine deposits and phyllosilicate minerals (Rapin et al., 2023). Similarly, Lanzarote experienced varying climatic conditions during the Late

63

Quaternary, as evidenced by layers of palaeosols interbedded with aeolian deposits (Meco and Petit-Maire, 1997). These records highlight the role of climate in shaping sedimentary environments on both planets, demonstrating the potential for alternating dry and wet phases to influence deposition patterns.

Geomorphic features in both Lanzarote and Mars bear witness to processes that are no longer active. The branching angles observed in river valleys on Mars resemble those in Lanzarote's southern region, particularly in Los Ajaches, where valleys such as the Higueral Valley have been shaped by sporadic rainfall events. On Mars, it is believed that episodic heavy rainfall events over extended periods contributed to the formation of valley networks, mirroring the development of anastomosed valleys in Lanzarote. These features suggest that both planets experienced high-energy hydrological events that rapidly shaped their landscapes. The similarities between the two locations provide a compelling analogy for how short-lived water flows on Mars may have influenced surface morphology, just as episodic rain shapes valleys in Lanzarote.

Additionally, wind activity leaves its mark on the terrains of Lanzarote and Mars giving rise to unique features such as dust storms and dune. During Martian summer, dust storms can cover the entire planet surface. A similar process occurs in the Canary Islands during the *Calima* dust storm.

Wind activity has also left a significant imprint on both terrains, with features like **dust storms and dunes** being prevalent on both planets. On Mars, global dust storms can blanket the entire planet, while in Lanzarote, the Calima wind transports dust from the Sahara

Figure 36.The Calima phenomenon observed in February 2020 in Tenerife.

Desert, carrying fine particles that influence soil composition and deposition patterns (Fig. 36). The

Calima events, generated by high pressure over the Sahara, bring fine dust particles rich in minerals and nutrients across the Atlantic, shaping the soils of Lanzarote and contributing to dune formation. The **dune systems** in Lanzarote, predominantly composed of weathered volcanic rock sands and bioclasts, provide a useful analogue for studying Martian dunes, particularly in how aeolian processes shape these landscapes.

Playa de la Arena in Lanzarote's southern region features a **black dune** composed of heavy minerals, offering an interesting comparison with the Namib Dune in the Bagnold Dunes on Mars. Both dunes display similar characteristics, such as grain flow, surface ripples, and a well-defined toe (Fig. 37). These features help link aeolian processes between the two planets, suggesting that wind-driven sediment transport operates in comparable ways on both Earth and Mars. This comparison deepens our understanding of how dunes form and evolve in low-atmosphere, high-wind environments.

Figure 37. Above: the black dune in Playa de la Arena, Lanzarote. Below: image taken by Curiosity's Mastcam showing lee side of the Namib Dune, part of the black sand field of the Bagnold Dunes along the northwest flank of Mount Sharp.

2.3.1 Target of the thesis: on-going processes

The central focus of this thesis is the study of the **El Jable plain**, a depression located within the remnants of the **Famara Caldera rim**. This area serves as an important analogue for certain meteor craters on Mars and is even considered as a potential landing site for future robotic or human missions. Its geological features provide a unique opportunity to draw comparisons between the sedimentary processes in Lanzarote and those on the Martian surface.

One of the most significant parallels lies in the comparison between the **Famara alluvial fan system**, which represents sediment deposits eroded from the Miocene volcanic caldera, and the **Martian gullies.** Martian gullies are narrow channels typically linked to crater rim erosion and are associated with downslope sediment deposits. On Earth, a gully is defined as a small, narrow, and deeply incised stream course, often difficult to cross or ascend, and distinct from larger landforms such as valleys or gorges. As described by Goudie (2006), gullies are typically characterized by steep sides and headwalls, carved out of unconsolidated regolith through ephemeral flows, such as those generated by meltwater or temporary surface runoff.

The **erosive channels** observed in Martian gullies bear striking morphological similarities to the *barrancos* of the Famara cliffs, formed by ephemeral streams (Fig. 38). However, the primary agents driving these processes differ significantly between the two planets. On Lanzarote, although rainfall is sporadic, water remains the dominant force shaping these steep-walled, narrow barrancos. In contrast, on Mars, the most probable agent responsible for gully formation is the sublimation of carbon dioxide. Despite this divergence in processes, the overall geomorphic response is comparable, reflecting how transient flows shape steep terrain in both environments.

Both the **Famara *barrancos*** and **Martian gullies** culminate in similar depositional features known as aprons, which can be interpreted as alluvial fans. These aprons are crucial in understanding sediment transport and depositional processes, as they represent the accumulation of materials carried downslope by episodic flows. The study of these aprons and channels provides valuable insight into the dynamics of flow regimes on both Earth and Mars.

Moreover, by analyzing and dating these sedimentary deposits, we can reconstruct the paleoclimate that influenced their formation. On Lanzarote, dating the sequences within the alluvial fans and interbedded aeolian deposits allows us to track climatic oscillations during the Late Quaternary, which were characterized by alternating periods of aridity and episodic rainfall. Similarly, understanding the timing and development of gullies on Mars can offer clues about the planet's

past climate, especially regarding periods where transient flows of water or CO_2 sublimation may have been active. These sedimentary records are invaluable for understanding the evolution of planetary climates, helping us gain a clearer view of how both Mars and Earth transitioned through different climatic phases. Ultimately, the paleoclimatic implications derived from these deposits allow us to hypothesize about ancient Martian environments and their potential to support water-related processes in the past.
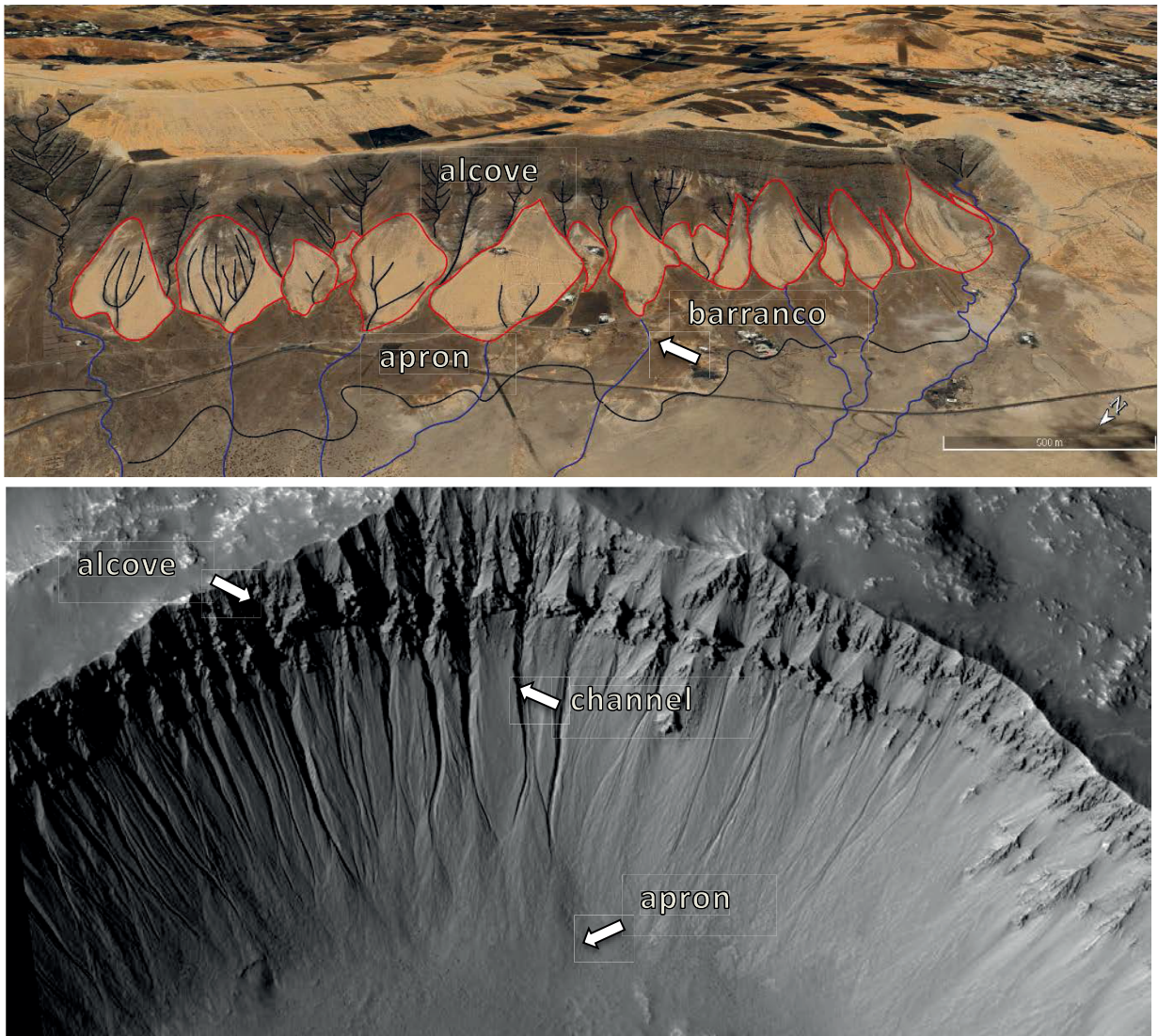
Figure 38. Comparison between terrestrial barrancos in Lanzarote (top) and Martian gullies (bottom). Above: Alluvial fan system of Famara, Lanzarote, consisting of colluvial fans (outlined in red), with barrancos marked by blue lines, and alluvial fans forming the apron. Below: Martian gullies in Los Crater (35.08° S, 76.22° W) on Mars with alcoves, channels, and apron deposits, similar to those observed in Lanzarote. HiRISE image ESP_020774_1445 (NASA/JPL/University of Arizona).

Chapter 3

Dating Mars recent deposits

3.1 Introduction

Missions to Mars have unveiled a history marked by diverse geologic and climatic processes, including aeolian, fluvial, periglacial, and volcanic activities. In its early history, Mars likely resembled Earth's present state, featuring a wetter climate, an active magnetic field, a denser atmosphere, and potential liquid water presence. To comprehend the transformation of Mars into its current cold and inhospitable state, it is imperative to investigate the dynamics of climate change and its impact on various geomorphic processes.

Currently, our knowledge of geological events within the last 3 billion years (Ga) on Mars is limited, relying on relative crater densities and an assumption of a lunar-like crater flux which refers to the idea that the rate of impact cratering on Mars is similar to the rate observed on the Moon (Hartmann & Neukum, 2001). Crater counting is a method to estimate the age of a planetary surface based on the concept that newly formed areas have no impact craters initially; then, craters accumulate over time at a presumed known rate. By counting various-sized craters in a specific area, we can determine how long they have been accumulating and, consequently, infer the age of the surface. This method has been refined through calibration with ages obtained from radiometric dating of samples returned from the Moon by the Luna and Apollo missions. Nevertheless, this approach offers poor temporal resolution and lacks utility in understanding the past billion years.

Therefore, there is a crucial need to bridge the temporal gaps in Martian geochronology. In this context, the present research seeks to propose luminescence as a potential method for dating Mars recent deposits, offering insights into recent geomorphological events as well as those in the more distant past. Luminescence dating, a well-established chronological method extensively employed in Archaeology and Earth Science, could significantly contribute to enhancing our understanding of Martian history.

Compared to alternative dating methods, luminescence stands out as a favourable choice for Martian geological studies due to its distinctive advantages. Radiocarbon dating, limited to recent timescales, relies on organic material yet to be detected on Mars. K-Ar dating, effective for volcanic rocks, faces challenges such as high-power requirements and the complexity of accurately estimating aliquot mass. Uranium-series dating's applicability on Mars depends on specific geological contexts, and U- and Th-decay-series methods are constrained in situ, limiting their measurement techniques. Cosmogenic nuclide dating encounters difficulties in remotely obtaining mineral separates and deciphering diffusion release mechanisms, posing challenges for sample collection and preservation. Laboratory experiments with mineral analogues offer insights into potential improvements for this technique.

Luminescence stands out in overcoming these challenges, offering a simpler in situ application that enhances measurement versatility, making it a more practical and adaptable choice for dating Martian geological features.

Various authors have already explored the potential of luminescence in dating Martian-like sedimentary processes, including the assessment of aeolian dust storms, polar layering, and fluvial activity. McKeever et al. (2003) previously introduced the concept of a robotic instrument designed for in situ luminescence dating of near-surface sediments on Mars. Subsequently, McKeever et al. (2006) examined the optically stimulated luminescence (OSL) characteristics of two potential Martian soil simulants to determine the most effective procedures for OSL dating of surface sediments on Mars. Jain et al. (2006) provided a preliminary exploration of the luminescence characteristics of Martian analogue mineral and rock samples, Hawaiian tephra. Blair et al. (2007) specifically focused on the "single-aliquot regenerative-dose" (SAR) technique, evaluating its utility using Martian regolith simulants and meteorites. Sohbati et al. (2012) proposed a new method for in situ surface exposure dating of non-terrestrial geomorphological features using optically stimulated luminescence (OSL).

However, luminescence does come with its set of challenges, as elaborated in the thesis introduction. These challenges can be summarized as rapid fading, resource-intensive experiments, and uncertainties in burial models. Additionally, on Mars, where lower natural dose rates and higher cosmic ray fluxes prevail, dating ranges may face further constraints, already being limited to up to 1 million years on Earth. Considering the time constraint, we are thus obligated to focus on deposits that have either recently formed or are currently active.

3.2 Luminescence dating technique

According to the IUPAC definition luminescence is the "spontaneous emission of radiation from an electronically excited species (or from a vibrationally excited species) not in thermal equilibrium with its environment" (Verhoeven, 1996). The source of energy that excites the species is the feature that distinguishes the different classes of luminescence: 1- Photoluminescence (absorption of electromagnetic radiation or photons) which includes Fluorescence (nanoseconds emission of photons as electrons jump from excited state to ground level) and Phosphorescence (delayed) emission of photons that have been trapped in a 'forbidden' state); 2- Chemiluminescence (chemical reaction) which includes Bioluminescence (biochemical reactions in living organisms) and Electrochemiluminescence (electrochemical reactions); 3- Crystalloluminescence (solid crystals that precipitate from a solution, melt or gas); Electroluminescence (electric current in a substance) which includes Cathodiluminescence (electrons striking a luminescent material); 4- Mechanoluminescence (mechanical action on a solid) which includes Triboluminescence (generated broken bonds by scratched, crushed, or rubbed material), Fractoluminescence (broken bonds by fractures), Piezoluminescence (pressure on certain solids), Sonoluminescence (imploding bubbles in a liquid when excited by sound); 5- Radioluminescence (bombardment by ionizing radiation); 6- Thermoluminescence (emission of absorbed energy through heat).

The use of luminescence as a chronological method began with Aitken (1985) a British archaeometrist who first discovered that "the amount of thermoluminescence is proportional to the time that has elapsed since the pottery was fired by ancient man". By heating mineral grains coming from pottery, brick, tile, and terracotta figures he measured the energy absorbed within the crystal lattice delivered from ionizing radiation (alpha, beta, gamma, and cosmic rays). He therefore validated the thermoluminescence (TL) technique. The same year Huntley et al. (1985) proposed a new method to determine the time since quartz grains extracted from a sequence of stranded beach dunes in South Australia were last exposed to sunlight. The so-called optically-induced luminescence utilized a 514.5-nm beam from an argon-ion laser to excite electrons and then measured the luminescence resulting from their recombination. Smith et al. (1986) developed a precise methodology to detect the Optically Stimulated Luminescence (OSL) from quartz coarse grains by removing the unstable components preheating the sample, bleaching the OSL signal, setting recuperation after bleaching, and building an OSL growth curve with different doses. Godfrey-Smith et al. (1988) discovered that infrared (IR) photons can be used to stimulate the natural luminescence

of k-feldspar grains and shortly thereafter Hütt et al. (1988) investigated the performances of k-feldspar grains by exposing them to both the visible (490 nm) and infrared light region (860 nm, 930 nm).

In his most famous book, Aitken (1998) explains in detail the working mechanism of Optically Stimulated Luminescence.

The luminescence dating technique relies on the exceptional properties of specific dielectric and semiconducting materials, enabling them to absorb, retain, and subsequently release energy acquired from environmental ionizing radiation (Fig. 39). When grains of these materials are buried in the ground or shielded from heat, they commence the accumulation of photons generated by natural environmental radiation resulting from the isotopic decay of elements such as Uranium (U), Thorium (Th), Potassium (K), and cosmic rays. This accumulated energy becomes entrapped within the crystal lattice of the material. Upon exposure to heat or sunlight during transportation or erosion, the stored energy is released—a pivotal process known as bleaching. This process effectively resets the internal clock of the material, ensuring that the luminescence signal reflects only the time since the last exposure to sunlight or heat.
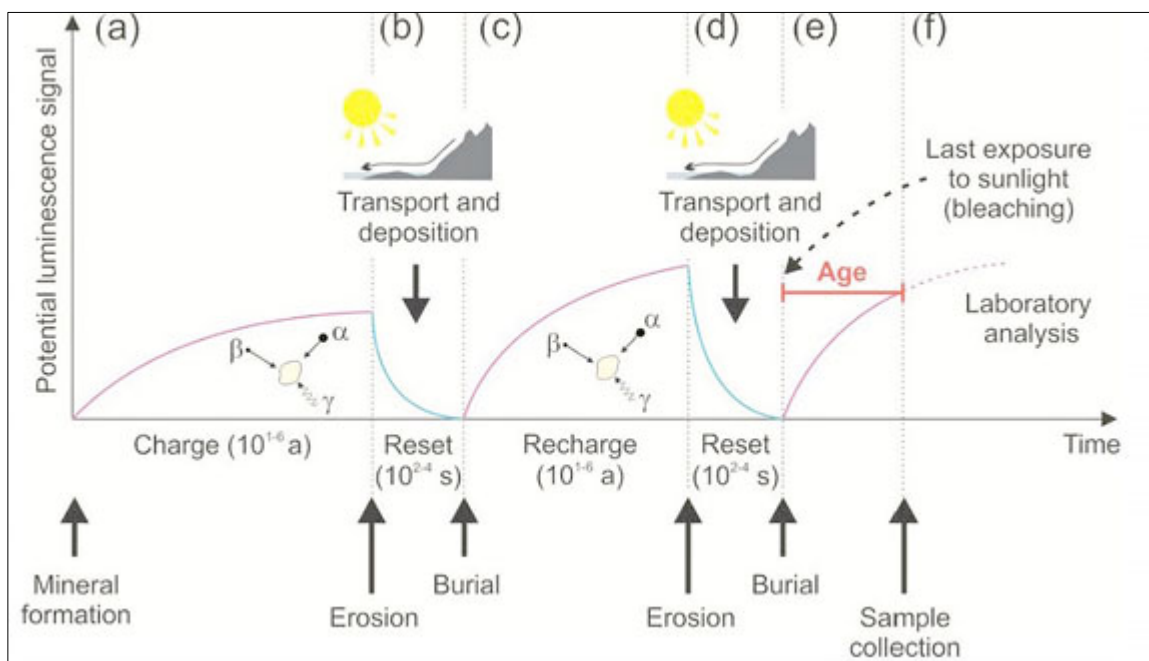
Figure 39. Processes involved in OSL dating: (a) Mineral grains acquire luminescence through exposure to ionizing radiation, trapping electrons. (b) Sunlight exposure during erosion and transport zeroes the luminescence in grains. (c) Burial and exposure to ionizing radiation lead to the storage of free electrons in charge defects within the crystal lattice of grains. (d) Subsequent light exposure during erosion and transport resets the luminescence in grains. (e) The grains undergo burial again, acquiring luminescence with exposure to ionizing radiation. (f) Careful sampling without light exposure, measuring the natural luminescence, and conducting a normalizing test dose (Ln/Tn) compared to the regenerative dose yield an equivalent dose (De) (adapted from Mellet, 2013).

From a physics standpoint, under typical initial conditions, defect sites within the crystal lattice of a mineral host both holes and electron traps. Some traps are maintained empty by thermal eviction at ambient temperature, while others are filled with electrons. A particular type of defect is a negative-ion vacancy, which attracts free electrons. The effectiveness of traps is correlated with their depth below the conduction band—those closer to the band release electrons with lower energy. During the burial phase, as the crystal is exposed to environmental radiation, electrons gain energy, evict from traps to a recombination centre near the conduction band, and leave holes in the valence band. The more prolonged the exposure to nuclear radiation, the greater the number of trapped electrons. During the fast recombination process, electrons reach luminescence centres, non-luminescence centres (killer centres), or other types of traps until saturation is achieved. During the bleaching phase, electrons situated in the luminescence centres lose the energy gained during irradiation, emitting part of it as a single photon of light—termed either thermoluminescence (TL) or Optically Stimulated Luminescence (OSL), depending on whether heat or light served as the de-trapping agent. The emitted light is proportional to the number of trapped electrons and, consequently, to the accumulated energy previously absorbed from nuclear radiation. The overall efficiency of the recombination process, the specific pathways taken by the released electrons, and the properties of luminescence centres influence the characteristics of the luminescence signal, such as its intensity and the time at which it occurs.

Duller (2008) likened the grain to a rechargeable battery: during the bleaching process, the energy diminishes until it disappears entirely within a few minutes. During the burial, the "battery" recharges over hundreds or thousands of years from natural radioactivity (Fig. 40). In the laboratory, the mineral grains are artificially stimulated to release the stored energy in the form of light, which is typically done using heat (thermoluminescence) or light (optically stimulated luminescence).

 The emitted light is detected using instruments such as photomultiplier tubes. This signal yields valuable information about the amount of stored energy within the minerals. This measure is employed to calculate the total energy accumulated during burial, known as the equivalent dose
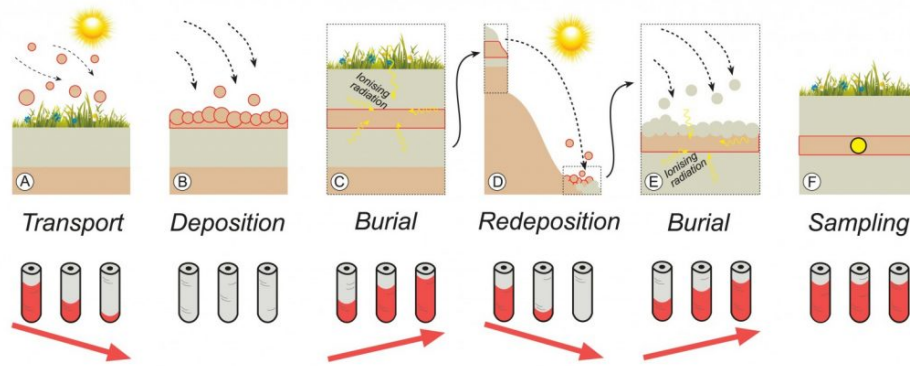
Figure 40. Accumulation and release of charge within mineral grains (image from blogs.egu.eu) :(A) During sediment transport, the accumulated charge is released with energy provided by natural sunlight. (B) Upon deposition, the charge is fully released, and the "battery" is emptied. (C) Charge can accumulate within the grain during burial due to natural ionizing radiation. (D) and (E) The described process can occur multiple times over geological timescales, depending on the environment and geological processes. (F) When a sample is taken in opaque tubes or using cores, the stored energy at that time is sampled and can later be released in the laboratory to obtain a luminescence age.

(D_e), and is expressed in the SI (Système International) unit Grays (Gy; where 1 Gy = 1 J·kg^{-1}). By dividing this accumulated energy by the annual energy input to the mineral grain from the radioactive decay of isotopes present in the surrounding environment, termed the dose rate (D_r), we can determine the duration for which the sample has been receiving energy. In other words, this calculation provides the time elapsed since the grain was last exposed to heat or light.

The age of the sample (in years) can be calculated using the formula:

Age(years) = Equivalent dose (Gy)/Dose rate (Gy year^{-1}).

3.2.1 Equivalent Dose (D_e) Measurement Methods

There are several methods used to measure the Equivalent Dose (D_e) in luminescence dating. These methods involve stimulating the luminescence signal in the laboratory and then measuring the emitted light. The choice of method depends on the type of luminescence dating (thermoluminescence or optically stimulated luminescence) and the specific characteristics of the sample. Here are some common methods: 1. Thermoluminescence (TL): the mineral sample is heated, and the resulting thermoluminescence is measured. This involves heating the sample in a controlled environment and measuring the light emitted as a result of the release of trapped electrons; 2. Optically Stimulated Luminescence (OSL): OSL dating involves exposing the sample to light (optical stimulation) and measuring the luminescence emitted during this exposure. The sample is typically illuminated with controlled light of specific wavelengths, and the resulting luminescence signal is measured; 3. Infrared Stimulated Luminescence (IRSL): this is a variation of OSL where the sample is exposed to infrared light instead of visible light. IRSL is often used with feldspar minerals; 4. Post-Infrared Infrared Stimulated Luminescence (pIRIR): a variant of IRSL, pIRIR involves a two-step stimulation process where the sample is first exposed to infrared light and then to a second infrared light of longer wavelength; 5. Thermally Transferred Optically Stimulated Luminescence (TT-OSL): this is a combined method where the sample is first heated to release any pre-existing TL signal, and then optically stimulated to measure the OSL signal; 6. Multiple Aliquot Regeneration (MAR): in this method, multiple aliquots (subsamples) of the same sample are measured to improve statistical accuracy. The measurements are repeated to account for any variability in the luminescence signal; 7. Single Grain Dating: instead of measuring a bulk sample, individual grains within the sample can be analysed separately. Single-grain dating can provide more precise results and allow the identification of variations within a sample.

These methods are applied based on the type of luminescence dating being performed, the specific properties of the mineral being analysed, and the goals of the research. Each method has its advantages and limitations, and researchers carefully select the appropriate technique for their particular study (Aitken, 1998; Murray and Wintle, 2000, 2003; Duller, 2004, 2008; Wintle and Murray, 2006; Lian and Roberts, 2006; Jacobs and Roberts, 2007; Wintle, 2008).

3.2.2 Dose Rate (D$_R$) Measurement Methods

Measuring the dose rate (D$_R$) in luminescence dating involves determining the rate at which ionizing radiation is delivered to the mineral grains in a geological or archaeological sample. The D$_R$ is typically expressed in units of radiation dose per unit of time (e.g., Grays per year). Various methods can be employed to measure or estimate the D$_R$. Here are some common methods: 1. Gamma Spectrometry: this method involves measuring the gamma-ray emissions from the decay of naturally occurring radioactive isotopes in the sample. Common isotopes include Uranium (U), Thorium (Th), and Potassium (K). The concentrations of these isotopes can be determined by analysing the gamma-ray spectra; 2. Beta Counting: beta particles emitted during the decay of certain isotopes, such as Potassium-40 (K-40), can be detected and counted. This method is often used in conjunction with gamma spectrometry; 3. Alpha Spectrometry: for the measurement of alpha-emitting isotopes like Uranium and Thorium, alpha spectrometry can be employed. This method involves detecting and quantifying the alpha particles emitted during decay; 4. Neutron Activation Analysis: this technique involves irradiating the sample with neutrons, causing certain isotopes to become activated. The resulting gamma-ray emissions are then measured to determine the concentrations of specific isotopes; 5. Dosimetry Calculations: Dose rate can also be estimated through dosimetric calculations. This involves assessing factors such as the concentrations of radioactive isotopes, the energy and type of radiation emitted, and the geometry of the sample; 6. Site-Specific Measurements: in some cases, direct measurements of environmental factors, such as cosmic ray flux or sediment accumulation rates, may be taken at the site to estimate the overall Dose Rate (Wintle, 1997; Ankjærgaard and Murray, 2007; Wintle, 2008; Guérin, 2018).

The specific method chosen depends on factors such as the nature of the sample, the isotopes present, and the laboratory facilities available. Often, a combination of techniques is used to obtain a comprehensive assessment of the D$_R$. It's crucial to accurately determine the Dose Rate to calculate the age of the sample in luminescence dating accurately.

3.2.3 Geological Materials for Luminescence Dating

The geological materials selected for luminescence analysis must adhere to specific criteria: 1. Material must be composed of minerals acting as dosimeters; 2. Luminescence energy within the minerals should have been zeroed at the time of sediment deposition and burial, serving as the

starting point for time counting.; 3. Energy storage in the minerals should not have reached saturation at the time of analysis, to ensure accurate time measurement.

Variables to be considered for an acceptable and correct final age can be summarized as follows:

- **Degree of bleaching**: the extent of bleaching is influenced by both environmental and sample characteristics. Environments with prolonged light exposure (e.g., beaches, dunes) exhibit higher bleaching.
- **Mineral Type**: Target minerals include quartz and K feldspar.
- **Grain size**: Ideal grain sizes are sand-sized or silt-sized.
- **Dose equivalent measurement** methods
- **Dose rate determination** methods

The degree of bleaching is a function of both the environment and sample characteristics: the environment characterized by repeated or lengthy light exposure, in other words, zeroed at the time of burial (e.g., beaches, dunes), has a high degree of bleaching, in contrast with those characterized by little light exposure (e.g., debris flows, rockfall) in which the grains are not very well bleached.

Generally, the geological material target of luminescence are dust, silt, sand, cobbles, and rock outcrops from different environments: aeolian (dunes, loess) (Madsen and Murray, 2009; Thiel et al., 2010; Andreucci et al., 2009; 2010a; 2010b; 2017); fluvial, alluvial, lacustrine (river terraces, alluvial fans, flood plains, lakes) (Andreucci et al., 2012; Preusser et al., 2016); marine (raised beaches, beach ridges, offshore) (Pascucci et al., 2014; Sechi et al., 2020); glaciogenic (moraine and till, outwash, glaciomarine) (Perez - Alberti et al., 2011); slope deposits (colluvium, rockfall, debris flows) (Fuchs and Lang, 2009); karstic (Romano et al., 2024); soils (modern, compound and buried soils) (Zucca et al.,2104); tectonic activity (Casini et al., 2020). The potential of luminescence dating can also be used as a sediment tracer and sediment fingerprinting tool (Gray et al., 2019).

The most exploited minerals in the luminescence dating technique are quartz and k-feldspar. They both have advantages and disadvantages (Table 1). Quartz is one of the most abundant minerals on Earth surface and is highly resistant to both chemical weathering and mechanical abrasion. This makes it stable and prevalent in various geological settings; quartz can be found in a wide range of environments, including aeolian (wind-blown), fluvial (river), lacustrine (lake), and glacial deposits.

The biggest disadvantage is that it saturates at lower doses which means that the upper dating limit is lower in respect to other luminescence-dating minerals. K-feldspar is abundant in certain geological deposits, particularly in granitic rocks. It can be a valuable luminescence dating tool in specific contexts; it is relatively resistant to mechanical abrasion, making it suitable for dating applications where the mineral may be subjected to physical processes. The disadvantages of k-feldspar could be summarized as: higher susceptibility to weathering compared to quartz; the signal tends to fade over time, necessitating corrections in the final age determination; the higher complexity of the signal respect that of quartz, requiring additional considerations during analysis.

Table 1. Advantages and drawbacks of commonly used luminescence minerals quartz and k-feldspar.

QUARTZ		K-FELDSPAR	
Advantages	**Disadvantages**	**Advantages**	**Disadvantages**
Resistant to weathering	Low luminescence intensity	Saturates at higher radiation doses → higher upper dating limit	Weathers rapidly
Bleaches rapidly	Saturates at low radiation doses → reducing upper dating limit	Bright signal	Signal fades over time (Fading correction)
Signal stable over time	Signal is sensitive to feldspar contamination (pureness test)	High K content → less sensitive to differences in dose received	Signal bleaches slowly

The choice between using coarse and fine-grained samples in luminescence dating depends on various factors, and each has its own advantages and limitations. Coarse grains, particularly in minerals like quartz, are more stable on the Earth's surface since they are less susceptible to weathering and mechanical abrasion, they often retain their luminescence signal well because they are less affected by exposure to sunlight (bleaching) or other environmental factors and are often preferred in environments with prolonged exposure to sunlight, such as beaches and dunes, where the degree of bleaching is significant. In contrast, fine grains, having smaller sizes, are more susceptible to the effects of environmental factors like sunlight, and they may be more effectively bleached by natural processes, they are generally more sensitive to light exposure which could be an advantage in environments where there is limited sunlight exposure, such as debris flows or rockfall deposits; in some geological settings, fine-grained sediments dominate, and using fine

grains is more practical, for example, in loess deposits, where fine-grained material is often more prevalent. Both coarse and fine grains receive ionizing radiation from alpha and beta particles, gamma rays, and cosmic rays. Due to the small size of alpha particles, they become trapped on the outer rim (25 μm) of coarse grains. To eliminate this outer layer, which can affect the accuracy of measurements, the coarse sample undergoes etching with hydrofluoric acid (HF). The final dose rate is then determined, considering only the contributions of beta particles, gamma rays, and cosmic rays. Conversely, the diameters of fine grains are such that alpha particles can penetrate them entirely. As a result, the dose rate calculation for fine grains must include the contribution of alpha particles.

3.3.3 Applications of Luminescence Dating

Luminescence dating has a wide range of applications across various scientific disciplines:

- **Archaeology**: Luminescence dating is extensively used in archaeology to determine the age of artifacts and archaeological sites. It is particularly valuable for dating pottery, burnt stones, and sediments associated with human activities (Wintle, 2008).

- **Quaternary Geology**: Luminescence dating helps reconstruct the chronology of Quaternary geological processes, including the timing of sediment deposition, landscape evolution, and the history of glacial and interglacial cycles (Rhodes, 2011).

- **Paleoenvironmental Studies**: Luminescence dating is applied to sediments in lakes, rivers, and oceans to reconstruct past environmental conditions. It helps in understanding changes in climate, sea levels, and landscape dynamic (Rhodes, 2011).

- **Earth Science**: Luminescence dating contributes to studies of tectonic activity, faulting, and seismic events by dating deposits associated with these geological processes (Wintle, 2013).

- **Geomorphology**: Luminescence dating is used to establish the timing of events shaping the Earth surface, such as landslides, rockfalls, and the formation of landforms like dunes and river terraces (Rhodes, 2011).

- **Glacial Studies**: Luminescence dating helps determine the timing of glacial advances and retreats, providing insights into past climatic conditions and the dynamics of ice sheets (Rhodes, 2011).

- **Coastal and Marine Geology**: Luminescence dating contributes to understanding the history of coastal evolution, sea-level changes, and the deposition of marine sediments (Wintle, 2008).

- **Sediment Transport Studies**: Luminescence dating is used in studies of sediment transport in rivers and coastal environments, helping to track the movement and deposition of sediments (Rhodes, 2011).

- **Sediment Fingerprinting**: Luminescence dating can serve as a sediment fingerprinting tool, tracing the origin and transport of sediments in river basins (Rhodes, 2011).

- **Dosimetry**: Luminescence dating techniques are applied in dosimetry studies, which involve measuring radiation doses for purposes such as radiation protection and radiation therapy (Wintle, 2008).

- **Environmental Monitoring**: Luminescence dating can contribute to environmental monitoring by providing information on sedimentation rates, helping to assess the impact of human activities on landscapes and ecosystems (Wintle, 2008).

4.1 Initial phase

The initial stage consisted of exploring various Mars analogue areas to conduct luminescence tests on basalt-derived deposits. Aerial photographs and satellite images helped to better compare the depositional environments of Lanzarote with those on Mars. Alluvial and colluvial sediments from Famara and braided deposits collected in Los Ajaches underwent tests to evaluate their response to the Infrared Stimulated Luminescence protocol (Fig. 41).
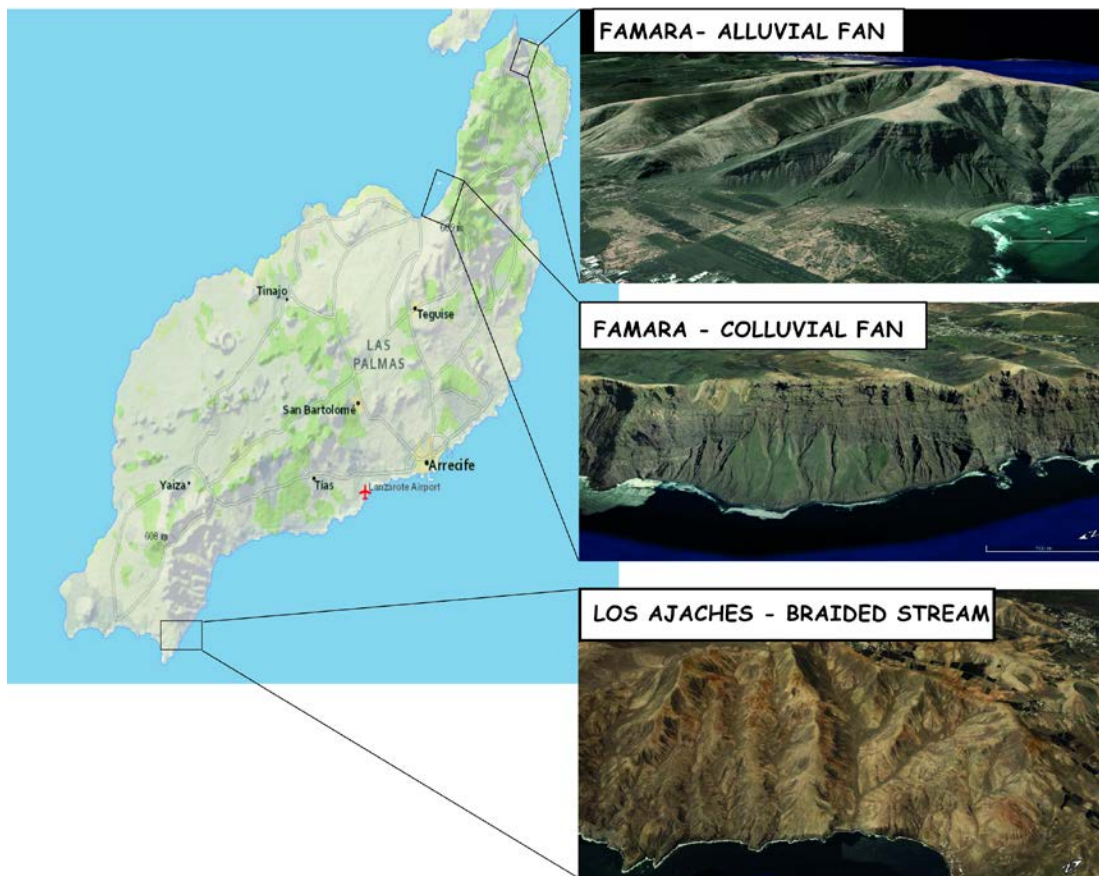

Figure 41. Surveying distinct geological formations in Lanzarote to evaluate luminescence responses on basalt-derived deposits during the initial testing phase.

4.1.1 Studied area: Famara massif

According to the Geological map of Spain scale 1:50.000 (1:25.000 in the particular cases of the Canary Islands) MAGNA (2nd Series) published by the Spanish Geological Survey (IGME-CSIC), the Famara massif of Lanzarote is represented in two distinct geological sheets: sheet 1080 Haria (48-35) and sheet 1082 Arrecife (48-36). The two sheets are subsequently divided in sections as follows: 1080-I-IV (Caleta del Sebo) (Balcells Herrera et al., 2004a), 1080-II (Haría) (Balcells Herrera et al., 2004e); 1080-III (Sòo) (Balcells Herrera et al., 2004b), 1082-I (Guatiza) (Balcells Herrera et al., 2004f), 1082 IV (Teguise) (Balcells Herrera et al., 2004c). The geological characteristics of Famara are examined based on the information provided in the respective maps, along with insights from the Geode map (Bellido et al., date of map consultation April 15, 2024), organized by geological time scale. In the later stages of the Miocene epoch, volcanic activity shifted towards the northeast, leading to the formation of the Famara volcanic shield which currently dominates the landscape of the northern part of Lanzarote. The edifice has maximum altitude of 671 m and stretches approximately 20 km from Punta Fariones in the north to the vicinity of Teguise in the south, with gradually declining elevations towards the south (Fig. 44).

Originally, this structure likely extended farther westward than its current boundaries, but over time, it has been heavily eroded, altered and largely obscured by more recent volcanic activity from the Quaternary period. A large marine abrasion platform dating back to the Pleistocene-Holocene period indicates a lateral collapse of its western flank followed by extensive erosion (Carracedo, 1994; Páez et al., 2002; Troll & Carracedo, 2016).

4.1.1.1 Late Miocene – Pliocene

The volcano Famara has undergone three distinct eruptive episodes during Miocene:

- *"Tramo inferior"* (10.2-8.3 Ma): This segment comprises layers of basaltic lava flows and interspersed pyroclastic deposits, some of which originate from volcanic eruption centres. It appears on the lower sections of Famara's western and eastern cliffs, often partially obscured by debris from slope erosion. Predominantly, these layers consist of thick, solid basaltic lava flows with rugged surfaces, showing columnar jointing and slabs, usually with scoriaceous bases. These flows typically measure between 1 and 3 meters thick, and collectively, they seem to slope gently towards the E-SE direction. Additionally, "pahoehoe"

lava types are frequently found within this sequence, forming layers of multiple units. These lava types are thinner, highly vesicular, and often heavily oxidized, containing notable amounts of zeolite and carbonate fillings. Chemically, the lavas are characterized by the presence of olivine and olivine-pyroxene compositions. Although not abundant, there are occasional layers of interbedded pyroclastic deposits distributed at various levels within the sequence. These deposits may appear as thin stratified layers or remnants of once-prominent eruption centres, sometimes causing minor inconsistencies with the underlying lava flows. The combined thickness of this section, including outcrops beyond this specific area, is estimated to be close to 200 meters. The network of veins in the lower part of the volcanic structure tends to be denser, although it's not characterized by an abundance of dykes. These dykes, primarily composed of olivine basalt, sometimes exhibit a fine-grained texture and are typically around 1 to 1.5 meters thick. In this particular area, dykes display varied orientations rather than following a specific pattern, ranging from N-S to N 30º E and E-O directions. Often, these dykes are associated with buried eruption centres, displaying a wide range of orientations (Carracedo & Rodríguez Badiola, 1992; Coello et al., 1992; Fúster et al., 1968; Greensmith, 2000; Hausen, 1959).

- *"Tramo medio"* (7.2 -5.3 Ma): The midsection of the volcanic complex exhibits better representation than the previous one, extending along the entire western and eastern cliffs. It comprises a substantial stack of basaltic lava flows interspersed with numerous scoriae and layers of pyroclastic material, forming a gently sloping tabular structure oriented towards the east. At its northernmost point, Punta Fariones, there's a slight tilt towards the N-NE direction. The lava flows, typically "aa" type, measuring 1 to 2 meters in thickness, display columnar jointing internally and rubble at the base and top, often showing signs of significant alteration. These are predominantly dark, massive, and porphyritic rocks, with olivine phenocrysts altered to iddingsite. Commonly, vesicles are filled with zeolites and carbonates. Throughout the lava flows, there are frequent occurrences of scoriae and pyroclastic layers, some linked to eruption centres. Dikes are sporadic but present, sometimes creating protrusions due to uneven erosion and lacking a consistent orientation pattern. The visible depth of this entire section varies between 100 and 200 meters. In the eastern sector, erosion has carved deep valleys running E-W, cutting through the lava flows of this section, occasionally exposing the underlying strata. Morphologically, the eastern escarpment's alignment may be attributed to a presumed fault, which organizes the

arrangement of these landforms and contributes partially to their northward tilt. Moving southward, the Miocene deposits in this segment are nearly obscured by extensive lava flows from the Quaternary volcanoes of the La Corona group. In certain areas, remnants of the pre-Quaternary landscape are discernible, with instances of recent lavas cascading over these older formations (Fig. 42). Towards the south-eastern part of La Corona, minor outcrops of midsection lava are visible, although heavily coated with caliche encrustations and pyroclastic material from nearby volcanic activity (in the La Majadita area). In this segment, the network of veins predates that of the lower section, though dikes remain relatively sparse. They are predominantly associated with eruption centres interleaved within the lavas. These dikes typically consist of olivine basalt and exhibit orientations mostly aligned with

Figure 42. Basaltic lava flows originated from La Corona that descended the Miocene western slope of the Famara Massif, creating a small delta upon entering the sea and extending the island's perimeter.

the north-south axis, occasionally displaying transverse orientations (Carracedo & Rodríguez Badiola, 1992; Coello et al., 1992; Fúster et al., 1968; Greensmith, 2000; Hausen, 1959). Dating of the flows, particularly those near the cliffs of Orzola and Guinate, suggests an eruption period ranging from 7.2 to 5.3 million years, as outlined by Coello et al. (1992).

- "*Tramo superior*" (3.9 - 3.8 Ma): the upper section is distinguished by the presence of minor local discordances and paleo reliefs, facilitating its differentiation from the middle one. The columnar nature of the lava flows in this part sometimes aids in its delineation, as the contact with the underlying layers is not consistently discordant. However, its coverage on the map is more limited than the previous section, mainly restricted to higher elevations and obscured by extensive superficial or Quaternary pyroclastic deposits. This upper portion is characterized by stacked basaltic lava flows arranged relatively horizontally over those of

the middle section, forming a tabular morphology with a flat upper surface. Some areas display adaptations to irregularities and minor paleo reliefs in the underlying lava flows, resulting in slightly steeper inclinations, typically not exceeding 5 degrees. The segment comprises multiple lava units stacked atop each other, occasionally interspersed with layers of scoriae or pyroclastic. Generally, these lavas exhibit an "aa" type morphology, with narrow scoriaceous bases and internally massive and coherent structures, often featuring well-defined columnar jointing (Fig. 43). They appear dark with low vesicularity, displaying a porphyritic texture characterized by abundant iddingsitized olivine phenocrysts in a

Figure 43. Columnar jointing forms lying above reddish palaeosols. View from Mirador de Guinate.

fine-grained matrix. The thickness of individual lava flows in this section varies from 1 to 4 meters on average, occasionally reaching thicknesses exceeding 10 meters in specific locales, such as the Guatifay area. Overall, the cumulative thickness of the segment is estimated to range between 100 and 130 meters. The eruption centres associated with this segment, like those of the preceding sections, were likely situated to the west of the present outcrops. However, within this segment, there may also be smaller buried local eruption centres obscured by subsequent volcanic activity. In the Mirador del Río area, a highly scoriaceous and oxidized pyroclastic deposit corresponding to a localized eruption centre of this segment is observed. Due to complete erosion of its original morphology, reconstruction is limited to some extent based on the periclinal dips of the structure. The vein network in this segment is less extensive compared to the previous sections, with no documented dikes cutting across the lava flows in this area (Carracedo & Rodríguez Badiola, 1992; Coello et al., 1992; Fúster et al., 1968; Greensmith, 2000; Hausen, 1959; Tomasi et al., 2023).

Aeolian bioclastic calcarenite deposits are intercalated between volcanic eruptions on the northern area of the Famara massif, at sites like Valle Chico, Valle Grande, and Fuente Gusa. These deposits show high fossiliferous content, comprising terrestrial gastropods, bird and tortoise remnants (Casañas, 1990; Páez et al., 2002; Lomoschitz et al., 2016; Troll & Carracedo, 2016), and bear witness to a long period of volcanic inactivity. Ranging in thickness from 0.6 m and 3 m, they are dated back to the Early Pliocene, ca. 4.3 and 3.78 Ma, representing a transition from flat plains to aeolian and fluvial sedimentary environments (Lomoschitz et al., 2016).

Glacis deposits are found sparingly in the upper regions of the Famara massif. They form small pockets where detrital materials accumulate, such as in the elevated areas of Lomo del Zalahar, Fuente Dulce, and Fuente Salada. Comprising subrounded basaltic fragments ranging from millimetres to centimeters in size, they are surrounded by a fine sandy or clayey matrix. These deposits often display a superficial layer of caliche. Typically, their thickness is minimal, rarely exceeding one meter.

4.1.1.2 Lower Pleistocene

After the cessation of Miocene volcanic activities, there is a hiatus in volcanic events in this region until the Lower Pleistocene, although volcanic activity persists elsewhere on the island during the Pliocene. This subsequent phase of volcanic activity differs significantly from the earlier period. It continues almost uninterrupted until historical times and it is characterized by its sporadic nature, yet it is governed by a fissural regime, leading to the formation of aligned volcanic structures following the dominant NESO structural orientations.

The emission centres that emerged within Miocene-Pliocene-era ravines, guided lava flows through "intracanyon" channels. The Atalaya de Haría edifice exhibits pyroclastic cone morphology with abundant lapilli, scoria, and bombs, while lava flows include "pahoehoe" and "aa" types. The Mala building features highly oxidized pyroclastic deposits and emitted basaltic lava flows, channelled through the Barranco Valle del Palomo. The Tenegüime building emitted a significant "aa" lava flow, exhibiting vertical columnar jointing (Fig. 44).

The Guantesive-Temeje Alignment consists of Montaña or Lomo Guantesive and Montaña Temeje, with Montaña Temeje positioned above intracanyon lava flows dated at 1.4 million years ago. Montaña Temeje is a small, conical tephra edifice characterized by pyroclastic material and stratified layers of lapilli.

Figure 44. Miocene and Lower Pleistocene toponymy of Famara (Esri map modified).

The Chimia-San Rafael Alignment comprises volcanic formations on the southern slopes of the Famara massif, with lava flows spreading towards the northwest. San Rafael Structure is located near Teguise, while Chimia Mountain Structure lacks a crater and is predominantly made up of basaltic scoria (Fig. 45).

Figure 45. Basaltic lava flows from the Montana Chimia (Pleistocene) building, discordant over the lava piles of the Famara stratovolcano, in barranco Las Piletas.

The Nazaret-El Calvario Alignment and Guanapay Volcano are significant formations near Teguise. It consists of Nazaret East, Nazaret West, and El Calvario structures, while Guanapay Volcano features basaltic lava flows and dispersed pyroclasts.

The Guantesive-Temeje alignment is located along the Teguise-Haría road and features a horseshoe-shaped crater open towards the northeast, composed mainly of lapilli and scoria with olivine basaltic bombs and lava blocks.

The southwestern boundary of the Famara sector is defined by the Zonzamas-Téjida- Tinaguache Caldera alignment, featuring basaltic lava flows, tephra cones, and scattered pyroclasts oriented along a N70ºE direction. Montaña Téjida, primarily located in the Teguise area, comprises layered lapilli-sized pyroclastic deposits and volcanic bombs, displaying moderate preservation with some erosion. Montaña Tinaguache, the main cone in the alignment, has a horseshoe-shaped crater facing southeast and consists of layered lapilli with larger components like bombs and blocks. Extensive lapilli deposits surround both structures, resulting from eruption fallout and later covered by

Tahíche volcano lava flows. Lava emissions from these formations created a vast malpaís extending eastward, overlaying Guanapay lava flows. The malpaís surface is characterized by highly scoriaceous lava forming moraines, with internal lava flows showing less vesicularity and greater coherence.

Simultaneously, sedimentary deposits are formed, interspersed with volcanic materials. An initial stage of alluvial fans generated from Famara massif's escarpment erosion, is found exclusively in the southwestern sector of Famara region (Fig. 48). The fans display a lobular, quasi-triangular shape, with a pointed apex directed towards the source area. Comprised of assorted sands and gravels, these detrital deposits display variable stone sizes, ranging from 2 cm to 60 cm. Their sandy-clay matrix, predominantly basaltic fragments, and irregular thickness contribute to their heterogeneous nature, with depths ranging from 1-2 meters near the source to 10-15 meters at the base. The fans are dissected by natural drainage channels-ravine (*barrancos* in Spanish). Currently, these ancient fans appear overlain by younger slope deposits, indicating their age as predating the formation of adjacent landforms and succeeding the initial development of the Famara massif.

Different alluvial-colluvial deposits are predominant in the southeastern region, occupying depressed horizontal areas, most extensive around the Guanapay volcano. They spread outward towards the Famara ridges to the north and the Quaternary *malpaíses* to the south, facilitated by natural basin closures. These materials, sandy and clayey, typically display an orange coloration and powdery texture, occasionally containing basaltic pebbles within a sandy matrix and intermittent intercalations of pyroclastic material mixed with sand. While poorly consolidated, allowing for vertical cuts, they are susceptible to erosion features such as gullies, ravines, and minor collapses, with visible thickness ranging from 1 to 3.5 meters (Fig. 46).

Figure 46. Gully formed on Pleistocene sandy clay, near Los Valles.

Caliche (or calcrete) deposits, consisting of calcium carbonate, are common in desert or semidesert climates, with calcretes in the Canary Islands generally forming since the Pliocene during periods of relatively lower aridity (Alonso-Zarza & Silva, 2002; Genise et al., 2013). The texture of the calcrete varies depending on its formation environment and processes. In some cases, it exhibits laminar structures, or fill cracks and fissures in the lavas while in others, it may display massive horizon with sub-horizontal cracks which may be occasionally up to 3-4 meters in heigh particularly in locations west of Teguise (Fig. 47). Additionally, calcrete formed on clay-silt substrate from weathered lapilli can have a distinct texture, and incipient calcrete on aeolian sand-sheets may show rhizocrections and insect trace fossils (Huerta et al.,2015). Carbonate calcium deposits can also provide greater consolidation to coastal windblown sands. The calcrete formations examined by Huerta et al. (2015) in Lanzarote and Fuerteventura exhibit a complex mineral composition, dominated by calcite and phyllosilicates, alongside other minerals like feldspars, aragonite, and

Figure 47. Calcrete formation observed on the basal host rock at the Famara cliffs.

clinopyroxene, with quartz varying in abundance. Trace elements such as dolomite, ankerite, kutnahorite, epsomite, gypsum, foids, and Fe oxides/hydroxides are also present. The calcium, crucial for the formation of the calcretes, is believed to originate from aeolian dust, as suggested by the same authors. The presence of Mg-carbonates and chabazite in a cal/dolocrete profile studied in Mirador del Rio by Alonso-Zarza et al., (2016) underscores the intricate interplay between groundwater and vadose processes in basaltic sourced host rocks within arid to semiarid climates. The prevalence of calcite at the profile's summit suggests a rising Ca/Mg ratio attributed to the influx of aeolian dust. These dolocrete profiles provide valuable insights into the shift from volcanic to paedogenic environments and the development of alkaline surficial paragenesis. According to Alonso-Zarza & Silva (2002), the microfabrics in calcretes implies that climate and vegetation played

crucial roles in their formation. In fact, calcretes are indicators of arid to semi-arid climates, suggesting their formation during relatively humid periods among arid conditions (Genise et al., 2013).

This is also confirmed by Vega (2010) which also offers valuable perspectives into the formation of caliche-calcrete layers above the first generation of alluvial fans. Initially, marine bioclastic sediments, resembling climbing dunes, covered the fans in El Jable plain. Over time, palaeosols developed over some of these layers. Subsequently, an arid period, coupled with intense evapotranspiration, facilitated the transformation of these carbonate deposits into robust caliche layers. However, during a later stage in the Lower Pleistocene, characterized by intense precipitation, the Famara Cliffs experienced significant erosion, causing the large calcareous crust to fracture. This erosion continued to the Holocene, leading to the deposition of subsequent slope debris, darkened due to the terrigenous material, which partially overlaid the calcrete, resulting in the distinctive fan-shaped morphology observed today (Fig. 48).

Figure 48. Alluvial fan system in the western escarpment of Famara. The oldest fans, correspond to the first generation, easily recognisable by the whitish calcrete layer covering them.

4.1.1.3 Middle Pleistocene

During the Middle Pleistocene, sedimentary deposits covered extensive lava flows and remnants of Miocene reliefs, forming small basins. These deposits, influenced by prevailing winds, are a mix of detrital materials and pyroclasts, with some partially unaltered pyroclasts visible. The Ubigue-Cabrera-Chica alignment marked volcanic activity, featuring cone-shaped formations with varying crater orientations and lava flows. Montaña Ubigue, Montaña Cabrera, and Montaña Chica lack clear stratigraphic relationships. Tahiche volcano, southeast of the region, is a well-preserved tephra cone associated with lava malpaíses, exhibiting layered pyroclastic mantles and olivine-bearing basaltic rocks (Fig. 50).

4.1.1.4 Upper Pleistocene

Los Helechos, La Corona, and La Quemada de Orzola are very well-known volcanic structures in the northern Famara region. These structures are oriented N50ºE, with the extreme buildings located approximately 6.9 km apart, considering the presence of the small emission centre of El Valle at the southwestern end of the alignment. The volcanic complex erupted basaltic lavas, resulting in the formation of a vast lava field known as *malpaís* which increased the island's perimeter, but also pyroclasts, scoria, blocks, and bombs. The lavas in the area vary in thickness and composition, with olivine basalt being the predominant type and exhibits various geological formations, including moraines, lava tubes, and volcanic caves. One remarkable feature is the "Tunnel of Atlantis," an extensive volcanic tube extending 7.6 km underground and underwater (Tomasi et al., 2022). On the surface, this tube is marked by depressions called "jameos." The interior of the tube showcases diverse lava formations, such as galleries, corridors, terraces, and stalactites. The La Corona *malpaís* is not only significant geologically but also attracts tourists due to its accessible volcanic features, including the Jameos del Agua cave system (Carracedo et. al., 2003).

The slopes of the entire Famara cliff or escarpment are partially covered by detrital deposits resulting from gravitational dismantling of the reliefs. Two types have been distinguished: Gravitational Landslide Deposits and Hillside Deposits. The first ones are very coarse and heterometric, composed of pebbles and fragments of irregularly shaped basic rocks, sometimes large, originating from massive detachments of the cliff walls (Fig. 49). The matrix surrounding them is sandy, and in some cases, it provides some cohesion to the deposit, although, in general, the degree of cementation and cohesion is low. They reach very steep slopes, adopting triangular shapes, and increase in thickness and amplitude from the apex to the distal zones. Their terminations are often abruptly cut, causing high cliffs of great height.

Figure 49. Gravitational Landslide Deposits close to Punta Fariones in Famara.

Like the previous ones, hillside deposits also develop triangular shapes and cover a large part of the Famara cliffs on the North and the slopes of the valleys and ravines excavated in the Miocene relief. Composed of detrital, coarse, and heterometric materials, they lack internal classification or ordering but are generally smaller in size than the gravitational landslide deposits. The fragments are angular in shape, and the surrounding matrix is sandy. The consolidation of the deposits is low, making their stability precarious, though in some cases, partial cementation by caliche provides some cohesion.

In their distal parts, both types of deposits often show greater development and amplitude, acquiring very gently sloping inclinations, as observed near the Salinas del Río or in some inland ravines. Along the eastern coast, they may be deeply incised by the subsequent incision of the ravines, presenting vertical walls. A more detailed analysis indicates the existence of several

generations of deposits, with their apexes located in the ravines that cut into those of the previous generation. This situation is well appreciated in the deposits of the western cliff of Famara.

The most significant aeolian deposit is located east of Mala, currently being exploited in a quarry that reveals a thickness of about 22 m (Fig. 50). This site has been studied from many researchers due to its paleoclimatic importance consisting of alternating sequences of aeolian deposits and palaeosols (Danmati, 1997; Ortiz et al., 2006; Meco et al., 2011; Suchodoletz et al., 2013). These wind-blown sands show cross-bedding, are golden or whitish in colour, fine-grained, and formed by tiny calcareous fragments of marine fauna. They also contain numerous remains of terrestrial snails of the Helicid type and show evidence of calcification and limited consolidation.

Figure 50. Medium, Upper Pleistocene and Holocene toponymy (Esri map modified).

93

4.1.1.5 Holocene

The dismantling of the massif continued to generate two types of alluvial deposits: those located in low-lying areas and small enclosed basins, and those primarily found in the valley bottoms and ravines carved into the Miocene formations of Famara. The first exhibit extensive accumulations concentrated in the Orzola region, resting atop the La Quemada de Orzola flows. Composed of sandy-clay compositions with fine granulometry, these deposits often display brownish-orange hues and an earthy texture, occasionally

Figure 51. Alluvial fan near Orzola.

interspersed with pebble layers (Fig. 51).

The latter type comprises sands, gravels, and sometimes large basaltic boulders, lacking significant internal sorting or arrangement. Pebble sizes vary from a few centimetres to 60-80 cm, with occasional diameters exceeding a meter. Although surrounded by considerable fines, localized zones may feature concentrated pebbles and reduced matrix. While visible sections suggest thicknesses of 1-2 meters, subsurface depths can be three to four times greater.

According to Balcells & Barrera (1993f), these deposits belong to the Holocene Epoch, while according to Bellido et al., (map consulted on April 15, 2024), they are attributed to the Pleistocene.

Certainly, the gravitational landslide deposits and alluvial deposits of the western side of Famara massif are of Holocene age. The gravitational-colluvial deposits are characterized by a chaotic composition of coarse detrital materials, including sands, pebbles, and blocks, all basaltic in nature. These deposits lack internal organization, with angular blocks and intercalated aeolian sands displaying cream-white coloration and low-angle cross-bedding. Those generated above Playa de Famara are considered to be the second generation of Famara slope deposits (Fig. 52).

Figure 52. Second generation of gravitational landslide deposits above Playa de Famara.

On the other hand, the alluvial deposits are much more well developed on the slopes of the southeastern relief, extending towards the El Jable plain. They are composed of coarse detrital materials, including sands, angular and subangular pebbles and blocks, all basaltic in composition. These deposits also lack internal ordering, with pebbles embedded in a sandy matrix. They exhibit a pseudo-triangular plan shape, with the acute vertex pointing towards the head zone. Often, they overlap and indent, forming distinctive coalescent cones or fans. These are identified as the third and final generation of fans, although distinguishing between these last two generations is not always straightforward (Fig. 53).

Figure 53. The alluvial fan system on the western escarpment of Famara. Fans covered with a light-brown layer are associated with the first generation, while the darkener fans, sloping towards the El Jable plain, belong to the third generation.

The Holocene volcanism in Famara is represented around Guatiza by two eruptive fissures: Fisura de Guenia and Alineación de Calderetas de Guatiza (Fig. 50).

Montaña Guenia, a sizable cone, features craters facing northeast and northwest, comprising layers of scoria, lapilli, blocks, and coarse fragments, along with vesicular lava fragments. Wind-dispersed pyroclasts cover the surrounding area, forming a striking landscape. Basaltic lavas from fissures at the base flowed north-eastward, overlapping Miocene reliefs of Famara, and westward, forming

powerful flows resting on older Guanapay centre emissions. The Calderetas de Guatiza alignment includes four main volcanic structures and smaller ones, extending N30oE, with lava flows altering the coastline morphology. The largest structure, La Caldera or Montaña Tinamala, boasts a horseshoe-shaped crater with layered pyroclasts. Surrounding basaltic lava flows create rugged terrain. Las Calderetas features irregular coarse scoriae, abundant bombs, and lapilli fragments. Adjacent Las Calderas structures consist of lapilli-poor deposits with coarse materials, including vesicular scoriae and large bombs.

Holocene marine terraces are named *Rasa Marina Erbanense* (from *Erbania*, old name of Fuerteventura) (Meco et al., 1986) and are found scattered on the east side of Famara (Playa del Tio Joaquìn, Punta Prieta and La Caleta), typically at elevations slightly above modern beaches but about 1 m lower than the Pleistocene terraces (known as *Jandiense*). The deposits consist of boulders from the Jandian sandstone, light-coloured bioclastic

Figure 54. *Rasa Marina Erbanense* terrace in Las Cocinitas.

sandstone with occasional conglomerates of basic pebbles and marine fossils. They occur in patches, ranging from 10 to 60 cm thick, resting on Quaternary lavas, sometimes filling small depressions or lying between current rock formations (Fig. 54). The fossil content is diverse, resembling contemporary fauna, with species assemblage predominated by *Cerithium vulgatum*, *Patella* and *Columbella rustica* (Meco et al., 1986; Shimmield et al., 1997). According to radiocarbon dating conducted in Fuerteventura, the deposits are dated between 4 ka and 2 ka.

In this coastal area, a variety of beach types can be found. Playa de Famara located at the foot of the Famara massif, is the most prominent stretching for about 4 km. The beach primarily consists of light grey sands, a result of the disintegration of surrounding materials. Additionally, it is supplemented by Pleistocene-Holocene aeolian sands. Nearby, in the vicinity of Salinas del Río, beaches feature rounded basaltic pebbles embedded within a sandy matrix of medium and fine grains. Conversely, on the eastern coast, sand beaches like Playa del Risco (Fig. 55), La Cantería, and certain coves are characterized by fine-grained golden or white sands, predominantly derived from the breakdown of seashells. Despite these distinctions, the overlapping of beach deposits with colluvium and slope materials covering the Miocene scarps can sometimes make their individualization challenging.

Figure 55. Pebbles and sandy beach Playa del Risco at the foot of the western escarpment of Famara.

4.1.2 Studied area Los Ajaches massif

Los Ajaches corresponds to the first volcanic event in Lanzarote happened during the Miocene. According to the Geological map of Spain scale 1:50.000 (1:25.000 in the particular cases of the Canary Islands) MAGNA (2nd Series) published by the Spanish Geological Survey (IGME-CSIC), the area is represented in two distinct geological sheets: sheet 1084 Femés (47-37) (Gómez Sainz de Aja et al., 2004a) and sheet 1081 Tinajo (47-36). The Tinajo sheet is subsequently divided in two sections as follows: 1081-I (Tinajo) (Gómez Sainz de Aja et al., 2004b) and 1081-II (Yaiza) (Balcells Herrera et al., 2004h). Considering the only one sample collected in the barranco del Higueral, the geological characteristics of Los Ajaches are examined based only on the information provided in the sheet

Femés and Yaiza, along with insights from the Geode map (Bellido et al., date of map consultation April 15, 2024). These data are integrated with the research conducted by Driscoll et al. (1965), Carracedo and Rodríguez Badiola (1992), and Rodríguez Badiola et al. (1994).

The Ajaches edifice constitutes a high massif occupying the southeastern part of Lanzarote. It is composed of a monotonous stack of basaltic lava flows over 550 meters thick. Generally, these flows exhibit a gentle dip of about 6-8 degrees to the east-southeast. Interbedded within the lava stack, locally observed are some levels of scoria and/or buried cones, representing small contemporaneous vents with the lava emissions. Dikes cutting across the succession are also observed. Both the dikes and the pyroclastic intercalations are more abundant in the southern end of the sheet (Papagayo sector). This area presents somewhat different characteristics from the rest of the massif, with a higher proportion of intrusive rocks with sialic and intermediate compositions. The flows constituting the classic Los Ajaches escarpment were dated by Ibarrola et al. (1988) and Coello et al. (1992), from bottom to top, at 15.5-12.3 Ma.

Nowadays the massif shows high degree of erosion which do not allow the structure of the primitive building to be clearly established.

4.1.2.1 Miocene

During the Miocene, intense volcanic activity was widespread across the archipelago. Specifically, in the eastern Canary Islands, the Basal Complex was exposed on the surface of Fuerteventura, and an NNE-SSW-trending fissure developed, stretching from Fuerteventura to Lanzarote. This fissure led to the construction of two edifices in Lanzarote (Ajaches to the south and Famara to the north). The oldest basaltic formations are identified by Fuster et al. (1968) as "Basaltic Series I".

The ancient flows of Los Ajaches can be grouped in two categories:

- *"Tramo inferior"*: The lower geological formation is predominantly composed of ancient basaltic lava flows and pyroclasts. These materials are primarily found in the southernmost part of the area, specifically the El Papagayo-Playa Blanca region, and at the base of the western escarpment of the Los Ajaches massif, as well as within some barrancos cutting through the Miocene terrain. In the Papagayo area, characterized by smoother relief and lower elevation, there is a dense concentration of dykes and numerous intrusive bodies of intermediate composition. Dykes converge toward Punta del Papagayo, and buried emission centres are prevalent, featuring lapilli, scoriae, and a few basaltic bombs. Similar emission

centres are noted in the northern sector near Femés and the south slope of the Los Dises ravine. The northern sector mainly comprises altered, thin lava flows exhibiting greyish alteration tones and increased dyke presence. These lava flows, predominantly olivine basaltic or olivine-pyroxenic "pahoehoe" types, show signs of intense weathering, with olivine commonly iddingsitized and secondary fills of zeolites and carbonates. Crossing the basaltic lava flows are two small outcrops of microgranular rocks classified as gabbro, located approximately 700 m northeast of Playa Mujeres and 450 m south of Playa del Pozo. Basic lithic breccias are observed east of Femés in the Las Casitas area, characterized by chaotic composition and basaltic fragments of varying sizes. In the Papagayo sector, small, isolated outcrops of intermediate composition Mugearitic and Benmoreitic intrusions are present, representing more differentiated terms than trachybasalts. Salic and intermediate tuffs and breccias are exclusively found in the Papagayo zone, displaying monomictic breccias with angular fragments resembling extrusion breccias or dome collapse remnants. Mixed breccias with variable-sized salic fragments and basic juveniles are also present, along with zones containing "ribboned" juveniles and lithics up to 15-20 cm in size. The breccias near Punta del Papagayo consist of subangular fragments of trachybasaltic composition, filling an old crater and discordant over the reddish scoriae of an old basaltic emission centre. Lastly, four small outcrops of basic intrusions composed of olivine basalts with abundant phenocrysts occasionally showing "pegmatoid" veinings are present.

- *"Tramo superior"*: This section is primarily represented in the Domain of the Los Ajaches massif. It consists mainly of a thick stacking of basaltic lava flows. The discordance between the lower and upper sections is not always visible. In some coastal areas (Los Dises, Parrado), it's more apparent due to the presence of alluvial sediment layers, considered the base of this range, marking a sedimentary interruption in the lava emissions. These alluvial deposits consist of subangular-subrounded cobbles, variable sizes, predominantly basaltic in composition in a reddish and brownish sandy matrix. Some cobbles exhibit a ferruginous patina, and occasional orientations and diffuse stratification indicate paleocurrents from the interior to the coast. Basaltic Lava Flows and Pyroclasts form prominent relief features in the sector, such as Pico de la Aceituna, Pico Redondo, Morro de los Dises, and Hacha Grande. They are mostly massive and coherent with few pyroclastic intercalations, forming stepped reliefs. Occasional levels of red-coloured "almagre" are intercalated between these lava flows. Pyroclastic deposits are also present, with two emission centres mapped in the

southern slope of the barranco Higuera and the northeastern slope of Hacha Grande. The former consists of reddish lapilli, somewhat rounded scoriae, and some basaltic olivine-augitic bombs. Almost all dikes are of basic composition, with only one trachytic dike in the Coloradas beach. Most dikes have north-oriented orientations, converging toward Punta del Papagayo. However, in the northern sector of the Femés massif, there's a lower density of dikes with mostly N-60ºE orientations. Dikes are mostly subvertical with thicknesses between 0.3 and 1.2 m, predominantly composed of olivine basalts, although other compositions like aphanitic and olivine-pyroxenic are also present. Some coastal areas show multiple intrusions, double and triple dikes. Late-stage basaltic lava flows are represented by small outcrops found at the head of the Casita ravine and an isolated site along the coast at Baja Cumplida. These outcrops, composed of olivine basalts, likely resulted from late dikes or nearby vents, shaping the landscape of the Miocene stratovolcano.

4.1.2.2 Pliocene

During the Pliocene period, volcanic and sedimentary activities occurred in the region. The volcanic activity is represented by the volcano Montaña Roja, dated to approximately 2.7 million years ago by Coello et al. (1992). Sedimentary formations from this period include the Pliocene marine terrace, aeolian sands, and conglomerates and sands.

The Pliocene marine terrace is found along the southeastern coast, lying unconformably over Miocene basaltic flows at an elevation between 70 and 40 m above the current sea level. This unit consists of thin but continuous layers of marine sandstones and conglomerates containing numerous basaltic clasts, with rounded pebbles ranging from 1-2 cm to 10-15 cm in size. The sandstones exhibit bioclastic features and have whitish and greyish color. These deposits, like those observed in Fuerteventura, were previously described by various researchers and were dated to the early Pliocene based on paleontological studies by Meco (1982). Faunal remains found in these deposits suggest a warm coastal environment during the Pliocene. Common fossils include *Grypahaea virleti, Nerita emiliana, Strombus coronatus, Ancilla glandiformis, Lucina leonina, Rothpletzia rudista*, and *Patella ambroggii (*Zazo et al., 2002; Meco et al., 2007). On the contrary, Zazo et al. (2002) presume that these deposits are of Pleistocene.

Glaciys deposits of Sands and Conglomerates are found exclusively in the western Los Ajaches massif, consisting of heterogeneous sands and gravels, predominantly basaltic, with variable sizes and a sandy-clayey matrix.

Aeolian Sands of this Epoch are only located in the southeastern sector overlaying the Pliocene marine terrace, representing a regression phase. These are bioclastic calcarenitic dunes with abundant terrestrial gastropods, reaching up to 7 meters thick, showing a cream-white colour and are superficially hardened by a calcareous crust (caliche). This calcification likely marks the end of the Pliocene or the beginning of the Quaternary. Conglomerates and Sands are present in the southeastern sector of the region, between the Valle de Juan Perdomo and Vértice Papagayo, consisting of conglomerate

Figure 56. Los Ajaches Lower-Middle Pleistocene events (Esri map modified).

lenses of basaltic pebbles and sandy layers, heavily encrusted with carbonates.

The Montaña Roja volcanic structure, located in the southwest of the island, comprises a well-preserved circular crater atop an irregular scoria cone, reaching 194 meters above sea level. Its internal structure reveals layers of pyroclastic material, primarily strombolian-type lapilli, scoriae, bombs, and dense lithic fragments, with "Kugelapilli" deposits evident. The upper section of the cone consists of compacted scoriae, while extensive lava flows, displaying "pahoehoe" morphology, cover the northern slopes. These flows, ranging from 40-60 cm to 2 meters thick, consist of dark greyish basalt containing olivine phenocrysts. Extending over 25 square kilometres, the flows radiate northward from the crater, overlaying Pliocene abrasion platforms and reaching Las Salinas del

Janubio. In some areas, these flows overlay Miocene basaltic materials, showing signs of alteration and occasional dike intrusions.

4.1.2.3 Lower-Medium Pleistocene

The Montaña Bermeja-Cortijos Viejos volcanic structure in the northeastern area includes a relatively intact crater facing northeast, with pyroclastic cone containing various volcanic materials. It spans about 900 meters north-south, reaching a maximum height of 229 meters. Overlaying Miocene basaltic flows, the lava flows exhibit an "aa" texture and contain olivine-rich basalts with iddingsitized olivine's. The Gritana-Bermeja-Mina alignment features lava flows primarily directed south-eastward, covering the Playa Quemada-Puerto del Carmen area, characterized by olivine-rich basalts and frequent dunite nodules. The Caldera Riscada Building, situated on Miocene lava flows in the Femés valley, is a large structure with mixed origin, featuring stratified layers of oxidized lapilli and volcanic bombs, along with phreatomagmatic deposits (Fig. 56).

Other volcanic structures in the area include La Majada, Montaña Casa, Montaña Mojón which are mostly composed of lapilli, scoria, blocks, and volcanic bombs, with moderate to low preservation levels. The lava emissions from these volcanoes covered extensive areas, flowing predominantly south-southeast, but also north-northwest near Uga. These lavas exhibit scoriaceous surfaces, compact interiors, and occasional vesicularity, containing olivine phenocrysts and dunitic nodules.

The Femés Alignment is located on the dividing line between the valleys of Fena and Femés with their orientation (NE-SW) parallel to that of the two valleys mentioned above. Emerging from Miocene relief, these structures form the highest elevations in the southern part of the island, with La Atalaya de Femés reaching 608 meters. The alignment comprises several nested craters, with only the southern flank visible on this sheet. The alignment's lava flows cover significant areas in the Yaiza and Femés sheets, discordantly overlying Montaña Roja's flows (Pliocene). They are darker and more scoriaceous compared to Montaña Roja's flows, with fresher olivine and no iddingsitization processes evident. Most of the flows are "aa" type with well-developed scoriaceous bases, with some "pahoehoe" flows displaying corded structures south of Las Breñas.

Caliche deposits characteristic of desert or semi-desert climates, have a relatively limited aerial development, primarily outcropping in the southwestern sector, over the Pliocene Montaña Roja lava flows and to the east of Playa Blanca, over the Miocene lava flows (Fig. 57). The deposit consists mainly of calcium carbonate and is distinguished by its whitish or cream-colored appearance. This soil type forms a hard or "crusted" surface layer under extremely arid conditions.

Figure 57. Caliche formation above Miocene lava flow.

Attribute to Lower Pleistocene is the marine terrace founded at +20m (Salinas de Janubio) and three marine terraces at +40m (Punta del Papagayo, Rincón de Palo, Caletón del Rio, Punta Gines, Punta del Águila), above sea present level. Attribute to Medium Pleistocene is the marine terrace located at +10m (Punta Pechiguera) above sea present level. All the three terraces are characterized by warm fauna assemblage with the presence of *Ostrea virleti, Nerita emiliana*, and *Strombus* (S. cf. *coronatus*–S. cf. *bubonius*) (Zazo et al., 2002).

4.1.2.4 Upper Pleistocene- Holocene

The marine terraces above 1.5-2 m on the present sea level are of the Upper Pleistocene named "jandiense" by Meco et al. (1986), and identified in Playa Quemada, Salinas del Berrugo, and Punta Pechiguera. The outcrop at Salinas del Berrugo is the best preserved, with abundant fauna including *Strombus bubonius*, *Patella ferruginea*, and *Murex saxatilis*. Both conglomeratic and arenaceous levels are observed, with the latter composed of light-colored bioclastic sandstones distinguished by a "drusy" cement around the grains under the microscope. The Punta Pechiguera outcrop is correlated with *Strombus* levels to the Tirrenian stage of the Mediterranean, with the presence of

additional species such as *Thais haemastoma* and *Conus testudinarius* noted (Meco and Stearns 1981; Meco, 1982; Meco et al., 1986; Meco 1990, Zazo et al., 2002).

The Erbanense marine terrace, situated at +0.5 meters elevation, is the Holocene marine deposits. The terraces are mainly found on the eastern and southern shores, ranging from Playa Quemada to Punta Pechiguera, with identified outcrops at various locations. Distinguishing these deposits from the Jandia terrace can be challenging due to basins carved into the

Figure 58. Los Ajaches Upper Pleistocene-Holocene events with barrancos (Esri map modified).

Jandia deposits by the Erbanense terrace. This geological unit, defined by Meco (1991) comprises fine-grained sandstones, consolidated with abundant fauna, alternating with conglomeratic layers, typically less than 1-1.5 meters thick. Faunal remains within these deposits resemble present-day fauna, including species such as *Thericium vulgatum*, various *Patella* species, *Columbella rustica*, *Linga Columbella*, *Conus mediterraneus, Erosaria spurca,* and *Thais haemastoma*. Radiocarbon dating conducted at La Jaqueta and Corralejo outcrops (Fuerteventura island) yielded ages of 1.400 BP and 3.640 ± 160 BP.

The aeolian sand have very limited areal development, confined to small outcrops located in the southernmost part, at Playa Mujeres, Playa del Pozo, and the Papagayo-Caleta del Congrio area (Fig. 58). Likely, after a period of wind inactivity during the early Holocene, wind activity resumed during the late Holocene, reworking Pliocene and Pleistocene sands to form current or sub-current dunes known locally as "jables." These biodetritic sands resemble Pliocene sands, consisting of tiny mollusc shells, characterized by their cream-white colour, cross-bedding, and somewhat degraded dune morphology.

Alluvial deposits related to valleys and barrancos are almost exclusively located in the eastern sector including barrancos Fraile, Higueral, Casita, Dises, Parrado, Negro, and Juan Perdomo (Fig. 59). Due to low precipitation and irregularity, these ravines are often dry, except during heavy rain when they can act as flash floods, carrying large volumes of materials. Generally, these deposits consist mostly of heterogeneous sands and gravels, primarily basaltic in composition, with a minor component of silt-clay fraction. They vary in thickness, generally ranging from 1-2.5 meters.

The beach deposits in the eastern and southeastern sectors consist mostly of pebbles and are located at the mouths of ravines. Some of the best beaches for tourists are found in the Punta del Papagayo area. These beaches are sandy and influenced by small ravines, but their main sediment source is aeolian sand deposits. Typically, less than 400 meters in length, these beaches feature pebbles ranging from 3-4 cm to boulders over 15 cm, with a predominantly basaltic composition and grey to blackish colours.

Hillside Deposits and Colluvium materials are primarily found in the central-western sector of the map. This generation of hillside deposits is later than the first generation of alluvial fans, which appear chalky and are intersected by them. They are composed of coarse detrital material: sands, pebbles, and angular to subangular blocks, highly heterogeneous, and predominantly basaltic in composition embedded in a sandy matrix without any observable internal structuring.

Figure 59. Barrancos in the eastern section of Los Ajaches.

The Barranco del Higueral is the location where the sample was collected for the initial phase of the experiment. This area is within the Upper Pleistocene alluvial deposits (Fig. 60).

Figure 60. Barranco del Higueral, site of the collecting during the first phase of the experiment.

4.2 Second phase

Once the effectiveness of the chosen protocol on basalt-derived deposits was confirmed (refer to Results Chapter), the study advanced to the second phase. This phase aimed to assess the feasibility of applying the 'Martian' protocol to reconstruct the evolutionary history of a Martian analogue depositional environment. The chosen area for this investigation is the El Jable sedimentary basin, a remnant of a caldera, which bears similarities to a Martian meteoritic impact crater. The alluvial fan systems on the western flanks of Famara extend towards the basin, where alluvial sediments interbed with aeolian deposits. This environmental setting establishes a connection to depositional systems associated with dry-wet phases on Mars (Fig. 61).

Four barrancos (*Lz403*, *Horca*, *Las Piletas*, *Falls*) from the alluvial system of Famara and one site in El Jable plain have been selected for stratigraphic reconstruction (Fig. 62). The site in El Jable is related to the sandy pit studied by Heinrich et al. (2021). A total of 13 samples were collected from barranco *Las Piletas* for luminescence dating, and a total of 31 samples were collected for radiocarbon dating from barrancos *Las Piletas*, *Falls*, and from the sand pit in El Jable.
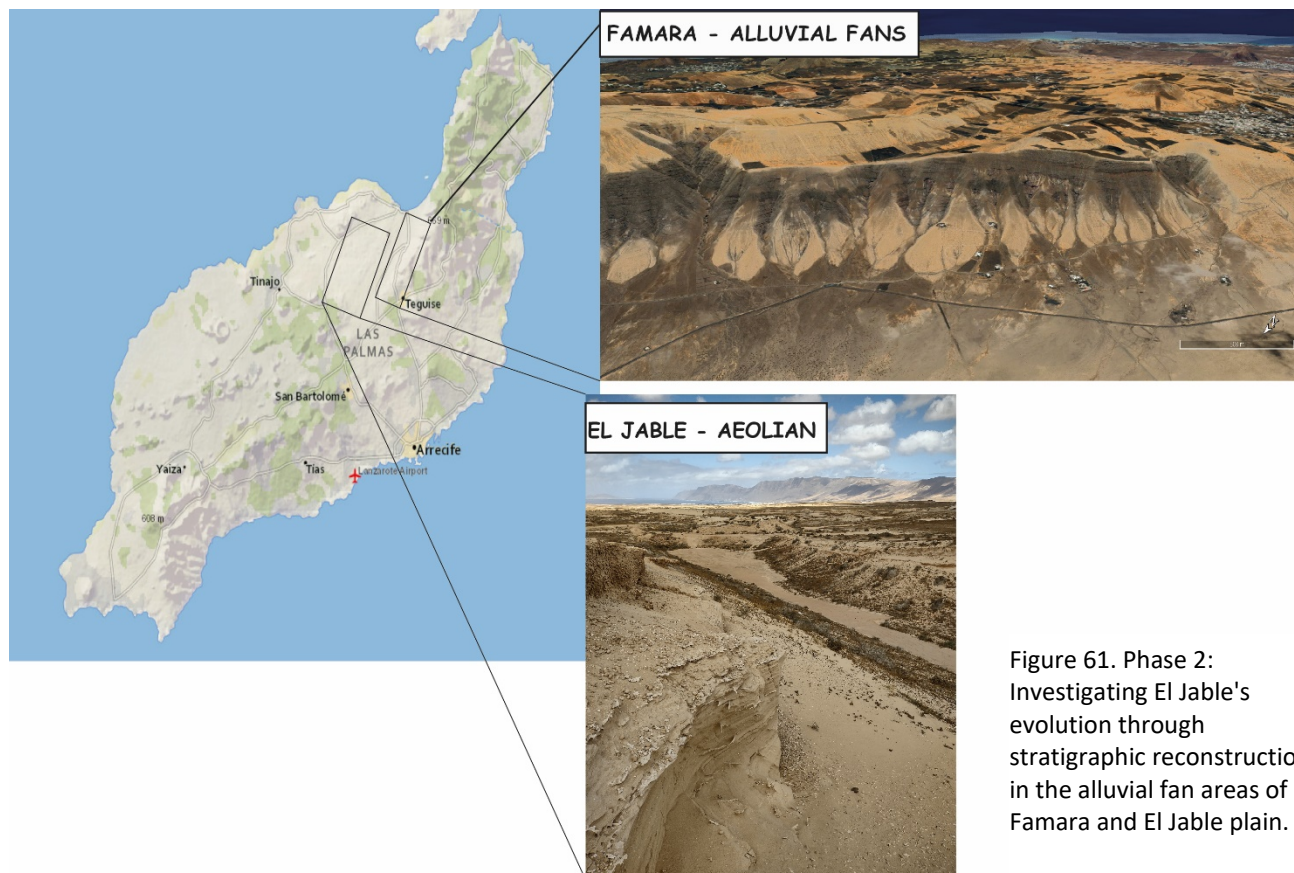

Figure 61. Phase 2: Investigating El Jable's evolution through stratigraphic reconstruction in the alluvial fan areas of Famara and El Jable plain.

Figure 62. Satellite images displaying the five studied areas for the reconstruction of the depositional system in El Jable plain. Above the alluvial fan system characterized by colluvial fan (red), ephemeral river (blue) and alluvial fan deposit (black). Below general view of El Jable plain and alluvial fan system.

4.2.1 Studied area El Jable plain

Known locally as *jables* (from the French *sables*), El Jable plain covers approximately 90 km², making it the largest aeolian deposit in the Canary Islands (Fig. 63). The plain is in the central lowland region spanning 21 km in length and ranging from 4 km to 10 km in width. The terrain exhibits a gentle

relief, with an average slope of 1.2°, excluding volcanic cones, and reaches a maximum height of 200 meters above sea level.

The El Jable plain is bordered by various volcanic formations, including remnants of intense fissure volcanism and numerous volcanic cones. The northern alignment features Montaña Chica and Montaña Cavera from the Middle Pleistocene, as well as the Soo volcanoes from the Late Pleistocene. Towards the south, Monte Mina and a bifurcated lava flow from the 1736 eruption of Montaña de Las Nueces are found. Additionally, volcanic cones line the western half of El Jable. The northeastern boundary is marked by the El Risco de Famara and alluvial fan system. The northern border coast consists of a rocky platform with small coves, primarily composed of volcanic sands and pebbles; the northeastern extremity includes Playa de Famara; and the southern coast is defined by extensive beaches comprised of marine sediment rich in organic matter.

According to the Geological map of Spain scale 1:50.000 (1:25.000 in the particular cases of the Canary Islands) MAGNA (2nd Series) published by the Spanish Geological Survey (IGME-CSIC), El Jable is represented in two distinct geological sheets: sheet 1080 Haria (48-35) and sheet 1082 Arrecife (48-36). The two sheets are subsequently divided in sections as follows: 1080-III (Soo) (Balcells Herrera et al., 2004b), 1082-IV (Teguise) (Balcells Herrera et al., 2004c); 1082-II-III (Arrecife) (Balcells Herrera et al., 2004d), 1082-I (Guatiza) (Balcells Herrera et al., 2004f). The geological

Figure 63. El Jable plain.

characteristics of El Jable are examined based on the information provided in the respective maps, along with insights from the Geode map (Bellido et al., date of map consultation April 15, 2024), organized by geological time scale.

The Miocene volcanic episodes of Famara are the foundational substrate upon which the younger volcanic cycles and the El Jable aeolian system have later deposited. Given that the volcanic events of Famara have been examined in the preceding section, the focus shifts to the Pleistocene volcanic events for analysis.

4.2.1.1 Mio-Pliocene

A significant climate shift occurred in the Canary Islands due to the closure of the isthmus of Panama during the Pliocene, which initiated the North Atlantic current. This current, flowing clockwise, extends southward along the northwest coast of Africa, reaching as far south as Senegal. As the current circulates around the Canary Islands, it brings cold water from the north and the humid trade winds, which mitigate the warming effect of the Sahara to the east.

Marine regression, resulting from climate changes, led to the extinction of the Miocene tropical fauna in the eastern Canaries. As these organisms eroded, they gave rise to organic sands, which were subsequently transported by Tradewinds into the island's interior (Troll & Carracedo, 2016) (Fig. 64).
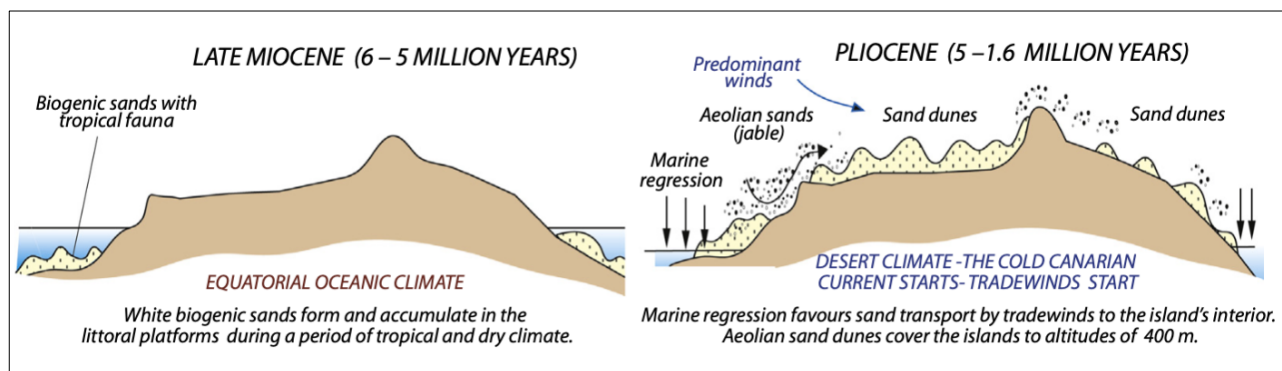

Figure 64. Evolution of the climatic and sedimentary environment from the Late Miocene to the Pliocene. Left: During the Late Miocene (6 – 5 million years ago), an equatorial oceanic climate dominated, with tropical conditions favoring the formation and accumulation of white biogenic sands on the littoral platforms. These sands contained tropical fauna and formed during a period of warm, dry climate. Right: By the Pliocene (5 – 1.6 million years ago), a shift to a desert climate occurred as the cold Canary Current established and trade winds began to dominate. Marine regression led to the exposure of previously submerged areas, and aeolian processes transported jable (aeolian sands) inland, forming sand dunes that covered the islands, reaching elevations up to 400 meters (Troll & Carracedo (2016).

An intriguing geological aspect is the presence of quartz crystals in aeolian sediments, despite their absence in Canarian igneous rocks. Although not directly related to the Canary magmatic suite, quartz is relatively abundant in aeolian sediments and is a main component of certain basement xenoliths. The quartz crystals found in surface sediments may originate from sand plumes generated

by large sandstorms in the Sahara Desert, which deposit significant amounts of aeolian dust in the Canarian Archipelago (Criado and Dorta, 2003, Muhs et al., 2010).

4.2.1.2 Lower Pleistocene

The Caldera del Cuchillo, located in the northwest, features a heavily eroded crater partially covered by lava flows, indicating past hydro magmatic activity. Aligned with Caldera Blanca, it forms part of a coastal alignment. Montaña Mina in the south comprises olivine basaltic lapilli and exhibits evidence of northward lava flows obscured by aeolian sand deposits. The Montaña Zonzamas-Montaña Maneje alignment borders the south El Jable plain and includes lava flows and basaltic tephra cones. Montaña Zonzamas displays overlapping vents forming a tephra structure, while Montaña Maneje is a conical tephra structure surrounded by Caldera de Zonzamas lava flows. Erosion, partly due to urban development, has impacted the landscape (Fig. 65).

Figure 65. Map of the boundaries of the El Jable plain with events from the Lower and Middle Pleistocene.

As previously discussed, it was during the Lower Pleistocene period that the erosion of Famara led to the formation of the first generation of alluvial fans. Their morphology and structures are detailed in the Famara-Lower Pleistocene section.

4.2.1.3 Middle Pleistocene

Basaltic lava flows and dispersed pyroclasts from alignments Montañas de Fuego cover a large part of the western sector, extending from Tinajo to La Santa town. These lava deposits are often

obscured by Pleistocene-Holocene aeolian sand deposits. The basaltic lava flows typically contain isolated olivine phenocrysts and small dunite nodules, appearing felty, vesicular, and scoriaceous on hand samples. Lava channels with block accumulations along the sides are common, resembling degraded volcanic terrain. Agricultural development often masks these outcrops. The dispersed pyroclasts from these alignments are predominantly found in Tiagua-Tao area, consisting mainly of fine lapilli.

The Montañeta-Caldera Honda is a well-preserved double volcanic cone near San Bartolomé, composed mainly of coarse basaltic tephra, featuring predominance of scoria, blocks, coarse lapilli, and porphyritic bombs with olivine phenocrysts. The lava flows extend south-eastward forming thick chaotic lava moraines in some areas exhibiting relatively high preservation levels.

Aeolian activity, leading to the development of extensive deposits of both loess and sand, began after the initial subaerial eruptive phase of the island. The exact timing of aeolian activity initiation on the Eastern Canary Islands has been a subject of ongoing investigation. Various studies have proposed different timeframes, ranging from Pliocene (Troll & Carracedo, 2016) to Upper Pleistocene. Ortiz et al. (2006) suggested Upper Pleistocene ages for most sequences based on amino acid racemization, while Edwards and Meco (2000) and Bouab and Lamothe (1995) discussed a Middle- to Upper Pleistocene dune formation. Roettig et al. (2020) provided a comprehensive correlation based on stratigraphic findings and luminescence dating, covering different dune fields on northern Fuerteventura. Similarly, Von Suchodoletz et al. (2013) discussed Middle-Upper Pleistocene ages for the Mala dune complex on Lanzarote.

Figure 66. The El Jable plain viewed from the volcano Mosta, with a car included for scale.

The aeolian system of El Jable is composed of loose, light-coloured grains with a fine-grained texture, exhibiting shades of white and yellow. The composition includes marine bioclasts (such as calcareous algae, bryozoans, foraminifera, and echinoderm spines, as well as remnants of other marine organisms), terrestrial bioclastic materials, carbonated crusts, volcanic material, and sediments resulting from the erosion of Famara (Fig. 66 and 67).

Figure 67. Aeolian system of El Jable. In the back, the alluvial - colluvial system of Famara.

Heinrich et al. (2021) describe the aeolian dune deposit in El Jable as comprising multiple sequences with a three-stage structure, labelled as DepoTypes 1-2-3. DepoType 1, forming the base of the sequence, is characterized by its high $CaCO_3$ content and low dust content. It lacks traces of vegetation and primarily consists of uncalcified brood cells, indicating arid conditions. DepoType 2 exhibits a similar granulometric composition to DepoType 1, but it is distinguished by the sudden appearance of land snails, calcified brood cells, and an increase in the dust fraction, primarily

composed of illites with some kaolinite. This suggests the presence of sparse shrub vegetation and low precipitation. Limited calciferous pore water flow results in solution and precipitation occurring in the same location. DepoType 3 deposits are brown clayey sediments with elevated levels of iron, quartz, and kaolinite.

Cabrera et al. (2006) and Vega (2010) identified six distinct sectors in El Jable through grain size analysis (Fig. 68). Sectors 1 and 4 exhibit polymodal distributions, suggesting diverse sediment sources—Sector 1 is characterized by bioclast predominance, while Sector 4 is enriched with pyroclasts. Sectors 2 and 3 display more uniform distributions, with Sector 2 comprising fine sand and Sector 3 featuring mainly medium sand. Sectors 5 and 6, situated along the coast, present contrasting sedimentary compositions—Sector 5, influenced by Famara Beach, showcases finer sands, while Sector 6 reflects aeolian dominance. Analysis of carbonate content reveals spatial gradients, with the northern half exhibiting higher concentrations (90% to 40%) compared to the more variable southern half (averaging 30-40%). Coastal areas, with up to 50% carbonate concentrations, likely receive external sediment inputs. Marine biogenic sediments are the main source of carbonate content, primarily transported by prevailing NNE trade winds through aeolian activity. Famara Beach serves as a key entry point for marine inputs into Sector 2, with slight decreases in carbonate

Figure 68. Grain size sectorisation of El Jable by Vega (2010).

content observed inland due to terrestrial contributions from volcanic erosion. Sector 1, lacking marine inputs, exhibits distinct sediment characteristics from Sector 2. Sector 3 displays aeolian deposits with better sorting than Sector 1, while Sector 4's wide range of grain sizes reflects influences from agricultural activities and volcanic processes. Sector 6 exhibits increased carbonate content from southern marine deposits. Variations in grain size parameters between Sectors 5 and 6 are attributed to wave and wind sorting processes.
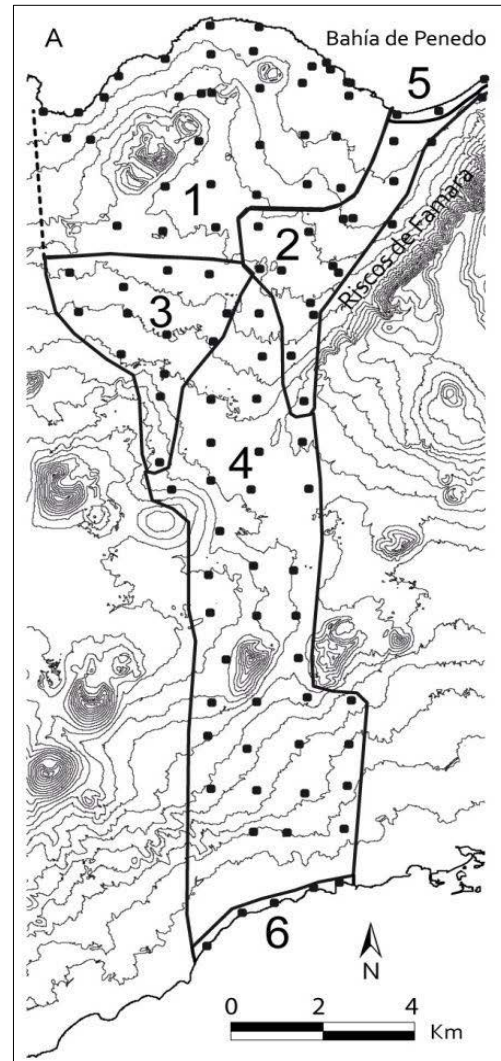
In Lanzarote, as well as in El Jable, insect trace fossils found within aeolian deposits, palaeosols and calcrete are quite common (Fig. 69 and 70). These traces hold significant importance due to their implications for understanding past climates. Trace fossils are attributed to bees, particularly anthophorids, (Edwards and Meco; 2000; Alonso-Zarza and Silva, 2002; von Suchodoletz et al., 2009), coleopterans or lepidopterans (Genise and Edwards, 2003), locusts (Meco et al., 2010; 2011), coleopteran, Curculionidae or Scarabaeidae (Genise et al., 2013) and gastropods, including *Theba geminata* (Mousson), *Hemycicla sarcostoma* (Webb & Berthelot), and *Rumina decollata* (Linné). Additionally, controversial findings include
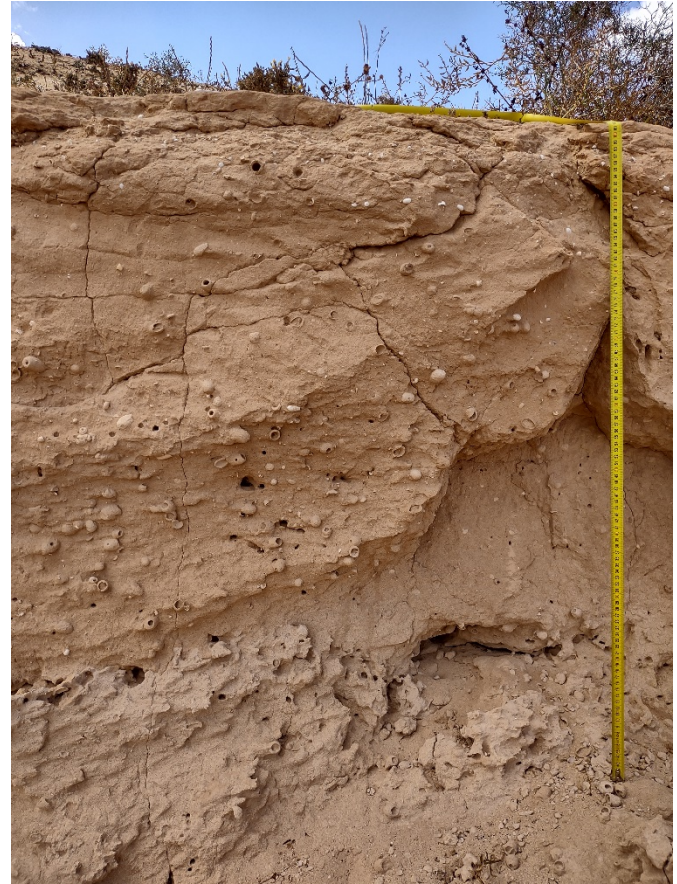

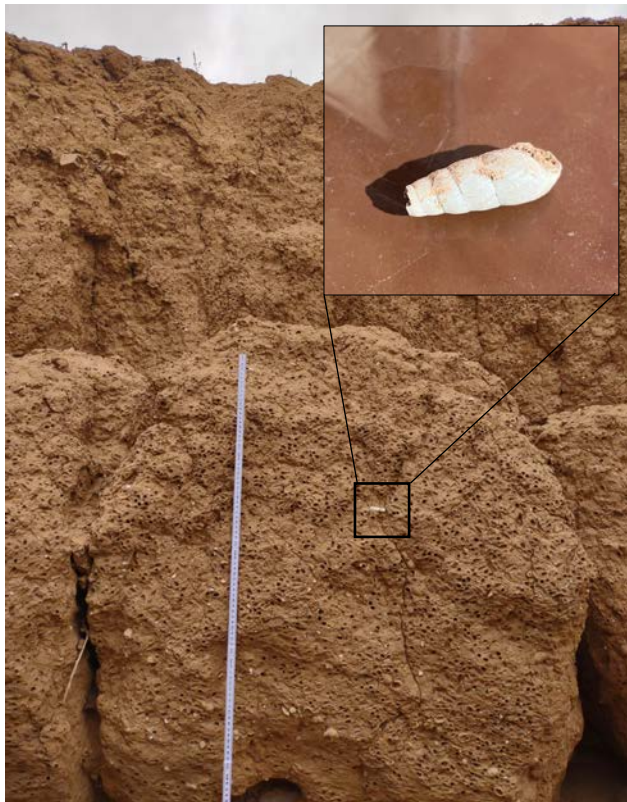Figure 69. Ootheca within aeolian deposits in El Jable.

fossil root casts (rhizoliths) and single brood cells with ovoid to subcylindrical shapes related (ootheca). The widespread occurrence of calcretes, aeolian deposits, and trace fossils across the easternmost and older Canary Islands is not merely coincidental but reflects both the geological evolution of the islands and the prevailing climatic conditions. These formations serve as valuable indicators of past environmental conditions, suggesting relatively wetter periods within the otherwise arid to semiarid climate of the region (Meco, 2008).

Between the Pliocene and Pleistocene periods, the Famara and Ajaches massifs started to be

Figure 70. Land snail shells, including *Rumina decollata*.

eroded, leading to the formation of gravity-slope and alluvial fan deposits. Erosion processes have persisted to the present day, resulting in the development of an alluvial fan system. In Famara, these systems are notably characterized by the presence of at least three distinct generations of alluvial fans developed in the southern-western sector in telescopic-like features, later eroded by the modern barrancos (gullies).

Subsequent volcanic emissions, occurring synchronously with the aeolization process, covered and fossilized some of the deposits, resulting in repeated successions of lavas, pyroclasts, and aeolian sands.

The volcanic alignment of Sóo comprises basaltic lava flows, strombolian cones, and hydro-magmatic structures. Oriented SW-NE, it consists of six main structures: Montaña Mosta, Pico Colorado, Caldera Trasera (Fig. 71 and 72), Montaña Cavera, and two hydro-magmatic features at the NE end. Montaña Mosta, located at the SW end. Pico Colorado, centrally positioned, exhibits a pseudo-circular crater and is composed of lapilli, scoria, and bombs. Montaña Juan del Hierro is irregularly shaped with an elongated base towards the NW, showcasing an elliptical crater to the NW. Montaña Chica presents an irregular sub-rounded shape with a well-preserved elliptical crater. Montaña Cavera, at the NE end, transitions from hydro-magmatic to strombolian phases, with a pseudo-circular shape and a circular crater. The lava flows display advanced coastal morphologies, primarily composed of grey aphanitic basalts with small olivine phenocrysts.

Figure 71. Map of the events from the Middle- Upper Pleistocene-Holocene in El Jable area.

Figure 72. View of Pico Colorado and Caldera Trasera from Famara cliff.

4.2.1.4 Upper Pleistocene- Holocene- Historical Period

The "jandiense" marine deposits, as designated by Meco et al. (1991), are prominently observed in Caleta de Famara, where they have been dated to approximately 129±5,1 ka using the Th/U method, (Zazo et al., 1997). Detailed sedimentological and fossiliferous characteristics of these deposits are documented in sections Famara and Los Ajaches.

The third generation of alluvial fan started to develop during the Holocene. Some of these deposits are interbedded with wind-blown sand layers deposits formed in El Jable plain. The sedimentological characteristics of the alluvial deposits are described in the Holocene section of Los Ajaches.

The marine deposits of the late Holocene referred to as "Erbanense" as identified by Meco et al. (1986), are located in La Caleta de Famara, Caleta del Caballo, and Playa Mejías (Fig. 71). These deposits, filling small basins, consist of sandstones and conglomerates of basaltic pebbles, with a thickness of less than one meter. Fauna assemblages is well descripted in the Famara and Los Ajaches section.

During the 18th century, the historical eruptions of Timanfaya produced basaltic lava flows and scattered pyroclasts that covered extensive areas of the Tinajo and Yaiza regions. The lava flows from Montaña de las Nueces are characterized as low-viscosity "pahoehoe" type, featuring corded and tubular volcanic structures. These flows extended over long distances, branching into two main arms—one heading north towards Caleta de Famara and the other initially southeast before turning south towards the coast near Salinas de Punta Chica in Arrecife (Fig. 73).

Figure 73. Historical pahoehoe lava flow overlaying sands of El Jable. In the back: Alluvial fan of Famara.

Loose sand accumulations are found along the coastal area from Caleta de Caballo to Caleta de Famara, in the northern zone of the Jable, and are characterized by small dunes of the nabkha type. These sediments consist mainly of fine sands of biogenic origin, derived from the erosion of the marine terrace of Caleta de Famara, and from cemented aeolian sands along the slopes of the Famara Massif, which are rich in calcium carbonate. Nabkha dunes form due to the presence of shrubs in the area and are of small dimensions, generally ranging from 1 to 3 meters in length and less than a meter in height (Vega, 2010) (Fig. 74).

These dunes are light in colour and sometimes are interspersed with colluvial or alluvial deposits. Soils have calcareous crusts and are rich in terrestrial gastropod shells and ootheca exposed by the erosive action of the wind. Along this dune field, it is common to find basaltic and pyroclastic lithic fragments, derived from the erosion of Miocene basaltic flows to the northeast and volcanoes of the Soo alignment to the northwest. According to Vega (2010) along the plain, close to El Risco de Famara it was possible to find Barchan dune, ranging in size from 5 to 10 meters, which moved towards the southern area of El Jable thanks to the trade winds, at a rate of approximately 20/23 meters per year and with an average speed of 20 km/h.

Figure 74. Active nabkha dunes in the back of Famara beach.

4.3 Methodologies

For both the areas analysed during the first and second phase of the experiment, a multidisciplinary approach was utilized, incorporating sedimentology, stratigraphy, luminescence dating, and radiocarbon dating.

4.3.1 Sedimentology and stratigraphy

Field observations were carried out to conduct sedimentological and stratigraphical analyses on the exposed formations. The sedimentary succession was characterized based on various facies, considering sedimentary parameters such as lithology, grain size, and sedimentary structures. Facies were classified into four categories according to their grain size and characteristics: conglomeratic, sandy, fine-grained, and calcrete. A more detailed analysis identified 16 distinct facies, differentiated by their texture, matrix composition, clast sorting, contact types, bedding structures, and sedimentary features (refer to Table 6). Facies associations were established by grouping the main identified facies for each area. Multiple logs were measured in all areas and subsequently correlated, considering the presence of unconformities to define unconformity-bounded units. The interpretation of facies followed the methodology outlined by Blair (1999a, 1999b), and Miall (2006), tailored for alluvial fan deposits and fluvial systems. This approach aimed to understand depositional processes in both high-energy debris flows and more stable environments characterized by fluvial and aeolian deposits. Furthermore, facies correlation was executed to comprehend the stratigraphy, identify depositional units, and subsequently construct stratigraphic sections.

4.3.2 Luminescence samples characteristics, collection and preparation

Regarding the first phase a total of four samples were collected: two from a colluvial fan in north-eastern Famara flank (FAM1 and FAM2), one from an alluvial deposit near Orzola town (ORZ), and one from the braided deposits of the Higueral Valley (HIG) (Fig. 75).

- FAM1 (Lat 29° 8'1.74"N, Lon 13°31'52.64" W) is well-cemented light-yellow sand taken within a colluvial fan located at the base of the western side of the cliff of Famara, 5 m asl

(Fig. 75 A). At the top of the sampled sand are angular pebbles, cobbles, and boulder, result of the erosion of the basaltic products of the Famara volcanic massif. The sample was chosen as an analogue of Martian gully deposits.

- FAM2 (Lat 29° 8'11.28"N, Long 13°31'34.91" W) is characterized by dark coarse-very coarse sand, with angular pebbles and cobbles, which are the result of the alteration of the basaltic lava flow, AA lava, and pyroclasts forming Famara massif (Fig. 75 B). Clastic sediments are very poorly sorted. The sampling area is located on a colluvial fan, 150 m asl.

- ORZ (Lat 29°13'13.51"N, Long 13°27'34.38" W) was taken within an alluvial fan characterized by angular pebbles made of pyroclasts and basaltic lava with a medium-coarse sandy matrix (Fig. 75 C). Debris flows were the main depositional features both channelled and not. Sheet floods consisting of low cemented sand with basalt pebbles occur secondarily. As FAM1, the sample was chosen as a Martian analogue of a gully apron.

- HIG (Lat 28°54'0.58"N Long 13°44'38.83" W) was collected within Valley de Higueral characterized by braided rivers alimented by lateral detrital colluvium. The sample was collected within a debris flow deposit (Fig. 75 D). The debris flow is characterized by inverse grading and is topped by plane-laminated gravelly sand. Boulders (60 cm) and cobbles (15 cm) of basaltic and calcium carbonate origin are present at the base.
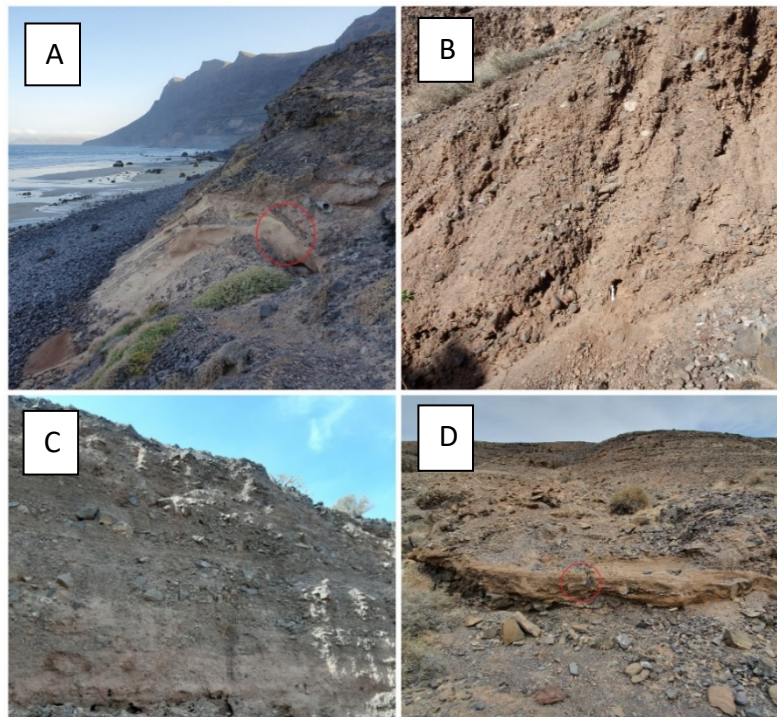

Figure 75. Samples collected for the first stage. A: FAM1 from a colluvial fan in Famara; B: FAM2, from a barranco within Famara colluvial fan; C: ORZ collected from alluvial fan of Famara; D: HIG sampled from valley de Higueral in Los Ajaches massif.

For the second part of the experiment, a total of 13 samples were collected from barranco Las Piletas, representing layers of diverse origins (Tab. 2, Fig. 76)

Table 2. Barranco Las Piletas. The 13 samples collected, for the second phase of the project, in the alluvial fan forming at the base of the Famara cliff.

Sample	Description	Image
PIL1	Loose sediment of pink massive fine sandstone	
PIL2	Block of sandstone of basaltic-pyroclastic granules, with lamination	
PIL3	Loose sand of grey dune, showing planar and trough cross-lamination structure	

PIL5	Loose sand of reddish-massive sandstone, highly bioturbated by insect brood cells and Gastropods	
PIL6-2	Block of cemented reddish-massive sandstone, slightly bioturbated	
PIL7	Loose sediment of grey dune, no evident structure	
PIL8	Block of well cemented dune, yellowish in colour, no evident structures, grains of basalt and pyroclasts	

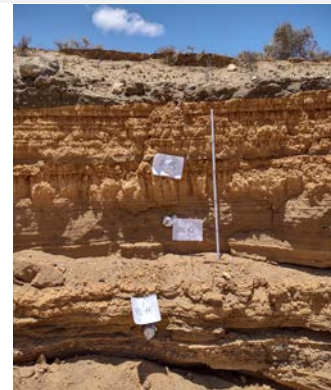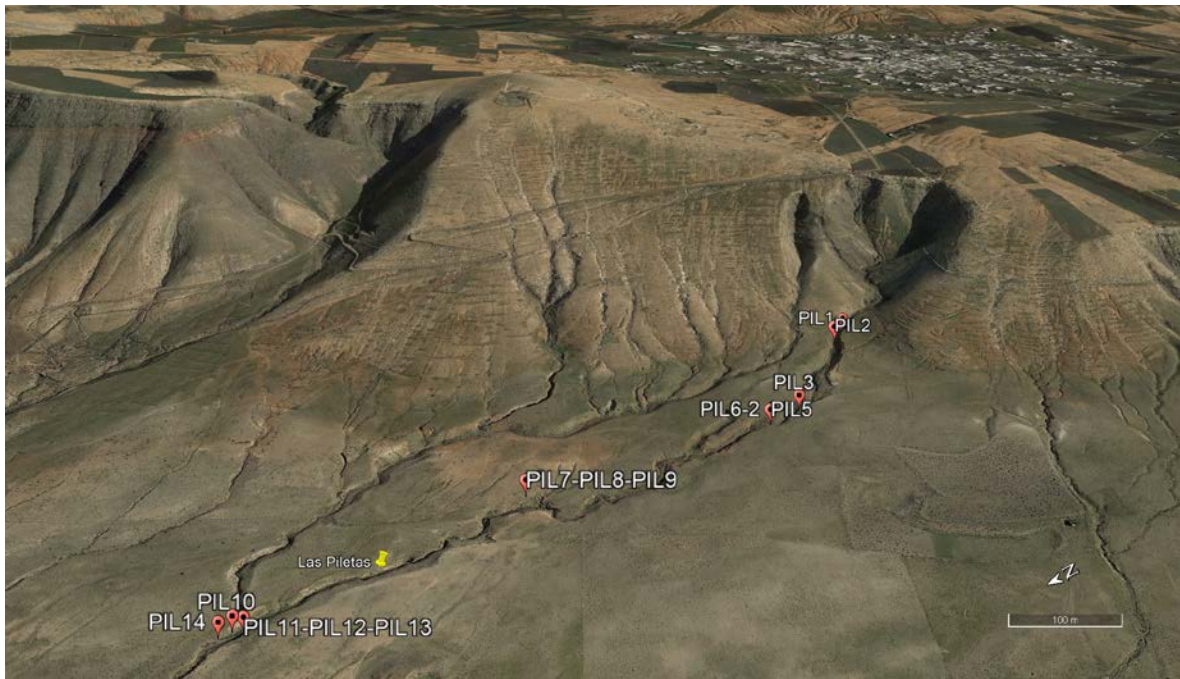|		
PIL9	Block of well cemented dune, dark grey in colour, no evident structures	
PIL10	Loose sand of grey dune, no visible structures	
PIL11 *PIL12* *PIL13*	Loose grey sand, laminated, some granules and pebbles are present (alternated with layers of clay)	
PIL14	Loose dark grey sand, pebbles are present, ripples are evident	

Figure 76. Barranco Las Piletas featuring the 13 samples collected for the second phase of the project.

In order to avoid sunlight, samples for luminescence were collected at night-time with the assistance of a red-light torch or during day-time by covering the sample with a plastic-black bag immediately after extraction. Loose sediments were extracted with a PVC tube (30 cm in length and 4 cm in diameter) inserted into the layer using a hammer (Fig. 77). To shield the sample from sunlight, in addition to cover the area with a plastic-black bag, a piece of tinfoil was placed inside the PVC tube, both on the outer and inner parts. The tube was then wrapped in another plastic black bag, sealed with American tape, and labelled. In cases where the sample was cemented, a block measuring 50x50x50 cm was extracted with the help of a hammer, enveloped in a plastic-black bag, sealed with American tape, and labelled.

All samples underwent processing under subdued red light at the Luminescence Dating Laboratory of the Department of Architecture, Design, and Planning, University of Sassari (Italy). Each sample was divided into three sub-samples: the outer portions were removed for dose rate (D_R) and water content calculations, while the core part, characterized by unbleached material, was retained for equivalent dose (D_e) calculations.

Figure 77. Collecting loose sediment for IRSL dating using a PVC tube during both day and night.

4.3.3 Equivalent dose (D_e) measurement

In luminescence dating, there is no universal best approach, and the workflow varies based on the selected variables. The principal considerations involve the choice of mineral, grain size, equivalent dose (D_e), and dose rate (D_R) measurement methods. K-feldspar has been selected as the mineral of interest due to the focus on dating basalt-derived deposits on Mars, where quartz is not produced by basaltic lava, and k-feldspar is more prevalent on the Martian surface. The very-fine silt grain size (4 -11 μm) was chosen for its applicability and efficiency, as it does not require acid hydrofluoric etching. Moreover, working on the polymineral fine grain fraction avoids additional chemical treatments required for separating quartz and k-feldspar. The selected product underwent routine laboratory protocols, including Hydrochloric acid (HCl) etch to remove calcium carbonate, Hydrogen peroxide (H_2O_2) treatment to eliminate organic matter, Sodium oxalate ($Na_2C_2O_4$) to disaggregate particles, and finally, the separation of 4-11 μm grains using Stokes' law settling (Aitken, 1985; Mauz et al., 2002).

In the case of Mars, this last treatment will be not done because of the non-presence of organic matter on the planet.

Polymineral fine-grain were mounted on stainless steel discs in the form of aliquots of ~2 mm in diameter (Duller, 2008). Measurements were made using automated Risø TL/OSL readers (DA- 20 and DA-15; Bøtter-Jensen et al., 2010) with calibrated 90Sr/90Y beta sources (~0.15 Gy/s and ~0.08 Gy/s). A Photomultiplier (PMT) was employed to detect K-feldspar luminescence signals. Infrared (IR) LEDs were used for stimulation of K-feldspar grains and the luminescence signal was detected in the blue-violet region through a Schott BG39/Corning 7– 59 filter combination (350–415 nm). K-feldspar D_e were measured with the Single Aliquot Regenerative (SAR) protocol for its efficiency despite being time-consuming with multiple aliquots (Murray and Wintle, 2003. To overcome the problem of fading in feldspar dating, a preliminary low-temperature IRSL step is employed to deplete luminescence traps susceptible to fading. This is followed by one or more IRSL steps at elevated temperatures, allowing the measurement of luminescence from more stable traps. This measurement procedure termed **post-Infrared Infrared stimulation protocol (post-IR-IRS, pIRIR)** dating, has been chosen for this study (Thomsen et al., 2008; Buylaert et al., 2009, 2011; Zhang and Li, 2020).

A Pre-heath plateau test with temperatures ranging between 140 °C and 280 °C was performed on one sample to choose a good temperature for the protocol (Buylaert et al.; 2012). As shown by Fig. 78, no change in Equivalent Dose up to 220 °C was detected, allocated in a plateau. As temperature increases to 240 °C, D_e also does. As a result, we have selected to work on $pIRIR_{200}$.
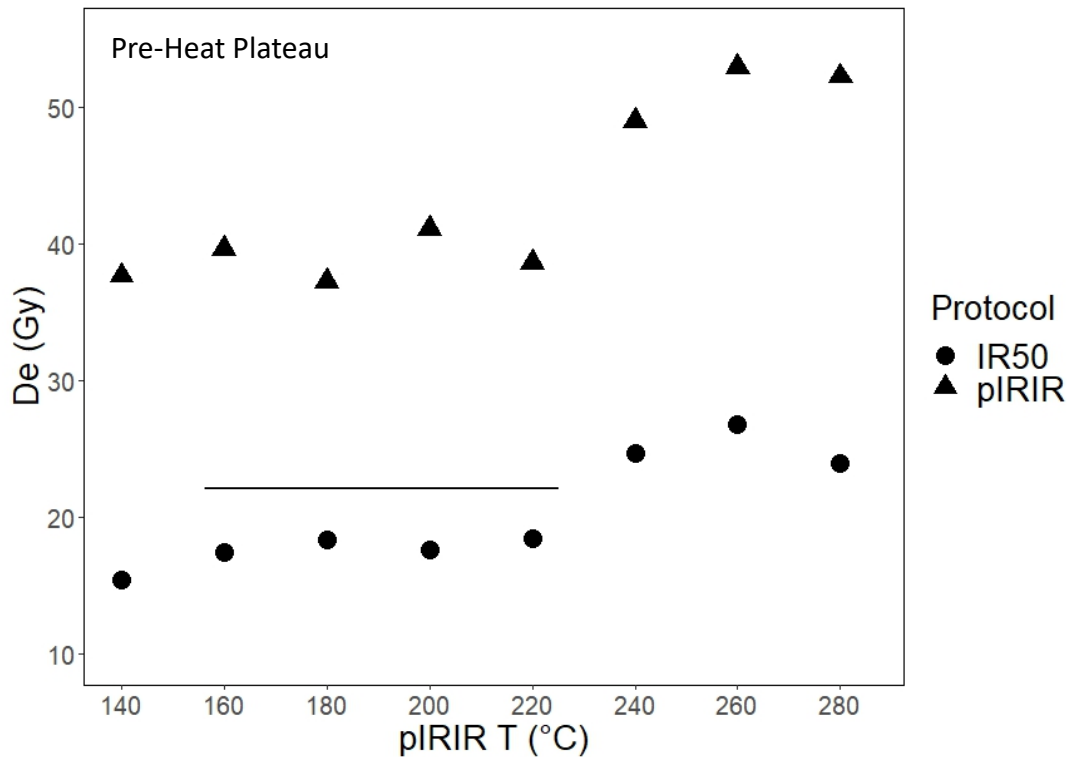
Figure 78. Pre-heat plateau test displaying De estimates in relation to pIRIR temperature.

The Equivalent dose was measured from 20 aliquots per sample. Standard luminescence tests were undertaken on all the samples: Dose recovery test, Residual dose, Thermal transfer, and Fading. Furthermore, the recycling (repetition of a SAR cycle) and recuperation (zero given dose SAR cycle) tests were monitored in each aliquot for all samples (Aitken, 1985; Mauz et al., 2002).

4.3.4 Dose Rate Determination

The total dose rate was determined with a beta multi-counter GM-25-5 employed to detect the beta count rate, associated with the analysis of concentrations of K, U, and Th via ICP-MS. The Risø low-level gas flow beta multi-counter GM-25-5 (BC; Bøtter-Jensen and Mejdahln, 1988), followed the procedure proposed by Cunningham et al. (2018) and was utilized at the laboratory in Sassari. A preliminary process involved sample counting, instrument sensitivity assessment, background determination (using pure wax), and the derivation of a count-rate conversion factor for each isotope at the specific activity (count/Bqkg-1) through calibration standards. Approximately 50 g of samples were ground, mixed with wax (to retain 222Rn), placed in small plastic containers, and stored for 21 days to reach Radon equilibrium (Ankjærgaard and Murray, 2007). Beta count rates

were measured over multiple cycles, corrected for background, sensitivity, and sample self-attenuation (stopping power). Radionuclide concentrations (U, Th, and K) were measured at Activation Laboratories Ltd. (Actlabs) in Canada via sodium peroxide fusion (ICP-MS). These concentrations, along with net corrected beta counts, were used to estimate the proportional dry gamma plus beta dose rate in samples from each source of dose rate. The approach has the advantage of providing precise beta count rates for sediment, enabling the estimation of the dry total dose rate in natural sediment even with imprecise prior information on the relative strength of radionuclide sources (Cunningham et al., 2018). Conversion factors and β-grain size attenuation were applied to calculate the dry β- and γ-dose rates (Guérin et al., 2012). The dry dose rate was corrected to an effective dose rate considering moisture, grain size attenuation, and cosmic contribution. Water content was measured as described in Casini et al. (2020) and Sechi et al. (2020). The cosmic contribution was based on geographical position and the reconstructed burial depth of deposits, following Prescott and Hutton (1994). Given the variability of K-content, the final K-feldspar dose rate incorporates the contribution of internal ^{40}K, assuming a sample grain-size of 12.5 ± 0.5% of K and Rb concentration of 400 ± 100 ppm (Huntley and Baril, 1997).

4.3.5 Radiocarbon dating ^{14}C

To cross-verify luminescence-based age estimates, gastropod shells of the genera *Hemicycla* and *Rumina*, were collected for radiocarbon dating (^{14}C) from two barrancos (Las Piletas, Falls), and the sand pit of EL Jable (Fig. 79).

Accelerator Mass Spectrometry (AMS) was utilized for the ^{14}C dating of a total of 31 samples, collected from two barrancos in the Famara alluvial fan and a quarry in the El Jable plain.

The analyses were conducted by BETA (Beta Analytic Radiocarbon Dating Laboratory, Florida). The "Conventional Radiocarbon Age" was calculated using the Libby half-life (5568 years), corrected for total isotopic fraction, and used for calendar calibration. The Age is rounded to the nearest 10 years and is reported as radiocarbon years before present (BP), "present" = AD 1950. The modern reference standard was 95% of the ^{14}C signature of NIST SRM-4990C (oxalic acid). Quoted errors are

1-sigma counting statistics. Calculated sigma less than 30 BP on the Conventional Radiocarbon Age are conservatively rounded up to 30.
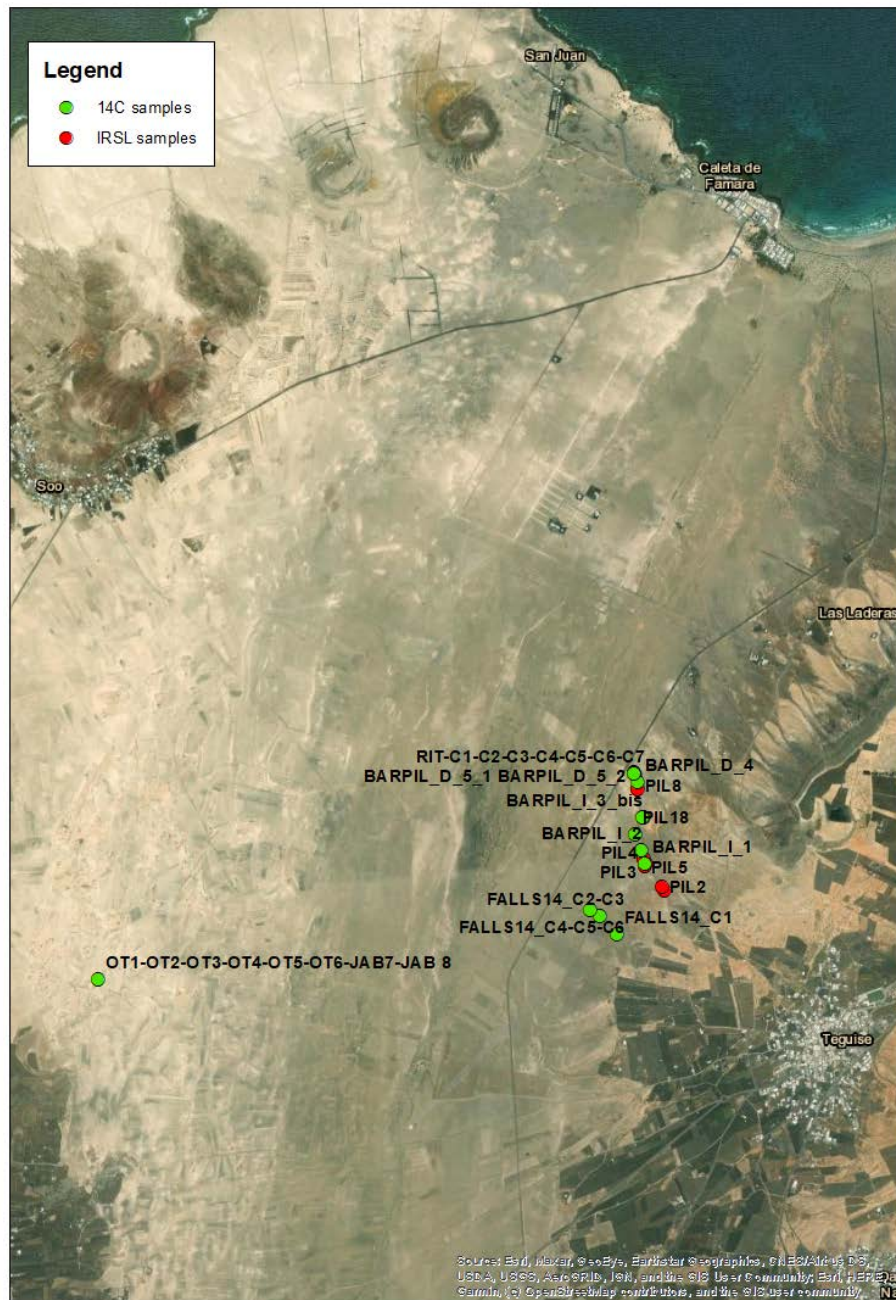

Figure 79. Satellite image of luminescence-dated samples (red dots) and radiocarbon-dated samples (green dots).

5.1 Introduction

The outcomes of this study will be structured according to the accomplished objectives. Firstly, the results related to the first phase of the experiment which investigates the luminescent characteristics of samples collected from the initial four areas (FAM1, FAM2, ORZ, HIG), will be presented.

The following section will deal with the sedimentological aspects of the examined El Jable plain.

Furthermore, the luminescent results obtained from the samples collected in *Las Piletas* will be integrated with the sedimentological analysis and compared with ^{14}C derived ages.

Finally, all the obtained results will be utilized to define the chrono-stratigraphic evolution of El Jable plain.

5.2 Luminescence results: phase one

The post-infrared infrared (pIRIR) protocol was applied to samples FAM1, FAM2, ORZ, and HIG, utilizing different temperatures (200°C and 225°C) (Tab. 3). Analysis of the data presented in the previous Chapter (Fig. 78) revealed that the pIRIR temperature had no discernible impact on the equivalent dose (D_e). Therefore, the choice between 200°C and 225°C did not yield any significant difference. To ensure signal stability, a preheat procedure was implemented to secure the natural signal stability before measurements (steps 2 and 6, Tab. 3). Heating the sample to a specific temperature will release any unstable charge. To minimize anomalous fading, an initial low-temperature stimulation at 50°C preceded the IRSL signal at 200°C or 225°C (steps 3 and 7, Tab. 3). The IR 50°C stimulation is designed to eliminate close trap-hole pairs, while higher temperatures stimulate the deepest, distant trap-holes, resulting in a signal with reduced fading. The test dose monitors the sensitivity of the sample and varies on the base of the signals of the samples (step 5, Tab. 3). The last step of the protocol includes bleaching the sample at high temperatures to remove all residual signals (step 9, Tab. 3).

Table 3. Post-IR IRSL protocol employed. "Lx" represents the Luminescence signal, "Tx" corresponds to the test dose signal.

STEP	MEASUREMENT	REMARK
1	Given dose	
2	Preheat for 60 s at 250°C or 220°C	Heating rate 5 (°C/s)
3	IR stimulation, 200 s at 50 °C	IR_{50}
4	IR stimulation for 200s at 200 °C or 225 °C → Lx	pIRIR
5	Test dose	
6	Preheat for 60 s at 250°C or 220°C	Heating rate 5 (°C/s)
7	IR stimulation, 200 s at 50 °C	IR_{50}
8	IR stimulation for 200s at 200 °C or 225 °C → Tx	pIRIR
9	IR stimulation at 240 °C or 290 °C	Remove all residual signals
10	Return to step 1	

In the examination of **luminescence signals** from the samples, critical parameters such as luminescence intensity and signal decay characteristics were thoroughly investigated. Luminescence intensity was assessed to comprehend emission levels under diverse conditions, while signal decay characteristics, including the rate of decay, offered insights into the temporal behaviour of the luminescent response. The luminescence intensity for all four samples is robust. The $pIRIR_{200/225}$ signal, characterized by a lack of rapid decay, suggests that it is not dominated by a fast component. In contrast, the IR_{50} signal, appears consistently brighter than the pIRIR signal (Fig. 79). Such variations in signal intensities may be attributed to differences in the sensitivity of mineral grains to the distinct stimulation methods.
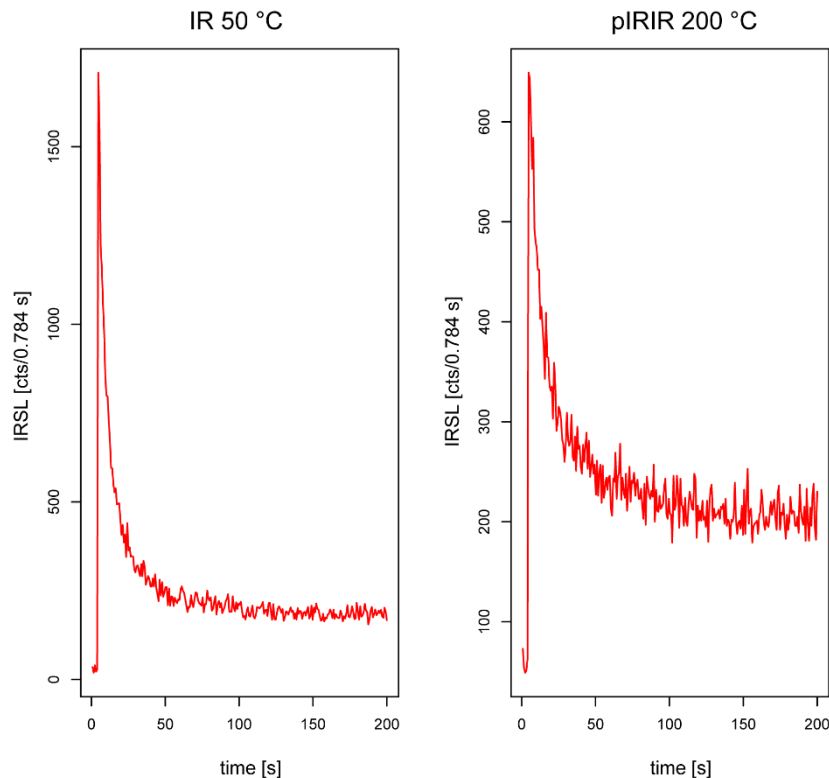
Figure 80. Natural decay curves of IR_{50} and $pIRIR_{200}$ signals from FAM1 aliquot.

Regenerative dose measurements were employed to validate the reliability of the luminescent signals, aiding in understanding the signal resetting. The samples underwent a reset through heating and then received various laboratory radiation doses, illustrating the growth of the luminescence signal with dose. Equivalent doses (De) were determined by identifying the laboratory radiation

doses that reproduced the luminescence signal observed in the sample during recovery. The **dose-response curve** for all samples consistently exhibited an increase in luminescence intensity with dose, a typical and expected behaviour in well-behaved luminescence systems, with no saturated signals detected (Fig. 81 and 82).
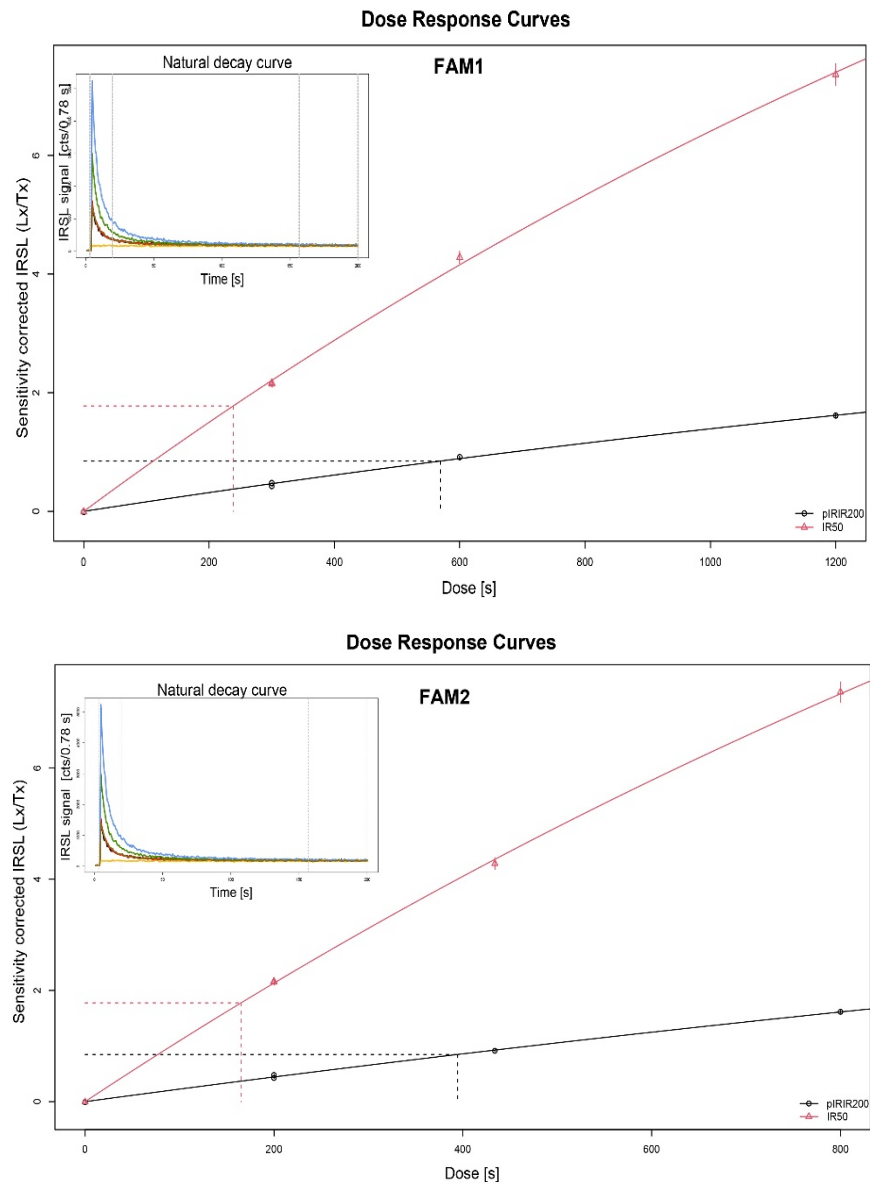

Figure 81. Dose-response curves for Infrared Stimulated Luminescence (IRSL) and complementary natural decay curves (insets) for samples FAM1 (above) and FAM2 (below). Two De values were obtained by fitting a single saturation exponential function to the regeneration dose points.
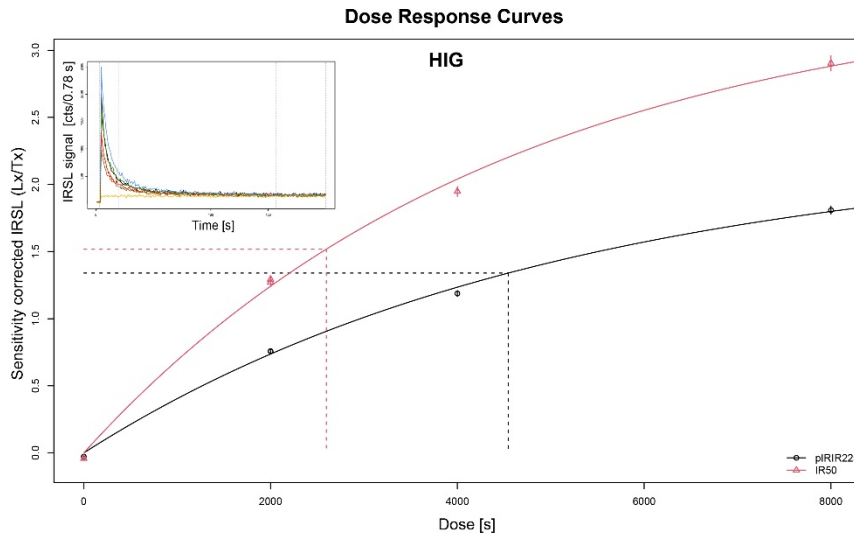
Figure 82. Dose-response curves for Infrared Stimulated Luminescence (IRSL) and complementary natural decay curves (insets) for sample HIG. Two De values were obtained by fitting a single saturation exponential function to the regeneration dose points.

Quality control measures were rigorously implemented during the luminescence analyses, focusing on factors such as signal stability, reproducibility, and reliability. **Dose Recovery Tests** were conducted to validate dose estimation accuracy (Fig. 83). This involved the bleaching of 5 aliquots of each sample for 10 days under sunlight, irradiating the sample, and comparing the measured luminescence signal with the expected value. The optimal value is around 1, and aliquots with values below 0.9 or above 1.1 were excluded. In the case of FAM1, only one out of the five aliquots deviated
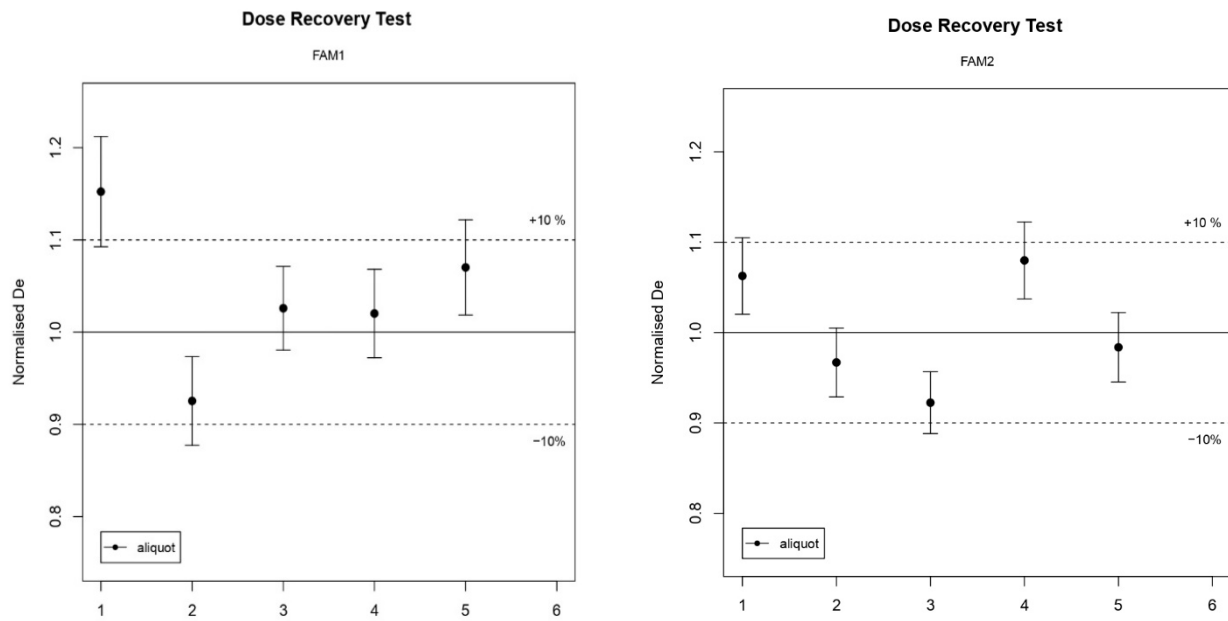

Figure 83. Results from dose recovery tests performed on FAM1 (left) and FAM2 (right). The laboratory dose given to each sample was close to its natural dose.

137

from the acceptable range, indicating a slight discrepancy. FAM2 exhibited excellent performance, with none of its aliquots exceeding the acceptable range. However, ORZ presented a challenge, as only one out of the five aliquots fell within the acceptable range, indicating potential issues with dose recovery (Fig. 84). In contrast, HIG showed consistent and reliable dose estimates, as all five aliquots remained within the acceptable range. These results confirm the robustness of the dose estimation process, providing confidence in the accuracy of the luminescence dating outcomes.
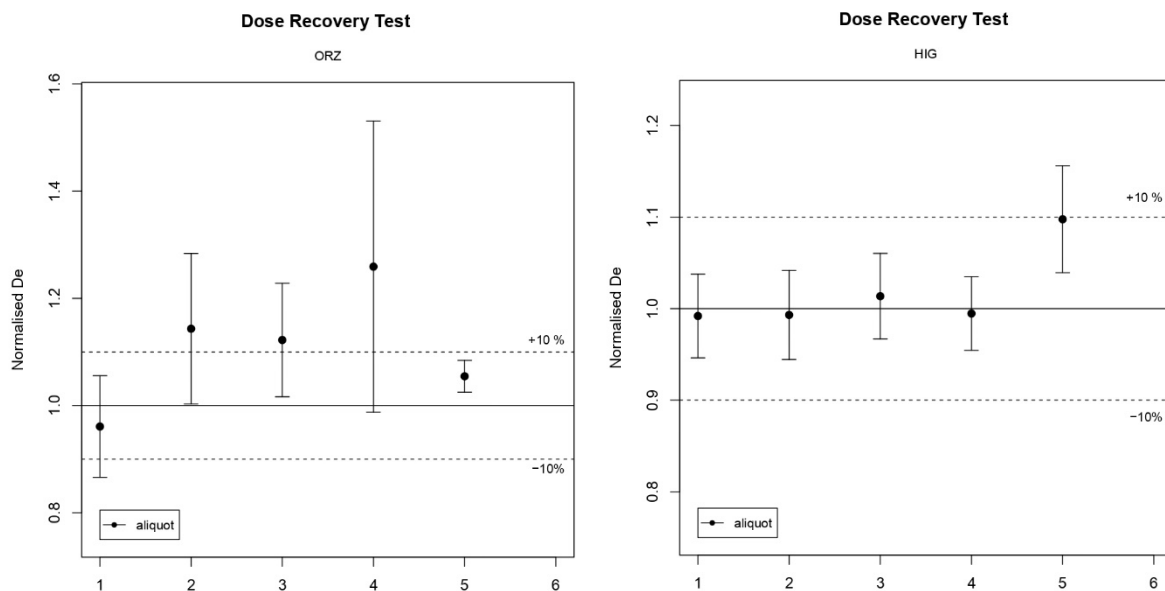

Figure 84. Results from dose recovery tests performed on ORZ (left) and HIG (right). The laboratory dose given to each sample was close to its natural dose.

In addition, the **recycling ratio**, a crucial metric for evaluating the consistency of luminescence signals, was calculated by applying the same regeneration dose in two different measurement cycles. The resulting sensitivity-corrected luminescence signals were compared to assess reproducibility and reliability. In an ideal scenario, a well-functioning SAR protocol should yield a recycling ratio of 1, with acceptable values falling between 0.9 and 1.1. Any aliquots outside this range were systematically rejected (refer to Table 4 for details).

As part of the SAR protocol, **recuperation** is a critical step to assess the deviation from the expected signal. The negative recuperation values observed for all samples consistently indicate an underestimation in dose calculation. FAM1 shows a minor underestimation of -0.96%, while FAM2, ORZ, and HIG exhibit more substantial underestimations of -9.08%, -14.09%, and -17.36%, respectively (Tab. 4). These consistent negative recuperation values raise concerns about potential inaccuracies in dose estimation, emphasizing the need for careful consideration and potential

corrections in age calculations. Possible factors contributing to these underestimations include incomplete bleaching, signal instabilities (such as fading or anomalous fading), and sensitivity changes in the luminescence signal due to radiation exposure. Addressing these factors is crucial for ensuring the reliability of luminescence dating results.

K-feldspar, known for its challenge in achieving complete bleaching, deep traps, leading to residual doses typically falling within the range of 10 to 20 Gy. The difficulty in achieving full bleaching introduces a potential source of uncertainty in luminescence dating analyses, underscoring the necessity of addressing and minimizing residual doses during the measurement process. To assess the **residual natural signals**, a De was obtained using the following protocol: five aliquots per sample were bleached for 10 days under sunlight, followed by the application of five test doses (25s, 50s, 110s, 200s, 0s), and subsequent as for the Post-IR IRSL protocol (Tab. 4).

As the culmination of these analyses, the **abanico plot** emerges as a crucial visual tool, offering a radial representation of equivalent dose (De) values across a minimum of 20 aliquots for each sample. The variation in equivalent doses (De) observed across the samples could be attributed to several factors influencing the luminescence response. In the case of FAM1 and FAM2, the moderate variability might stem from a consistent depositional environment, possibly characterized by similar sedimentary processes. The asymmetry in their distributions, as indicated by skewness and kurtosis, could suggest specific post-depositional alterations affecting the luminescence signal. HIG's remarkably consistent luminescence response, with a tight distribution of equivalent doses, may imply a more stable geological setting or less post-depositional disturbance. The higher mean equivalent dose in ORZ, accompanied by a broader distribution, could point to variations in the sedimentary context, perhaps influenced by different depositional episodes, environmental conditions, or post-depositional processes affecting the luminescence signal. The data within 2σ offers insights into the typical range of variation for each sample, helping to discern populations of equivalent doses within a specified confidence interval. It is plausible that these variations reflect different sedimentary environments, burial histories, or post-depositional alterations that contribute to the diversity in luminescence responses observed in each sample (Fig. 85).
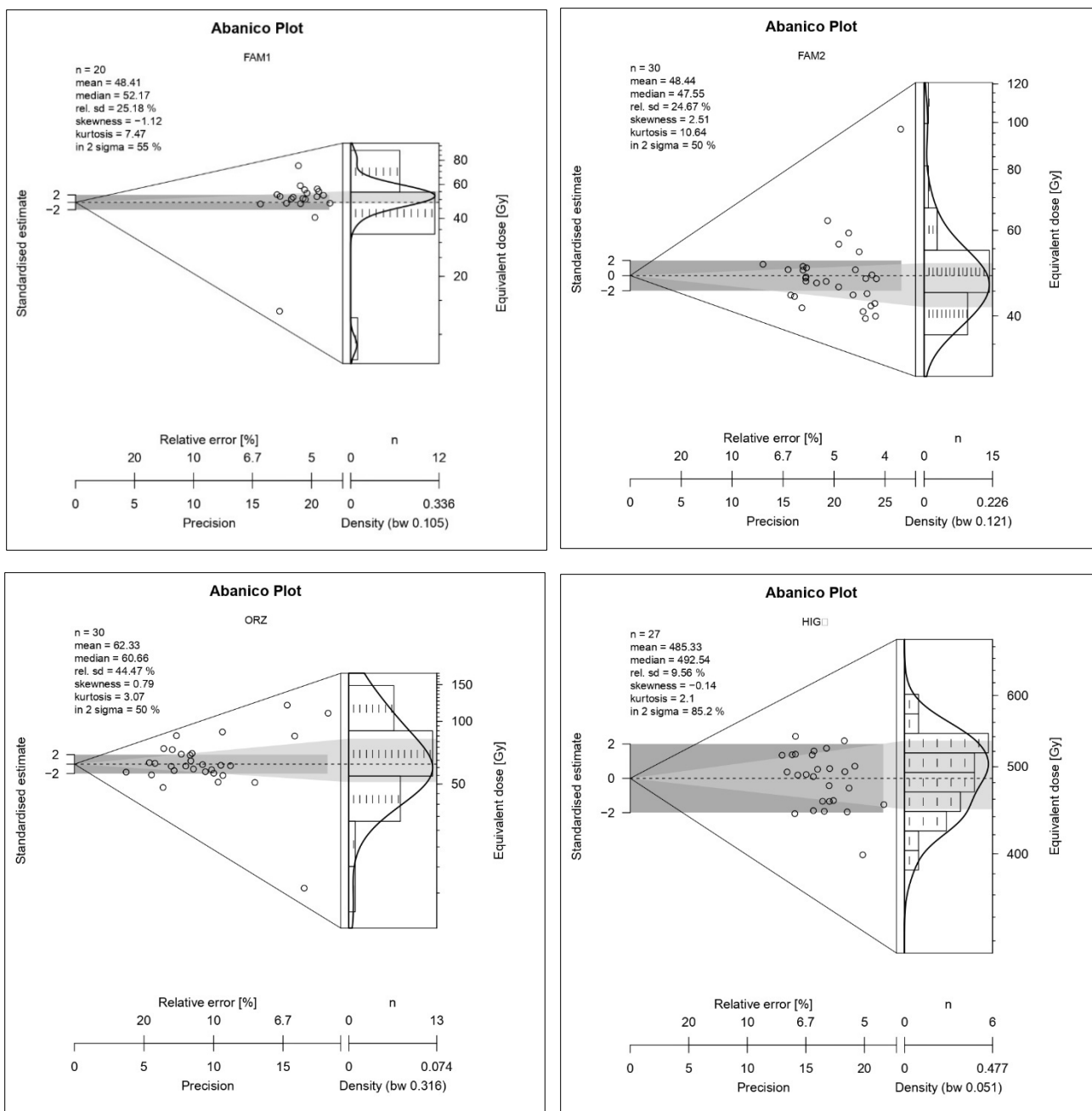
Figure 85. Variation in equivalent doses (De) among samples (FAM1, FAM2, HIG, ORZ) indicates distinct luminescence responses. FAM1 and FAM2 exhibit moderate variability (mean = 48, median = 52.17, relative standard deviation (rel.sd) = 25.18%), suggesting a consistent depositional environment with potential post-depositional alterations. HIG shows a remarkably stable luminescence response (mean = 485.33, median = 492.54, relative standard deviation (rel.sd) = 9.56%), while ORZ displays higher mean De (mean = 62.33, median = 60.66, relative standard deviation (rel.sd) = 44.47%), indicating diverse sedimentary conditions or post-depositional influences. Data within 2σ provides insights into population characteristics, reflecting variations in burial histories or environmental contexts.

The IR$_{50}$ and pIRIR$_{200/225}$ Lx/Tx values for equivalent doses were employed in age calculations, and a comprehensive summary of all analyses conducted on the samples, including dose rates, is presented in Table 4.

Table 4. A summary of analyses, including dose equivalent measurements and luminescence ages of the four samples: FAM2, ORZ, FAM1, and HIG. The columns represent various parameters used in the dating process, including Saturation (SAT), Recycling ratio (Rec), Recuperation (Rec), Residual dose (Gy), Dose recovery ratio (Gy), Equivalent dose (De in Gy), and Age (in ka).

Sample	SAT	Rec	Rec %	Residual dose (Gy)	Dose recovery ratio (Gy)	De (Gy)	Age (ka)
FAM2	0.05	1.04	-9.08	2.2 ± 0.3	0.98 ± 0.03	47.3 ± 2.2	**22.4 ± 1.7**
ORZ	0.18	1.11	-14.09	1.11 ± 0.08	1.11 ± 0.04	67.1 ± 5.6	**36.7 ± 10.7**
FAM1	0.14	1.02	-0.96	3.02 ± 1.5	0.98 ± 0.04	48.5 ± 3.2	**43.8 ± 4**
HIG	0.57	0.69	-17.36	20.2 ± 4	1.02 ± 0.02	464.1 9.0	**184.9 ± 10.7**

The table below presents concentrations of elements essential for dose-rate calculation, determined through inductively coupled plasma mass spectrometry (ICP-MS) and beta reader analyses.

Table 5. Summary of dosimetry data including concentrations of major radioactive elements.

Sample	Moisture Avg (%)	Depth (Cm)	Grainsize (μm)	^{238}U (Bg/Kg)	^{232}Th (Bg/Kg)	^{40}K (Bg/Kg)	Total Dr (Gy ka $^{-1}$)
FAM2	2.29	100	4-11	14.9 ± 1.2	20.6 ± 0.4	217.9 ± 2.6	**2.1 ± 0.02**
ORZ	2.45	500	4-11	16.1 ± 1.2	21.5 ± 0.4	200.5 ± 2.6	**1.8 ± 0.03**
FAM1	1.89	100	4-11	14.9 ± 1.2	3.2 ±0.4	58.8 ± 2.6	**1.1 ± 0.05**
HIG	2.80	100	4-11	14.9 ±1.2	16.6 ± 0.4	324.8 ± 2.6	**2.5 ± 0.02**

In conclusion, the luminescent signals from the samples have offered valuable insights, yet challenges, note the consistently negative recuperation values indicating underestimation in dose calculation. This underscores the complexity of dating with luminescence colluvial and alluvial basalt-derived deposits, where factors like incomplete bleaching and sensitivity changes can influence results.

5.3 Evolution of Alluvial Fan system and El Jable plain

In the second section of the Results Chapter, the sedimentological and stratigraphic analyses performed in four significant barrancos—LZ403, HORCA, LAS PILETAS, and FALLS—provided valuable insights into the spatial and temporal evolution of the Famara alluvial fan system together with El Jable plain.

An alluvial fan is a geological landform that develops at the base of a mountain or hill where a steep, confined valley abruptly opens onto a flat plain. It forms as a result of the rapid deposition of sediment carried by a river or stream emerging from a narrow canyon onto a broader, lower-lying surface (Blair, 1994). The fan-shaped deposit consists of coarser materials near the source and finer sediments farther away, creating a characteristic fan pattern (Fig. 86 and 87). Alluvial fans are dynamic features shaped by the interplay of sediment transport, water flow dynamics, and changes in topography, playing a crucial role in understanding landscape evolution and sedimentary processes, mostly connected to climate changes. The sediments deposited within alluvial fans act as archives, recording changes in precipitation, hydrological patterns, and sediment transport dynamics over time. Analysing the stratigraphy and composition of these sediments, it is possible to reconstruct climatic events, fluctuations, and trends. Alluvial fans, therefore, serve as valuable geological records that contribute to our understanding of Planet's climatic history, providing insights into the factors influencing environmental changes and their impacts on landscapes.

The classification of the sedimentary environments and facies of Famara alluvial system and El Jable plain refer to Blair (1994; 1999a; 1999b), Blair and McPherson (2009), and Miall (2006).

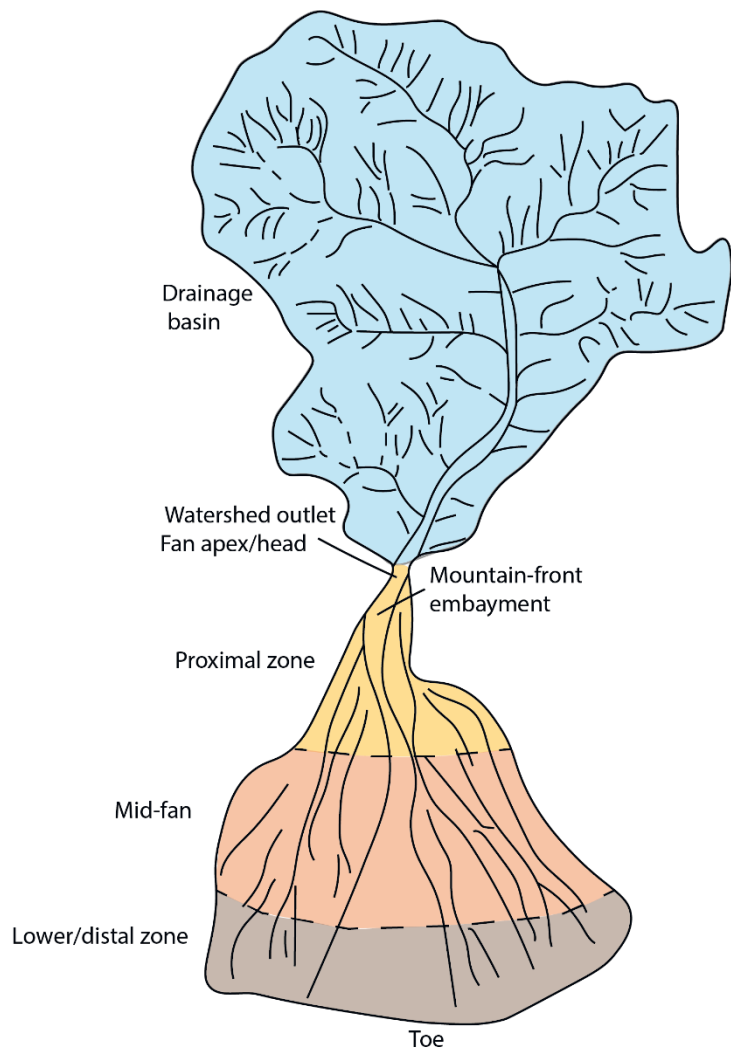Figure 86. A standard alluvial fan system comprises the fan itself, its associated zones, and the contributing catchment sourced from mountainous bedrock, incorporating various channel orders (adapted from Blair and McPherson, 1994).
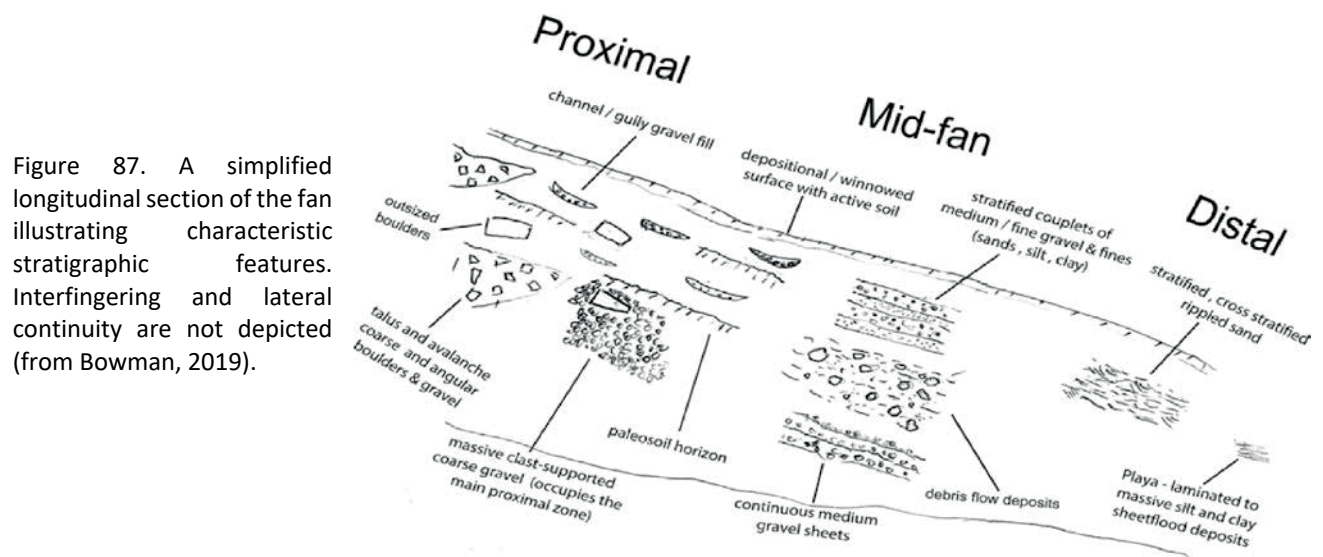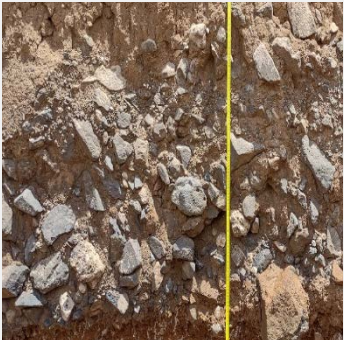

Figure 87. A simplified longitudinal section of the fan illustrating characteristic stratigraphic features. Interfingering and lateral continuity are not depicted (from Bowman, 2019).

5.3.1 Facies analyses

The comprehensive analysis of stratigraphy and sedimentological features in the four barrancos along with the aeolian deposit in the El Jable plain, has led to the identification and characterization of 16 distinct facies, as detailed in Table 6. This facies association enables the differentiation of five deposit types: **talus cone, alluvial fan-head (proximal), alluvial mid-fan, alluvial distal part, and aeolian system**. The observed evolution of deposits in the four barrancos demonstrated a trend from north to south. In the northern areas with steeper slopes, gravity flow deposits predominate, while moving southward, the dominance shifts to water-flow deposits, complemented by the presence of aeolian dunes. Next figures and logs provide a visual representation, with clear captions and legends aiding in the interpretation of the observed features.

Table 6. Simplified description of the observed sedimentary facies on the study areas.

Label	**Facies**	*Facies characteristics*	*Interpretation*	*Image*
Cl	Laminar calcrete	Indurated laminated sheets of calcrete crusts, typically undulose, coating basaltic gravels and/or penetrating basaltic host rock; minor sand to finer-grained matrix. Chaotic arrangement of gravel	Multiple stages of sedimentation, soil formation, erosion, and reworking, influenced by climatic conditions. Brecciation of calcrete profiles reflects degradation due to insufficient sedimentation, exacerbated by vegetation and erosion (Wright and Tucker, 1991; Alonso-Zarza and Silva, 2002; Alonso-Zarza and Tanner, 2009)	
Gcd	Disorganized conglomerate	Very poorly sorted and disorganized, with or without sandy matrix. Basalt boulders of variables size, sub-angular to rounded	Deposited by gravity flows generated by flash floods or rock avalanches in proximal fan settings. These events occur rapidly, transporting large and poorly sorted clasts (Blair and McPherson, 1994; 2009)	
Sp	Planar-cross-bedded sand	Planar-bedded couplets alternating between fine to medium pebble, cobbly gravel and sandy granule-pebble gravel; very low concentration of silty matrix; Planar to trough-bedded. Reworked gastropod shells	Cyclical sediment deposition influenced by varying flow regimes over time. Likely formed during sheetflood or pyroclastic reworked material sediment gravity flows or fluvial floods, where rapid flow changes deposited alternating coarse and fine materials (Blair, 1999; Miall, 2006).	

Label	Facies	Facies characteristics	Interpretation	Image
Gci	Clast-supported gravel	Isolated chaotic clasts, poorly sorted and disorganized, clay-sandy matrix is absence or very low. Erosive base. Basalt (85%), carbonate (10%), and pyroclastic (5%) angular, sub-angular clasts. Abundant boulders present	Generated by high-energy sediment gravity flows associated with colluvial slope failure during flood periods. Represents non-cohesive debris flows where clasts were transported rapidly (Blair and McPherson, 1994; 2009; Miall, 2006)	
Gmm	Matrix-supported conglomerates	Poorly sorted gravel, reddish to brownish clay-sandy-matrix-supported. Rare imbrication. Basalt (70%), carbonate (20%), and pyroclastic (10) angular, subangular pebbles to boulder	Deposited by cohesive, plastic debris flows during flood periods. The matrix-supported nature and poor sorting indicate more plastic, cohesive flows with limited downslope tractional transport (Blair and McPherson, 1994; 2009; Miall, 2006)	
Ss	Scour-fill sand	Shallow scour and fill structures, composed of very coarse, light brown sand. Trough cross-beds present	Formed in small channels or scour hollows, typically found in confluences or on sloped surfaces. Represents localized high-energy flow events during channel scour or confluence areas (Gibling, 2006; Miall, 2006)	

Label	Facies	Facies characteristics	Interpretation	Image
Sm	Massive sand	Fine-very fine sand, pink-peach in colour; dispersed pebble. Massive- structureless; lensing body	Represents low-energy sediment gravity flows, likely formed during periods of channel avulsion or bank collapse. The massive, structureless nature reflects rapid deposition and subsequent dewatering (Slingerland and Smith, 2004; Miall, 2006)	
Gi	Imbricated conglomerates	Moderately sorted, subangular, subrounded basaltic, carbonate pebbles and cobbles; clast-supported, low concentration of silty to clay matrix. Imbrication; normal graded bedding; eroded base	Longitudinal bar gravel formation indicating vertical accretion due to selective tractional transport. Reflects medium to low energy flow conditions, where clast size decreases upward as shear stress diminishes (Hein and Walker, 1977; Miall, 2006)	
Gh	Horizontally stratified conglomerates	Horizontal and parallel beds, with some cross-bedding. Decreasing bed thickness upward. Current ripple marks and imbrication present. Poorly to moderately sorted basaltic and carbonate clasts, ranging from fine to very coarse pebbles, in a sandy matrix. Occasionally includes floating boulders	Represents longitudinal gravel bars, accreted by selective tractional transport in high-energy environments. Reflects the migration of gravel bars due to changes in shear stress along the fan (Hein and Walker, 1977; Miall, 2006)	

Label	Facies	Facies characteristics	Interpretation	Image
Gt	Gravel trough cross-beds stratified	Moderately sorted fine to medium subrounded pebbles in a sandy matrix. Features cross-lamination and crude stratification, with an erosive base	Formed through lateral accretion in gravel point bars, typically influenced by downfan selective tractional transport during high-energy flow events (Miall, 2006)	
Smf	Massive sand bioturbated	Brown/reddish sands and clays, well sorted, structureless, and extensively bioturbated by gastropods and Hymenoptera shells. Incised by abandoned channels	Sediment gravity flow deposits in low-energy alluvial fan environments. The bioturbation and post-depositional rain-wash processes indicate long periods of surface stabilization, where biological activity modified the original deposit (Miall, 2006)	
Sr	Ripple-cross laminated sand	Dark-grey, very coarse to medium sand with abundant subrounded to rounded carbonate and basaltic intraclasts. Thinly bedded (~5 mm), with asymmetric ripple cross-lamination	Represents fluvial channel sands deposited during downstream migration under low flow regime conditions. The transition from subcritical to supercritical flow contributes to ripple cross-lamination (Miall, 2006)	

Label	Facies	Facies characteristics	Interpretation	Image
Fm	Massive silt-clayey	Laminated to massive red mudstone with parallel bedding. Erosive base. Thickness ranges from 2 cm to 30 cm. Contains shell fragments and vertical desiccation cracks	Deposited by decantation in floodplain ponds or slackwater areas. Typically forms in low-energy environments where fine sediment accumulates over time (Kochel and Baker, 1982; Saynor and Erskine, 1993)	
Ssa	Aeolian sand-sheet	Fine to very fine laminated grey sand; interbedded with Fm and Sh. Parallel beds	Wind-blown laminae formed in interdune ponds, interchannel areas, or along the lateral margins of dune fields. Reflects aeolian processes during periods of reduced fluvial activity (Trewin, 1993)	
Sh	Sandstone, laminated	Horizontal laminae of grey sand, with thicknesses between 6 cm and 17 cm. Interbedded with Fm and Ssa. Includes floating carbonate pebbles and cobbles	Represents low-energy slackwater or interchannel areas. Laminated sands formed under low flow conditions, occasionally interrupted by higher-energy fluvial events that transported carbonate pebbles and cobbles (Trewin, 1993). Likely deposited during episodic flash floods	

Label	Facies	Facies characteristics	Interpretation	Image
Sa	Aeolian dune field	Yellowish-greyish well-sorted fine- to medium-fine sand. Planar and trough cross-lamination. Bioturbation is present	Formed through the migration of aeolian dunes by avalanching in the lee slope. Reflects arid or semi-arid conditions where wind is the dominant agent of sediment transport (Miall, 2006)	

By analysing the facies assemblage, four distinct environments were identified: **talus**, **fan-head**, **mid-fan**, and **distal**. A subsequent correlation of these environments across the four logs from the barrancos improved the understanding of the sedimentary history. Simplified logs for the barrancos (LZ403, Horca, Las Piletas, Falls) are presented in the next section (Fig. 88). The identification of these four environments—talus, fan-head, mid-fan, and distal—was achieved through a comprehensive cross-sectional representation. This representation, developed by correlating data from the four barrancos, facilitated the reconstruction of the geological history and spatial distribution of facies within the alluvial fan system. The observed intricate pattern highlights the complexity of the interdigitation with the aeolian system, offering valuable insights into the dynamic geological processes that have shaped the El Jable plain (Fig. 89).

Figure 88. Simplified sedimentary logs of four barrancos (LZ403, Horca, Las Piletas, Falls) within the alluvial fan system, illustrating distinct fan environments: talus, fan-head, mid-fan, and distal fan, as identified through lithofacies analysis. Talus deposits are characterized by laminar calcrete (Cl) and disorganized conglomerates (Gcd), indicative of sediment gravity flows. The fan-head displays alternating gravelly and sandy units (Gmm, Gci, Sm, Sp), reflecting episodic water events. The mid-fan features a transition to finer-grained deposits (Smf) and conglomerates (Gi, Gh, Gt), suggesting both higher and lower-energy flows, while the distal fan is dominated by well-bedded sandstones and finer sediments (Ssa, Sh, Fm), deposited in a low-energy environment.

Additionally, wind-driven deposits are present, although they are not part of the alluvial fan system. These aeolian deposits either cut through or are cut by the alluvial fan sediments, representing lateral interactions. While these dunes interact stratigraphically with the fan, they do not influence the classification of alluvial fan processes.

151
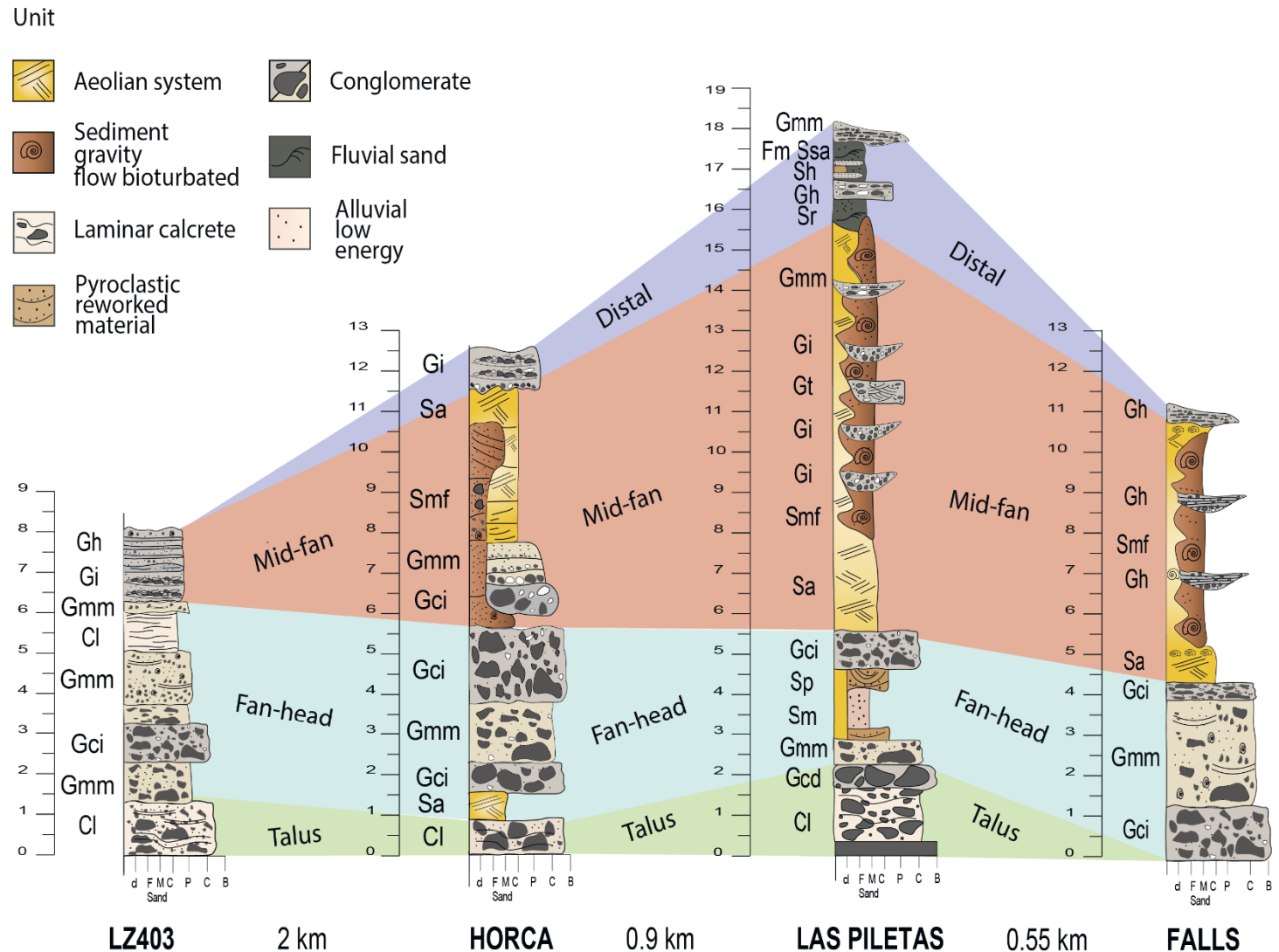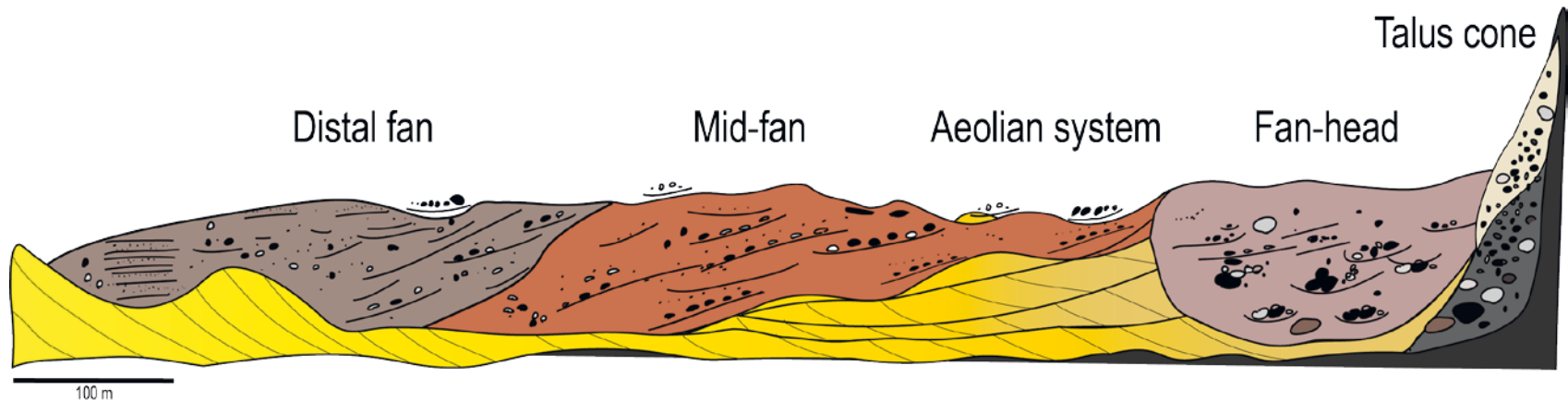
Figure 89. Alluvial fan system of the Famara cliffs. Above: Satellite image showing the barrancos (gullies) of the alluvial fan system of Famara. Key locations such as LZ403, Horca, Las Piletas, and Falls are marked, indicating different parts of the fan system. The image highlights the geomorphological relationship between the mountain front and the depositional plain. Below: Cross-section of the alluvial fan system, illustrating the sedimentary architecture of the fan. The diagram shows the transition from proximal (near the source) debris flow-dominated deposits, composed of coarse-grained sediments, to finer-grained deposits in the mid and distal portions of the fan, where aeolian and fluvial processes become more prominent. The yellow zones indicate aeolian processes, while the brown and grey sections represent fluvial and debris flow deposits.

5.3.1.1 Talus cone
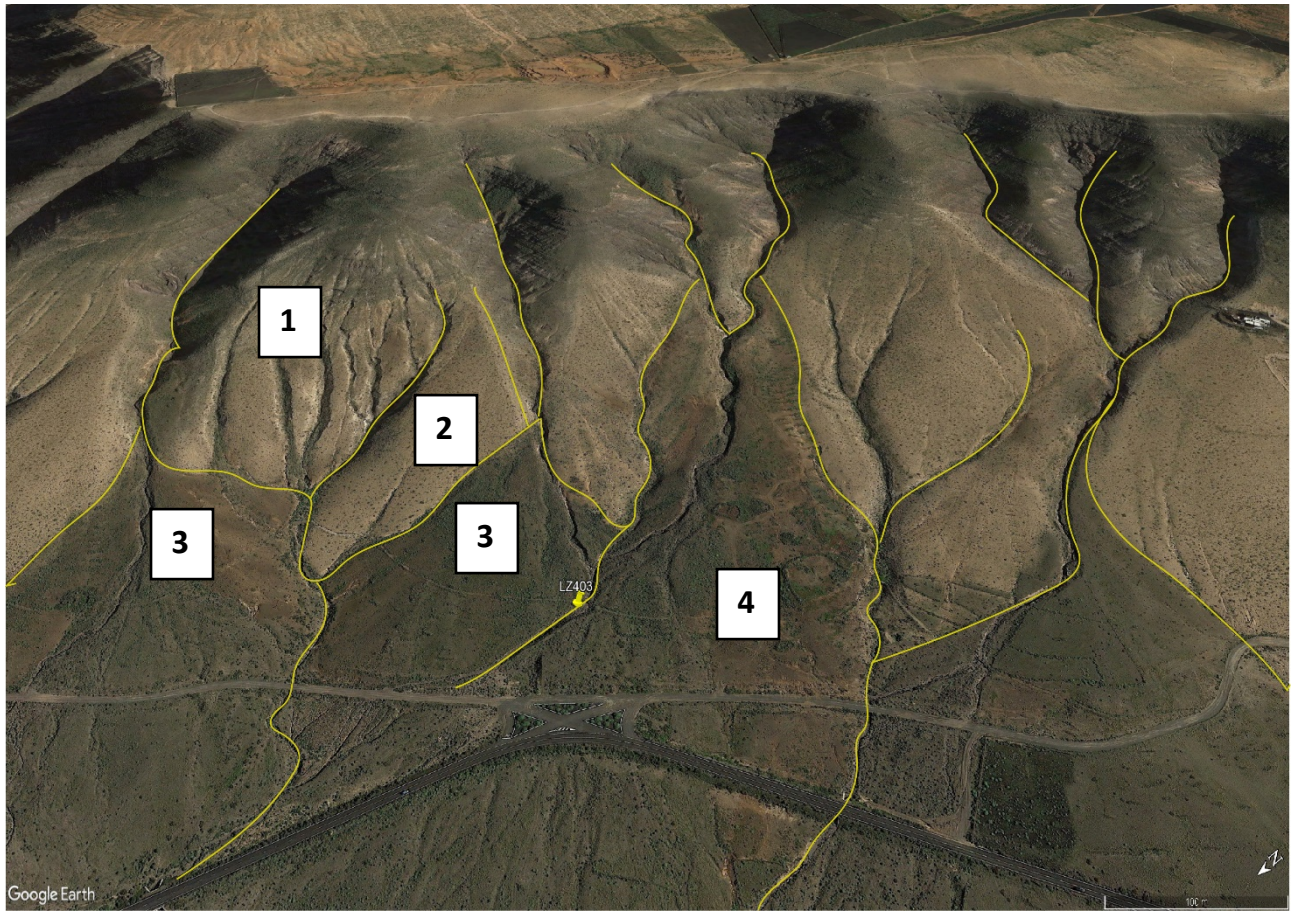
Figure 90. The oldest alluvial fan of the first generation covered by calcrete layer; 3-4 youngest fans of the third generation covered by brown-green layer. Satellite image of barranco LZ403.

As mentioned by Balcells et al. (2004b) the first and oldest generation of alluvial fan system are those covered by a light-brown layer, while the younger ones of the third generation, are those covered by a green-brown layer. A more accurate differentiation can be achieved by examining satellite images (Fig. 90). The *Disorganized conglomerate* (Gcd) *and Laminar calcrete* (Cl) *and* are the most prominent facies in this depositional environment (Fig. 90).

Facies Gcd is categorized as a primary sedimentary process active on alluvial fans, generated by bedrock cliff failure of rockfalls type (Blair and McPherson, 1994). The facies is constitued by basalt boulders of variables size, angular to sub-angular, very poorly sorted, disorganized, with or without sandy matrix, thickness of circa 1m. The deposits mantle the bases of Famara bedrock cliffs in the drainage basin forming talus cones. They are evident in all four barrancos.

The facies Cl is distinguished by hardened, laminated sheets of calcrete crusts, typically undulose, covering basalt host rock and/ or penetrating it, with minimal fine-sand matrix present, thickness up to 4m. The basalt host rock appears weathered and fragmented due to the penetration of white veins of laminated caliche, which follow pre-existing cracks and contribute to the opening of fissures increasing the weathering of the basalt (Fig.91 A). Based on correlation with the Macher profile examined by Alonso-Zarza and Silva (2002), the groundmass of the calcrete consists of micrite. Some of the calcrete deposits exhibit laminar horizons at the top (Fig. 91 B), which according to the same authors, may have evolved in response to short periods of sedimentation followed by periods of soil formation. Numerous researchers associated the calcareous formations in Lanzarote to periods of aridity. Alonso-Zarza and Silva (2002) detail a profile located southwest of the study area, developing on Middle to Upper Pleistocene basalt comprises two layers: a basal one of basalt, with micrite filling its grooves and cracks, and an upper stratum featuring a 1.2-meter-thick calcareous crust housing numerous insect ootheca. Similar situation has been found in barranco Horca, where fragments of Gastropod shells were present on the upper part of the crust (Fig. 91 C). Additionally, Meco et al. (2006) delineate a significant calcrete formation from the Lower Pleistocene, spanning alluvial fans and basalt formations across Lanzarote and Fuerteventura. This calcrete is intersected by a network of ravines, established during the same Lower Pleistocene epoch. According to Vega (2010), the first generation of fans occurred during the Lower Pleistocene, when a wet period with significant precipitation levels caused erosion of the cliff slopes. Subsequently, marine bioclastic sediments in the form of ramping dunes covered these scree deposits and slopes. This period coincided with the formation of the volcanic cones of Montaña Chimia and the shield volcanoes of Mozaga and Guanapay (Fig 44). Palaeosols formed on some of these levels. A later arid period, combined with intense evapotranspiration on these slopes, led to the transformation of these carbonate deposits into a thick calcrete crust. Later, still during the Lower Pleistocene and during a climatic stage characterized by intense precipitation, the cliffs of Famara underwent intense erosion once again. This erosion caused the large calcareous crust to break and further erode the slopes of the Famara massif, generating a new generation of fans, which are very dark due to the terrigenous material. These cover part of the calcrete, giving it the characteristic shape of an alluvial fan.

Facies Cl is particularly prominent in barrancos LZ403 and Horca.
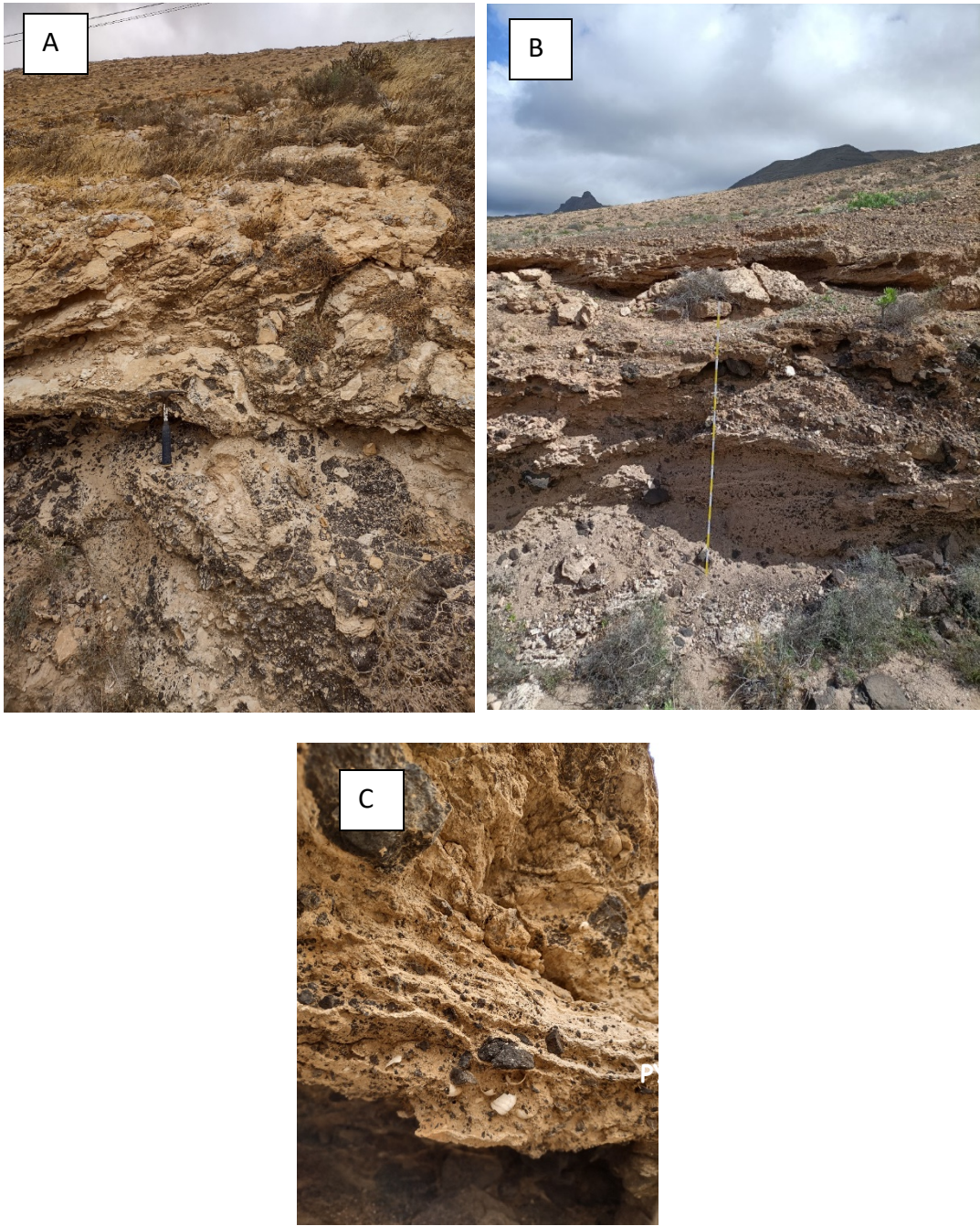
Figure 91. Facies *Cl* (laminar calcrete) in Horca and LZ403. A: coating the basalt host rock prompting its weathering; B: showing laminated crust on top; C: hosting fragments of Gastropod shells.

5.3.1.2 Debris-flow dominated and waterlaid alluvial Fan-head

The fah-head of the alluvial fan comprises facies related to debris-flow and waterlaid deposits. The most frequent are those related to debris-flow deposits comprising *Clast-supported gravel* (Gci) and *Matrix-supported conglomerates* (Gmm). The two deposits represent the primary processes responsible for actively transporting sediment from the drainage basin to the fan site, marking a brief but impactful phase in fan evolution (Blair and McPherson, 1994). The waterlaid deposits comprise facies of *Planar-cross-bedded sand* (Sp), *Scour-fill sand* (Ss), and *Massive sand* (Sm).

Their association is linked to gravity-driven processes, rockfall, debris flow, erosional stage and high-energy channel deposits.

Both Gci and Gmm are constitued of isolated chaotic clasts, angular, subangular pebbles to boulders (Fig. 92), theit thicnkness range from 0.5 m up to 2m. Gci is made of basalt (85%), carbonate (10%), and pyroclastic (5%), open work or with very low concentraion of clay-sandy matrix. Structures like imbrication are rarely present. The deposits represents clast-rich non-cohesive debris flows, (high-strength) (Miall, 2006). The Gmm facies comprises poorly sorted gravel supported by a reddish to brownish muddy-sandy matrix. Clasts consist of basalt (70%), carbonate (20%), and pyroclastics (10%). The angular and sub-angular clasts mixed with sand and very fine pebbles in a light-brown matrix, suggest post-depositional processes involving infiltration and entrapment during waning flood stages. Imbrication is present but infrequent. Gmm deposits are

Figure 92. Stratigraphic Profile with Alternating Gci and Gmm Units in Barranco LZ403. The image shows alternating layers of Gci (Gravelly Clast-supported Imbricated conglomerate) and Gmm (Massive Matrix-supported conglomerate). The Gci layers indicate high-energy fluvial processes, while the Gmm layers suggest lower-energy debris flow deposits. This alternation reflects shifts in depositional environments.

associated with plastic cohesive debris flows characterized by sedimentary particles and small

percentages of entrained water and air moving downslope due to gravity. Two mechanisms initiate the debris flow: disintegration of colluvial slides into debris flow by entrainment of air and water, and fast-moving water intersecting a sediment-mantled drainage basin slope. Rapid entrainment of sediment, air, and water occurs as water dissipates energy through churning, tossing, and mixing (Blair and McPherson, 1994).

The Gci and Gmm define sediment gravity flows triggered by colluvial slope failure, differing only in physical characteristics. Pseudoplastic debris flow (Gmm), with low strength, is generally more viscous than plastic clast-rich debris flow (Gci), which has high strength. This difference arises because pseudoplastic flow contains fine, sandy material, making it behave more fluidly and less cohesively than clast-rich flow, which contains variable-sized clasts (Blair and McPherson, 1994). Gmm can exhibit laminar, or turbulent characteristics. Evidence like occasional imbrication and its occurrence at the base of gullies suggests deposition by high-energy fluvial flows during phases of substantial sediment influx. These flows, typically initiated by heavy rainfall, erode underlying deposits, mix sediment components, and carry the matrix downstream. Gci facies can form through brief turbulent flows as documented by Miall (2006) and Einsele (2000). Characteristics like a high proportion of fine matrix, a non-erosive base, and the absence of imbrication indicate transportation by dense, viscous laminar flows that move clasts through buoyancy. When shear forces decrease below the flow's yield strength, resulting in the flow ceasing, a poorly sorted fabric emerges, with clasts dispersed randomly. The low viscosity and shear strength under conditions of low liquid discharge explain the lack of alignment, rare imbrication, and infrequent gullying bases, typical of rivers experiencing significant increases in flow and solid loads during heavy rainstorms.

Both Gci and Gmm are frequent in all the barrancos frequently interbedding with Sm.

The Sm, Sp, and Ss are part of sandy lithofacies.

The Sm facies, characterized by massive, pink-peach-colored fine-very fine sand with dispersed basaltic pebbles, lacks internal structures and is observed just in the fan-head where it appears as a lensing body with erosive boundaries, thickness of 0.5m. The absence of internal structures suggests rapid deposition of suspended bed load during declining flood periods (Todd, 1989) or sediment gravity flows in low-energy environments. Post-depositional processes like dewatering may further contribute to the lack of internal structure (Miall, 2006). Furthermore, it might suggest short-term patterns of anastomosis, especially when there's a need to supply a large sediment sheet, disappearing when low areas of the flood basin are filled and flows move into a new single-thread

channel. Avulsions, or channel relocations, are expected results of long-term buildup and are essential for creating large alluvial deposits (Slingerland and Smith, 2004).

The Sp facies consists of planar-bedded couplets of alternating pyroclastic fine-to-medium pebble, cobbly gravel, and sandy granule-pebble gravel, with a total thickness of 2.4 meters. The gravels show minimal silty matrix, suggesting deposition by high-energy, sediment gravity flows. Reworked gastropod shell fragments are present. The sharp, planar beds reflect alternating pulses of debris flows or hyperconcentrated flows, each depositing material rapidly as flow energy dissipated.

The clear horizontal stratification with distinct textural changes between layers indicates variations in sediment load and flow energy during each depositional event. The absence of significant trough-bedding structures suggests that the flow was largely unidirectional and planar, possibly linked to flow expansion and subsequent deceleration across the fan.

These deposits are interpreted as episodic sediment gravity flows, possibly triggered by storm events or slope failures, with each layer representing a single high-energy depositional event. As the flow transitioned from supercritical to subcritical conditions, coarse gravels were deposited first, followed by finer sands, indicating a rapid loss of energy (Blair and McPherson, 1994; Blair and McPherson, 2009).

The facies Ss is characterized by an erosional scour surface, followed by a trough cross beds of very coarse-grained sandstone containing intraclasts of mudstone and siltstone, with a thickness of up to 30 cm. This sedimentary structure is defined by a concave-upwards erosion surface, formed by the action of high-velocity water flow cutting into the underlying bed. During the waning stage of the flow that caused the scour, the concavity is filled by coarse sediment. This scour facies is typically associated with erosion processes intrinsic to fluvial channels, particularly at bends, confluences, and control points. It has been observed exclusively at the head-fan position, positioned above the Gmm facies. The formation of these scours may be linked to the erosion of small channels or the deposition on sloped surfaces, as suggested by Gibling (2006) and Miall (2006).

The facies analysis in the fan-head area reflects a combination of alluvial fan and fluvial deposits. These deposits are primarily shaped by high-energy events, often triggered by intense rainfall, particularly storms, typical of arid to semi-arid environments. The section shows a variety of facies, with episodic, high-energy debris flows (Gci, Gmm) alternating with periods of lower-energy fluvial processes (Ss, Sm). The Gci and Gmm facies indicate slope failures as the main mechanism, with colluvial material being rapidly transported and deposited onto the fan. In contrast, during calmer

intervals or smaller events, the scour-fill sands (Ss) and massive sands (Sm) suggest localized channel activity and the accumulation of finer sediments.

All the mentioned deposits have been detected in all four barrancos. Only facies Sp has been found in Las Piletas, likely indicating the coalescence area of the two adjacent fans.
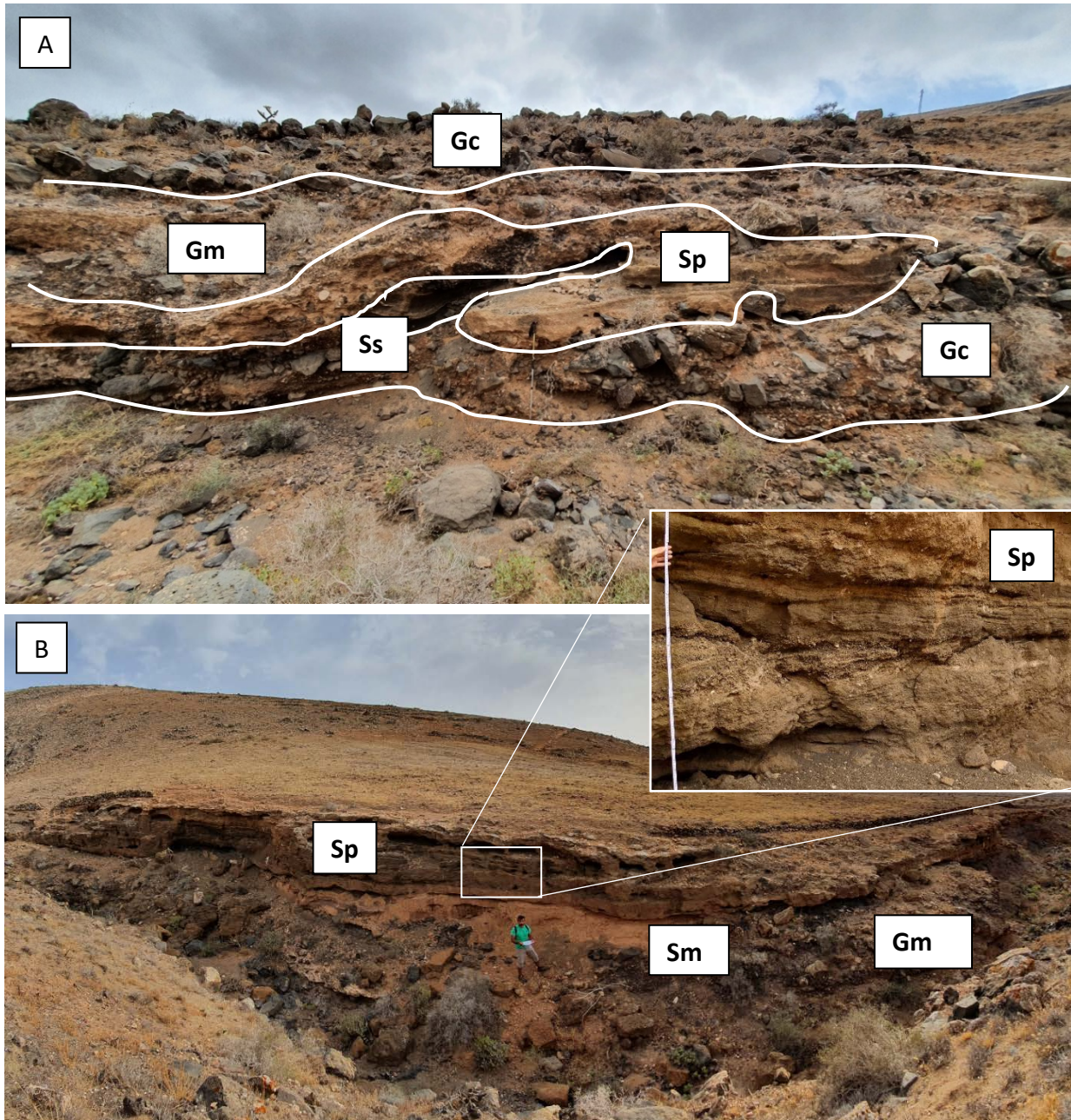
Figure 93. Sedimentary facies from the proximal section of the alluvial fan. (A) Stratigraphic section showing facies Gci (clast-supported gravel), Gmm (matrix-supported conglomerates), and Ss (scour-fill sands) in an erosional sequence, indicative of episodic sediment gravity flows and fluvial processes. Gci represents high-energy non-cohesive debris flow deposits, while Gmm corresponds to cohesive debris flows with a higher matrix content. Ss marks localized channel activity with scour-and-fill structures. (B) The opposite side of the same channel wall, showing facies Sp (planar cross-bedded sands) and Sm (massive sands). Sp represents high-density gravity flow deposits or tractional reworking under supercritical flow conditions, while Sm suggests sediment gravity flows in a low-energy environment. The inset highlights the sharp contact and clear stratification between sandy and gravelly units, indicative of episodic high-energy depositional events.

5.3.1.3 Gravel-channel bar dominated Alluvial Fan (Mid Fan)

The mid-section of the alluvial fan system is characterized by complex interactions between gravity-driven sedimentary processes, fluvial dynamics, and aeolian influences. The dominant processes observed reflect alternating periods of high-energy debris flow deposition and low-energy fluvial and aeolian activity, creating a stratigraphic succession that includes conglomerates, bioturbated sands, and aeolian features. Each facies represents different depositional mechanisms active in this part of the fan. The sediments exhibit an intermediate grain size between the coarser materials found in the apex and the finer fractions downstream. There are clear alternations between coarse
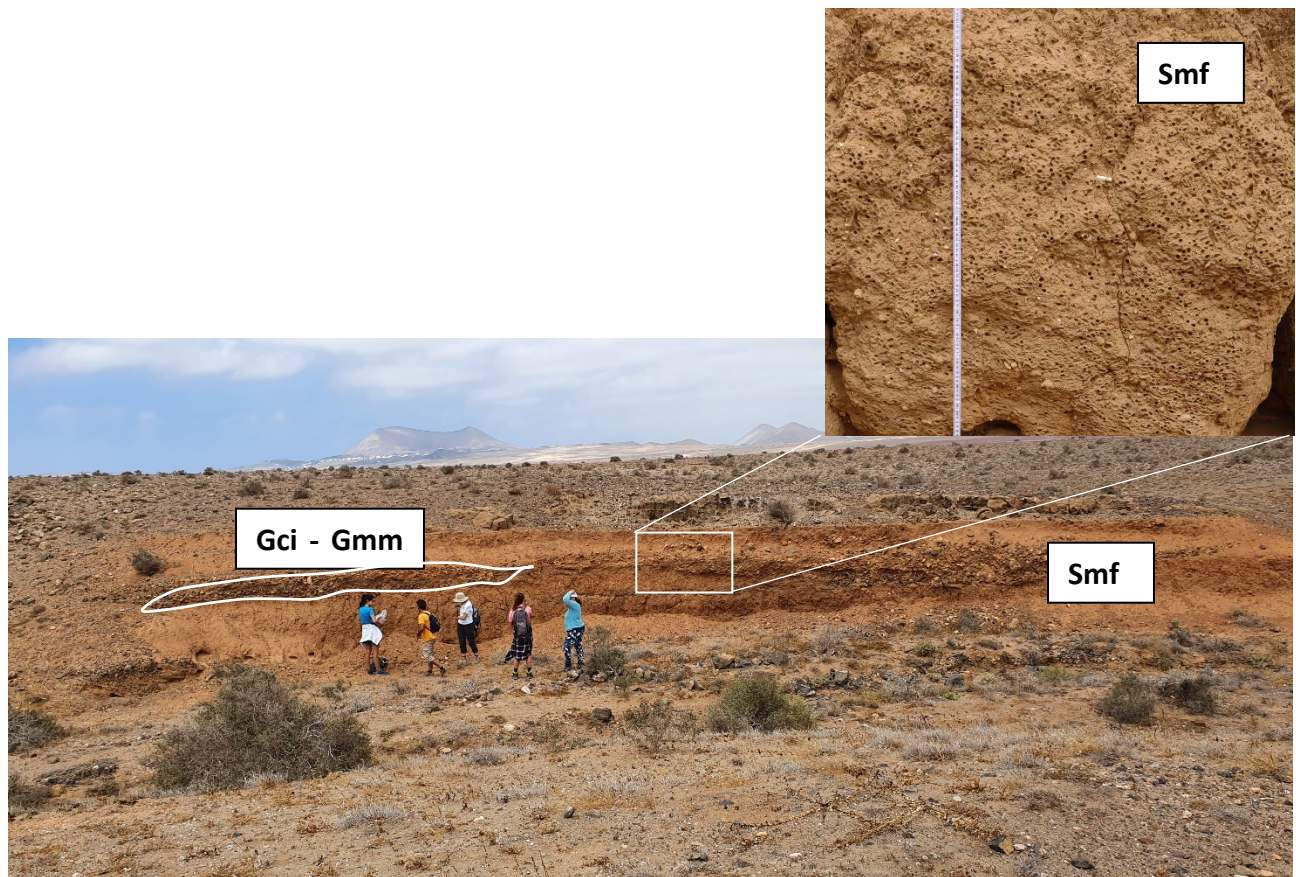
Figure 94. Lenses of Channel Bar Deposits cutting the reddish sandstone. In the zoom, bioturbation by oothecas. Las Piletas.

and fine deposits, with an increase in finer-grained sheet deposits that gradually dominate. This trend is particularly pronounced in the southern region of the alluvial fan system, particularly in the barranco Falls, where the mid-fan area extends over significant axial lengths. The predominant deposit in this region is characterized by brown/reddish, well-sorted, structureless *Massive Sand Bioturbated* (Smf), attaining thicknesses of up to 5 meters, interspersed with gravel bar bedforms (Fig. 94). This deposit is believed to originate primarily from the erosion of the cliff, with fine material

transported downslope and deposited as gravity flows. The absence of sedimentary structures, such as cross-bedding or laminations, supports the interpretation of these sands as the result of low-energy gravity-driven processes, rather than fluvial or sheetflood mechanisms. The Smf facies is highly bioturbated, containing abundant ootheca and Gastropod shells, which provide evidence for extended periods of inactivity on the fan surface. These biological markers suggest that the fan surface was abandoned or experienced prolonged stability, allowing for the colonization of organisms. The presence of bioturbation is a strong indicator that post-depositional processes played a significant role in the modification of the original sediment. This bioturbation likely disturbed the primary sedimentary structures, contributing to the facies' structureless, massive appearance. The Smf facies is incised by abandoned channels, which are filled by deposits of clast-supported gravel (Gci) and matrix-supported conglomerates (Gmm). These channel incisions suggest episodic, higher-energy events, possibly flash floods or debris flows, that cut through the previously deposited Smf sands. The presence of Gci and Gmm within these channels further supports the interpretation of gravity-driven flows, with Gci reflecting non-cohesive debris flows and Gmm indicating more cohesive flows with a finer matrix. The Smf facies is interpreted as a secondary process resulting from sediment gravity flows, modified over time by post-depositional alterations such as dewatering and bioturbation (Miall, 2006). Dewatering, the expulsion of water from the sediment post-deposition, would have contributed to the compaction and stabilization of the deposit, further enhancing its massive appearance. These post-depositional processes, combined with the bioturbation from biological activity, have erased any primary structures, leaving a homogenous and featureless sedimentary body. The substantial thickness (up to 5 meters) of this Smf deposit suggests it represents a significant phase of sediment accumulation, possibly reflecting a period of reduced depositional energy, where the fan surface was relatively inactive and allowed for the slow, incremental buildup of fine material sourced from the cliff erosion. During this time, the dominant processes were mass wasting and gravity-driven transport, leading to the deposition of this thick, bioturbated sand body.

The Gravel bars bedform are the second most present macroforms in the study area, represented by facies *Imbricated conglomerates* (Gi)*, Horizontally stratified conglomerates* (Gh) and *Gravel trough cross-beds stratified* (Gt) (Fig. 95). Gi and Gh are often together. In river systems, bars are categorized into midchannel and bank-attached types, the latter known as point, alternate, or lateral bars depending on their shape and position. The evolution of midchannel bars involves processes like chute cutoff, where a point bar forms initially, separated from the bank by a scour pool. As the midchannel bar stabilizes, erosion removes newly developed point bars on the opposite bank. Additionally, a less significant type of midchannel bar called a counterpoint bar can emerge on the outside of meander bends due to turbulence and shoaling near the bend entrance. These bar types can transition into one another over time due to changes in flow patterns caused by meander migration and channel avulsion (Miall, 2006).

To distinguish between different types of bars in the study area, various structures have been analysed. Gi exhibits moderately sorted, subangular to subrounded basaltic and carbonate pebbles and cobbles with a low concentration of silty to clay matrix, up to 50cm of thickness. The presence of imbrication, normal graded bedding, and an eroded base suggests a longitudinal bar gravel formation, indicating vertical growth due to selective tractional transport from water flows in a medium to low energy environment. This results in a decrease in shear stress and an upward reduction in clast size (Hein and Walker, 1977; Miall, 2006).
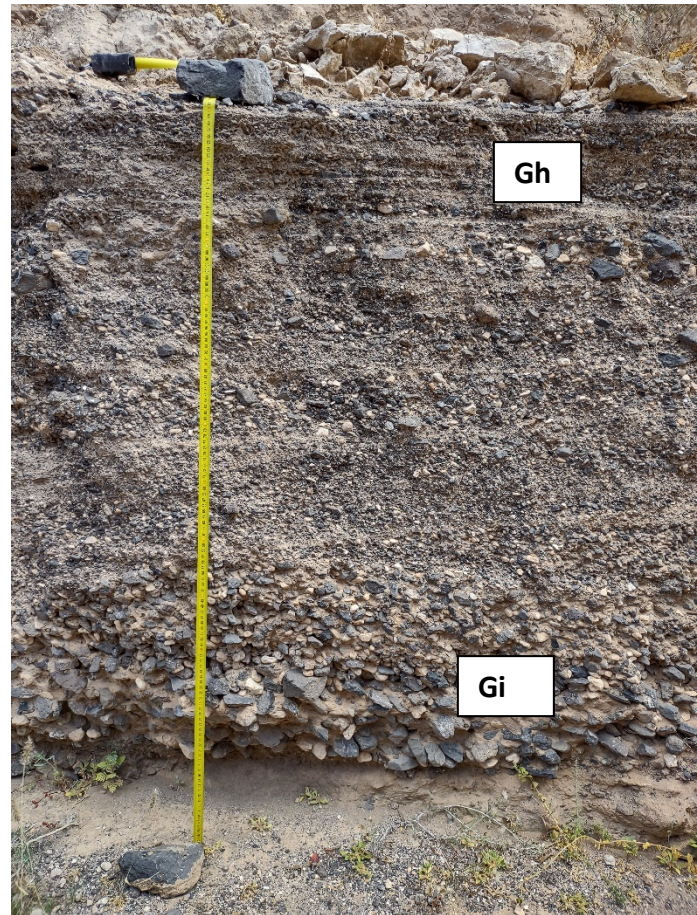
Figure 95. Longitudinal Bar in Horca showing normal graded bedding. The image depicts a longitudinal bar from the Horca section, with clear normal graded bedding. The upper unit is labeled Gh (Gravelly horizontal stratification), indicating relatively stable water flow during deposition, while the lower unit, Gi (Gravelly imbricated stratification), reflects a higher-energy environment with fluvial imbrication of clasts. This grading suggests a decreasing flow energy over time, from the coarser gravels at the base to the finer materials at the top.

Gh displays horizontal and parallel beds, limited cross-bedding, decreasing bed thickness upward, current ripple marks, and imbrication, up to 1 m of thickness. Clasts consist of basaltic and carbonate material, ranging from subangular to subrounded fine to very coarse pebbles, poorly to moderately sorted, within a sandy matrix, sometimes with floating boulders. This unit is interpreted as the accretion or migration of a longitudinal gravel bar, influenced by downfan selective tractional transport from water flows in a high-energy environment, leading to changes in shear stress.

The only lateral gravel bar identified corresponds to Gt, characterized by moderately sorted, fine to medium subrounded to rounded pebbles within a sandy matrix (Fig. 96). It often exhibits frequent cross-lamination, crude stratification, and an erosive base. This unit is interpreted as a lateral accretion of a gravel point bar. The formation is likely influenced by downfan selective tractional transport from water flows in a high-energy environment (Miall, 2006).

Figure 96. Lateral bar in Las Piletas. This image captures a lateral bar from the Las Piletas section, exhibiting stratified conglomerates interbedded with finer sediments. The alternating layers suggest deposition along the side of a river channel, where changes in flow energy led to the accumulation of both coarse and fine materials. The coarser gravels represent higher-energy flow conditions, while the finer sediments indicate lower-energy flow during slackwater phases, typical of lateral bar formations in fluvial environments.

In this transitional zone, the emergence of the *Aeolian Deposit* (Sa) denotes a noteworthy geological shift, interdigitating laterally with the (Smf) deposits (Fig. 97- 98 - 99) across all barrancos except for for the barranco LZ403, which is dominated by more prominent gravity flow processes such as debris flows (Gci and Gmm). These aeolian sands, characterized by well-sorted fine to medium grains and cross-lamination, indicate a phase where the fan was largely inactive, and aeolian reworking became the primary agent of sediment transport. This interbedding of aeolian and gravity flow deposits suggests alternating climatic conditions, with seasonal or episodic shifts between wetter periods dominated by gravity flows (in the form of debris flows and channelized transport) and drier intervals where

aeolian processes took over. The lateral variation between these deposits across different barrancos reflects the spatial variability in sediment supply, wind patterns, and flow energy, characteristic of alluvial fan systems in semi-arid environments.

Figure 97. Lenses of Channel Bar Deposits cutting through the reddish sandstone in Falls. The conglomerates (Gi-Gh), consisting of clast-supported gravel, represents a high-energy channel deposit that have incised into the underlying Smf facies. This channel incision highlights the shift from a relatively low-energy environment, where fine, bioturbated sands accumulated (Smf), to a higher-energy event that deposited the conglomerate. The arrow indicates the point where the aeolian deposit Sa is truncated by the overlying fine sandstone deposits Smf illustrating the complex interplay of aeolian processes, gravity-driven, and fluvial incision in the mid-fan area.
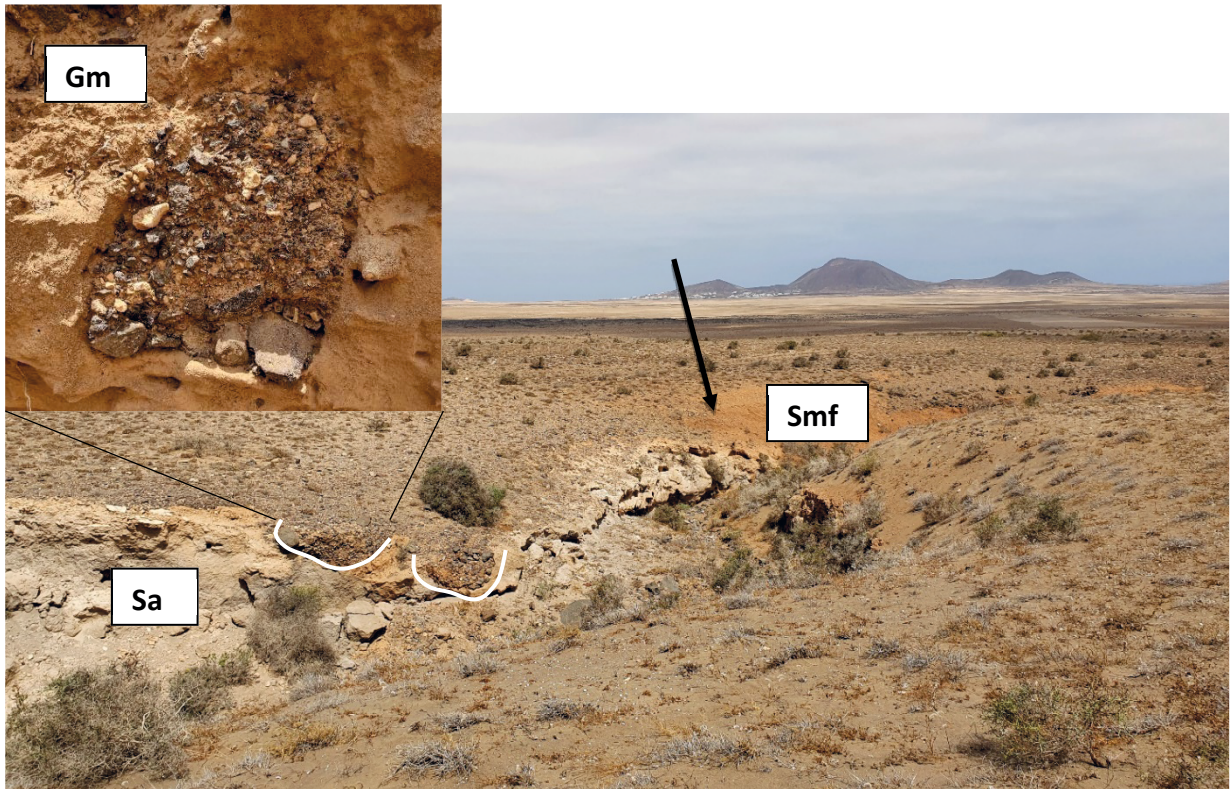
Figure 98. Interdigitation between Aeolian Deposit (Sa) and Massive Bioturbated Sand (Smf) with debris flow incision in Las Piletas. The arrow indicates the point where the Aeolian Deposit (Sa), consisting of wind-blown sands, interdigitates with the brown/reddish Massive Bioturbated Sand (Smf), a fine-grained sandstone. This transition marks the interplay between aeolian and gravity-driven processes. The inset zoom shows a normal-graded debris flow deposit (Gm), characterized by coarse clasts grading upward into finer material, cutting through the aeolian deposit. This debris flow represents a high-energy event, potentially triggered by slope failure, that disrupted the previously deposited wind-driven sediments. Location: Las Piletas.
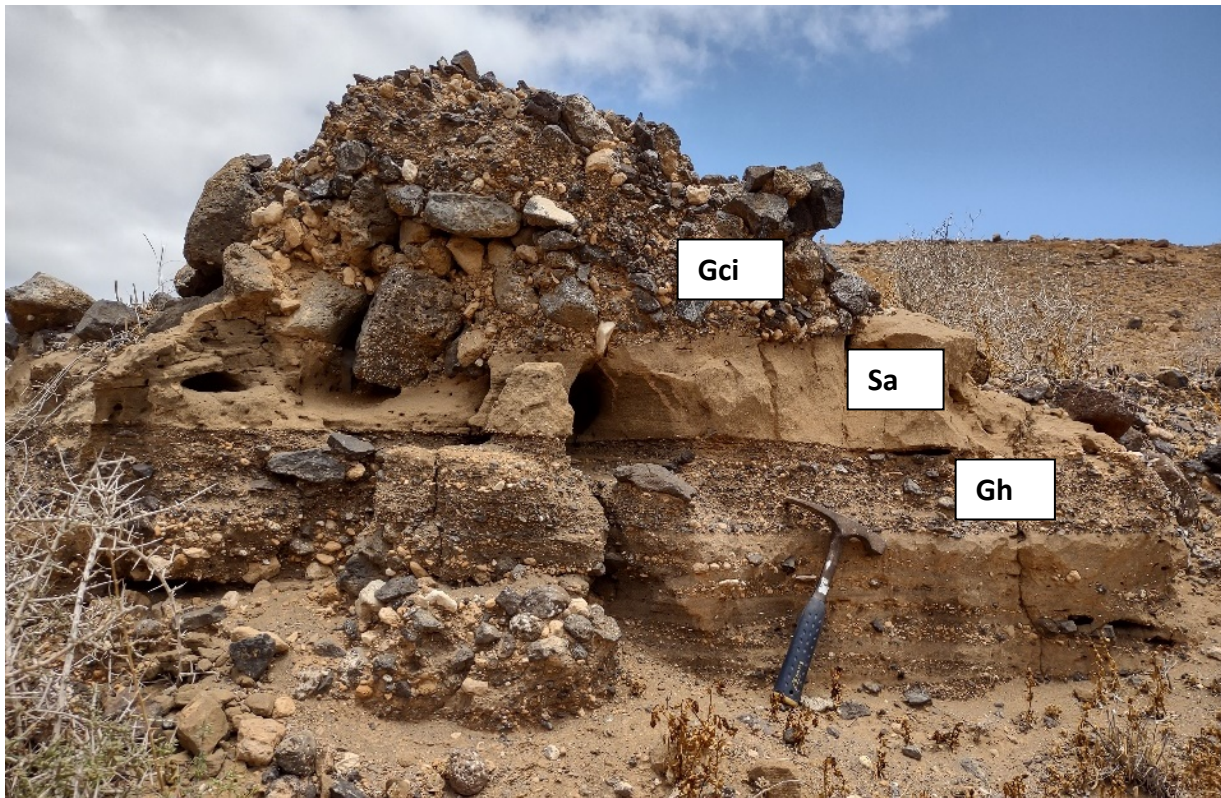
Figure 99. Aeolian deposit (Sa) cut by imbricated and laminated conglomerates (Gh) and overlain by clast-supported conglomerates (Gci) in Las Piletas. The Aeolian Deposit (Sa) is composed of well-sorted, fine sands, representing periods of wind-driven sedimentation. This deposit has been cut and overlain by a sequence of horizontally stratified conglomerates (Gh) with imbricated clasts, indicating a fluvial environment where tractional transport dominated. The overlying clast-supported gravel (Gci) represents a high-energy debris flow event, with large, angular basaltic clasts transported and deposited in a chaotic manner. Flow direction is from right to left, as indicated by the imbrication of clasts within the Gci layer.

5.3.1.4 Fluvial dominated Alluvial Fan (Distal Fan)

This part of the fan displays a transition from channel flow to shallow sheet flows. The slowing of the flow in the distal area is caused in this case by the low slope gradients, leading to a depositional environment dominated by *Ripple cross-laminated sand* (Sr), debris flow deposits (Gi and Gh), and silty-clay deposits (Fm) (Fig. 100).

The Sr facies comprises dark-grey sand ranging from very coarse to medium, containing numerous subrounded and rounded intraclasts pebbles, predominantly made of carbonates and basaltic material. The sediment exhibits asymmetric ripple cross-lamination and horizontally stratified layers, laminae typically around 5 mm thick, with an overall deposit thickness of approximately 1.5 m. Interpreted as a channel fill sand bedform, this lithofacies showcases various asymmetric ripple types which reflect the changing in flow velocity (typically forming at low flow speeds, <1 m/s) and sediment supply rate. "Type-A" ripples form through mutual erosion during low sedimentation rates from suspension, while "type-B" ripples, featuring partially preserved stoss sides and climbing of the ripple train, occur when sediment is added during migration (Miall, 2006; Nichols, 2009).

The presence of horizontal to low-angle lamination in the deposit suggests deposition by shallow flows, possibly due to flow expansion and reduced flow competence as discharge exits the channel. This deposition might occur under two distinct conditions: during the transition from subcritical to supercritical flow and during initial sand bed movement at low flow speeds.

In the debris flow deposits, Gi-Gh (gravelly inverse to gravelly horizontal stratification) layers indicate deposition by high-energy, poorly sorted debris flows. The conglomerates contain subangular to subrounded clasts, reflecting rapid sediment transport with minimal sorting. These debris flows suggest a high-energy environment, likely occurring in response to sudden high-discharge events in proximal fan areas.

The silty-clay deposits (Fm) likely represent low-energy suspension fallout in more distal fan environments, intergrading with sand deposits. The entire sequence displays a gradual transition between facies, where the coarser gravelly units (Gi-Gh) interfinger with the finer silty-clay layers, indicating fluctuating flow conditions across the fan.

This deposit intergrades with the silty-clay deposit, and together they are incised by conglomerates. The conglomerates represent high-energy channel incision, cutting through the underlying finer-grained deposits, which suggests episodic flooding or debris flow events in this part of the alluvial fan.
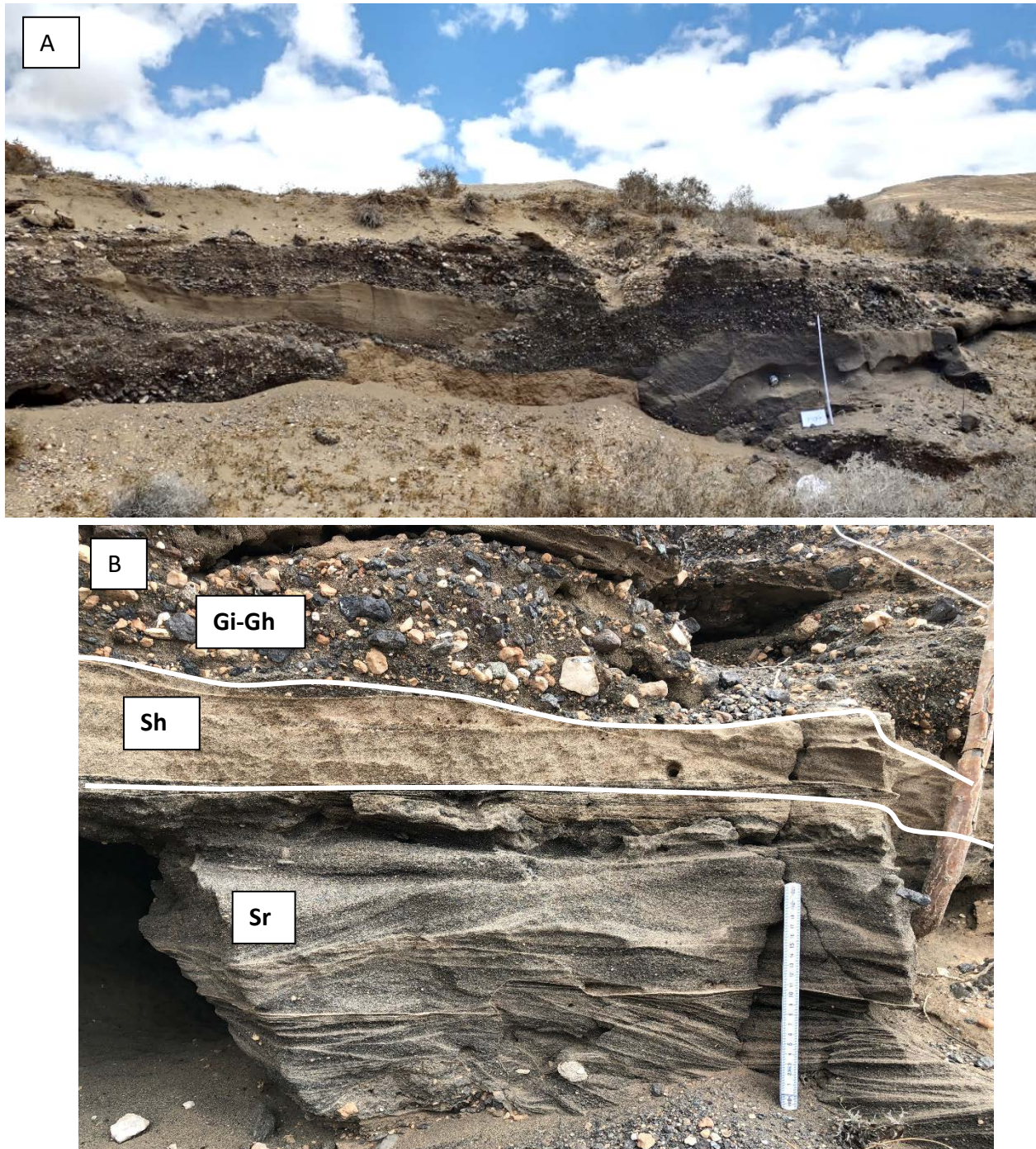
Figure 100. A. General view of the distal fan in Las Piletas showing a stratigraphic section with alternating lithologies. The upper gravel-rich conglomerate layer, indicative of a high-energy environment, overlies finer, sand-dominated units with horizontal bedding. Erosional surfaces and channel-fill features are present. B. Close-up of sedimentary structures: Gi-Gh (gravelly inverse to gravelly horizontal stratification) represents high-energy deposition by traction currents; Sh (horizontally laminated sandstone) reflects lower-energy, unidirectional currents; and Sr (ripple cross-laminated sandstone) suggests deposition in a lower-energy, waning flow environment.

168

The distal area marks the transition between the alluvial deposits and the aeolian system of the plain. The slackwater deposits serve as indicators of this shift, observed only in Barranco Las Piletas. These deposits are characterized by an alternation of three distinct facies: *Massive silt-clayey* (Fm), *Aeolian sand-sheet* (Ssa), and *Laminated sandstone* (Sh).

The Massive silt-clayey (Fm) facies exhibits laminated to massive red mudstone with both highly eroded bases and tops, indicating periods of erosion followed by deposition. These mudstones range in thickness from 2 cm to 30 cm and contain parallel bedding and mud cracks, suggesting cycles of flooding followed by desiccation in a low-energy environment. The presence of these features' points to episodic standing water in the distal fan, possibly in shallow floodplain ponds or slackwater zones that experienced intermittent drying. These characteristics reveal a fascinating record of ancient climatic shifts, where alternating wet and dry phases are preserved in the sedimentary record.

The Ssa and Sh facies exhibit thin parallel laminae of grey sand, with thicknesses ranging from 6 cm to 17 cm. The Ssa facies is interpreted as wind-blown laminae, formed in interdune ponds, interchannel areas, or along the lateral margin of dune fields (Trewin, 1993). This suggests that during drier periods, aeolian processes were dominant, depositing fine sand in low-energy settings where wind played a critical role in sediment transport.

In contrast, the Sh facies, representing flash flood deposits, is characterized by its laminated structure and the presence of floating carbonate pebbles and cobbles, distinguishing it from the aeolian deposits. These horizontally laminated sandstones were likely deposited during sudden high-energy flash floods, where rapidly moving water transported and deposited sediments in a short time. The Sh facies is indicative of rapid flow deceleration, where sediment was deposited as floodwaters lost energy upon entering slackwater zones or broadening channels. The transition from subcritical to supercritical flow or the initial movement of sand during low flow speeds could have contributed to the structure of these deposits. Flash floods in this context would carry not only sand but also larger clasts, resulting in the distinctive texture of Sh, where coarser particles are present among laminated fine sands.

These deposits likely accumulated in confined bedrock channels or in areas where flood velocities diminished significantly, such as near channel margins where reverse eddies formed or where the channel widened abruptly. The slackwater deposits preserve records of large flood events, with each flood leaving a new layer of sediment. If these layers are shielded from subsequent erosion, they

can provide a long-term archive of flood history, showing how water flow and sedimentation fluctuated over time.

Given the alternating deposition of silty and sandy facies, which are derived from both aeolian and fluvial processes, it is plausible that these slackwater deposits were situated between the floodplain margin and the dune system, possibly within interdune corridors (Kochel and Baker 1982; Saynor and Erskine, 1993; Trewin, 1993). The alternation of laminated layers suggests seasonal variations or climatic cycles, potentially recording shifts in topography, climate, and hydrological conditions over time. These cyclic deposits offer insights into the region's palaeoenvironment, indicating periodic flooding followed by intervals of wind deposition during arid phases, and thus provide a unique window into the interaction between fluvial and aeolian systems.
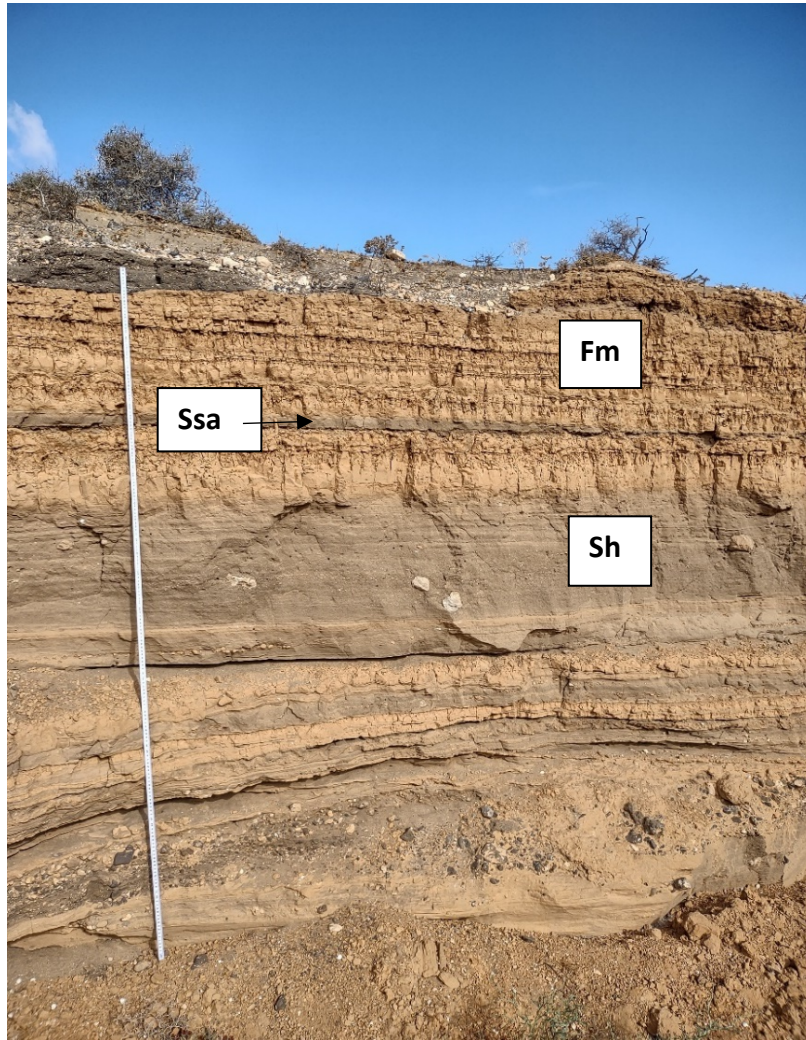
Figure 101. Stratigraphic section showing interbedded Aeolian, Flash Flood, and Floodplain Deposits. The section exhibits interbedded deposits of Aeolian Sand-Sheet (Ssa), Massive Silt-Clay (Fm), and Laminated Sandstone (Sh). The Ssa facies consists of fine, well-sorted aeolian sands, likely formed by wind-blown deposition during dry periods. The overlying Fm (Massive Silt-Clay) represents low-energy floodplain or slackwater deposits, characterized by laminated to massive red mudstones, indicative of deposition in stagnant water settings. The Sh facies (Laminated Sandstone) is interpreted as a product of flash flood events, where horizontally laminated sands were rapidly deposited during sudden, high-energy water flows. This section reflects alternating climatic conditions, with dry periods dominated by aeolian processes and wetter periods experiencing flash floods and floodplain deposition.

5.3.1.5 Aeolian System

The El Jable plain is part of an aeolian system dominated by active dunes and palaeodunes. The aeolian deposits are part of the *Aeolian dune field* (Sa), characterized by medium-fine to fine grain sizes, with thicknesses ranging from 0.5 m to 3 m. Grain composition varies between sectors: El Jable contains a higher concentration of bioclasts, while the Famara cliffs are dominated by volcanic-origin grains, predominantly basaltic (70%) and pyroclastic (10%), plus quartz and feldspar. This difference imparts a yellowish hue to El Jable's sediments, in contrast to the darker, greyish tones of Famara's volcanic-rich sediments (Fig. 102).

Cross-bedding observed in both El Jable and the Famara area indicates ancient wind-driven dune migration (Fig. 102 C-D). Along the Famara cliffs, these structures are linked to climbing dunes that migrated upslope, influenced by the steep topography. The cross-beds exhibit moderate to low angles, likely reflecting the topographic influence rather than wind regime alone (Fig. 102 C). In some areas, the cross-bedding forms sets with a fining-upward sequence, where coarser grains transition to finer ones, suggesting periods of active migration followed by stabilization, likely controlled by changes in wind strength or sand supply. The palaeodunes are particularly prominent in the southernmost barrancos, such as in Falls, and are also identified beneath talus deposits in the proximal parts of the cliffs, like Horca (Fig. 103).

In contrast, the dunes in El Jable display gentler slopes and show greater biological influence, evidenced by extensive bioturbation and root traces (Fig. 102 B-D). Similar bioturbation is also present in the palaeodunes near the Famara cliffs, indicating that both areas experienced periods of stabilization during wetter climatic phases (Fig. 102 A). The flatter topography in El Jable led to gentler dune slopes, while the steeper slopes near the cliffs facilitated the development of climbing dunes. Root casts and insect burrows in both regions suggest that vegetation periodically halted dune migration. In some sections, extensive bioturbation has significantly disturbed the dune strata, indicating prolonged periods of vegetation growth. These episodes of stabilization occurred in both areas but were shaped by the contrasting topographies of the Famara cliffs and the El Jable plain.

The presence of calcium carbonate crusts, around the root traces of palaeodunes (Fig. 102 D) in El Jable plain suggests that these features formed in arid conditions where groundwater evaporation led to calcium carbonate precipitation. These encrustations are typically found as hardened, cement-like layers that fill the voids left by the roots, most commonly found in the lower to middle sections

of the palaeodunes. They provide evidence of post-depositional processes and offer insights into the local groundwater chemistry and evaporation rates during the periods of dune stabilization.

Overall, the El Jable plain offers a prime example of an aeolian system characterized by alternating phases of dune migration and stabilization. The contrast between the bioclast-rich palaeodunes of El Jable and the volcanic-rich sediments of the Famara area underscores the significance of local sediment sources in controlling dune composition and morphology. The bioturbation and cross-bedding features provide valuable insights into palaeoenvironmental conditions, indicating alternating periods of aeolian activity and dune stabilization by vegetation.
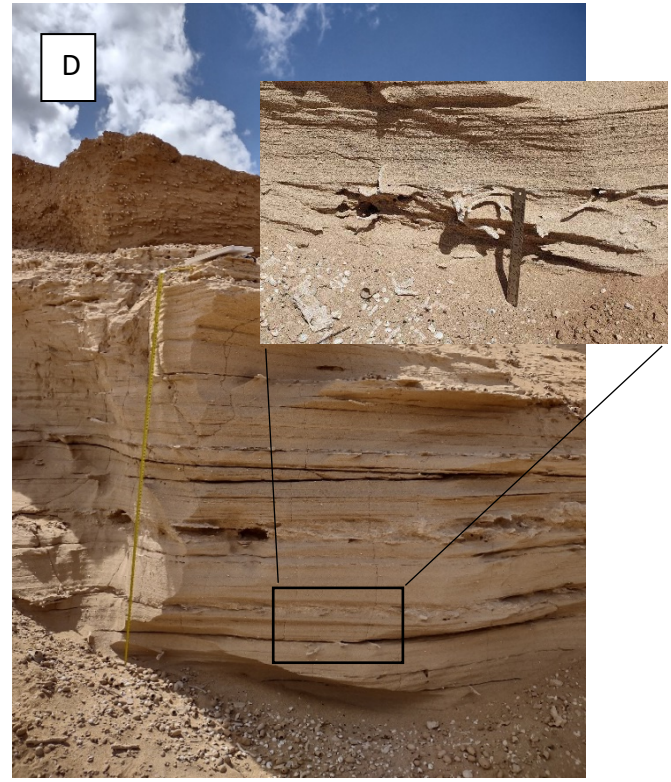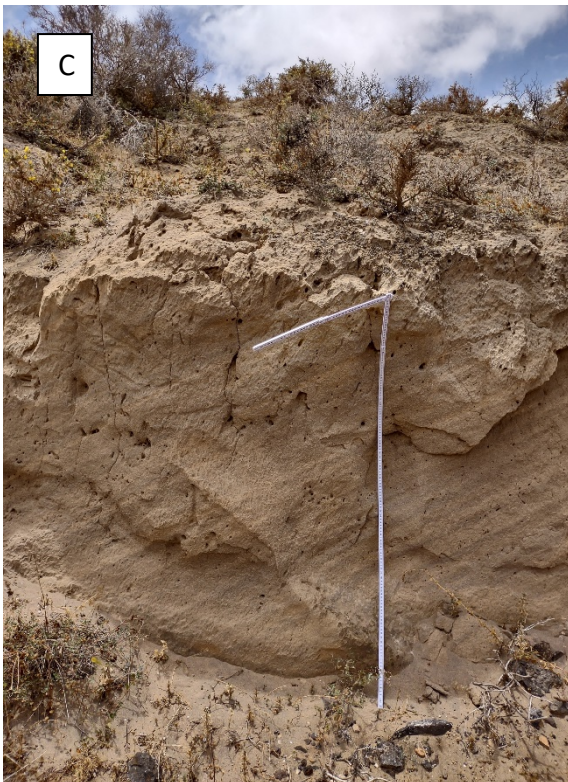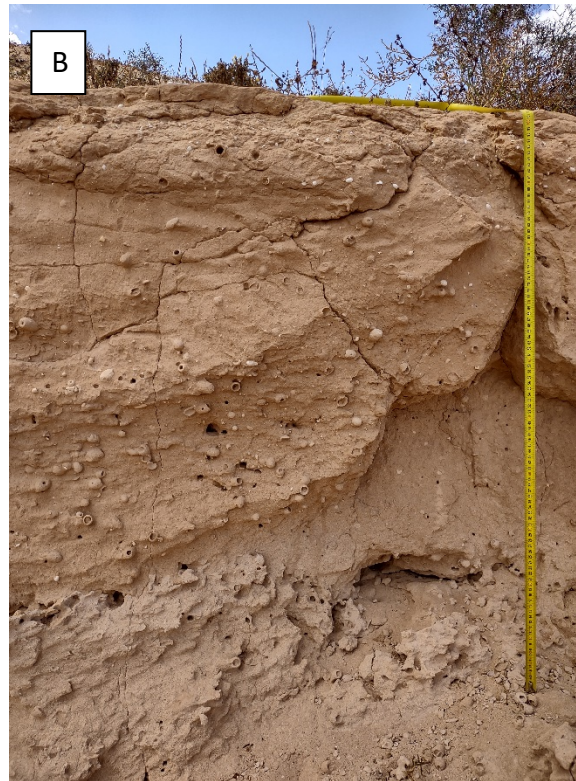
Figure 102. Palaeodunes of Famara (A-C) and El Jable (B-D) showing different structures. A: signs of bioturbation, with visible encrusted root traces. This indicates the stabilization of dune structures over time, likely from periods of vegetation growth in a semi-arid or arid climate. B: insect brood cells, which further support the interpretation of biological interactions within the dune systems. C: well-preserved tabular cross-bedding, characteristic of migrating dunes, likely formed under strong wind regimes. D: further examples of cross-bedding and fossilized root traces.
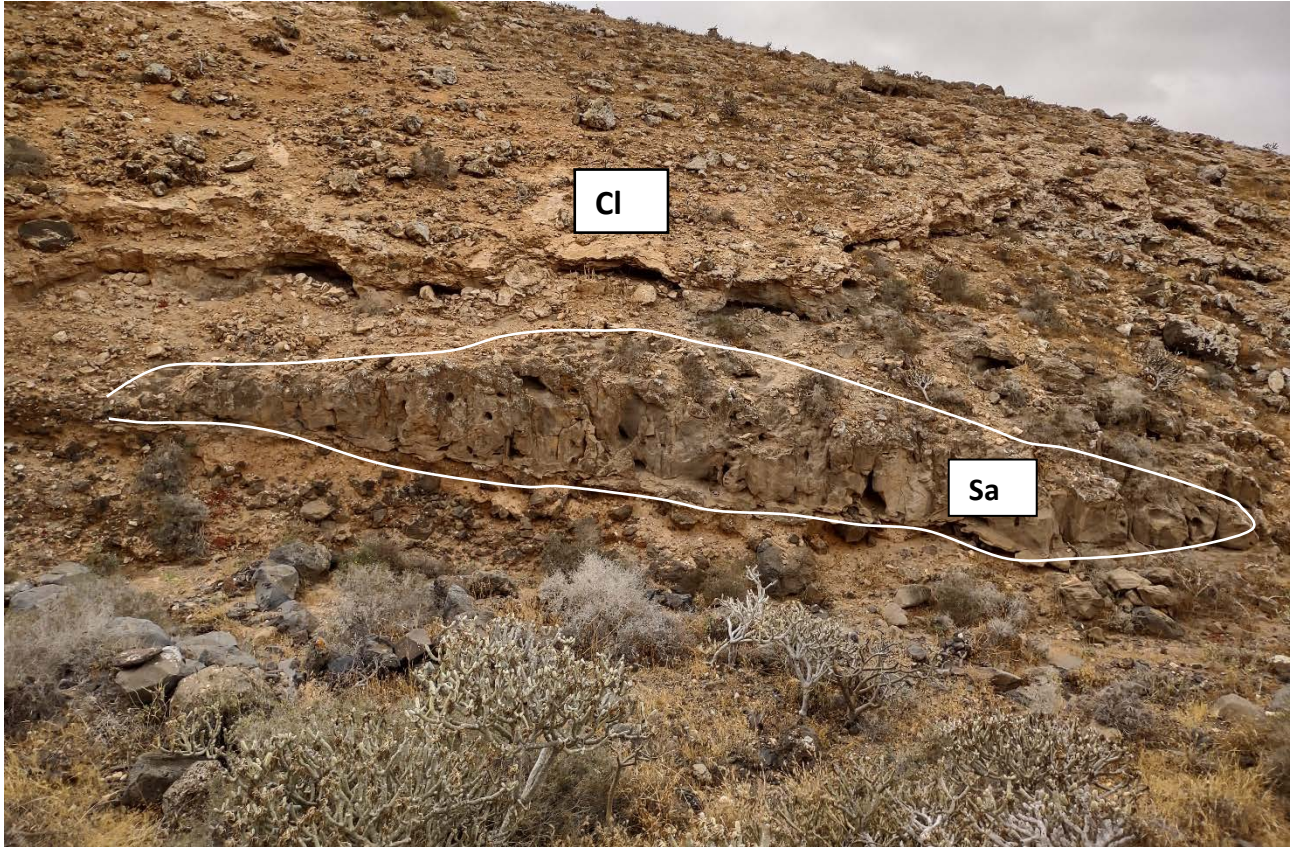
Figure 103. Proximal part of the cliff in Horca, revealing a climbing palaeodune underlying talus cone.

5.4 Luminescence results: phase two

The evolution of the El Jable plain has been analysed not only through a stratigraphic approach but also by employing the previously listed dating techniques: Infrared Stimulated Luminescence (IRSL) and radiocarbon (^{14}C). These dating methods contribute significantly to constrain the timing of the Famara alluvial fan systems development and their interaction with the aeolian system of El Jable.

Thirteen samples collected from Las Piletas were dated using Infrared Stimulated Luminescence method. Las Piletas barranco has better exposition and continuity of the outcrops. Therefore, it has been selected to date the complete alluvial fan succession. Thirty-four samples collected from Las Piletas, Falls, and El Jable were dated using AMS radiocarbon dating ^{14}C (Fig. 104).
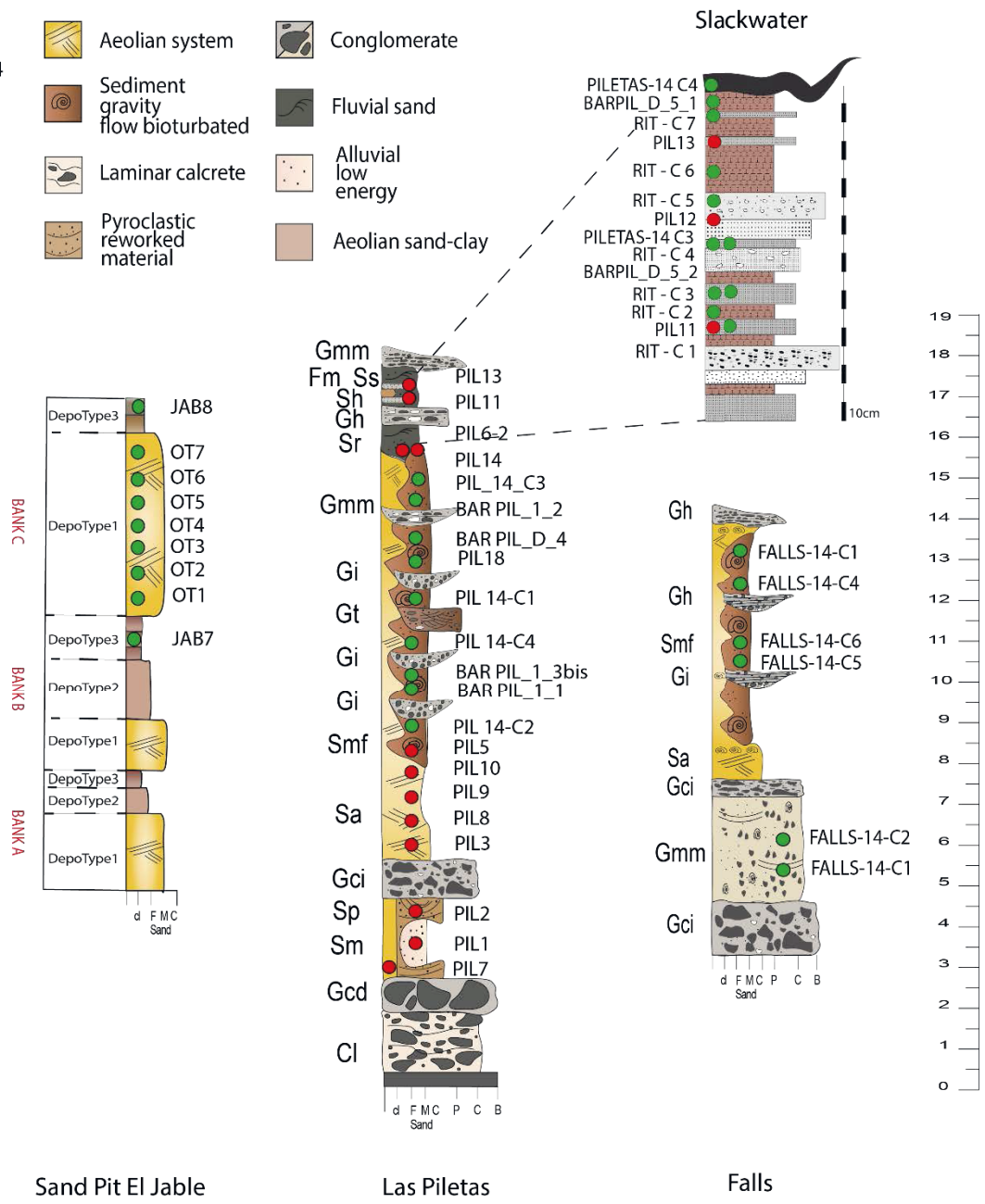
Figure 104. IRSL (Infrared Stimulated Luminescence) and radiocarbon dating samples were collected from two barrancos (Falls and Las Piletas) and a sand pit in El Jable. The stratigraphic profiles from these sites show various sedimentary units, including aeolian sands, alluvial deposits, and fluvial sand layers. In the zoomed-in section, the slackwater deposits are highlighted. Red circles indicate IRSL dating samples, while green circles represent radiocarbon dating samples, providing chronological control across the stratigraphic columns.

As mentioned in the previous Section, Infrared Stimulated Luminescence (IRSL) dating entails a series of meticulous steps, encompassing not only the measurement of Equivalent Dose (D_e) and Dose rate (D_R) but also the comprehensive quality assessments of the final measurements. These quality tests play a crucial role in ensuring the reliability and accuracy of the luminescence dating results.

In Table 1, all the analyses related to D_e conducted for each sample, both for signals IR_{50} and $pIRIR_{200}$ are summarized.

In the pIRIR protocol, two distinct D_e values were obtained, one associated with the IR_{50} signal and one with the $pIRIR_{200}$ signal. As illustrated in Table 7, the D_e values exhibit variability across each sample. The correlation between lower D_e values and IR_{50} could be explained by the possibility that this signal was not strong enough to fully eliminate the signal prone to fading (Li and Li, 2012).

The absolute difference between the D_e value of the IR_{50} signal and the D_e value of the $pIRIR_{200}$ signal is expressed in Fig. 105. Higher values suggest a greater dissimilarity in equivalent doses, while lower values indicate consistency. Sample PIL1 and PIL2 exhibit the highest difference, while the D_e values of both signals for PIL6-2, and PIL14 are similar.

Upon correlating the ages of the sample with the two signals, a pattern emerges: as we approach the younger samples (PIL 6-2, PIL14), the behaviour of the IR_{50} signal starts to resemble that of the $pIRIR_{200}$ signal, as the D_e values are similar. Specifically, the IR_{50} signal tends to bleach faster than the $pIRIR_{200}$ signal when exposed to sunlight. This consideration aligns with the prevailing trend, where the IR_{50} protocol is considered to be suitable primarily for young samples (<50 ka; Huntley and Lamothe, 2001).

This observed pattern can be attributed to a combination of factors, including bleaching rates, signal stability, sensitivity to environmental conditions, and inherent signal characteristics.

The examination of **overdispersion** in Equivalent Doses (D_e) (OD in Table 7) calculated across sample grains is related to the depositional histories within varied environments. Elevated overdispersion values, indicative of heightened variability in D_e, suggest a diverse assembly of grains with distinct radiation exposure histories. This correlation implies that grains within a specific environment, have
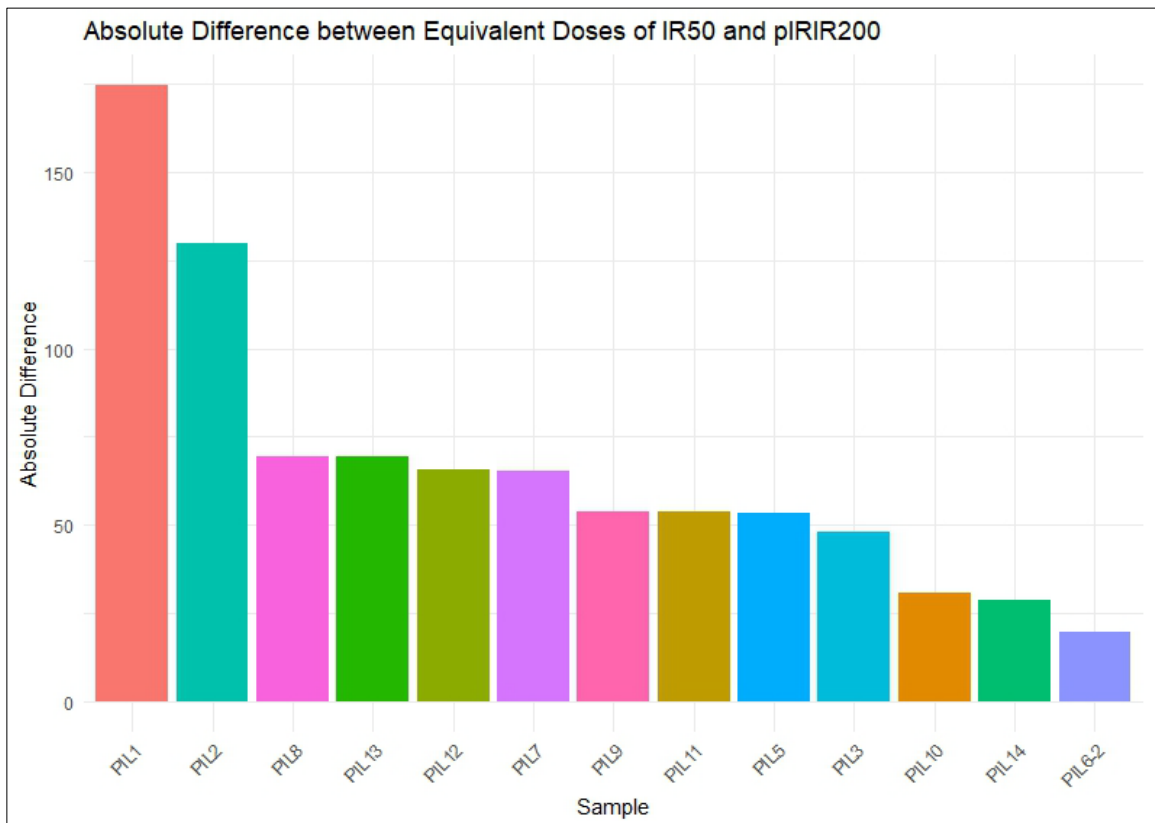
Figure 105. The absolute difference between the D_e of the IR_{50} signal and the D_e of the $pIRIR_{200}$ signal for each sample provides insights into the sensitivity of the signals. Sample PIL1 and PIL2 exhibit the highest difference, while the De values of both signals for PIL6-2, PIL14, and PIL19 are similar.

undergone dissimilar transportation mechanisms, or different depositional pathways, potentially originating from diverse geological or environmental sources (Duller et al., 2000; Thomsen et al., 2005). An illustrative case is the outlier PIL3, whose elevated value may correspond to a deposit comprising grains of aeolian origin coming from El Jable and grains derived from the erosion of the Famara cliff.

In the broader context of overdispersion values across different environmental conditions (Aeolian, Colluvial, Alluvial, Slackwater), the dataset reveals noteworthy variations. The comparison between overdispersion values derived from the IR_{50} and $pIRIR_{200}$ signals offers intriguing insights into the variability of equivalent doses within distinct environments (Fig. 106). In the Alluvial environment, as represented by samples PIL6-2, PIL14, PIL5, and PIL1, both signals generally exhibit moderate overdispersion values, implying a comparable stability. However, sample PIL14 stands out with a higher overdispersion value in the $pIRIR_{200}$ signal (32.8%), suggesting a unique context that may not be as pronounced in the IR_{50} signal. Moving to the Slackwater deposits (PIL11, PIL13, PIL12), both signals reveal variations in overdispersion values, probably influenced by a diversity of grain history and low bleaching degree. Analogously, the Aeolian environment, represented by samples PIL10,

PIL9, PIL3, PIL8, and PIL7, displays a wide spectrum of overdispersion values in both signals. The outlier PIL3, with a substantially high overdispersion value of 34% in the IR_{50} signal, presents a parallel anomaly in the $pIRIR_{200}$ signal, emphasizing a potentially distinctive depositional history involving grains from diverse geological sources.

Conversely, the Colluvial sample (PIL2) exhibits lower overdispersion values in both the IR_{50} and $pIRIR_{200}$ signals, indicative of a more constrained sample distribution within this specific environmental context.
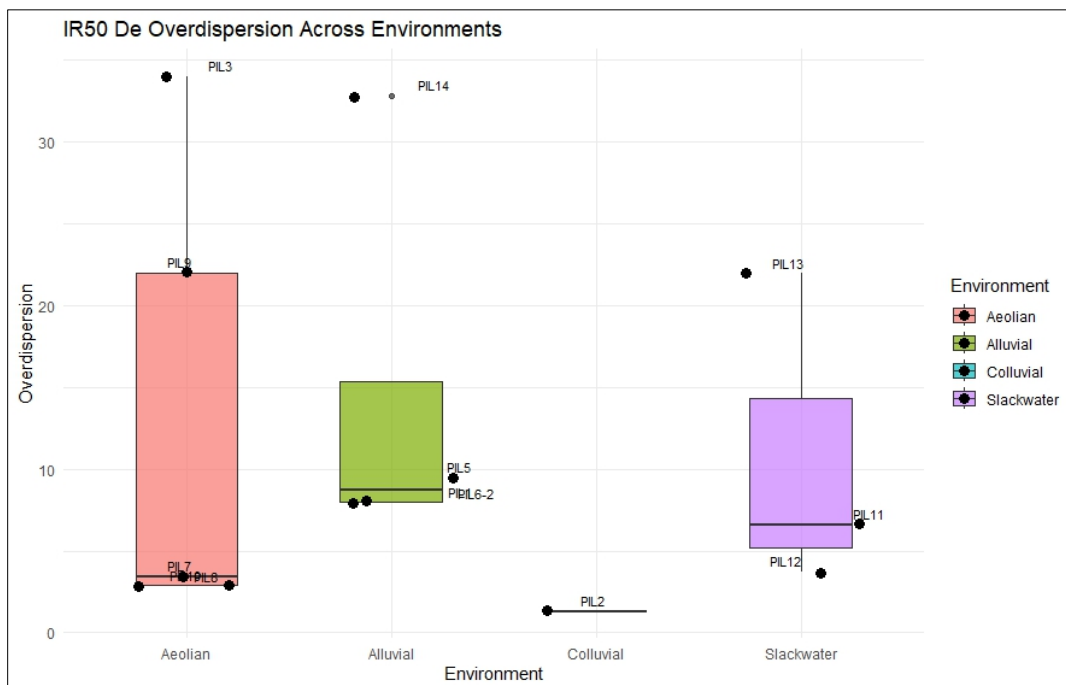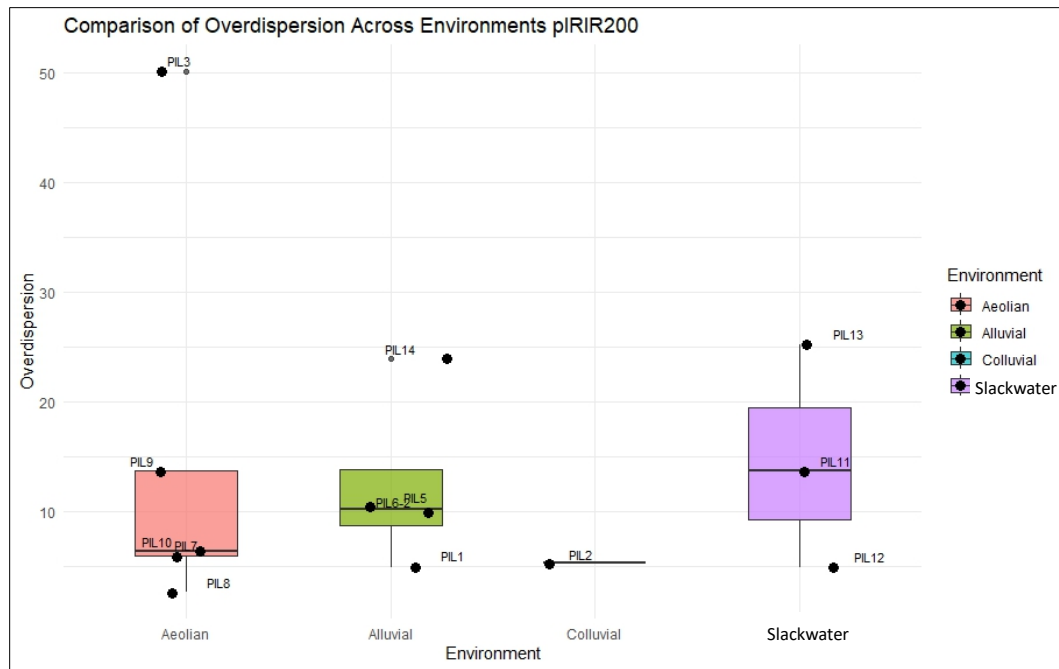
Figure 106. Comparison of overdispersion De values obtained with $pIRIR_{200}$ (above), and IR_{50} (below), categorized by different environments.

Table 7. Luminescence measurements on each sample both with pIRIR$_{200}$ and IR$_{50}$. Al= aliquots, De= equivalent dose, OD= overdispersion of De values, RR1= regenerative ratio, Recup= recuperation, DRR= dose recovery ratio, RD= residual dose, g-Value= fading value, Dr= Total Dose rate, Age ka (corr)= age corrected for fading.

SAMPLE	Signal	Al	De (Gy)	OD (σ)	RR1	Recup	DRR	RD (Gy)	g_value (%/decade)	Dr (G/ka)	Age (ka)	Age ka (corr)
PIL6-2	pIRIR$_{200}$	21	67.8 ± 1.49	10	1.01	0.09	0.98 ± 0.24	2.67 ± 0.08	1.7 ± 0.2	3.00 ± 0.03	21.7 ± 1.6	23.7 ± 1.7
	IR$_{50 (200)}$	21	48.3 ± 0.89	7.9	1.00	0.39	0.94 ± 0.37	-	3.5 ± 0.45		15.7 ±1.4	19.1 ± 1.6
PIL14	pIRIR$_{200}$	20	48.6 ± 2.6	24	0.93	-4.93	0.95 ± 0.02	4.1 ± 2.04	2.7 ± 2	2.07 ± 0.04	21.5 ± 3.7	25 ± 6
	IR$_{50}$ ($_{200}$)	18	20 ± 1.3	32.8	0.9	-1.06	0.99 ± 0.01	-	5.6 ± 0.9		9.7 ± 1.5	13.6 ± 2.7
PIL5	pIRIR$_{200}$	20	165.9 ± 4.52	10.5	0.99	0.64	1.01 ± 0.01	8.23 ± 0.84	1.5 ± 1.35	3.67 ± 0.02	43.0 ± 2.5	46.8 ± 4.7
	IR$_{50 (200)}$	20	112.4 ± 2.78	9.5	0.99	0.46	1.02 ± 0.0	0.37 ± 0.05	2.5 ± 0.62		30.6 ± 1.81	35.3 ± 2.45
PIL11	pIRIR$_{200}$	20	87.5 ± 2.39	13.7	0.62	0.6	0.93 ± 0.01	2.6 ± 0.10	1.7 ± 0.8	1.79 ± 0.05	47.5 ± 3.7	52.4 ± 4.2
	IR$_{50 (200)}$	20	33.8 ± 0.55	6.6	0.61	0.29	0.95 ± 0.01	0.25 ± 0.04	4.2 ± 0.75		18.4 ± 1.7	23.6 ± 2.5
PIL10	pIRIR$_{200}$	20	94.1 ± 1.5	6.4	1.05	0.02	0.94 ± 0.01	1.13 ± 0.11	1.5 ± 0.04	1.52 ± 0.06	61.2± 4.9	66.9 ± 5.3
	IR$_{50 (200)}$	20	63.2 ± 0.56	2.9	1.03	0.01	1.04 ± 0.07	0.12 ± 0.02	3.3 ± 0.45		40.8 ± 2.6	49.9 ± 3.3
PIL13	pIRIR$_{200}$	21	107.8 ± 7.12	25.2	1	0.38	0.93 ± 0.01	6.4 ± 0.67	2.7 ± 1.28	1.69 ± 0.05	60.0 ± 3.7	72.9 ± 9
	IR$_{50 (200)}$	21	38.5 ± 1.75	22	1	-0.6	0.96 ± 0.0	0.22 ± 0.11	3.08 ± 0.82		22.3 ± 2.1	26.6 ± 3
PIL12	pIRIR$_{200}$	20	104.1 ± 5.61	4.9	1.03	1.01	0.96 ± 0.02	3.37 ± 0.48	2.5 ± 1.22	1.62 ± 0.06	62.3 ± 6	74.7 ± 10.7
	IR$_{50 (200)}$	20	38.41 ± 0.8	3.7	1.01	0.67	0.93 ± 0.01	-	3.4 ± 0.6		25 ± 2.3	31 .7 ± 3.4
PIL9	pIRIR$_{200}$	24	91.1 ± 3.18	13.7	1.0	-2.5	1.1 ± 0.05	-	4.3 ± 0.12	1.65 ± 0.06	55.2 ± 4.7	77.6 ± 7.3
	IR$_{50 (200)}$	24	37.2 ± 2.05	22	1.0	-3.1	0.99 ± 0.01	-	4.2 ± 0.09		22.1 ± 2.4	28.6 ± 3.1
PIL3	pIRIR$_{200}$	29	90.5 ± 8.69	50.1	1.03	-13.96	1.26 ± 0.03	-	3.5 ± 0.26	1.26 ± 0.08	72 ± 9.6	91 ± 13.7
	IR$_{50 (200)}$	29	42.3 ± 2.79	34	1.05	-37.67	1.04 ± 0.02	-	5.6 ± 1.81		33.6 ± 4	49.7 ± 9.8
PIL8	pIRIR$_{200}$	20	211.6 ± 2.19	2.7	1.01	0.21	1.05 ± 0.02	4.65 ± 0.18	2.2 ± 0.7	2.53 ± 0.03	81.7 ± 4.4	93.6 ± 6.8
	IR$_{50 (200)}$	20	142.2 ± 1.60	2.8	1.01	-0.14	1.09 ± 0.02	0.42 ± 0.07	3.4 ± 0.58		56 ± 3.2	69.5 ± 4.7
PIL2	pIRIR$_{200}$	20	315.6 ± 3.3	5.3	1	0.92	1.01 ± 0.01	7.54 ± 0.29	1.8 ± 0.74	2.88 ± 0.03	106.8 ± 5.8	119.3 ± 9.1
	IR$_{50 (200)}$	20	185.6 ± 2	1.3	1.01	0.73	1.00 ± 0.01	0.16 ± 0.04	3.1 ± 0.48		64.3 ± 3.6	78.3 ± 5.7
PIL1	pIRIR$_{200}$	20	440.6 ± 3.2	8	1.00	0.51	1.01 ± 0.20	8.81 ± 0.16	2.6 ± 0.4	4.22 ± 0.02	102.3 ± 4.5	120.9 ± 6.8
	IR$_{50 (200)}$	20	266.1 ± 2.83	8	0.99	0.17	1.01 ± 0.20	0.45 ± 0.03	3.4 ± 0.56		62.9 ± 2.9	78.3 ± 5.6
PIL7	pIRIR$_{200}$	20	180.7 ± 4.28	6	1.02	0.17	0.99 ± 0.20	6.23 ± 0.64	-	1.32 ± 0.07	132 ± 12.3	132 ± 10.8
	IR$_{50 (200)}$	20	115.5 ± 2.5	3.4	1.01	0.12	1.03 ± 0.20	0.8 ± 0.06	2.8 ± 0.55		86.8 ± 8	103.8 ± 11.2

Table 8. Summary of dosimetry: Depth= elevation of samples collected, WC= water content, U= uranium, Th= Thorium, K= Potassium, α-Dr= alfa dose rate, β-Dr= beta dose rate, γ-Dr= gamma dose rate, Dr= total dose rate, De= equivalent dose, Age ka (corr) = age corrected for fading. The grain size for all samples is 4-11 μm.

Sample	Depth (cm)	WC (%)	U (ppm)	Th (ppm)	K (%)	α-Dr (Gy/ka)	β-Dr (Gy/ka)	γ-Dr (Gy/ka)	Dr (Gy/ka)
PIL13	80	14.6 ± 4.0	1.3 ± 0.10	3.8 ± 0.10	1.0 ± 0.01	0.28 ± 0.08	0.76 ± 0.02	0.50 ± 0.01	1.69 ± 0.05
PIL14	100	19.6 ± 4.0	1.5 ± 0.10	5.4 ± 0.10	1.3 ± 0.01	0.35 ± 0.08	0.96 ± 0.02	0.66 ± 0.02	2.07 ± 0.04
PIL11	180	8.0 ± 4.0	1.3 ± 0.10	4.0 ± 0.10	1.0 ± 0.01	0.30 ± 0.08	0.82 ± 0.02	0.51 ± 0.01	1.79 ± 0.05
PIL6-2	100	12.5 ± 4.0	1.5 ± 0.10	7.6 ± 0.10	2.1 ± 0.01	0.43 ± 0.08	1.53 ± 0.02	0.93 ± 0.02	3.00 ± 0.03
PIL12	100	14.7 ± 4.0	1.3 ± 0.10	3.8 ± 0.10	0.9 ± 0.01	0.28 ± 0.08	0.70 ± 0.02	0.48 ± 0.01	1.62 ± 0.06
PIL5	100	12.5 ± 4.0	1.8 ± 0.10	9.4 ± 0.10	2.9 ± 0.01	0.51 ± 0.08	1.97 ± 0.02	1.22 ± 0.02	3.67 ± 0.02
PIL10	200	5.1 ± 4.0	1.1 ± 0.10	3.3 ± 0.10	0.8 ± 0.01	0.25 ± 0.09	0.68 ± 0.02	0.41 ± 0.01	1.52 ± 0.06
PIL9	30	5.5 ± 4.0	1.2 ± 0.10	3.9 ± 0.10	0.8 ± 0.01	0.28 ± 0.08	0.70 ± 0.02	0.45 ± 0.01	1.65 ± 0.06
PIL3	100	18.8 ± 4.0	1.1 ± 0.10	3.0 ± 0.10	0.6 ± 0.01	0.23 ± 0.09	0.50 ± 0.02	0.37 ± 0.01	1.26 ± 0.08
PIL8	100	12.9 ± 4.0	1.6 ± 0.10	5.8 ± 0.10	1.7 ± 0.01	0.39 ± 0.08	1.26 ± 0.02	0.77 ± 0.02	2.53 ± 0.03
PIL2	80	13.7 ± 4.0	1.6 ± 0.10	8.7 ± 0.10	1.8 ± 0.01	0.48 ± 0.08	1.37 ± 0.02	0.93 ± 0.02	2.88 ± 0.03
PIL1	220	15.2 ± 4.0	2.2 ± 0.10	11.6 ± 0.10	3.1 ± 0.01	0.64 ± 0.08	2.20 ± 0.02	1.39 ± 0.02	4.22 ± 0.02
PIL7	300	18.0 ± 4.0	1.4 ± 0.10	2.9 ± 0.10	0.7 ± 0.01	0.26 ± 0.08	0.55 ± 0.02	0.40 ± 0.01	1.32 ± 0.07

Recycling Ratio (**RR1**) is a crucial parameter in the analysis of luminescence signals. Calculated as the ratio of luminescence measured during the first regenerative stimulation to the initial test stimulation, RR1 ideally approaches 1, indicating efficient regeneration and electron trapping during the luminescence process (Murray and Wintle 2000). This parameter is instrumental in assessing the sensitivity of luminescent signals to initial stimulation and regeneration, thereby ensuring accuracy in luminescence dating.

A thorough examination of RR1 values for IR_{50} and $pIRIR_{200}$ signals across diverse samples reveals significative trends (Fig. 107). Both signals consistently demonstrate good RR1 values, signifying similar responses to stimulation and regeneration processes. However, specific samples, PIL11 and PIL14 fall below the threshold, prompting further investigation. RR1 differences between IR_{50} and $pIRIR_{200}$ signals can be attributed to various factors such as the sensitivity to different light wavelengths, unique signal-specific properties, variations in trapping and release mechanisms, sample-specific characteristics (mineral composition and depositional history), environmental influences, and instrumental.
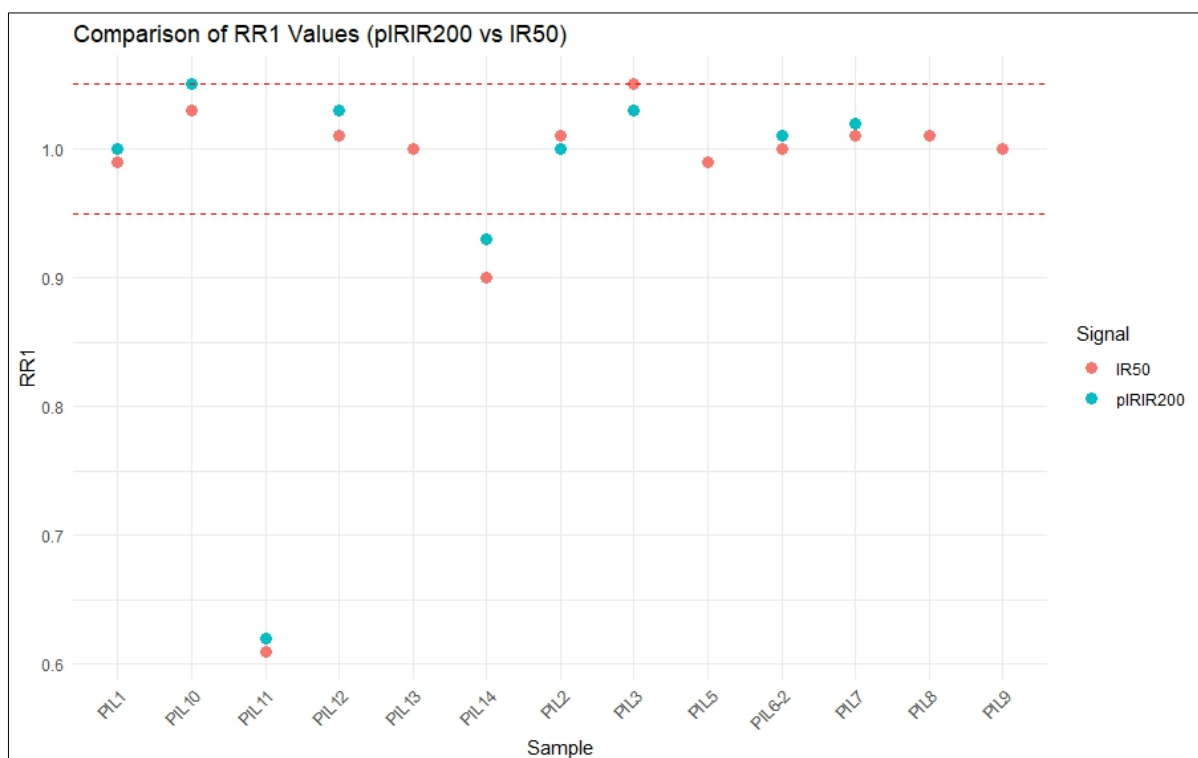
Figure 107. A comparison of the recycling ratio for the IR_{50} and $pIRIR_{200}$ signals reveals that samples PIL11 and PIL14 exhibit values outside the acceptable range. PIL13, PIL5, PIL8, and PIL9 show the same value for both signals.

Recuperation refers to the recovery of a luminescence signal after exposure to light or heat, that is, the response to a zero-Gy laboratory dose measured after the SAR cycle containing the largest regenerative dose (Murray and Wintle 2000). In luminescence dating, certain materials may experience a decrease in luminescence signal during the first stimulation (known as bleaching) but show an increase in signal upon subsequent stimulations. Recuperation is observed when the luminescence signal recovers or recuperates after initial bleaching. Understanding recuperation is crucial for accurate dating, especially in samples where the luminescence signal may vary with repeated stimulation. In many luminescence dating studies, a low level of recuperation is often preferred since it indicates that the luminescence signal is effectively bleached or reset by natural environmental processes, enhancing the accuracy of the age determination. The comparison of recuperation values between IR_{50} and $pIRIR_{200}$ signals shows distinct responses across the samples (Fig. 108). Generally, the value ranges between 1 and -5. Only PIL3 exhibits a unique behaviour with the highest overdispersion value, suggesting a potential link to transportation and mixing processes which might have influenced the sample luminescence history, leading to diverse contributions from different grains within the sample.
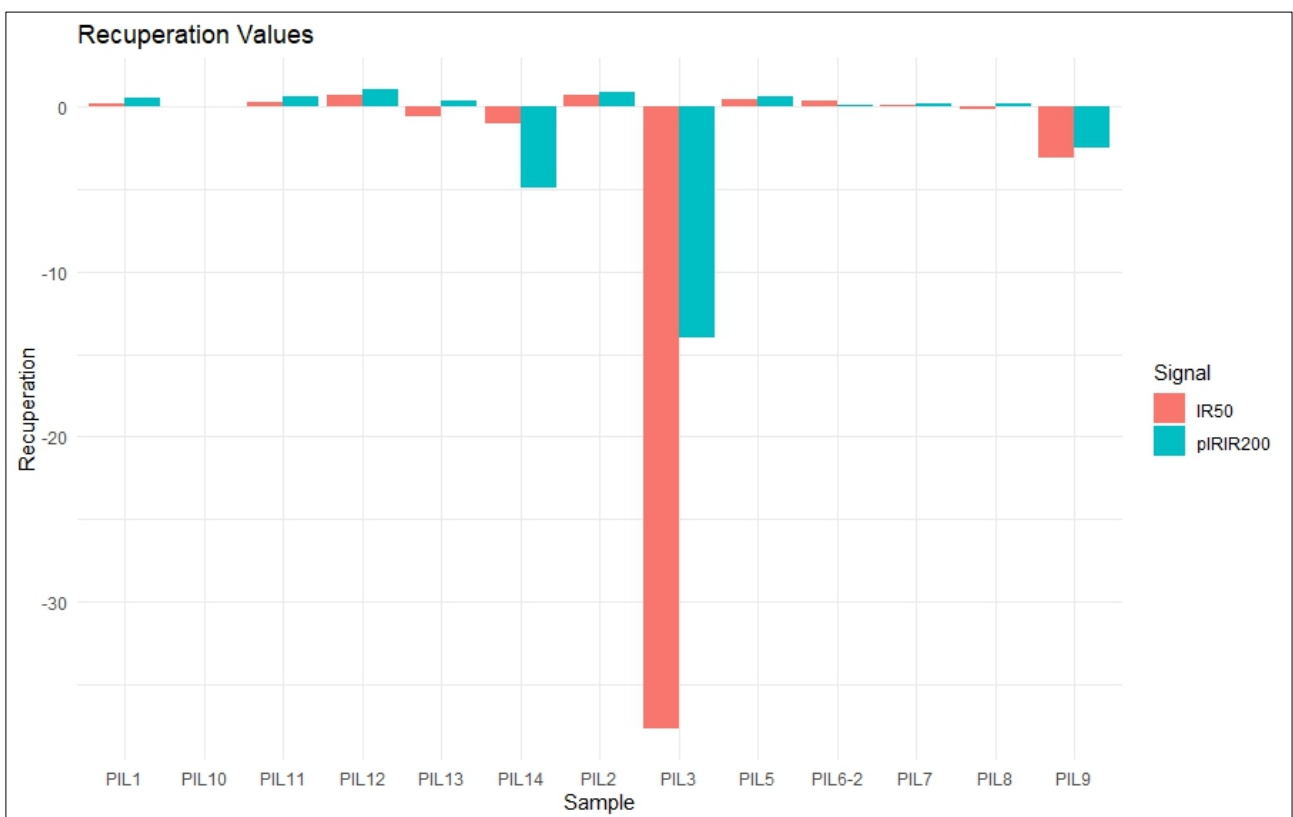
Figure 108. Comparison of Recuperation values between samples and signals.

The **dose recovery tests** (or dose recovery ratio **DDR**) asses the validity of D_e estimation (Murray and Wintle, 2003). A desirable value, approaching 100% (which is equivalent to 1 when expressed as a decimal), signifies optimal performance, indicating that the measured luminescence signal faithfully reflects the regenerative dose applied to the sample. The tolerance range is 10%. Firstly, the natural OSL signal is eliminated from five aliquots per sample by exposing them to sunlight for ten days. Then, the aliquot received a known beta dose before any measurements, assuming this given dose represented an unknown natural dose. The D_e was then determined using the SAR methods. A detailed comparative analysis of IR_{50} and $pIRIR_{200}$ signals (Fig. 109) showed generally consistent behaviour across the two signals, where DDR shows similar (or identical) values per sample. However, variations appeared particularly in PIL3, where both signals did not fall within the ±10% range and PIL9 is at the limit.
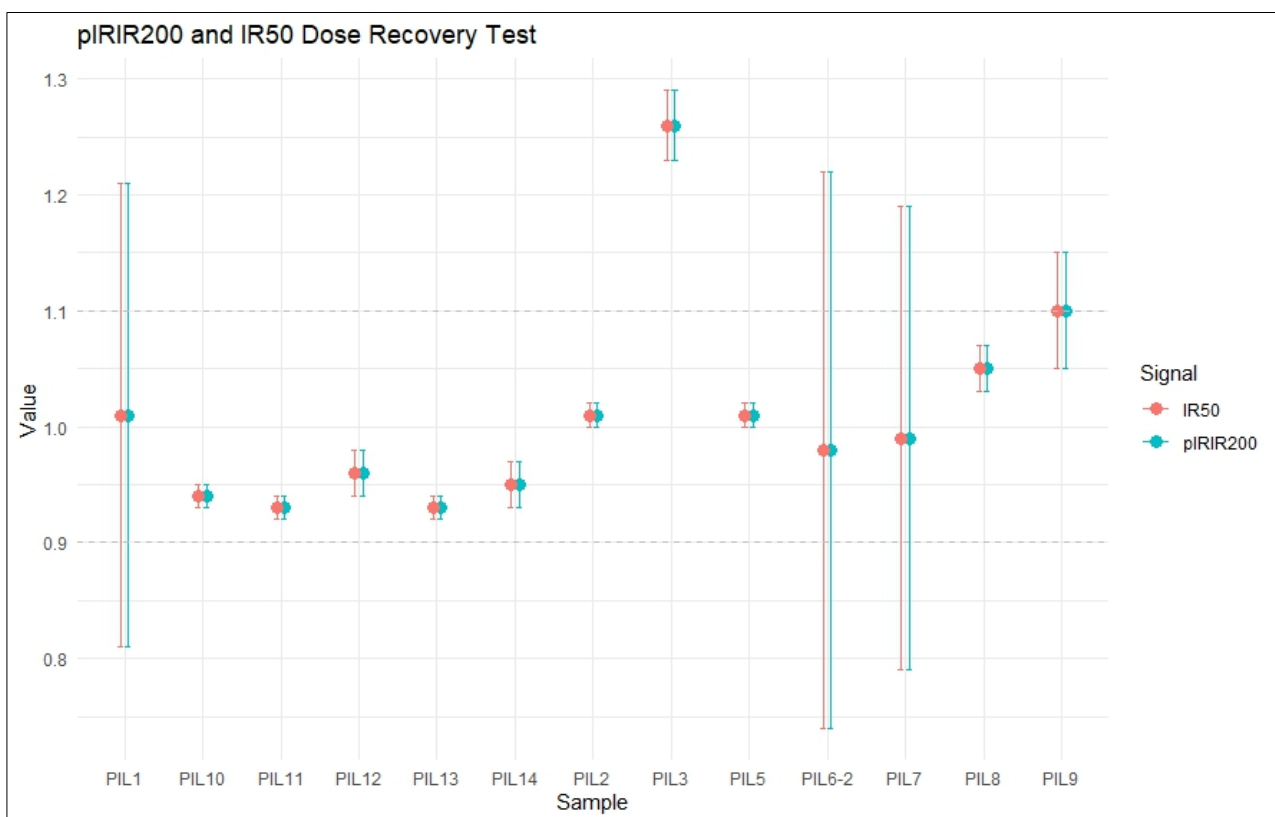
Figure 109. Dose recovery tests across the samples, comparing the IR_{50} and $pIRIR_{200}$ luminescence signals. Each data point represents a specific sample. The dashed lines represent the ±10% range. PIL3 exceeds the maximum allowable limit, PIL9 is at the limit.

The anomalous fading may lead to an unwanted loss of the IRSL signal (Spooner, 1994) and thus the IRSL age is underestimated. The laboratory fading rate, indicated by the percentage decrease in signal intensity per decade (known as the **g-value**; Aitken, 1985), was assessed using artificially irradiated aliquots. Fading measurements were carried out on five aliquots from each sample using the same SAR protocol used for D_e determinations. The g values were normalized to a tc = 2 days (Huntley and Lamothe, 2001; Auclair et al., 2003). The initial ~2 s of the luminescence signal, less a background derived from the last ~10 s, was used for all calculations. Results are outlined in Table 7 and Figure 110. In general, a consistent pattern is observed across all samples, with lower g-values for the $pIRIR_{200}$ signal and higher g-values for the IR_{50} signal. This corresponds with the overall trend where the fading rate tends to decrease with higher stimulation temperature. This phenomenon can be attributed to the varying stability levels of feldspar: during laboratory IR stimulation, there is a shift from the ground state to the excited state of the electron trap. This transition facilitates the rapid recombination of electron-hole pairs on a laboratory timescale, depleting the system of pairs that would have naturally taken thousands of years to recombine during burial. Subsequent IR stimulation at elevated temperatures then excites any remaining electrons into high-energy states, enabling them to access distant hole traps and generate a luminescent signal (Auclair et al., 2003; Thomsen et al. 2008; Jain and Ankjærgaard, 2011). The spread in g-values across different samples can be attributed to a multitude of influencing factors. Sensitivity to ionizing radiation, unique signal characteristics, dosimeter properties, variations in environmental conditions during deposition and burial, measurement nuances, and sample homogeneity collectively contribute to the nuanced g-value landscape.
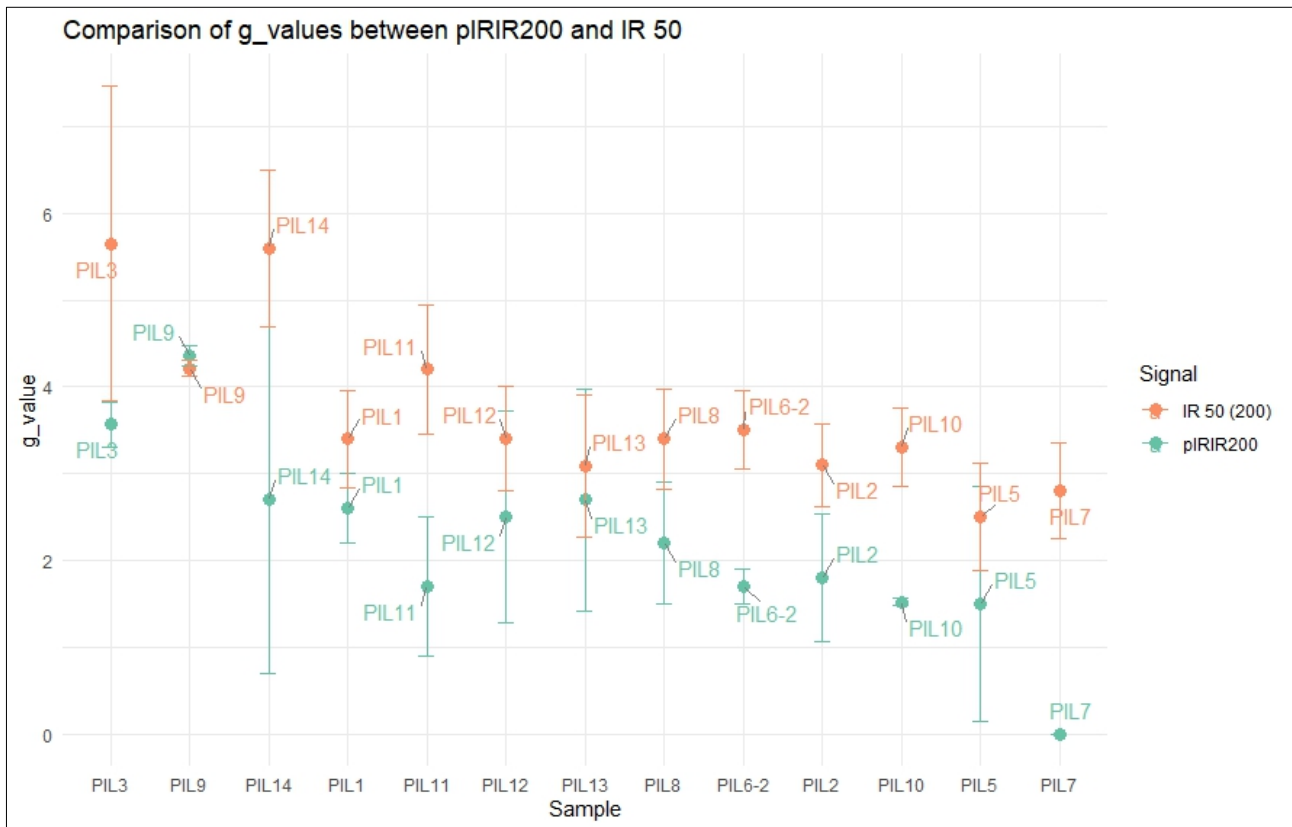
Figure 110. Variations in g-values across different samples and luminescence signals. The consistent pattern reveals lower g-values for the pIRIR$_{200}$ signal and higher g-values for the IR$_{50}$ signal, highlighting systematic differences in luminescence response among the studied samples.

To estimate the incomplete zeroing of the luminescence signal or **residual dose** (**RD**), five aliquots per sample were bleached under sunlight for 10 days and then D$_e$ values were calculated with the same SAR protocol. The residuals (Table 7) follow the main trend where the pIRIR signal is much more difficult to bleach than the IR$_{50}$ signal (Buylaert et al., 2012; Sohbati et al., 2012) and therefore, higher residual dose values are measured for the pIRIR$_{200}$. In general, there is a significant variation in remnant doses for both alluvial and aeolian environments, as well as slackwater deposits, and it is not possible to make a precise distinction between these environments. However, it appears that

the samples are well-bleached, with relatively minor residual doses (<10 Gy) (Tab. 3). For final age calculation, the residual is subtracted from each D_e value.

Table 8 illustrates the measured environmental radiation for each sample. The comprehensive **Dose Rate** analysis of environmental dosage data has unveiled intriguing patterns, particularly when samples are grouped based on their values and corresponding environments (Fig. 111). Samples originating from colluvial, and alluvial settings tend to exhibit a trend toward higher values. In contrast, those from aeolian and pond environments showcase lower values. This distinction suggests a reflection of the diverse geological and environmental influences to which the samples have been subjected over time such as water movement and sedimentation patterns.
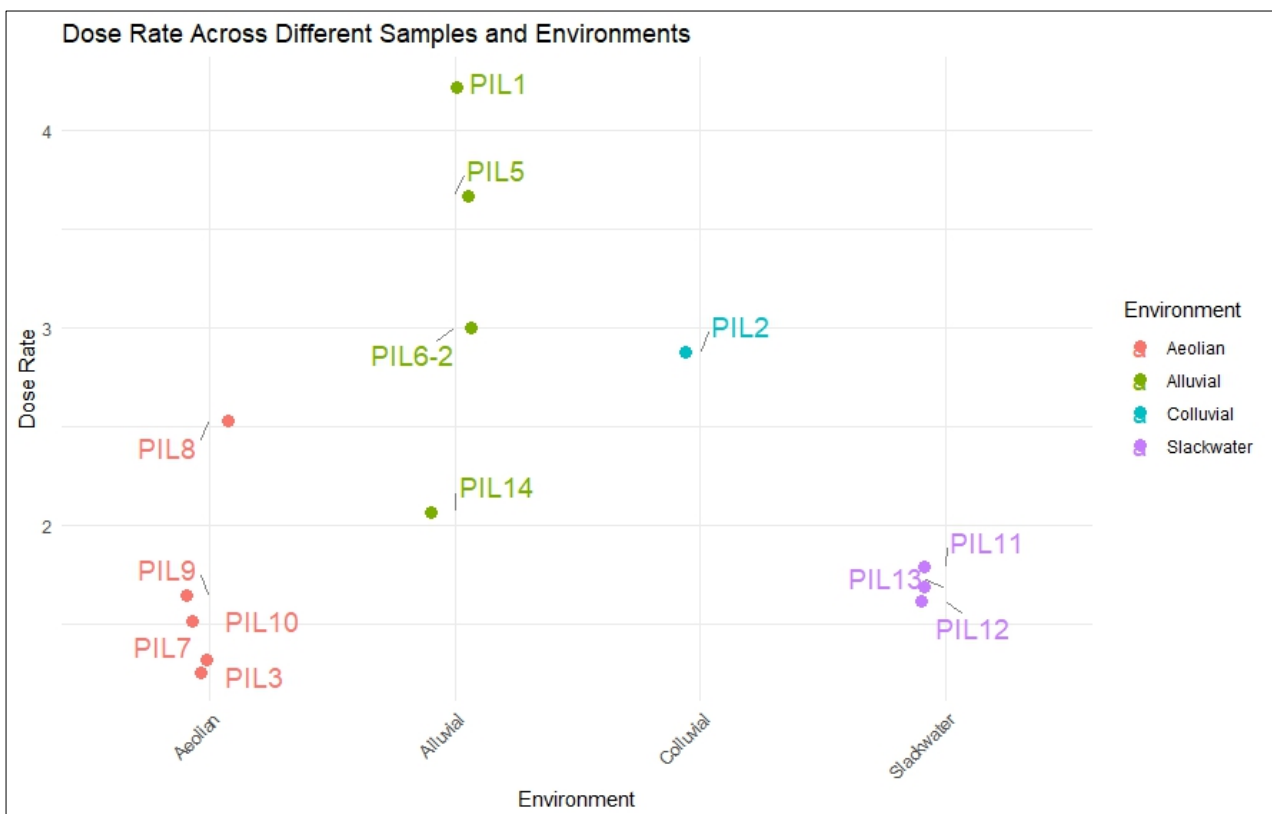
Figure 111. The dose rate values for samples grouped by distinct environmental conditions. The observed trends reveal contrasting patterns, with colluvial (light blue) and alluvial (green) environments exhibiting higher values, suggesting uniform deposition dynamics. In contrast, aeolian (orange) and Slackwater (purple) environments display lower values.

Finally, once all measurements were completed, the age was calculated by dividing the D_e by the D_R, and corrected for fading,

However, a crucial decision had to be made regarding which ages to use, whether those of pIRIR$_{200}$ signal or those of IR$_{50}$ signal.

To determine the most suitable, a thoroughly assessment of the consistency of the results has provided, considering factors such as reproducibility and RR1 (recuperation ratio) for each sample. Additionally, the fading characteristics has been examined associated with each protocol. It is a common practice to prefer a protocol with minimal fading, as it indicates more reliable and stable results over time (Huntley & Lamothe, 2001; Thomsen et al., 2008). Given our evaluation, we observed that PIL7 consistently exhibited lower fading and provided more robust results. Therefore, we opted for pIRIR$_{200}$ as the selected protocol for dating, prioritizing its reliability and potential for a more accurate chronological assessment.

The measured ages are listed in the next Table 9.

Table 9. Ages of samples calculated with signal of pIRIR$_{200}$. Ages are expressed in ka.

Sample	Age ka	Age ka (corr)
PIL6-2	21.7 ± 1.6	23.7 ± 1.7
PIL14	21.5 ± 3.7	25 ± 6
PIL5	43.02 ± 2.50	46.8 ± 4.7
PIL11	47.5 ± 3.7	52.4 ± 4.2
PIL10	61.15 ± 4.90	66.9 ± 5.3
PIL13	60.0 ± 3.7	72.9 ± 9
PIL12	62.3 ± 6	74.7 ± 10.7
PIL9	55.21 ± 4.68	77.6 ± 7.3
PIL3	71.96 ± 9.62	91 ± 13.7
PIL8	81.67 ± 4.44	93.6 ± 6.8
PIL2	106.81 ± 5.81	119.3 ± 9.1
PIL1	102.31 ± 4.46	120.9 ± 6.8
PIL7	131.96 ± 12.27	132 ± 10.8

5.5 AMS Radiocarbon dating

The table 10 provides an overview of radiocarbon ages obtained with ^{14}C.

The earliest ages from Las Piletas are 3727 - 3575 cal BP, likely signify the culmination of distal fan formation, shedding light on the conclusive stages of sedimentation in this area. As we traverse through time, subsequent dates reveal a continuity in sedimentation processes, capturing distinct phases of fan development.

A temporal gap between approximately 10,000 and 27,000 BP observed in Las Piletas becomes apparent in Falls and El Jable, although with less frequent ages. Remarkably, a near-continuous series of ages spanning from around 30,000 BP to the limit of radiocarbon dating is evident across all three areas. This period may correspond to specific events or shifts in sedimentation dynamics, suggesting potential synchronicity in sedimentation events within all regions. The ages range in the two barrancos, correspond to the intermediate part of the alluvial fan system.

In El Jable, the dating results reveal a wide range of time, illustrating the complex sedimentation processes in this extensive plain.

Table 10. List of radiocarbon ages divided by areas: Piletas and Falls barrancos, El Jable sand pit. Ages are expressed in cal BP.

FAMARA-BARRANCOS				EL JABLE	
LAS PILETAS		FALLS		SAND PIT	
Sample	age cal BP	Sample	age cal BP	Sample	age cal BP
PILETAS-14 C3	3727 - 3575	FALLS-14 C2	27787 - 27378	JAB 8	12754 - 12707
RIT - C 4	3872 - 3694	FALLS-14 C3	40369 - 39167	OT 5	27365 - 27145
RIT - C 7	4086 - 3897	FALLS-14 C4	40445 - 39260	JAB 7	30996 - 30359
BARPIL_D_5_2	6279 - 6170	FALLS-14 C6	41911 - 40716	OT 6	34435 - 33798
RIT - C 3	6640 - 6450	FALLS-14 C5	41986 - 40953	OT 1	35196 - 34418
RIT - C 5	8346 - 8187	FALLS-14 C1	44337 - 42736	OT 2	36971 - 36132
RIT - C 2	10240 - 10145			OT 4	39100 - 37356
BARPIL_I_2	31863 - 31299			H-14 C1	41707 - 40463
BARPIL_D_4	39968 - 39089			OT 3	44229 - 42676
PIL 18	41523 - 40329				
PILETAS-14 C1	41531 - 40223				
BARPIL_D_5_1	42006 - 41149				
RIT - C 6	42224 - 41340				
RIT - C 1	42250-41379				
PILETAS-14 C4	45555 - 43238				
BARPIL_I_3bis	45937 - 44352				
BARPIL_I_1	> 43500				
PILETAS-14 C2	> 43500				

5.6 IRSL and radiocarbon dating difficulties

During the stratigraphic comparison of radiocarbon and luminescence samples, challenges emerged in correlating the dates of the slackwater deposits.

In particular, the IRSL ages obtained from PIL11, PIL12, and PIL13 lack a proper stratigraphic sequence, as illustrated in Fig. 112. Moreover, when comparing the IRSL ages with radiocarbon dates, no consistent match is observed.
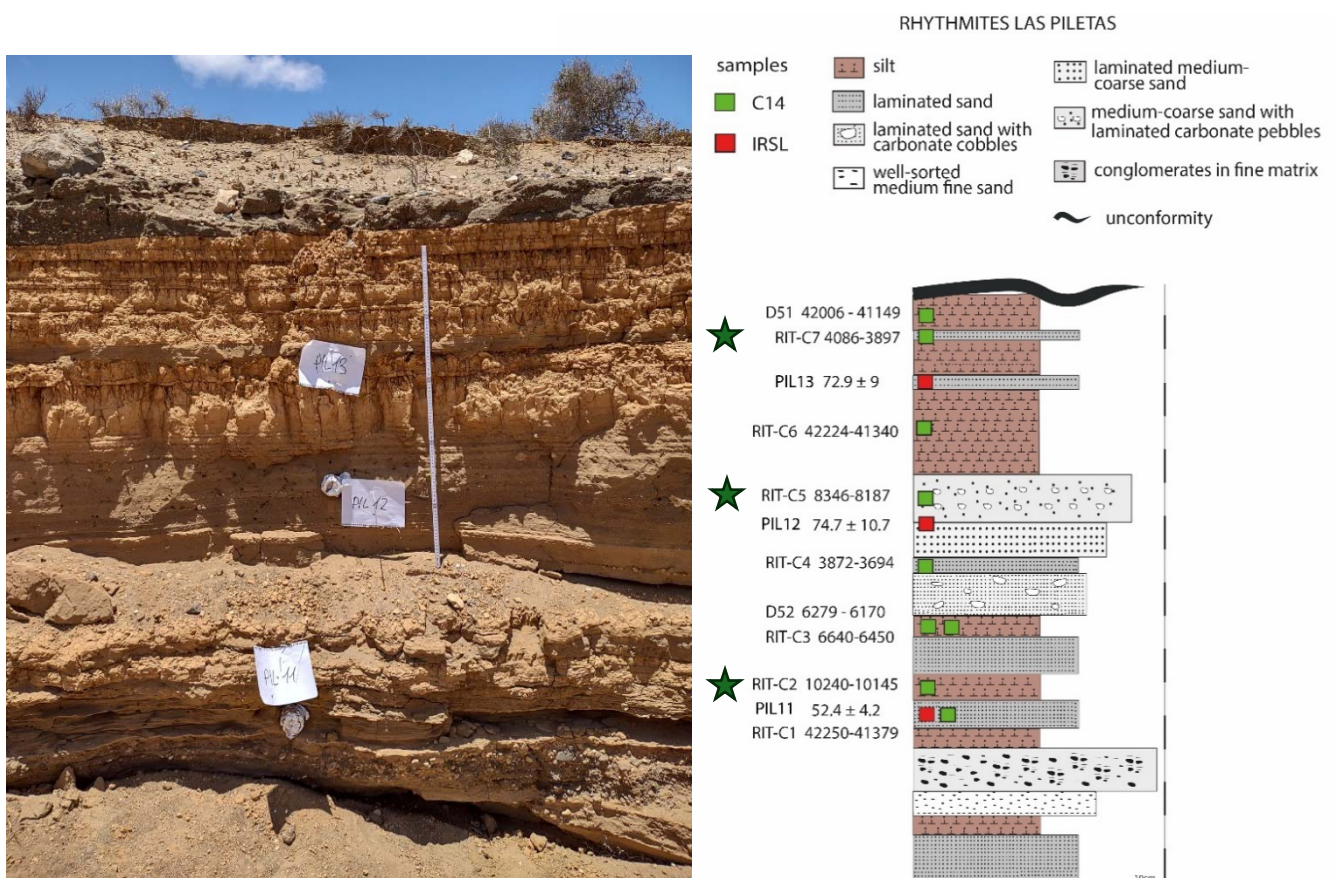
Figure 112. Image of slackwater deposits and its relative log. Green squares indicate samples dated with radiocarbon, and red squares with IRSL pIRIR200. It is evident an incorrect stratigraphic sequence among the various dates obtained. The green stars denote organic material considered for analysis, while the remaining materials are presumed to be reworked.

To attempt to resolve this issue, an adjustment was made in the IRSL dating protocol. Recognizing the relatively young ages of organic samples, it was postulated that the IRSL samples might exhibit a similar youthfulness. Consequently, the protocol temperature for pIRIR was lowered from 200°C

to 160°C for specific samples—PIL11, PIL12, and PIL13. This modification was undertaken to enhance data consistency and minimize potential age discrepancies between luminescence and radiocarbon results. The decision aligns with a common practice in luminescence analysis, where lower temperatures are employed for younger samples to mitigate fading effects, thereby refining the precision of dating outcomes (Kars et al., 2014).

Table 11 shows the luminescent characteristics of the three samples with the new protocol.

Table 11. Luminescent data for samples PIL13, PIL12, and PIL11 across different protocols ($pIRIR_{200}$, $pIRIR_{160}$, $IR_{50,200}$, $IR_{50,160}$). Key metrics include Equivalent Dose (De), Overdispersion (OD %), Recycling Ratio (RR1), Recuperation (Recup), Residual Dose (RD), g-value and Age (ka).

SAMPLE	Signal	De	OD (%)	RR1	Recup	RD (Gy)	g_value (%/decade)	Age ka (corr)
PIL13	$pIRIR_{200}$	107.8 ± 7.12	25.2	1	0.38	6.4 ± 0.67	2.7 ± 1.28	**72.9 ± 9**
	$IR_{50,200}$	38.5 ± 1.75	22	1	-0.6	0.22 ± 0.11	3.08 ± 0.82	**26.6 ± 3**
	$pIRIR_{160}$	57.1 ± 9.56	63	1.05	0.29	4.6 ± 0.32	1.8 ± 0.04	**34.4 ± 6.5**
	$IR_{50,160}$	19.1 ± 2.3	52	1.03	1.2	-	3 ± 1.17	**13.3 ± 2.6**
PIL12	$pIRIR_{200}$	104.1 ± 5.61	4.9	1.03	1.01	3.37 ± 0.48	2.5 ± 1.22	**74.7 ± 10.7**
	$IR_{50,200}$	38.41 ± 0.8	3.7	1.01	0.67	-	3.4 ± 0.6	**31 .7 ± 3.4**
	$pIRIR_{160}$	70.5 ± 3.9	15.7	1.02	-0.35	2.89 ± 0.35	1.1 ± 0.36	**44.4 ± 5.1**
	$IR_{50,160}$	32.1 ± 1.57	15.7	1.01	0.82	0.15 ± 0.11	3.7 ± 0.68	**24.6 ± 3.3**
PIL11	$pIRIR_{200}$	87.5 ± 2.39	13.7	0.62	0.6	2.6 ± 0.10	1.7 ± 0.8	**52.4 ± 4.2**
	$IR_{50,200}$	33.8 ± 0.55	6.6	0.61	0.29	0.25 ± 0.04	4.2 ± 0.75	**23.6 ± 2.5**
	$pIRIR_{160}$	77.6 ± 2.46	9.6	1.02	0.50	4.08 ± 0.15	0.8 ± 0.09	**42.9 ± 3.7**
	$IR_{50,160}$	27.8 ± 0.65	6.9	1.01	0.45	0.07 ± 0.03	4 ± 0.20	**19.5 ± 2.2**

What emerged when decreasing the temperature protocol was the high variability of D_e, residual dose (RD), and g_value within individual samples.

Generally, it is evident a trend between temperature dependence and bleaching decay: the IR_{50} signal of both $pIRIR_{160}$ and $pIRIR_{200}$ is identified as the most easily bleachable signal, evidenced by its low value of residual dose (RD) across all samples. Moreover, the natural bleaching conditions have a more significant influence on the $pIRIR_{200}$ signal compared to IR_{50} and $pIRIR_{160}$ signals. In fact, the RD value of $pIRIR_{200}$ is higher (except for PIL11 where the RD value for the $pIRIR_{160}$ signal is higher than the $pIRIR_{200}$ signal).

The complex bleaching behaviour observed could be attributed to the reduced light intensity underwater, leading to slower bleaching of feldspar IRSL signals. This process is less effective compared to exposure under full daylight, as indicated by Lowick et al. (2012).

The g-values show a dependence on temperatures too. The susceptibility to the signal at lower temperatures is indicated by lower values of g_value. At the same time, the g-values of the IR_{50} signal are higher than those of the $pIRIR_{200}$ and $pIRIR_{160}$ signals, which agrees with the behaviour of feldspar. A change is not observed in the g_value of the IR_{50} signal across all samples (of both $pIRIR_{200}$ and $pIRIR_{160}$) which remains consistent. This observation suggests that the IR_{50} signal might be more stable.

The variability in equivalent doses (D_e) at different temperatures can be attributed to various intrinsic factors in the luminescence dating process. One contributing factor is sensitivity to fading.

Our findings support the application of low-temperature post-IR protocols for luminescence dating of young samples. The bleaching of these low-temperature signals occurs more rapidly, resulting in lower remnant doses compared to high-temperature pIRIR signals (except for PIL11). This trend was also observed by Kars et al. (2014).

Given that the study area pertains to a slackwater environment, it's crucial to consider the geological context. The challenging conditions characterized by sediment saturation and potentially reduced light exposure may influence the ease with which luminescent grains can be effectively bleached. The complexities could contribute to variations in bleaching dynamics, further influencing the observed variability in luminescent characteristics. These considerations highlight the importance of interpreting the data carefully, bearing in mind both the geological context and the specific environmental conditions influencing luminescence behaviour.

After careful consideration, we have chosen the IR_{50} signal from the $pIRIR_{160}$ protocol as the most valid for the slackwater deposit. However, as the age of PIL12 does not align with the stratigraphy, we have excluded it from consideration. Therefore, the new ages are PIL11: 19.5 ± 2.2 ka, PIL13: 13.3 ± 2.6 ka.

The absence of stratigraphical correlation is evident in certain radiocarbon dating ages from the slackwater deposits. This discrepancy may be attributed to the reworking of older materials incorporated into younger sedimentary layers. This phenomenon has been also noticed in the Canary Islands by Yanes et al. (2007). Therefore, only a few radiocarbon samples were taken in consideration: RIT- C1, RIT- C5, RIT- C7 (Fig. 112).

Nevertheless, uncertainties persist concerning the samples RIT-C4, RIT-C3, D52. These seemingly young samples found in old layers present a paradox, as such occurrences are deemed impossible. Consequently, further investigations are imperative to resolve this dilemma.

Chapter 6
Discussion

6.1 Terrestrial Perspective

Luminescence dating has provided essential insights into the temporal evolution of depositional environments within the alluvial fan system of Famara and the El Jable plain. These systems developed under predominantly arid to semi-arid climatic conditions, although indications of more humid periods are evident from the stratigraphic records. Based on the data obtained from facies assemblages, it is possible to discern the various modes of sediment transport from the upland catchment to the fan site. These include a combination of mass-wasting events and water-flow deposits, both contributing to the formation of the fan and plain.

The four barrancos (ephemeral streams) reflect arid and semi-arid climatic conditions, experiencing short bursts of water flow following intense rainfall, alternating with long periods of dryness. These streams range from large destructive flash floods to minor water flows, varying in magnitude across seasons (Picard and High, 1973). Two primary depositional methods were identified within these barrancos:

Flash floods, characterized by large volumes of water carrying detrital sediments that spread across the fan as debris flows.

Stream deposits, formed under sustained water flows, cutting deeply through the substrate, resulting in braided stream deposits.

Debris flow deposits are more pronounced at the fan head and gradually diminish toward the plain. The interfingered and overlapping nature of these deposits with stream deposits in the intermediate and distal areas suggests an increase in humid conditions during periods of higher erosion rates (Reineck and Singh, 2012).

The alluvial fan system of Famara is composed of closely spaced, coalescing alluvial-fan complexes, each representing multiple generations of stacked fans. Three depositional generations have been identified:

- **Early fans**, visible through aerial photography, are covered by a calcrete layer and characterized by steep slopes, mainly composed of debris-flow deposits.
- **A larger fan**, composed of multiple fan lobes dominated by stream-flow deposits, with active channel bars and dissected by barrancos.
- **Youngest fans**, shaped by stream-flow deposits and merging with the aeolian system of El Jable, where slack-water deposits are present.

According to the classification of alluvial fans based on several characteristics outlined by Blair and McPherson (1994), fans can be categorized as Type I (debris flow dominated) and Type II (sheetflood dominated). The modern alluvial fan system of Famara exhibits a combination of both types. The dominant primary processes are debris flows (Type I), with typical grain sorting and size being poorly sorted clayey boulders, pebbles, and cobble gravel (Type I). The trend in maximum clast size decreases from boulders to pebbles or sand down the fan (Type II), and typical grain shape is angular to subangular (Type II). Additionally, there is a predominance of a distal sand skirt facies (Type II), presence of depositional clay matrix (Type I), short to moderate feeder channel length (Type I).

Variations in depositional styles within the alluvial fans can be directly linked to **climatic oscillations**. During arid periods, sediment transport is dominated by mechanical weathering and erosion, which is driven by the lack of vegetation and sparse rainfall. These dry conditions favor flash floods and debris flow deposition. In contrast, wetter periods encourage chemical weathering and soil development, with vegetation cover stabilizing the fan surface. Sediment deposition during these periods is characterized by the accumulation of finer-grained sediments and bioturbated deposits (Dorn, 1994).

The integration of **luminescence dating** provides an essential tool for understanding the timing of these processes.

The **reliability** of luminescence ages in this study is contingent upon several factors, including overdispersion, signal fading, and the consistency between $pIRIR_{200}$ and IR_{50} protocols. The comparison of these factors across the samples allows for a critical evaluation of the reliability of the derived ages.

For most samples, the $pIRIR_{200}$ ages are systematically higher than the IR_{50} ages, which is expected due to the different electron traps each signal targets. The $pIRIR_{200}$ signal, which accesses deeper electron traps, provides more stable and less faded age estimates, especially for older samples. This is evident in samples like PIL1 and PIL2, where the ages obtained from the $pIRIR_{200}$ signal are significantly higher and likely more reliable than those derived from the IR_{50} signal. For younger samples like PIL6-2 and PIL14, where the ages are closer between the two signals, the similarity in ages suggests that both signals offer reliable estimates, though the $pIRIR_{200}$ signal remains preferable due to its better bleaching characteristics and reduced fading.

Samples with lower overdispersion values, such as PIL6-2 and PIL14, exhibit more consistent De values and, as a result, more reliable ages. These samples, both younger in age, show that the IR_{50} and $pIRIR_{200}$ signals produce similar results, further supporting their reliability. Conversely, samples with higher overdispersion values, like PIL3 and PIL13, display greater variability in De values. This suggests that these samples experienced more complex depositional histories, leading to less reliable age estimates. The high overdispersion values in PIL3, in particular, highlight the potential for partial bleaching or mixed sediment sources, making the age estimates for this sample less dependable.

Regarding the fading, the $pIRIR_{200}$ signal exhibited significantly lower fading rates (g-values) compared to the IR_{50} signal, especially in older samples like PIL7 and PIL8. This supports the use of $pIRIR_{200}$ for final age calculations, as the lower fading rates suggest that the ages obtained are less likely to be underestimated.

Additionally, the dose recovery ratios (DRR) provide further validation of the reliability of the ages. Most samples fall within the acceptable ±10% range, indicating that the De values accurately reflect the natural doses. However, outliers such as PIL3, which exhibit dose recovery values outside this range, underscore potential issues with the accuracy of the age estimate. These discrepancies suggest that the age of PIL3, which is characterized by both high overdispersion and poor dose recovery, is less reliable.

In terms of age reliability, the most consistent and reliable ages are found in samples like PIL6-2, PIL14, PIL5, and PIL10. These samples exhibit low overdispersion, minimal fading, and acceptable dose recovery ratios, making the final age estimates robust. The $pIRIR_{200}$ signal, in particular, provides stable and reliable ages across these samples.

On the other hand, samples like PIL3 and PIL13, with higher overdispersion and dose recovery issues, present challenges in providing accurate age estimates. These samples likely represent more complex depositional histories, with partial bleaching or mixed grain sources, resulting in less reliable age determinations.

Overall, the luminescence ages derived from this study are reliable for most samples, particularly those with consistent De values, low overdispersion, and minimal fading. The use of the $pIRIR_{200}$ signal for final age calculations ensures greater accuracy, particularly in older samples, while younger samples like PIL6-2 and PIL14 exhibit reliability with both IR_{50} and $pIRIR_{200}$ protocols.

Based on the obtained ages, the alluvial fan and aeolian plain systems developed during stadial and interstadial periods, between Marine Isotope Stage 6 (MIS 6) and Marine Isotope Stage 1 (Holocene), covering approximately 132 ka to 13.3 ka. Five distinct aeolian deposits, interbedded with alluvial and fluvial deposits, are evidence of climatic cyclicity during the late Quaternary in Lanzarote (Table 12 and Figure 113). The evolution of the alluvial fans system together with the aeolian system of El Jable plain are indicates in Figure 114.

Overall, deposits associated with humid periods are more evident in Famara due to the increased availability of material resulting from the erosion of basalt and pyroclastic materials of the massif. During humid periods, rainfall and weathering contribute to the breakdown, transportation, and deposition of volcanic rocks in Famara. Conversely, in El Jable, the presence of these sediments is less pronounced, and the corresponding layers are relatively thin.

In contrast, during drier periods, weathering may be less pronounced, and there might be a reduction in the availability of freshly weathered sediment. However, in the specific context of El Jable Plain, drier conditions facilitate the formation of aeolian (wind-driven) deposits, such as dunes, exhibiting a directional trend climbing towards the Famara Massif, or sand sheets.

Furthermore, during arid conditions, the crucial process involves the formation of aeolian carbonate grains transported from the plain toward the massif constituting the basis for the calcrete-dolomite matrix observed in the talus deposit.

Table 12. Relative ages of Barranco Las Piletas samples determined through Infrared Stimulated Luminescence (IRSL) correlated with the respective environmental developments and Marine Isotope Stages (MIS).

Sample	Age ka (corr)	Environment	MIS
PIL13	13.3 ± 2.6	Slackwater	2
PIL11	19.5 ± 2.2	Slackwater	2
PIL 6-2	24.2 ± 1.7	Alluvial	2
PIL 14	25 ± 6	Fluvial	2
PIL 5	46.8 ± 5	Alluvial	3
PIL 10	67.9 ± 5.3	Aeolian	4
PIL 9	77.6 ± 7.3	Aeolian	5a
PIL 3	91 ± 13	Aeolian	5c
PIL 8	95.6 ± 7	Aeolian	5c
PIL 2	119.3 ± 9.1	Alluvial	5e
PIL 1	120.4 ± 7.1	Alluvial	5e
PIL 7	132 ± 12.3	Aeolian	5-6
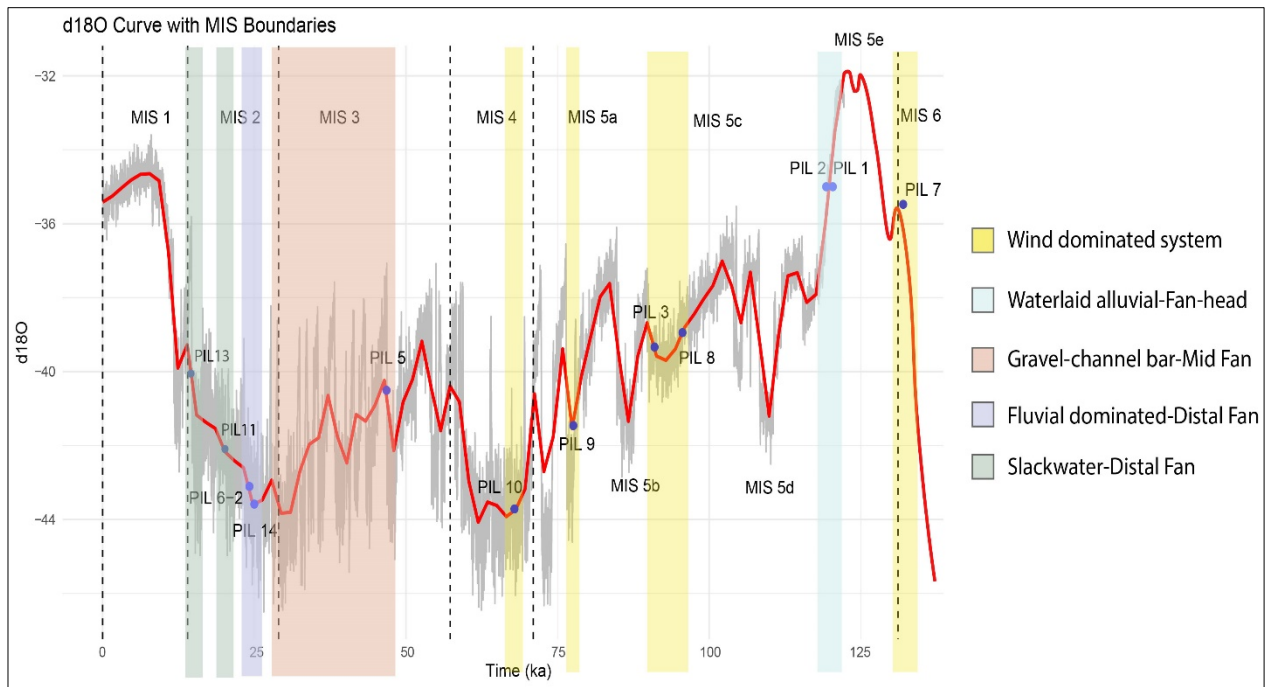
Figure 113. The image shows a d18O (oxygen isotope) curve with Marine Isotope Stage (MIS) boundaries, illustrating global climate variations over time. Marine oxygen–isotope data are from Vinther et al. (2006), Rasmussen et al. (2006), Andersen et al. (2006), Svensson et al. (2007), Wolff et al. (2010). The x-axis represents time in thousands of years (ka), while the y-axis displays d18O values, reflecting fluctuations associated with glacial and interglacial periods. Coloured bands denote distinct sedimentary depositional environments: Yellow: Wind-dominated system, Light Blue: Water-laid alluvial fan-head, Brown: Gravel-channel bar mid-fan, Purple: Fluvial-dominated distal fan, Green: Slackwater distal fan. The red d18O curve shows significant variations across MIS stages (MIS 1 to MIS 6), corresponding to global climate shifts. Blue dots mark specific sample labelled "PIL" (e.g., PIL 1 to PIL 14), indicating collected samples used for stratigraphic and paleoenvironmental analysis throughout the different climate stages. Blue points labelled "PIL" (e.g., PIL 1 to PIL 14) represent relative ages measured through Infrared Stimulated Luminescence (IRSL), based on samples collected from Barranco Las Piletas.
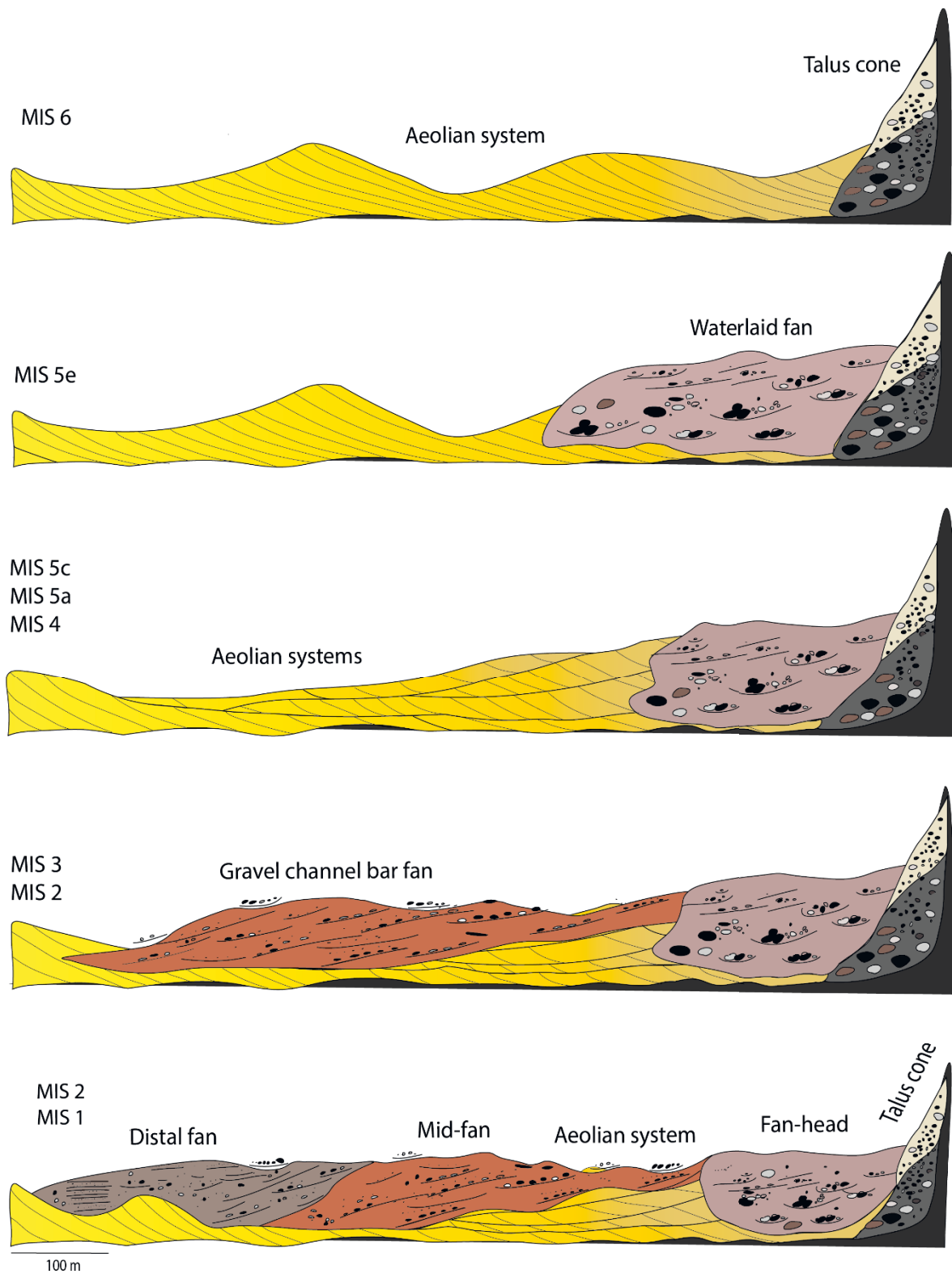
Figure 114. Evolution of El Jable from MIS 6 to MIS1. During MIS6, an aeolian system was already established on the plain, with climbing dunes situated near the Famara cliff. In contrast, MIS 5e marks a period of climate deterioration, triggering erosion along the cliff and leading to the formation of the initial alluvial fan primarily composed of debris flow deposits. Subsequent transitions towards drier conditions during MIS4, MIS5a and MIS5c resulted in the deposition of three distinct types of aeolian deposits. Conversely, shifts towards more humid conditions during MIS 3 and MIS 2 gave rise to the development of a second alluvial fan characterized by gravel channel bars. Finally, during the more recent periods of MIS 2 and MIS 1, corresponding to the most humid phases, the third generation of fans formed, predominantly consisting of fluvial deposits.

The **geographic location** of the Canary Islands between Arctic and tropical waters makes it particularly sensitive to global climate fluctuations. Oscillations of the Arctic polar front and the influence of the Intertropical Convergence Zone (ITCZ) are well-documented in both marine and aeolian sediments (Meco et al., 1992; 2002), and in humid-climate palaeosols (Petit-Maire et al., 1986).

Furthermore, the archipelago is situated in a region where Atlantic-generated and African-generated winds converge. Tus it is influenced by the oscillations of the sub-tropical Azores anticyclone and the African monsoons. According to various authors (Rahmstorf, 2002; McManus et al., 2004), there is a correlation between climate variability in the North Atlantic, Europe, the Mediterranean, and northern North Africa, and changes in the strength of the Atlantic Meridional Overturning Circulation (AMOC). The AMOC, a major component of the Global Conveyor Belt, circulates warm water from the South to the North Atlantic Ocean. During glacial periods, a weakening of the AMOC occurs due to freshwater input at high latitudes, resulting in the cooling of North Atlantic waters, strong westerly winds, and the southward migration of the Intertropical Convergence Zone (ITCZ), leading to arid events in North Africa. Conversely, through deglaciation, a stronger AMOC and the northward return of the rain belt to its northernmost position promote a more humid climate. The AMOC is thought to have strongly affected climate variability in the Northern Hemisphere between MIS 5b and MIS 3 (96–29 ka; Henry et al., 2016; Li & Born, 2019).

During the Last Glacial period two types of abrupt climate changes occurred: **Heinrich events** (H or HE) associated with a decrease in temperatures, and **Dalsgaard–Oeschger events** (D-O) related to an increase in temperatures (Heinrich, 1988; Dansgaard et al., 1982 1993; Bond et al., 1992; 1993; 1997; Rasmusen et al., 2003).

Heinrich events, linked to glaciological processes, involve the expansion of Arctic Sea ice below 45° North, causing a 2-3°C temperature drop. As these events conclude, icebergs with lithic grains (Ice Rafted Debris, IRD, deposited mainly in the IRD belt, 40°N-60°N) drift across the North Atlantic, depositing layers on the ocean floor upon melting. Six Heinrich events occurred during the Last Glacial period showing a periodicity of six thousand years, with a duration ranging from 208 to 2280 years (Hemming, 2004).

Some researchers propose generally dry conditions during Heinrich events (Goñi et al., 2000, Turon et al., 2003), while others suggest wet and extremely cold winters with increased runoff and enhanced summer aridity (Boessenkool, 2001). Additional studies propose two distinct phases

particularly for Heinrich events H4, H2, and H1, outside the IRD belt between 45 and 18°N: the first phase is characterized by atmospheric cooling, intensified precipitation, and increased river discharges across western Europe. Simultaneously, extremely dry conditions warmer than the previous phase, leading to the expansion of semi-desert plants, have been detected in both western Iberia and France during the second phase. This alternative perspective is supported by the southward shift of the Arctic Front, redirecting winter cyclones off Iberia. Before Heinrich events, the thermal front, representing the strong temperature gradient between the warm south and cold north, was likely in the northern IRD belt. Icebergs released during the first phase of an H event moved southward, causing IRD peaks around 40°N and a consequently North Atlantic sea-surface temperature drop, shifting the thermal front southward to the mid-latitudes. The Thermohaline Circulation (a large-scale oceanic circulation) weakening by freshwater influx prevented warm, moist conditions, causing substantial cooling of the SST (sea surface temperature). During the second phase, the relative warming in mid-latitude areas outside the IRD belt indicated a northward displacement of the thermal front. This movement was associated with the southward shift of the Intertropical Convergence Zone (ITCZ) while the Atlantic Meridional Overturning Circulation (AMOC) remained weak (Naughton et al., 2009).

More humid climatic conditions during a Heinrich event are also evident in the Mediterranean with the presence of Mediterranean-type woodland during H4, associated with a climate featuring mild, wet winters and hot, dry summers (López-García et al., 2013).

Dansgaard Oeschger events (D.O.) encompass various time scales featuring rapid warm interstadial states (in order of decades) followed by slower cold stadial (less than a century) in the North Atlantic region. These events are marked by changes in temperature, precipitation, and atmospheric circulation patterns (Rahmstorf, 2003). Despite their millennial duration, these events do not align with significant external forces like solar variability. Instead, their causes might be related to intricate interactions within the atmosphere-ice-ocean system of the Northern Seas. Positive feedback mechanisms, driven by factors such as stochastic wind forcing, gradual changes in ice sheets, or convective instability, contribute to the abrupt climate swings reminiscent of D.O. events (Li and Born, 2019).

Heinrich events and D.O. events are organized into "Bond Cycles," each comprising a major D–O interstadial (warm period) followed by shorter and less intense interstadials, concluding with a

prolonged stadial (cold period) terminated by an H event (Dansgaard et al., 1982 1993; Bond et al., 1993).

Cycles of depositional sequences associated with glacial–interglacial stages are found elsewhere in the Canary Islands. According to Meco (2008) and Meco et al. (2011), four different sedimentary deposition phases took place during Pleistocene: 1, calcareous dunes related to glacial, arid and cold climate; 2, Palaeosols formed during the beginning of an arid interglacial, which climate became progressively warm and wet; 3, marine deposits deposited during the interglacial peak; 4, calcrete formed during arid and temperate climate indicating the start of next glaciation (Fig. 115).
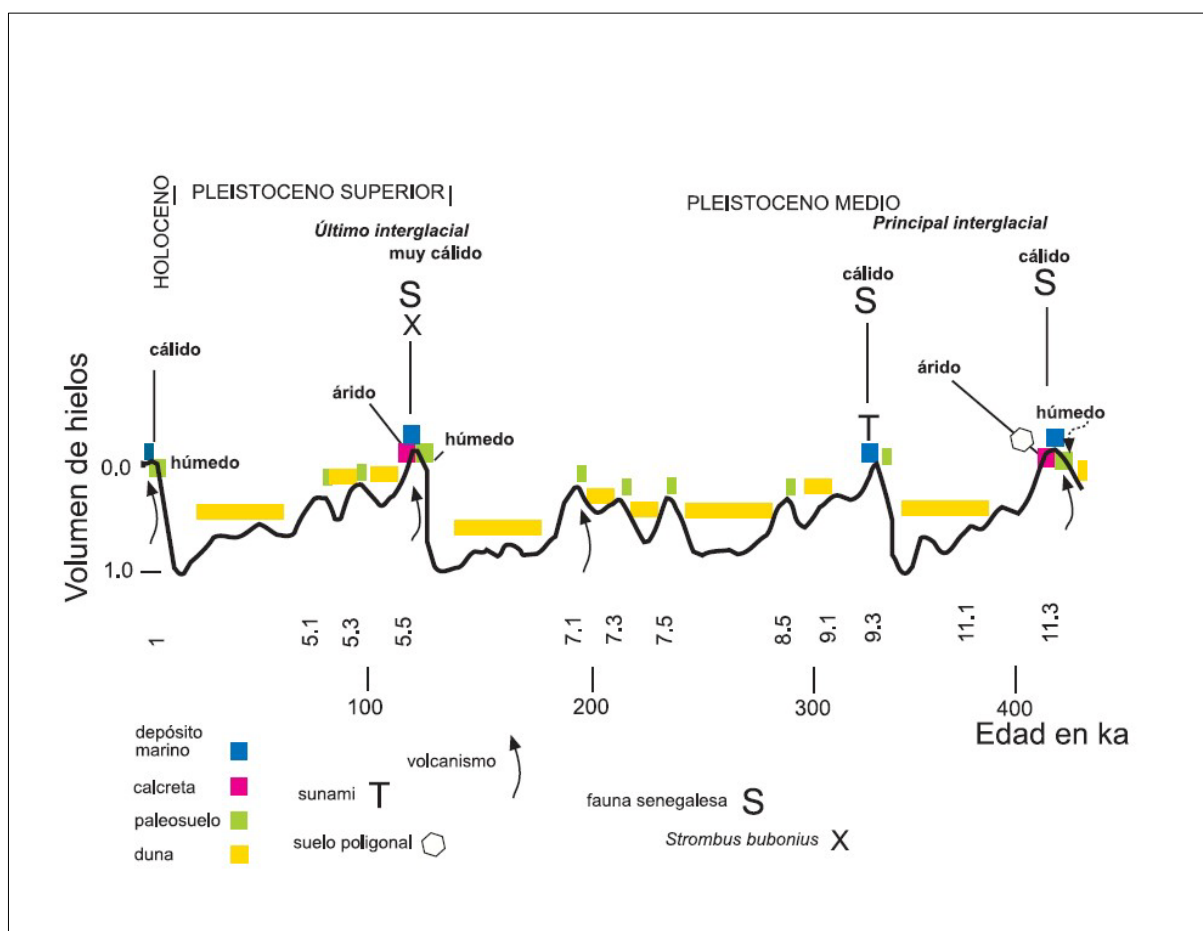
Figure 115. This curve, taken from Meco (2008), illustrates climatic variations spanning the past 420 ka. It shows the alternating patterns of dunes, palaeosols, marine deposits, and calcretes, indicative of cycles involving warm-wet episodes followed by sea level rises, accompanied by the arrival of Senegalese fauna. These climatic cycles culminate in warm-arid periods transitioning into prolonged cold-aridity. Evident shifts occurred during interglacial periods like MIS 11.3, MIS5e, and continue into the present (MIS 1), with an anticipated warm-arid phase preceding future glaciation.

El Jable experienced the formation of aeolian deposits during glacial stages and cold oscillation (substadial periods) during interglacial times. These deposits can be linked to the heightened wind intensity induced by the onset of the glacial periods, which amplified both coastal upwelling and the

influx of aeolian material from the Sahara/Sahel regions. The prevailing westerlies and the intensification of the Azores anticyclone during these colder phases may have facilitated the transport of finer sediments, contributing to the formation of widespread dune systems in El Jable. In contrast, no significant palaeosols were detected in the alluvial fans of Famara, suggesting limited soil development and stabilization during arid periods, though the fan system did begin to develop as the climate transitioned into more humid phases after the peak of the arid interglacial. This increase in humidity and precipitation resulted in renewed fluvial activity and sediment transport from the Famara massif.

The alluvial fan system of Famara aligns with the multiple sedimentary sequences studied by Heinrich et al. (2021) in the El Jable Plain. Near the village of Muñique, a sand pit reveals three sequences of deposits: Bank A, B, and C, from oldest to youngest. Each sequence consists of an alternation between aeolian deposits (DepoType 1 and 2) and brown clayey sediments (DepoType 3). These brown clayey sediments were dated by Heinrich et al. using IRSL and correlated with three Heinrich events—H2, H4, and H7a—corresponding to 23.6 ± 1.5 ka, 36.3 ± 2.3 ka, and 71.6 ± 4.6 ka, respectively.

The gaps in the age data within the stratigraphy of Muñique can be addressed by incorporating the new ages obtained in this thesis (Fig. 116). Luminescence dating of the alluvial and aeolian systems in Famara and El Jable fills in these temporal gaps, providing a more continuous record of the Late Quaternary climatic oscillations. The distinct aeolian layers interbedded with alluvial and fluvial deposits in Famara offer strong evidence for periods of enhanced wind activity, corresponding with global climatic events like the Heinrich events and Dansgaard-Oeschger cycles. These sedimentary records serve as paleoclimatic markers, helping to reconstruct the environmental conditions during key transitions between glacial and interglacial stages.
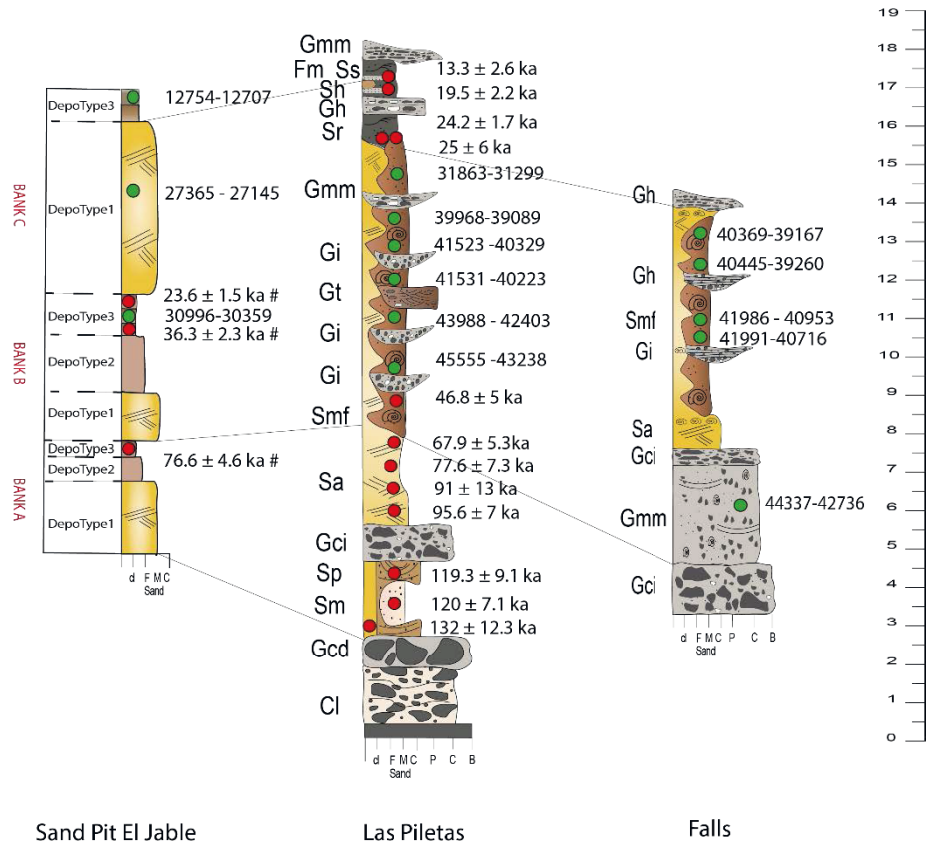
Figure 116. The image illustrates sedimentary logs from three different sections (sand pit in El Jable, Las Piletas and Falls) showing stratigraphic sequences and corresponding depositional facies. The logs are color-coded according to sediment types, including aeolian sands, conglomerates, fluvial sand, sediment gravity flow, pyroclastic reworked material, and alluvial low-energy deposits. Red dots represent Infrared Stimulated Luminescence (IRSL) ages, while green dots indicate Carbon-14 ages. Reworked samples are not included. Ages labelled with a hashtag (#) are calculated from Heinrich et al. (2021) data. The sediment layers are classified into different facies, such as conglomerates (Gmm, Gi, Gt), fluvial sands (Sm, Sp), and aeolian systems (Sa), with facies codes on the right.

6.1.1 Marine Isotope Stage (MIS) 6-5

Between MIS 6 and MIS 5e, a dune system developed at the base of the western side of the massif. Likelihood, these dunes dated at (132 ± 12.3 ka, PIL 7), originated in the El Jable plain and migrated towards the Famara massif. They are presumed to represent the inner part of the coastal dune system formed during the MIS 5e high stand, when sea level was about 6 meters higher than the present (Meco et al., 2022). Furthermore, calcareous-rich dunes were widespread across the Canary Islands during this period, attributed to a substantial African sand supply (Meco, 2008; Meco et al., 1997, 2002, 2011; Zazo et al., 2002; Maréchal et al., 2020).

The mobilization of sand in the dune system may be either linked to the extremely dry climatic conditions characterizing Heinrich event 11 (between 129 and 133 ka) or to the abrupt aridification event that occurred in 125.6 ka in northwest Africa (Menviel et al., 2021). Alternatively, the dune could be the result of the reactivation of the calcrete broke during the second erosive cycle (Meco et al., 2008). The age of the dune system matches the descriptions provided by Vega (2010), where marine bioclastic sediments formed climbing dunes covering the first generation of the alluvial fan of the Lower Pleistocene. Vega (2010) also noted that the dune system in El Jable was well developed by the end of the Middle Pleistocene.

The aeolian deposits in Famara dated 132 ± 12.3 ka could be reliably correlated with the oldest layer of aeolian deposits described by Heinrich et al. (2021) which have not been dated. Following the climatic optimum of MIS 5e, conditions shifted towards higher humidity, leading to the development of the alluvial deposits dated at 119.3 ± 9.1 ka (PIL 2) and at 120.4 ± 7.1 ka (PIL1). Castañeda et al. (2009) also noted wetter conditions during a significant dispersal period particularly between 120 and 110 ka, marked by the expansion of C3 vegetation in the Sahara region. In El Jable, this transition is marked by the formation of palaeosols, rich in insect ootheca, terrestrial gastropods, and reddish quartz-rich sediment from Africa, as documented by Vega (2010).

As the climate transitioned back to drier conditions, two aeolian deposits, dated 95.6 ± 7 ka and 91 ± 13 ka (PIL 8, PIL 3), formed during MIS 5c. The PIL 3 dunes, found near the top of the massif, are interpreted as climbing dunes. A later generation of aeolian deposits, dated 77.6 ± 7.3 ka (PIL 9), corresponds to the cold substadial MIS 5a.

Generally, between 100-70 ka, a cooling trend in coastal waters and a decrease in fluvial discharge were observed in the central East Mediterranean (Mauz, et al, 2012), suggesting arid conditions not

only in the study area but also in the broader eastern Mediterranean region. However, the period related to H7a is associated with an increase in humidity, which led to the formation of brown clayey layer in Bank A in El Jable (Heinrich et al., 2021), and palaeosols in the eastern cost of Lanzarote (von Suchodoletz et al., 2013). Therefore, the aeolian deposits dated 77.6 ± 7.3 ka are likely related to less arid conditions.

6.1.2 Marine Isotope Stage (MIS) 4

MIS 4 represents a major glacial advance that spanned from approximately 71 ka to 57 ka. While it was cooler than the preceding MIS 5, it is typically seen as less extreme than the subsequent MIS 2, which was marked by the Last Glacial Maximum (LGM). However, the aridification and cooling trends during MIS 4 played a significant role in shaping the Famara alluvial fan and the El Jable aeolian system.

The luminescence age of 67.9 ± 5.3 ka (PIL 10) corresponds to the aeolian-dominated sedimentation during MIS 4. This age falls between Heinrich Event H7a (around 71.6 ka) and H6 (around 60 ka), capturing a phase of active sediment deposition within the broader glacial period.

The age obtained for the PIL 10 deposit aligns closely with the aeolian deposits described by Heinrich et al. (2021) in DepoType 1 of Bank B, where deposits were formed under similarly dry and windy conditions. These arid climates, as described by Heinrich, were conducive to the formation of aeolian systems, reflecting the same processes observed in both Famara and El Jable during this time.

The correlation between the age of our deposit and the stratigraphy described by Heinrich et al. supports the conclusion that the dry conditions of MIS 4 facilitated the development of wind-driven sedimentary systems. This cold period is also documented in Mediterranean records, where cooler sea surface temperatures and intensified westerly winds are linked to stronger Mediterranean deep currents (Bardají et al., 2022). These winds likely played a key role in the accumulation of aeolian sediments in the El Jable plain, where Saharan dust was transported and deposited.

From a global perspective, MIS 4 coincided with the onset of increased ice sheet expansion in both the Northern Hemisphere and Antarctica (Shackleton et al., 2021). As ice sheets advanced, sea levels dropped significantly, exposing more land for aeolian processes to act upon. The lower sea levels

also impacted coastal dynamics in the Canary Islands, potentially influencing sediment transport from the inland plains toward the coast.

During this time, the Famara alluvial fan system may have been less active due to reduced water availability. However, the presence of dune deposits highlights the significance of wind-driven processes during glacial periods.

Furthermore, the weakening of the African monsoon during MIS 4 contributed to increased aridity across North Africa (Niedermeyer et al., 2010), likely reinforcing the dominance of aeolian deposition in the Canary Islands and reducing the influence of fluvial processes, as seen in the dune layers of El Jable.

6.1.3 Marine Isotope Stage (MIS) 3

MIS 3 is well known in the North Atlantic region for its high climate variability, characterized by Heinrich and Dansgaard–Oeschger (D.O.) events. The relatively humid, quasi-interglacial conditions of this period are reflected in the luminescence age of PIL5 (46.8 ± 5 ka) from Famara, which aligns well with the ^{14}C ages obtained from both Famara and El Jable (see Table 10). This congruence between luminescence and radiocarbon dating supports the interpretation that MIS 3 was a period of active sedimentation driven by climatic oscillations.

The mid-distal section of the Famara alluvial fan is well-developed, consisting primarily of clay and sand eroded from the surrounding cliffs, which overlay older aeolian deposits. This phase of sediment deposition corresponds to episodic wet periods during MIS 3, when enhanced erosion from the Famara cliffs contributed to the thickening of the alluvial fan. These newly deposited layers provided a stable substrate for gastropods and insects, as indicated by the organic remains found in these sediments.

The transition between MIS 3 and MIS 2 (around 45 ka and 27-30 ka, respectively) was particularly favorable for the development of terrestrial gastropods, as evidenced by numerous samples dated to this period. The close match between the luminescence age of PIL5 and the ^{14}C ages, alongside the potential correlation with Heinrich's DepoType 2 of Bank B, further supports the conclusion that MIS 3 was generally characterized by humid conditions. This period of increased humidity was more pronounced in the Famara region, as seen in the development of alluvial deposits. A direct indicator

of increased soil moisture during this time are the paleosols observed across Lanzarote by von Suchodoletz et al. (2009, 2010).

However, dry peaks associated with Heinrich events occasionally disrupted these moist periods. As noted by Heinrich et al. (2021), these events were associated with changes in atmospheric circulation over Northwest Africa and the North Atlantic, leading to enhanced dust transport from the subtropical Sahel to the Canary Islands. While these events typically involve colder and drier conditions, some interstadial phases during or after Heinrich events may have been marked by increased moisture. These fluctuations are clearly depicted in the oxygen isotope curve (Fig. 117), which shows the alternation between warm D.O. events and cold Heinrich events throughout MIS3.

The identified Heinrich and D.O. events during MIS 3 include:

- Warm peak between D.O.4 and D.O.5 (30996 – 30359 BP).
- Heinrich Event H3 (31863 – 31299 BP).
- Heinrich Event H4 (from 39167 BP to 41911 BP).
- Warm peak Between D.O. 11 and D.O. 12 (44337 – 42736 BP).

Currently, achieving precise alignment with the high-frequency cyclicity of D.O. events (approximately 1500 years) remains challenging due to inherent uncertainties and margins of error in luminescence dating, which limit our ability to pinpoint exact correlations with these rapid climate oscillations.
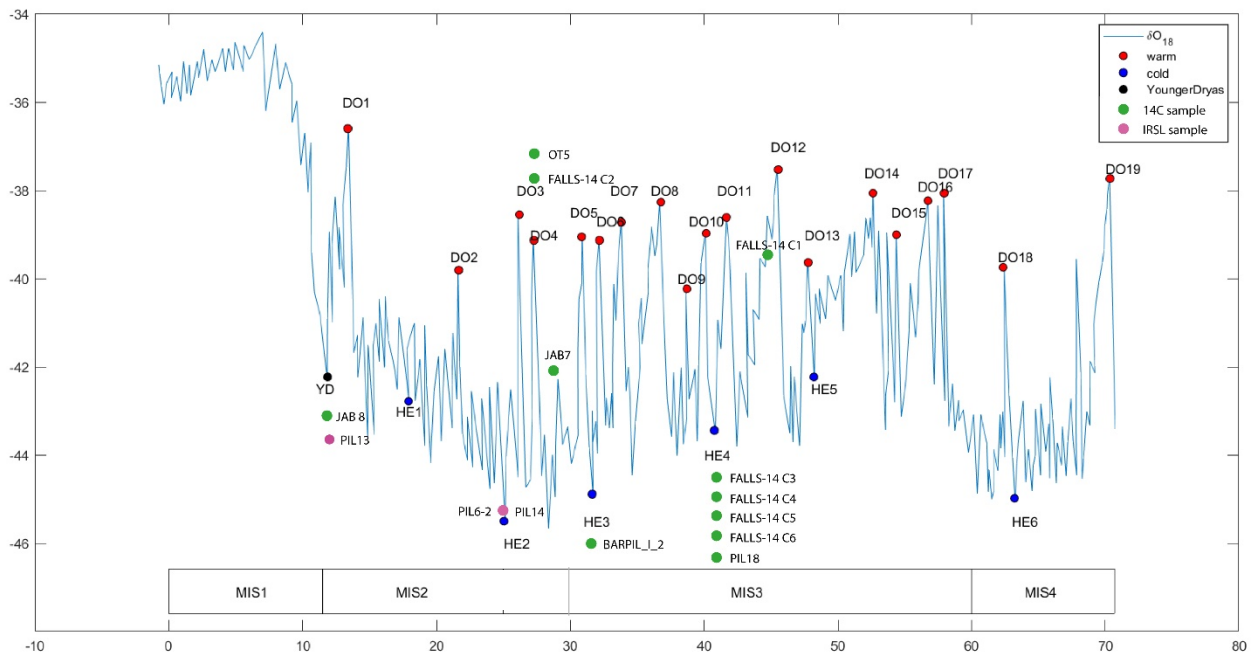
Figure 117. Oxygen isotope (δ¹⁸O) curve illustrating climate variability from MIS 1 to MIS 4, highlighting warm periods (red points), cold periods (blue points), and notable climatic events such as Dansgaard-Oeschger (D-O) cycles and Heinrich events (HE). The curve also includes sample points from this study (pink for IRSL samples, green for ¹⁴C samples) from the Famara alluvial fan and El Jable plain. The dataset reflects major stadial and interstadial periods, with important paleoclimate markers such as the Younger Dryas (YD) and Last Glacial Maximum (LGM). Adapted from oxygen isotope data from NGRIP and other Greenland ice cores (Vinther et al., 2006; Svensson et al., 2008; Rasmussen et al., 2014).

6.1.4 Marine Isotope Stage (MIS) 2

Despite MIS2 being generally described as a glacial stage, fluvial and alluvial deposits in the distal part of the fan dated with luminescence at 24.2 ± 1.7 ka (PIL 6-2) and 25 ± 6 ka (PIL 14), along with organic samples collected from both Famara (FALLS-14 C2: 27787 – 27378 BP) and El Jable (OT5: 27365 – 27145 BP; JAB 8: 12754 –12707 BP) reveal wet conditions. However, the climatic conditions were not conducive to the proliferation of insects and gastropods as during MIS3, given the few organic samples from this period. Yet, the slackwater deposit (related to samples PIL11: 19.5 ± 2.2 ka and PIL13: 13.3 ± 2.6 ka) suggest a fluctuation between wet and dry conditions. Nevertheless, the thickness of the fluvial deposits suggests extremely intense rainfall events.

More moist conditions during glacial have also been highlighted by Vega (2010) and Yanes et al. (2011, 2013). Equally, von Suchodoletz et al. (2010) concluded increased humidity during glacial periods, possibly caused by stronger westerly winds, proposing a cyclicity model describing

212

subsequent phases of (1) sand accumulation; (2) dust imprint and soil formation, and (3) water-induced erosion.

The ages extracted from the dated layers could potentially correspond to the following climatic peaks:

- Interstadial D.O. 4 (from 27145 BP to 27787 BP).
- Last Glacial Maximum (LGM) period and/or HE2 (25 ± 6 ka; 24.2 ± 1.7 ka).
- Younger Dryas (12754 –12707 BP; 13.3 ± 2.6 ka).

The Last Glacial Maximum, HE2, and Younger Dryas mark sudden shifts to glacial conditions characterized by cooler and drier climates (Clark et al., 2009). Generally, the climate in the Northern Hemisphere was more extreme during H Events than during the LGM, with the tropical rain belt (ITCZ) positioned farther south than it is today (Heinrich et al., 2021).

During HE2, the heightened precipitation and increased dust supply contributed to the formation of DepoType 3 of Bank B in the El Jable plain, while in Famara, they resulted in the deposition of fluvial and alluvial sediments.

The top of the stratigraphic sequence analysed by Heinrich et al. (2021) could be associated with the Younger Dryas, which led to the formation of sand sheets in Famara, while the dune system of El Jable accumulated layers of deposits primarily composed of Saharan dust. The transition from the Pleistocene to the Holocene, spanning from 11.5–5.5 ka, also saw the onset of the African Humid Period (AHP), although reworked deposits suggest the need for further investigation to better understand the stratigraphy from this period.

6.2 Martian Perspective

The application of luminescence dating techniques in this study has provided invaluable insights into the temporal evolution of depositional environments within Martian analogues, such as the alluvial fan system of Famara and the El Jable plain. These findings underscore the significance of understanding past Martian climates, as the observed variations within the alluvial fan and aeolian systems of Lanzarote reflect climatic oscillations. By studying terrestrial analogues, we gain critical insights into how similar processes may have shaped the Martian landscape, particularly during periods when climate shifts resulted in alternating phases of water-driven and wind-driven sedimentation.

Luminescence dating has proven to be a versatile and robust tool, not only for dating geological deposits but also for reconstructing paleoenvironments. In this study, we successfully applied luminescence dating to various sedimentary facies, including aeolian deposits, as well as those mixed with volcanic grains, demonstrating the wide applicability of this technique. While alluvial deposits on Mars may be too old for luminescence dating, active deposits, such as dunes, offer promising targets for chronological studies, as their younger age makes them more suitable for this method.

A possible site to study both active gullies and active dunes on Mars is **Proctor Crater** and its surrounding areas (Fig. 118). From an exploration perspective, Proctor Crater offers several advantages. Its proximity to the equator ensures consistent solar energy availability, which is critical for powering a rover throughout the Martian year, similar to what was essential for missions like Opportunity and Spirit (Fenton et al., 2003). Additionally, the favorable terrain—featuring well-organized barchan dunes and moderate slopes—makes it a safer and more navigable environment for a rover, reducing the risk of getting stuck or encountering steep, hazardous terrain (Bourke et al., 2008).

Scientifically, Proctor Crater is unique due to its ongoing aeolian processes (active dune migration) and sublimation-driven gully formation. Studies show that dunes within Proctor Crater are predominantly basaltic, shaped by wind erosion and seasonal climatic changes (Fenton et al., 2006). The gullies in this region are formed by CO_2 sublimation, leading to debris flow down crater walls, providing insights into recent climatic fluctuations on Mars (Dundas et al., 2019). The interaction between these two processes offers valuable insights into the recent climatic history of Mars.

Moreover, the relatively stable environmental conditions and diverse sedimentary structures, including alluvial fans and intermixed volcanic and aeolian deposits, make this region ideal for in-situ luminescence dating to investigate Mars' dynamic surface evolution (Fenton et al., 2003). Proctor Crater's combination of safe terrain, active processes, and equatorial location enhances its potential for extended rover operations, maximizing the scientific returns while ensuring mission success in terms of power management and navigation.

The ability to date Martian dunes using luminescence dating provides valuable insight into the recent geological history of Mars, shedding light on ongoing processes that continue to shape its surface. These active deposits, particularly in regions where wind-driven sediment transport dominates, serve as critical indicators of Mars' dynamic surface processes and climate. By dating these dunes, we gain a clearer understanding of how aeolian processes have evolved in response to Martian climate variations, providing a window into the planet's most recent geological activity.

The study of terrestrial analogues, such as those in Lanzarote, has revealed the importance of paleoclimatic reconstruction through luminescence dating. The alternating layers of alluvial-fluvial and aeolian deposits in the El Jable plain reflect changes in climatic conditions during the Late Quaternary, offering a valuable analogue for interpreting similar climatic oscillations on Mars. By analyzing and dating these deposits, we can reconstruct the history of Martian climates, particularly during periods when water may have been intermittently present, creating conditions conducive to fluvial activity.

The comparison between terrestrial and Martian landscapes also highlights key differences that must be considered when applying these techniques to Martian environments. While both planets exhibit alluvial fans and dune systems, Mars' atmospheric composition and lower gravity significantly influence the processes shaping these landscapes. Nevertheless, the paleoclimatic implications derived from terrestrial analogues provide a robust framework for interpreting Martian paleoenvironments, suggesting that Mars, like Earth, underwent significant climatic changes that influenced sedimentary processes over time.

As exploration missions continue to probe the Martian surface, luminescence dating stands poised to play a pivotal role in unraveling the planet's geological history. Future missions equipped with luminescence dating instruments could apply these techniques to in-situ investigations of Martian surface deposits, offering a direct means of dating active environments. By targeting young and active deposits, such as dunes, we can gain a clearer picture of Mars' recent climate, overcoming the

limitations posed by the age of older alluvial deposits. The ability to date these active surfaces will provide unprecedented insights into the ongoing processes shaping Mars' surface, offering valuable information for future exploration missions and human presence on the planet.

As we continue to explore Mars, luminescence dating will be significant for understanding its geological and climatic history, guiding future missions in their quest to unravel the mysteries of our neighboring planet.
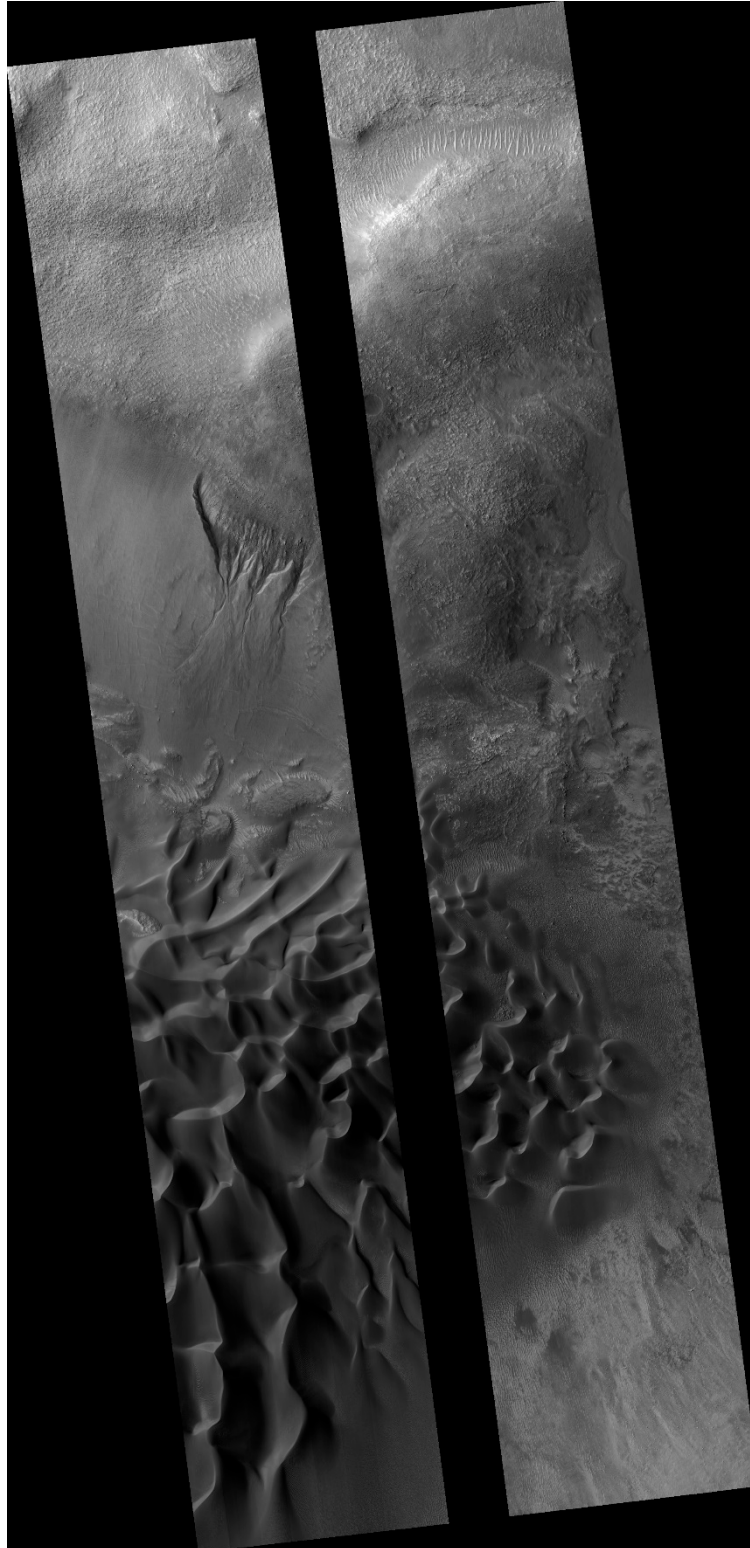
Figure 118. Tracking Gully and Dune Changes in Crater East of Proctor Crater (ESP_082037_1325). This HiRISE image, acquired on 26 January 2024, reveals active gullies along the steep crater walls, located in the upper section of the image. These gullies, likely formed by CO_2 sublimation, display well-defined channels that carry debris downslope. In the lower portion of the image, dark barchan dunes dominate the crater floor, shaped by prevailing Martian winds, showcasing active aeolian processes. The image resolution is 50 cm/pixel, allowing objects as small as 151 cm across to be identified. The center of the image is located at -47.023° latitude and 37.307° longitude East, with North oriented up.

Chapter 7
Conclusion

This thesis draws several key conclusions that offer unique perspectives on Martian exploration, luminescence dating techniques, and sedimentary stratigraphy. These conclusions not only provide deeper insights into Martian environments but also refine the methodologies needed for studying extra-terrestrial geological processes. Through careful protocol selection, analysis of environmental influences, identification of sample distinctions, and addressing challenges in stratigraphic comparison, this study has laid the groundwork for a more comprehensive understanding of luminescence dating protocols for Martian deposits. Below, these conclusions are explored through the lenses of Martian perspectives, luminescent analysis, and sedimentological stratigraphy.

Protocol Selection

In the context of Martian analogs, selecting the pIRIR$_{200}$ protocol demonstrates the importance of choosing a method that ensures reliability under the distinct environmental conditions found on Mars. This protocol proved effective for nearly all samples derived from basalt deposits in Lanzarote, offering consistent performance with minimal fading issues. Given Mars' extreme conditions, where cosmic radiation and low atmospheric pressure pose additional challenges, the robustness of this protocol is crucial. It contributes significantly to the accuracy of chronological assessments, ensuring that Martian sedimentary deposits can be dated with precision, despite the unique challenges posed by the Martian landscape.

Environmental Influences

The analysis of dose rates across different settings reveals the profound impact of environmental factors on luminescence dating. In particular, the elevated levels of cosmic radiation on Mars, much higher than on Earth, complicate dose rate assessments. This heightened cosmic exposure not only

increases the complexity of luminescence signals but also risks altering geological markers over time. Understanding these environmental influences is essential for interpreting luminescence data from Martian sediments accurately. As future Martian missions target similar depositional environments, it will be critical to account for cosmic radiation's effect on dose rates to ensure reliable chronological interpretations.

Sample Distinctions

The distinctions in luminescence behaviour between IR_{50} and $pIRIR_{200}$ signals highlight important differences in sediment sources and formation processes. The challenging behaviour of outlier sample PIL3, likely derived from mixed sources, underscores the need to carefully distinguish between sediment origins when interpreting luminescence data. This is particularly relevant for Martian missions, where mixed-source sediments may complicate age determinations. Notably, samples from dune environments exhibited more consistent luminescence behaviour, suggesting that future missions on Mars could prioritize sampling aeolian deposits to enhance the reliability of dating results. This finding points to the importance of selecting well-bleached sediments for more accurate age assessments in extraterrestrial studies.

Challenges in Stratigraphic Comparison

Correlating luminescence ages from slackwater deposits (e.g., samples PIL11, PIL12, PIL13) posed significant challenges. To address this, the temperature of the pIRIR protocol was reduced from 200°C to 160°C, a strategy typically employed for younger samples. However, this adaptation revealed highly variable luminescent characteristics within individual samples. The age discrepancies likely resulted from low bleaching efficiency, environmental sensitivity, and the complex depositional history of these grains. This variability highlights the intricacies of luminescence behaviour in environments where light exposure is limited, such as slackwater deposits. Future investigations should focus on refining dating protocols for specific depositional settings and explore methods to mitigate the challenges posed by incomplete bleaching.

Terrestrial Conclusions: Stratigraphy and Paleoclimatic Interpretation

This study provides significant insights into the influence of climatic oscillations on the sedimentary development of the El Jable plain and Famara alluvial fan systems. By integrating luminescence dating with broader paleoclimatic trends, it becomes evident how global climatic fluctuations shaped depositional environments in arid and semi-arid regions. The alternating wet and dry phases within the sedimentary sequences highlight the critical role of climate variability in controlling sediment transport and deposition.

The stratigraphic records from Lanzarote illustrate the dynamic interaction between aeolian and alluvial processes, driven by episodes of increased moisture and aridity. Based on the luminescence ages obtained, the following trends can be outlined for the Marine Isotope Stages (MIS):

- MIS 6: Associated with increased aridity, reflected in the dominance of aeolian processes. Arid conditions favored the formation and migration of dune systems across the landscape.
- MIS 5e: A relatively moist period characterized by increased rainfall and weathering, leading to enhanced alluvial deposition. This phase reflects more humid conditions, promoting the development of alluvial fans.
- MIS 5c and 5a: Periods of fluctuating humidity and aridity. Interspersed phases of enhanced aeolian activity and more humid conditions contributed to the deposition of alluvial layers.
- MIS 4: Marked by significant aridification, with cold and dry conditions leading to intense aeolian processes. Dune formation was particularly active, driven by wind-dominated sediment transport.
- MIS 3: Characterized by alternating periods of increased humidity and brief dry peaks. This relatively moist phase facilitated the development of alluvial deposits and episodic fluvial activity.
- MIS 2: Despite being a cold stage globally, MIS 2 in Lanzarote shows evidence of wet conditions, with fluvial and alluvial activity indicating episodic rainfall and increased moisture.

This pattern of alternating moisture and aridity provides valuable insights into the paleoclimatic conditions of the Late Quaternary in Lanzarote, forming a basis for comparative studies of sedimentary processes on Mars.

Martian Conclusions: Implications for Exploration

The Martian analogs studied in Lanzarote, offer critical insights for understanding sedimentary processes on Mars. The successful use of luminescence dating protocols in basalt-rich environments on Earth suggests that similar techniques can be applied on Mars to date volcanic and aeolian sediments. As aeolian processes are currently dominant on Mars, targeting well-bleached dune deposits offers the best opportunity for accurate in-situ dating. This has significant implications for future rover missions, which could focus on these deposits to reconstruct the planet's more recent geological history.

Moreover, by drawing parallels between Lanzarote's alluvial systems and Martian features, such as the Jezero Crater or the Proctor Crater dune fields, this study provides a framework for interpreting the interactions between water-driven and wind-driven processes on Mars. The stratigraphic findings from Earth serve as analogs, offering a deeper understanding of how Mars' landscapes may have evolved under fluctuating climatic conditions.

General Conclusion and Future Directions

The insights gained from this terrestrial luminescence dating study significantly enhance our understanding of the complex evolution of different depositional environments on Lanzarote. These findings, particularly the reconstruction of the El Jable basin's sedimentary history, provide a crucial framework for interpreting how similar processes may have occurred on Mars. The correlation of Earth's climatic oscillations with depositional patterns—such as the interplay between dune formation and alluvial fan systems—offers a valuable analog for envisioning potential paleoenvironmental scenarios on Mars.

Moreover, the facies correlation between Lanzarote's aeolian and alluvial deposits and Martian terrains deepens our knowledge of extra-terrestrial landscapes. By identifying how sediment transport and depositional mechanisms are influenced by climatic factors on Earth, we can more accurately hypothesize the conditions under which similar Martian deposits may have formed. This study serves as a foundational reference for guiding future Martian investigations, from rover missions targeting specific sedimentary structures to long-term studies aimed at unraveling the planet's geological history. Ultimately, this work provides key insights into the broader exploration

of Martian geological processes, advancing both planetary science and the methodologies used for in-situ dating of extra-terrestrial environments.

Bibliography

Agee, C.B., Wilson, N.V., McCubbin, F., Ziegler, K., Polyark, V.J., Sharp, Z.D., Asmerom, Y., Nunn, M.N., Shaheen, R., Thiemens, M.H., Steel, A., Foget, M.L., Bowden, R., Glamoclija, M., Zhang, Z., Elardo, S.M., 2013. Unique meteorite from early Amazonian Mars: water-rich basaltic breccia Northwest Africa 7034. Science 339, 780–785.

Aitken MJ. 1985. Thermoluminescence Dating. London: Academic

Aitken MJ. 1998. An Introduction to Optical Dating. Oxford: Oxford University Press

Alonso-Zarza, A. M., & Tanner, L. H. (2009). Carbonates in continental settings: facies, environments, and processes. Elsevier.

Alonso-Zarza, A. M., Bustamante, L., Huerta, P., Rodríguez-Berriguete, Á., & Huertas, M. J. (2016). Chabazite and dolomite formation in a dolocrete profile: An example of a complex alkaline paragenesis in Lanzarote, Canary Islands. Sedimentary Geology, 337, 1-11.

Alonso-Zarza, A.M., Silva, P.G., (2002). Quaternary laminar calcretes with bee nests: evidences of small-scale climatic fluctuations, Eastern Canary Islands, Spain. Palaeogeography, Palaeoclimatology, Palaeoecology 178, 1192135.

Amils R., Fernández-Remolar, D. and the Ipbsl Team. Río Tinto: a geochemical and mineralogical terrestrial analogue of Mars. Life, 2014, 4, 511-34.

Andersen, K. K., Svensson, A., Johnsen, S. J., Rasmussen, S. O., Bigler, M., Röthlisberger, R., ... & Clausen, H. B. (2006). The Greenland ice core chronology 2005, 15–42 ka. Part 1: constructing the time scale. Quaternary Science Reviews, 25(23-24), 3246-3257.

Andreucci, S., Bateman, M.D., Zucca, C., Kapur, S., Akşit, İ., Dunajko, A. and Pascucci, V. (2012) Evidence of Saharan dust in upper Pleistocene reworked palaeosols of northwest Sardinia, Italy: palaeoenvironmental implications. Sedimentology, 59, 917–938.

Andreucci, S., Clemmensen, L. B., & Pascucci, V. (2010a). Transgressive dune formation along a cliffed coast at 75 ka in Sardinia, Western Mediterranean: a record of sea-level fall and increased windiness. Terra Nova, 22(6), 424-433.

Andreucci, S., Clemmensen, L. B., Murray, A. S., & Pascucci, V. (2010b). Middle to late Pleistocene coastal deposits of Alghero, northwest Sardinia (Italy): Chronology and evolution. Quaternary International, 222(1-2), 3-16.

Andreucci, S., Pascucci, V., Murray, A. S., & Clemmensen, L. B. (2009). Late Pleistocene coastal evolution of San Giovanni di Sinis, west Sardinia (Western Mediterranean). Sedimentary Geology, 216(3-4), 104-116.

Andreucci, S., Sechi, D., Buylaert, J. P., Sanna, L., & Pascucci, V. (2017). Post-IR IRSL290 dating of K-rich feldspar sand grains in a wind-dominated system on Sardinia. Marine and Petroleum Geology, 87, 91-98.

Ankjærgaard, C., & Murray, A. S. (2007). Total beta and gamma dose rates in trapped charge dating based on beta counting. Radiation Measurements, 42(3), 352-359.

Auclair, M., Lamothe, M., & Huot, S. (2003). Measurement of anomalous fading for feldspar IRSL using SAR. Radiation measurements, 37(4-5), 487-492.

Ayoub, F., Avouac, J. P., Newman, C. E., Richardson, M. I., Lucas, A., Leprince, S., & Bridges, N. T. (2014). Threshold for sand mobility on Mars calibrated from seasonal variations of sand flux. Nature communications, 5(1), 5096.

Baker, V. R., Strom, R. G., Gulick, V. C., Kargel, J. S., Komatsu, G., & Kale, V. S. (1991). Ancient oceans, ice sheets and the hydrological cycle on Mars. Nature, 352(6336), 589-594.

Balcells Herrera, R., Barrera Morate, J.L., Gómez Sainz de Aja, J. A., Ruiz García, M.ª T. (2004a). Mapa geológico y Memoria de la Hoja n.º 95/96-69, 1080-I, IV (Caleta de Sebo). Mapa Geológico de España E. 1:25.000. Segunda Serie (MAGNA), Primera edición. IGME. Depósito legal: M-3932-2004 NIPO: 40504-012-9

Balcells Herrera, R., Barrera Morate, J.L., Gómez Sainz de Aja, J. A., Ruiz García, M.ª T. (2004b). Mapa geológico y Memoria de la Hoja n. º 95-70, 1080-III (Soo). Mapa Geológico de España E. 1:25.000. Segunda Serie (MAGNA), Primera edición. IGME. Depósito legal: M-3931-2004 NIPO: 40504-012-9

Balcells Herrera, R., Barrera Morate, J.L., Gómez Sainz de Aja, J. A., Ruiz García, M.ª T., Hoyos, M. (2004c). Mapa geológico y Memoria de la Hoja n. º 95-71, 1082-IV (Teguise). Mapa Geológico de España E. 1:25.000. Segunda Serie (MAGNA), Primera edición. IGME. Depósito legal: M-3935-2004 NIPO: 40504-012-9

Balcells Herrera, R., Barrera Morate, J.L., Ruiz García, M.ª T., Hoyos, M., Brändle, J. L. (2004d). Mapa geológico y Memoria de la Hoja n.º 95/96-72, 1082 II-III (Arrecife). Mapa Geológico de España E. 1:25.000. Segunda Serie (MAGNA), Primera edición. IGME. Depósito legal: M-3927-2004 NIPO: 40504-012-9

Balcells Herrera, R., Barrera Morate, J.L., Ruiz García, M.ª T., Hoyos, M. (2004e). Mapa geológico y Memoria de la Hoja n. º 96-70, 1080-II (Harìa). Mapa Geológico de España E. 1:25.000. Segunda Serie (MAGNA), Primera edición. IGME. Depósito legal: M-3930-2004 NIPO: 40504-012-9

Balcells Herrera, R., Barrera Morate, J.L., Ruiz García, M.ª T., Hoyos, M. (2004f). Mapa geológico y Memoria de la Hoja n. º 96-71, 1082-I (Guatiza). Mapa Geológico de España E. 1:25.000. Segunda Serie (MAGNA), Primera edición. IGME. Depósito legal: M-3929-2004 NIPO: 40504-012-9

Balcells Herrera, R., Barrera Morate, J.L., Ruiz García, M.ª T., Hoyos, M. (2004g). Mapa geológico y Memoria de la Hoja n. º 95-71, 1082-IV (Teguise). Mapa Geológico de España E. 1:25.000. Segunda Serie (MAGNA), Primera edición. IGME. Depósito legal: M-3935-2004 NIPO: 40504-012-9

Balcells Herrera, R., Gómez Sainz de Aja, J. A., Barrera Morate, J. L., Ruiz García, Mª T., Hoyos, M., Brändle, J. L. (2004h). Mapa geológico y Memoria de la Hoja n. º 93/94-72, 1081 II (Yaiza). Mapa Geológico de España E. 1:25.000. Segunda Serie (MAGNA), Primera edición. IGME. Depósito legal: M-3928-2004 NIPO: 40504-012-9

Bandfield, J. L. (2002). Global mineral distributions on Mars. Journal of Geophysical Research: Planets, 107(E6), 9-1.

Bandfield, J. L., Hamilton, V. E., & Christensen, P. R. (2000). A global view of Martian surface compositions from MGS-TES. Science, 287(5458), 1626-1630.

Bardají, T., Roquero, E., Cabero, A., Zazo, C., Goy, J. L., Dabrio, C. J., ... & Martínez-Graña, A. M. (2022). Abrupt environmental changes during the last glacial cycle in Western Mediterranean (Formentera Island, Balearic archipelago, Spain). Quaternary International, 638, 159-179.

Bellido Mulas, F., Pineda Velasco, A. y Puente Alvarez, N.; Mapa Geológico Digital continuo E. 1: 25.000, Zona Canarias - Lanzarote. (Zona-2910). in GEODE. Mapa Geológico Digital continuo de España.[en línea]. [Date of consultation 15/04/2024]. Disponible en: http://info.igme.es/cartografiadigital/geologica/geodezona.aspx?Id=Z2910

Berman, D. C., Crown, D. A., & Joseph, E. C. (2015). Formation and mantling ages of lobate debris aprons on Mars: Insights from categorized crater counts. Planetary and Space Science, 111, 83-99.

Bishop, J. L., Fairén, A. G., Michalski, J. R., Gago-Duport, L., Baker, L. L., Velbel, M. A., ... & Rampe, E. B. (2018). Surface clay formation during short-term warmer and wetter conditions on a largely cold ancient Mars. Nature Astronomy, 2(3), 206-213.

Blair, M. W., Kalchgruber, R., & McKeever, S. W. S. (2007). Developing luminescence dating for extraterrestrial applications: Characterization of martian simulants and minerals. Radiation measurements, 42(3), 392-399.

Blair, T. C., & McPherson, J. G. (1994). Alluvial fans and their natural distinction from rivers based on morphology, hydraulic processes, sedimentary processes, and facies assemblages. Journal of sedimentary research, 64(3a), 450-489.

Blair, T.C. (1999a) Sedimentary processes and facies of the waterlaid Anvil Spring Canyon alluvial fan, Death Valley, California. Sedimentology, 46, 913–940.

Blair, T.C. (1999b) Sedimentology of the debris-flow dominated Warm Spring Canyon alluvial fan, Death Valley, California. Sedimentology, 46, 941–965.

Blair, T.C., McPherson, J.G. (2009). Processes and Forms of Alluvial Fans. In: Parsons, A.J., Abrahams, A.D. (eds) Geomorphology of Desert Environments. Springer, Dordrecht. https://doi.org/10.1007/978-1-4020-5719-9_14

Boessenkool, K. P., Brinkhuis, H., Schönfeld, J., & Targarona, J. (2001). North Atlantic sea-surface temperature changes and the climate of western Iberia during the last deglaciation; a marine palynological approach. Global and Planetary Change, 30(1-2), 33-39.

Bond, G., Broecker, W., Johnson, S., McManus, J., Labeyrie, l., Jouzel, J., Bonani, G., 1993. Correlations between climate records from North Atlantic sediments and Green-land ice. Nature 365, 143–147.

Bond, G., Heinrich, H., Broecker, W., Labeyrie, l., McManus, J., Andrews, J., Huon, S., Jantschik, R., Clasen, S., Simet, C., Tedesco, K., Klas, M., Bonani, G., Ivy, S., 1992. Evidence for massive discharges of icebergs into the North Atlantic Ocean during the last glacial period. Nature 360, 245–249.

Bond, G., Showers, W., Cheseby, M., Lotti, R., Almasi, P., deMenocal, P., Priore, P., Cullen, H., Hajdas, I, Bonani, G., 1997. A pervasive millenial-scale cycle in North Atlantic Holocene and glacial climates. Science 278, 1257–1266.

Bøtter-Jensen, L., & Mejdahl, V. (1988). Assessment of beta dose-rate using a GM multicounter system. International Journal of Radiation Applications and Instrumentation. Part D. Nuclear Tracks and Radiation Measurements, 14(1-2), 187-191.

Bouab, N., Lamothe, M., 1995. Geochronological framework for the Quaternary paleoclimatic record of the Rosa Negra section. (Fuerteventura Canary Islands, Spain). In: Meco, J., Petit-Maire, N. (Eds.) Climate of the Past. International Union of Geological Sciences, Unesco, Earth Processes in Global Change. pp 37–42, Las Palmas de Gran Canaria; Universidad, 1997

Bourke, M. C., Balme, M., Beyer, R. A., Williams, K. K., & Zimbelman, J. (2006). A comparison of methods used to estimate the height of sand dunes on Mars. Geomorphology, 81(3-4), 440-452.

Bourke, M. C., Edgett, K. S., & Cantor, B. A. (2008). Recent aeolian dune change on Mars. Geomorphology, 94, 247–255. https://doi.org/10.1016/j.geomorph.2007.05.012 Mars. Geomorphology 81. http://dx.doi.org/10.1016/j.geomorph.2006.04.023.

Bowman, D. (2019). Principles of alluvial fan morphology (p. 151). Dordrecht: Springer.

Bridges, N. T., Ayoub, F., Avouac, J. P., Leprince, S., Lucas, A., & Mattson, S. (2012). Earth-like sand fluxes on Mars. Nature, 485(7398), 339-342.

Briere, P. R. (2000). Playa, playa lake, sabkha: Proposed definitions for old terms. Journal of Arid Environments, 45(1), 1-7.

Buylaert JP, Jain M, Murray AS, Thomsen KJ, Thiel C and Sohbati R, 2012. A robust feldspar luminescence dating method for Middle and Late Pleistocene sediments. Boreas 41: 435–451, DOI 10.1111/j.1502-3885.2012.00248.x.

Buylaert, J. P., Murray, A. S., Thomsen, K. J., and Jain, M. (2009). Testing the Potential of an Elevated Temperature IRSL Signal from K-Feldspar. Radiat. Measurements 44, 560–565. doi:10.1016/j.radmeas.2009.02.007

Buylaert, J. P., Thiel, C., Murray, A. S., Vandenberghe, D. A., Yi, S., & Lu, H. (2011). IRSL and post-IR IRSL residual doses recorded in modern dust samples from the Chinese Loess Plateau. Geochronometria, 38, 432-440.

Byrne, S. (2009). The polar deposits of Mars. Annual Review of Earth and Planetary Sciences, 37, 535-560.

Byrne, S., Sori, M. M., Russell, P., Pathare, A. V., Becerra, P., Molaro, J. L., et al. (2017). Mars polar cliffs: Stressed out and falling apart. European Planetary Science Congress, abstract EPSC2017-333

Cabrera, L., Alonso, I., & Alcántara-Carrió, J. (2006). Spatial changes in surface sediments derived from the different sediment sources and land uses at" El Jable"(Lanzarote, Spain). Journal of Coastal Research, 48, 29-34.

Cabrol, N. A., & Grin, E. A. (1999). Distribution, classification, and ages of Martian impact crater lakes. Icarus, 142(1), 160-172.

Cannon K. M., Mustard J. F., Salvatore M. R. Alteration of immature sedimentary rocks on Earth and Mars: Recording aqueous and surface-atmosphere processes. Earth Planet. Sci. Lett., 2015, 417, 78-86.

Carr Michael H., 2012. The fluvial history of Mars. Phil. Trans. R. Soc. A. 370, 2193–2215.

Carr, M. H. & Head, J. W. Oceans on Mars: An assessment of the observational evidence and possible fate. J. Geophys. Res. 108, 5042, 10.1029/2002JE001963 (2003).

Carr, M. H. (2007). The surface of Mars (Vol. 6). Cambridge University Press.

Carracedo, J. C., & Rodríguez Badiola, E. (1992). Evolución geológica y magmática de la isla de Lanzarote, Islas Canarias

Carracedo, J. C., Badiola, E. R., & Soler, V. (1992). The 1730–1736 eruption of Lanzarote, Canary Islands: a long, high-magnitude basaltic fissure eruption. Journal of Volcanology and Geothermal Research, 53(1-4), 239-250.

Carracedo, J. C., Singer, B., Jicha, B., Guillou, H., Rodríguez Badiola, E., Meco, J., ... & Láinez, A. (2003). La erupción y el tubo volcánico del Volcán Corona (Lanzarote, Islas Canarias).

Casañas, F. G.-T. (1990). Aves gigantes en el Mioceno de Famara (Lanzarote). Revista de La Academia Canaria de Ciencias:= Folia Canariensis Academiae Scientiarum, 2 (1), 71–79.

Casini, L., Andreucci, S., Sechi, D., Huang, C. Y., Shen, C. C., & Pascucci, V. (2020). Luminescence dating of Late Pleistocene faults as evidence of uplift and active tectonics in Sardinia, W Mediterranean. Terra Nova, 32(4), 261-271.

Castañeda, I. S., Mulitza, S., Schefuß, E., Lopes dos Santos, R. A., Sinninghe Damsté, J. S., & Schouten, S. (2009). Wet phases in the Sahara/Sahel region and human migration patterns in North Africa. Proceedings of the National Academy of Sciences, 106(48), 20159-20163.

Chapman, M. ed., 2007. The geology of Mars: evidence from earth-based analogs (Vol. 5). Cambridge University Press.

Chojnacki, M., Banks, M.E., Fenton, L.K., and Urso, A.C., 2019, Boundary condition controls on the high-sand-flux regions of Mars: Geology, v. 47, p. 427–430, https:// doi .org /10 .1130 /G45793.1.

Christensen, P. R. (2006). Water at the poles and in permafrost regions of Mars. Elements, 2(3), 151-155.

Christensen, P. R., McSween Jr, H. Y., Bandfield, J. L., Ruff, S. W., Rogers, A. D., Hamilton, V. E., ... & Moersch, J. E. (2005). Evidence for magmatic evolution and diversity on Mars from infrared observations. Nature, 436(7050), 504-509.

Christensen, P.R., Bandfield, J.L., Bell III, J.F., Gorelick, N., Hamilton, V.E., Ivanov, A., Jakosky, B.M., Kieffer, H.H., Lane, M.D., Malin, M.C. and McConnochie, T., 2003. Morphology and composition of the surface of Mars: Mars Odyssey THEMIS results. science, 300(5628), pp.2056-2061.

Christensen, P.R., Bandfield, J.L., Hamilton, V.E., Ruff, S.W., Kieffer, H.H., Titus, T.N., Malin, M.C., Morris, R.V., Lane, M.D., Clark, R.L. and Jakosky, B.M., 2001. Mars Global Surveyor Thermal Emission Spectrometer experiment: investigation description and surface science results. Journal of Geophysical Research: Planets, 106(E10), pp.23823-23871.

Clark, P. U., Dyke, A. S., Shakun, J. D., Carlson, A. E., Clark, J., Wohlfarth, B., ... & McCabe, A. M. (2009). The last glacial maximum. science, 325(5941), 710-714.

Clifford, S. M. & Parker, T. J. The evolution of the martian hydrosphere: Implications for the fate of a primordial ocean and the current state of the northern plains. Icarus 154, 40–79 (2001).

Clifford, S. M., & Parker, T. J. (2001). The evolution of the Martian hydrosphere: Implications for the fate of a primordial ocean and the current state of the northern plains. Icarus, 154(1), 40-79.

Coello, J., Cantagrel, J.-M., Hernán, F., Fúster, J.-M., Ibarrola, E., Ancochea, E., Casquet, C., Jamond, C., de Téran, J.-R. D., & Cendrero, A. (1992). Evolution of the eastern volcanic ridge of the Canary Islands based on new K Ar data. Journal of Volcanology and Geothermal Research, 53(1–4), 251–274. https://doi.org/10.1016/ 0377-0273(92)90085-R

Cohen, B. A., Malespin, C. A., Farley, K. A., Martin, P. E., Cho, Y., & Mahaffy, P. R. (2019). In situ geochronology on Mars and the development of future instrumentation. Astrobiology, 19(11), 1303-1314.

Coles, K. S., Tanaka, K. L., & Christensen, P. R. (2019). The atlas of Mars: mapping its geography and geology. Cambridge University Press.

Connerney, J. E. P., Acuna, M. H., Wasilewski, P. J., Kletetschka, G., Ness, N. F., Reme, H., Lin, R. P., and Mitchell, D. L., 2001, The global magnetic field of Mars and implications for crustal evolution: Geophysical Research Letters, v. 28, no. 21, p. 4015-4018.

Connerney, J., Acuna, M., Wasilewski, P. J., Ness, N. F., Reme, H., Mazelle, C., Vignes, D., Lin, R., Mitchell, D., and Cloutier, P., 1999, Magnetic lineations in the ancient crust of Mars: Science, v. 284, no. 5415, p. 794-798.

Conway, S. J., de Haas, T., & Harrison, T. N. (2019). Martian gullies: A comprehensive review of observations, mechanisms and insights from Earth analogues. Geological Society, London, Special Publications, 467(1), 7-66.

Costard, F., Séjourné, A., Kelfoun, K., Clifford, S., Lavigne, F., Di Pietro, I., & Bouley, S. (2017). Modeling tsunami propagation and the emplacement of thumbprint terrain in an early Mars ocean. Journal of Geophysical Research: Planets, 122(3), 633-649.

Criado, C., & Dorta, P. (2003). An unusual 'blood rain'over the Canary Islands (Spain). The storm of January 1999. Journal of Arid Environments, 55(4), 765-783.

Cunningham, A. C., Murray, A. S., Armitage, S. J., & Autzen, M. (2018). High-precision natural dose rate estimates through beta counting. Radiation Measurements, 120, 209-214.

Danmati, B., (1997). Mineralogical and sedimentological characterization of quaternary eolian formations and palaeosols in Fuerteventura and Lanzarote (Canary Island, Spain). In: Meco, J., Petit-Maire, N. (Eds.), Climates of the Past. Servicio de Publicaciones, Universidad de Las Palmas de Gran Canaria, pp. 71^77.

Dansgaard, W., Clausen, H.B., Gundestrup, N., Hammer, C.U., Johnsen, S.F., Kristindottir, P.M., Reeh, N., 1982. A new Greenland deep ice core. Science 218, 1273–1277.

Dansgaard, W., Johnsen, S.J., Clausen, H.B., Dahl-Jensen, D., Gundestrup, N.S., Hammer, C.U., Hvidberg, C.S., Steffense, J.P., Sveinbj¨ornsdottir, A.E., Jouzel, J., Bond, G., 1993. Evidence for general instability of past climate from a 250-kyr icecore record. Nature 364, 218.

Daubar, I. J., McEwen, A. S., Byrne, S., Kennedy, M. R., & Ivanov, B. (2013). The current martian cratering rate. Icarus, 225(1), 506-516.

de Haas, T., Ventra, D., Hauber, E., Conway, S. J., & Kleinhans, M. G. (2015). Sedimentological analyses of Martian gullies: the subsurface as the key to the surface. Icarus, 258, 92-108.

Detschel, M. J., & Lepper, K. (2009). Optically stimulated luminescence dating properties of Martian sediment analogue materials exposed to a simulated Martian solar spectral environment. Journal of Luminescence, 129(4), 393-400.

Di Achille, G., & Hynek, B. M. (2010). Ancient ocean on Mars supported by global distribution of deltas and valleys. Nature Geoscience, 3(7), 459-463.

Di Pietro, I., Schmidt, G., Tangari, A. C., Salese, F., Silvestro, S., Fairén, A. G., ... & Pondrelli, M. (2023). Groundwater-Controlled Deposition of Equatorial Layered Deposits in Central Arabia Terra, Mars. Journal of Geophysical Research: Planets, 128(3), e2022JE007504.

Dickinson W. W., Rosen M. R. Antarctic permafrost: An analogue for water and diagenetic minerals on Mars. Geology, 2003, 31, 199-202.

Doran, P. T., Clifford, S. M., Forman, S. L., Nyquist, L., Papanastassiou, D. A., Stewart, B. W., ... & Tanaka, K. (2004). Mars chronology: assessing techniques for quantifying surficial processes. Earth-Science Reviews, 67(3-4), 313-337.

Dorn, R. I. (1994). The role of climatic change in alluvial fan development. In Geomorphology of desert environments (pp. 593-615). Dordrecht: Springer Netherlands.

Dreibus, G., and Wanke, H., (1985) Mars, a volatile-rich planet: Meteoritics, v. 20, p. 367-381.

Driscoll, E. M., Tinkler, K. J., & Hendry, G. L. (1965). The geology and geomorphology of Los Ajaches, Lanzarote. Geological Journal, 4(2), 321-334.

Duller, G. A. (2004). Luminescence dating of Quaternary sediments: recent advances. Journal of Quaternary Science, 19(2), 183-192.

Duller, G. A. (2008). Luminescence Dating: guidelines on using luminescence dating in archaeology.

Duller, G. A. T., Bøtter-Jensen, L., & Murray, A. S. (2000). Optical dating of single sand-sized grains of quartz: sources of variability. Radiation Measurements, 32(5-6), 453-457.

Dundas, C. M., McEwen, A. S., Diniega, S., Hansen, C. J., Byrne, S., & McElwaine, J. N., (2019). The formation of gullies on Mars today. Geological Society, London, Special Publications, 467(1), 67-94.

Dundas, C.M., McEwen, A.S., Chojnacki, M. et al. Granular flows at recurring slope lineae on Mars indicate a limited role for liquid water. Nature Geosci 10, 903–907 (2017). https://doi.org/10.1038/s41561-017-0012-5

Edwards, N., Meco, J., 2000. Morphology and palaeoenvironment of brood cells of Quaternary ground-nesting solitary bees (Hymenoptera, Apidae) from Fuerteventura, Canary Islands, Spain. Proceedings of the Geologists' Association 111, 173–183.

Einsele, G., 2000. Sedimentary Basins: Evolution, Facies, and Sediment Budget. Springer, Berlin Heidelberg, p. 792.

El-Maarry M., Black S., Hynek B., Mchenry L. Mineralogy of fumarolic deposits from Iceland as analogs for ancient hydrothermal systems on Mars: role of temperature. LPSC 48. 2017, abst. 2870.

Esposito, P., Banerdt, W., Lindal, G., Sjogren, W., Slade, M., Bills, B., Smith, D., and Balmino, G., 1992, Gravity and topography: Mars, p. 209-248.

Fallacara G. & Netti V., 2023. Architecture beyond the planet earth. Inhabit Mars. Hive Mars: design of a hybrid-class, scalable settlement, on the martian surface. Gangemi Editore. ISBN: 9788849245714

Farrell, K. M. (2001). Geomorphology, facies architecture, and high-resolution, non-marine sequence stratigraphy in avulsion deposits, Cumberland Marshes, Saskatchewan. Sedimentary Geology, 139(2), 93-150.

Fassett, C. I., and Head III, J. W., 2008, The timing of Martian valley network activity: Constraints from buffered crater counting: Icarus, v. 195, no. 1, p. 61-89.

Fassett, C. I., and J. W. Head III (2008), The timing of Martian valley network activity: Constraints from buffered crater counting, Icarus, 195(1), 61–89, doi:10.1016/J.Icarus.2007.12.009.

Fedorova, A., Bertaux, J. L., Betsis, D., Montmessin, F., Korablev, O., Maltagliati, L., & Clarke, J. (2018). Water vapor in the middle atmosphere of Mars during the 2007 global dust storm. Icarus, 300, 440-457.

Fenton, L. K. (2006). Dune migration and slip face advancement in the Rabe crater dune field, Mars. Geophysical Research Letters, 33, L20201. https://doi.org/10.1029/2006GL027133

Fenton, L. K. (2006). Dune migration and slip face advancement in the Rabe crater dune field, Mars. Geophysical Research Letters, 33, L20201.

Fenton, L. K., Bandfield, J. L., & Ward, A. W. (2003). Aeolian processes in Proctor Crater on Mars: Sedimentary history as analyzed from multiple data sets. Journal of Geophysical Research: Planets, 108(E12).

Fenton, L. K., Bandfield, J. L., & Ward, A. W. (2003). Aeolian processes in Proctor Crater on Mars: Sedimentary history as analyzed from multiple data sets. Journal of Geophysical Research: Planets, 108(E12).

Fenton, L. K., Bishop, J. L., King, S., Lafuente, B., Horgan, B., Bustos, D., & Sarrazin, P. (2017). Sedimentary differentiation of aeolian grains at the White Sands National Monument, New Mexico, USA. Aeolian research, 26, 117-136.

Fenton, L.K., T. I. Michaels, and M. Chojnacki (2015), Late Amazonian aeolian features, gradation, wind regimes, and Sediment State in the Vicinity of the Mars Exploration Rover Opportunity, Meridiani Planum, Mars, Aeolian Res., 16(2015), 75–99, doi:10.1016/ j.aeolia.2014.11.004.

Fernández-Remolar D., Prieto-Ballesteros O., Rodríguez N., Gómez F., Amils R., Gómez-Elvira J., Stoker C. Underground habitats in the Río Tinto basin: a model for subsurface life habitats on Mars. Astrobiology, 2008, 8 (5), 1023-1047.

Fernando, B., Daubar, I. J., Charalambous, C., Grindrod, P. M., Stott, A., Al Ateqi, A., ... & Banerdt, W. B. (2023). A tectonic origin for the largest marsquake observed by InSight. Geophysical Research Letters, 50(20), e2023GL103619.

Fouchet, T., Lellouch, E., Ignatiev, N. I., Forget, F., Titov, D. V., Tschimmel, M., ... & Encrenaz, T. (2007). Martian water vapor: Mars Express PFS/LW observations. Icarus, 190(1), 32-49.

Fuchs, M., & Lang, A. (2009). Luminescence dating of hillslope deposits—A review. Geomorphology, 109(1-2), 17-26.

Fuster, J. M. (1968). Geología y volcanología de las Islas Canarias: Tenerife. CSIC, Instituto Lucas Mallada.

Fúster, J.-M., Fernández-Santin, S., & Sagredo, J. (1968). Geología y volcanología de las Islas Canarias: Lanzarote. Institudo Lucas Mallada, CSIC.

Geissler P.E., Johnson J.R., Sullivan R., Herkenhoff K., Mittlefehldt D., Fergason R., Ming D., Morris R., Squyres S., Soderblom L., Golombek M., 2008. First in situ investigation of a dark wind streak on Mars. J. Geophys. Res, VOL. 113, E12S31, doi:10.1029/2008JE003102.

Geissler, P. E., 2014. The birth and death of transverse aeolian ridges on Mars. J. Geophys. Res. Planets, 119, 2583–2599, doi:10.1002/2014JE004633.

Genise, J. F., & Edwards, N. (2003). Ichnotaxonomy, origin, and paleoenvironment of Quaternary insect cells from Fuerteventura, Canary Islands, Spain. Journal of the Kansas Entomological Society, 320-327.

Genise, J. F., Alonso-Zarza, A. M., Verde, M., & Meléndez, A. (2013). Insect trace fossils in aeolian deposits and calcretes from the Canary Islands: their ichnotaxonomy, producers, and palaeoenvironmental significance. Palaeogeography, Palaeoclimatology, Palaeoecology, 377, 110-124.

Genova, A., Goossens, S., Lemoine, F. G., Mazarico, E., Neumann, G. A., Smith, D. E., & Zuber, M. T. (2016). Seasonal and static gravity field of Mars from MGS, Mars Odyssey and MRO radio science. Icarus, 272, 228-245.

Gerstell, M. F., Oded Aharonson, Norbert Schorghofer, A distinct class of avalanche scars on Mars, Icarus, Volume 168, Issue 1, 2004, Pages 122-130, ISSN 0019-1035, https://doi.org/10.1016/j.icarus.2003.11.005.

Gibling, M. R. (2006). Width and thickness of fluvial channel bodies and valley fills in the geological record: a literature compilation and classification. Journal of sedimentary Research, 76(5), 731-770.

Gibson E. K., Wentworth S. J., McKay D. S. Chemical weathering and diagenesis of a cold desert soil from Wright Valley, Antarctica: An analog of Martian weathering processes. J. Geophys. Res. Sol. Ea., 1983, 88, A912-AA928

Godfrey-Smith DI, Huntley DJ, Chen WH. 1988. Optical dating studies of quartz and feldspar sediment extracts. Quat. Sci. Rev. 7:373–80

Golombek, M., K. Robinson, A. Mcewen, N. Bridges, B. Ivanov, L. Tornabene, and R. Sullivan (2010), Constraints on ripple migration at Meridiani Planum from Opportunity and HiRISE observations of fresh craters, J. Geophys. Res., 115, E00F08, doi:10.1029/2010JE003628.

Golombek, M.P., 2003. The surface of Mars: Not just dust and rocks. Science, 300(5628), pp.2043-2044.

Gómez Sainz de Aja, J. A., Balcells Herrera, R., Barrera Morate, J. L., Ruiz García, Mª T., Hoyos, M., Brändle, J. L. (2004a). Mapa geológico y Memoria de la Hoja n. º 93/94-73, 1084 I-IV (Femés). Mapa Geológico de España E. 1:25.000. Segunda Serie (MAGNA), Primera edición. IGME. Depósito legal: M-3926-2004 NIPO: 40504-012-9

Gómez Sainz de Aja, J. A., Balcells Herrera, R., Barrera Morate, J. L., Ruiz García, Mª T., Hoyos, M., Brändle, J. L. (2004b). Mapa geológico y Memoria de la Hoja n. º 94-71, 1081 I (Tinajo). Mapa Geológico de España E. 1:25.000. Segunda Serie (MAGNA), Primera edición. IGME. Depósito legal: M-3936-2004 NIPO: 40504-012-9

Goñi, M. F. S., Turon, J. L., Eynaud, F., & Gendreau, S. (2000). European climatic response to millennial-scale changes in the atmosphere–ocean system during the Last Glacial period. Quaternary Research, 54(3), 394-403.

Goossens, S., Sabaka, T. J., Genova, A., Mazarico, E., Nicholas, J. B., and Neumann, G. A. (2017). Evidence for a low bulk crustal density for Mars from gravity and topography: Geophysical Research Letters, v. 44, no. 15, p. 7686-7694.

Goudge, T.A., Head, J.W., Mustard, J.F., and Fassett, C.I., 2012, An analysis of open-basin lake deposits on Mars—Evidence for the nature of associated lacustrine deposits and post-lacustrine modification processes: Icarus, v. 219, p. 211–229 (doi:10.1016/j.icarus.2012.02.027).

Goudie, A.S., 2006. Encyclopedia of Geomorphology, Taylor & Francis e-Library.

Gray, H. J., Jain, M., Sawakuchi, A. O., Mahan, S. A., & Tucker, G. E. (2019). Luminescence as a sediment tracer and provenance tool. Reviews of Geophysics, 57(3), 987-1017.

Greensmith, J. T. (2000). Lanzarote, Canary Islands (Issue 62). Geologists' Association.

Guérin, G. (2018). Innovative dose rate determinations for luminescence dating. Elements: An International Magazine of Mineralogy, Geochemistry, and Petrology, 14(1), 15-20.

Guérin, G., Mercier, N., Nathan, R., Adamiec, G., & Lefrais, Y. (2012). On the use of the infinite matrix assumption and associated concepts: a critical review. Radiation Measurements, 47(9), 778-785.

Hamilton, W. B., 2007, Earth's first two billion years-The era of internally mobile crust: MEMOIRS-GEOLOGICAL SOCIETY OF AMERICA, v. 200, p. 233.

Hansen, C. J., Bourke, M., Bridges, N. T., Byrne, S., Colon, C., Diniega, S., ... & Thomas, N. (2011). Seasonal erosion and restoration of Mars' northern polar dunes. Science, 331(6017), 575-578.

Hartmann, W. K., 2003, A traveler's guide to Mars: the mysterious landscapes of the red planet, Workman Publishing.

Hartmann, W. K., and G. Neukum (2001), Cratering chronology and the evolution of Mars, Space Sci. Rev., 96, 165–194, doi:10.1023/A:1011945222010.

Hausen, H. (1959). On the Geology of Lanzarote, Graciosa and the Isletas (Canarian Archipelago): With a Geologic Map in the Scale of 1: 200 000 (Issues 23–24). Helsingfors

Hayward, R. K., Mullins K.F., Fenton L.K., Hare T.M., Titus T.N., Bourke M.C., Colaprete A., Christensen P.R., 2007. Mars Global Digital Dune Database and initial science results. J. Geophys. Res., 112, E11007, doi:10.1029/2007JE002943.

Hayward, R.K., Mullins, K.F., Fenton, L.K., Hare, T.M., Titus, T.N., Bourke, M.C., Colaprete, A., Christensen, P.R., 2008. Mars Global Digital Dune Database and initial science results. Journal of Geophysical Research 112 (E11). doi:10.1029/2007JE002943

Head III, J. W., Hiesinger, H., Ivanov, M. A., Kreslavsky, M. A., Pratt, S., & Thomson, B. J. (1999). Possible ancient oceans on Mars: evidence from Mars Orbiter Laser Altimeter data. Science, 286(5447), 2134-2137.

Head J., 2007. The geology of Mars: new insights and outstanding questions. The Geology of Mars: Evidence from Earth-Based Analog.

Hein, F. J., & Walker, R. G. (1977). Bar evolution and development of stratification in the gravelly, braided, Kicking Horse River, British Columbia. Canadian Journal of Earth Sciences, 14(4), 562-570.

Heinrich, H., 1988. Origin and consequences of cyclic ice rafting in the Northeast Atlantic Ocean during the past 130,000 years. Quat. Res. 29 (2), 142–152.

Heinrich, H., Schmidt, C., Ziemen, F., Mikolajewicz, U., & Roettig, C. B. (2021). Massive deposition of Sahelian dust on the Canary Island Lanzarote during North Atlantic Heinrich Events. Quaternary Research, 101, 51-66.

Hemming, S. R. (2004). Heinrich events: Massive late Pleistocene detritus layers of the North Atlantic and their global climate imprint. Reviews of Geophysics, 42(1).

Hewitt, C., Stouffer, R., Broccoli, A., Mitchell, J., & Valdes, P. J. (2003). The effect of ocean dynamics in a coupled GCM simulation of the Last Glacial Maximum. Climate Dynamics, 20, 203-218.

Hoernle, K. A. J., & Carracedo, J.-C. (2009). Canary Islands geology. University of California Press

Howari, F. M., Sharma, M., Xavier, C. M., Nazzal, Y., & AlAydaroos, F. (2021). Chronological Analysis and Remote Sensing of Craters on the Surface of Mars. Frontiers in Environmental Science, 9, 605893.

Huerta, P., Rodríguez-Berriguete, Á., Martín-García, R., Martín-Pérez, A., Fernández, Á. L. I., & Alonso-Zarza, A. M. (2015). The role of climate and aeolian dust input in calcrete formation in volcanic islands (Lanzarote and Fuerteventura, Spain). Palaeogeography, Palaeoclimatology, Palaeoecology, 417, 66-79.

Hugenholtz, C. H., and T. E. Barchyn (2017), A terrestrial analog for transverse aeolian ridges (TARs): Environment, morphometry, and recent dynamics, Icarus, 289, 239–253, doi:10.1016/j.icarus.2016.08.010.

Hughes, S. S., Haberle, C. W., Kobs Nawotniak, S. E., Sehlke, A., Garry, W. B., Elphic, R. C., ... & Lim, D. S. (2019). Basaltic terrains in Idaho and Hawai 'i as planetary analogs for Mars geology and astrobiology. Astrobiology, 19(3), 260-283.

Huntley, D. J., & Baril, M. R. (1997). The K content of the K-feldspars being measured in optical dating or in thermoluminescence dating. Ancient Tl, 15(1), 11-13.

Huntley, D. J., Godfrey-Smith, D. I., & Thewalt, M. L. (1985). Optical dating of sediments. Nature, 313(5998), 105-107.

Huntley, D. J., & Lamothe, M. (2001). Ubiquity of anomalous fading in K-feldspars and the measurement and correction for it in optical dating. Canadian Journal of Earth Sciences, 38(7), 1093-1106.

Ibarrola, E.; Cantagrel, J. M.; Fuster, J. M.; Coello, J., Jamond, E. (1988): Geocronología de las series volcánicas neógenas de Lanzarote, Islas Canarias. II Congreso Geológico de España, Granada, Tomo Simp. de volcanismo, pp. 345-348.

IGME, 2005. Mapa Geológico de España escala 1:100.000, hoja y memoria n° 88 Lanzarote. 1a edición. Madrid.

Ivanov, M. A., and J. W. Head, Chryse Planitia, Mars: Topographic configuration, outflow channel continuity and sequence, and tests for hypothesized ancient bodies of water using Mars Orbiter Laser Altimeter (MOLA) data, J. Geophys. Res., 106, 3275 – 3295, 2001.

Jacobs, Z., & Roberts, R. G. (2007). Advances in optically stimulated luminescence dating of individual grains of quartz from archeological deposits. Evolutionary Anthropology: Issues, News, and Reviews: Issues, News, and Reviews, 16(6), 210-223.

Jacqué, D. (2006). APS X-rays reveal secrets of Mars' core: Argonne National Laboratory. Retrieved on, p. 07-01.

Jain, M., & Ankjærgaard, C. (2011). Towards a non-fading signal in feldspar: insight into charge transport and tunnelling from time-resolved optically stimulated luminescence. Radiation Measurements, 46(3), 292-309.

Jain, M., Andersen, C. E., Bøtter-Jensen, L., Murray, A. S., Haack, H., & Bridges, J. C. (2006). Luminescence dating on Mars: OSL characteristics of Martian analogue materials and GCR dosimetry. Radiation Measurements, 41(7-8), 755-761.

Jensen, M. F., Nummelin, A., Nielsen, S. B., Sadatzki, H., Sessford, E., Risebrobakken, B., ... & Born, A. (2018). A spatiotemporal reconstruction of sea-surface temperatures in the North Atlantic during Dansgaard–Oeschger events 5–8. Climate of the Past, 14(6), 901-922.

Jiang, J., Zhu, Q., Huang, Y., Zhou, D., Zhao, L., Guo, L., ... & Luo, Y. (2023). Automated and Intelligent Synthesis of Oxygen-Producing Catalysts from Martian Meteorites by Robotic AI-Chemist.

Kalchgruber, R., Blair, M. W., McKeever, S. W., Benton, E. R., & Reust, D. K. (2007). Progress towards robotic in-situ dating of martian sediments using optically stimulated luminescence. Planetary and Space Science, 55(14), 2203-2217.

Kars, R. H., Reimann, T., & Wallinga, J. (2014). Are feldspar SAR protocols appropriate for post-IR IRSL dating? Quaternary Geochronology, 22, 126-136.

Kieffer, H. H., Martin, T., Peterfreund, A. R., Jakosky, B. M., Miner, E. D., and Palluconi, F. D., (1977). Thermal and albedo mapping of Mars during the Viking primary mission: Journal of Geophysical Research, v. 82, no. 28, p. 4249-4291.

Kite, E. S., Sneed, J., Mayer, D. P., & Wilson, S. A. (2017). Persistent or repeated surface habitability on Mars during the late Hesperian-Amazonian. Geophysical Research Letters, 44(9), 3991-3999.

Kochel, R. C., and Baker, V. R. (1982). Paleoflood hydrology. Science 215, 353-61.

Kocurek G, Lancaster N. 1999. Aeolian system sediment state: theory and Mojave Desert Kelso dune field example. Sedimentology 46: 505–515

La Roche, F., Genise, J. F., Castillo, C., Quesada, M. L., García-Gotera, C. M., & De la Nuez, J. (2014). Fossil bee cells from the Canary Islands. Ichnotaxonomy, palaeobiology and palaeoenvironments of Palmiraichnus castellanosi. Palaeogeography, Palaeoclimatology, Palaeoecology, 409, 249-264.

Lapôtre, M. G. A., Ewing, R. C., Lamb, M. P., Fischer, W. W., Grotzinger, J. P., Rubin, D. M., et al. (2016). Large wind ripples on Mars: A record of atmospheric evolution. Science, 353(6294), 55–58. https://doi.org/10.1126/science.aaf3206

Lee P., Bunch T. E., Cabrol N., Cockell C. S., Grieve R. A. F., McKay C. P., Rice J. W. Jr., Schutt J. W., Zent A. P. Haughton-Mars 97 - I: Overview of observations at the Haughton impact crater, a unique Mars analog site in the Canadian High Arctic. LPSC 29. 1998, abst. 1973.

Lepper, K., & McKeever, S. W. (2000). Characterization of fundamental luminescence properties of the Mars soil simulant JSC Mars-1 and their relevance to absolute dating of Martian eolian sediments. Icarus, 144(2), 295-301.

Li, B., & Li, S. H. (2012). Luminescence dating of Chinese loess beyond 130 ka using the non-fading signal from K-feldspar. Quaternary Geochronology, 10, 24-31.

Li, C., & Born, A. (2019). Coupled atmosphere-ice-ocean dynamics in Dansgaard-Oeschger events. Quaternary Science Reviews, 203, 1-20.

Lian, O. B., & Roberts, R. G. (2006). Dating the Quaternary: progress in luminescence dating of sediments. Quaternary Science Reviews, 25(19-20), 2449-2468.

Lomoschitz, A., Marco, A. S., Huertas, M. J., Betancort, J. F., Isern, A., Sanz, E., & Meco, J. (2016). A reappraisal of the stratigraphy and chronology of Early Pliocene palaeontological sites from

Lanzarote Island containing fossil terrestrial animals. Journal of African Earth Sciences, 123, 338–349. https://doi.org/10.1016/j.jafrearsci.2016.08.006

López-García, J. M., Blain, H. A., Bennàsar, M., Sanz, M., & Daura, J. (2013). Heinrich event 4 characterized by terrestrial proxies in southwestern Europe. Climate of the Past, 9(3), 1053-1064.

Losa-Adams, E., Gil-Lozano, C., Fairén, A. G., Bishop, J. L., Rampe, E. B., & Gago-Duport, L. (2021). Long-lasting habitable periods in Gale crater constrained by glauconitic clays. Nature astronomy, 5(9), 936-942.

Lowick, S. E., Trauerstein, M. & Preusser, F. 2012: Testing the application of post IR-IRSL dating to fine grain waterlain sediments. Quaternary Geochronology 8, 33–40.

Madsen, A. T., & Murray, A. S. (2009). Optically stimulated luminescence dating of young sediments: A review. Geomorphology, 109(1-2), 3-16.

Mahaffy, P., R. Webster, C., Sudhir, A., Franz, H., Wong, M., Conrad, P., Harpold, D., J. Jones, J., A. Leshin, L., Manning, H., Owen, T., O. Pepin, R., Squyres, S., Trainer, M., Science Team, M. S. L., Kemppinen, O., Bridges, N., R. Johnson, J., Minitti, M., and Vaniman, (2013). Abundance and Isotopic Composition of Gases in the Martian Atmosphere from the Curiosity Rover, 263-266 p.

Malin, M. C., & Edgett, K. S. (2000). Evidence for recent groundwater seepage and surface runoff on Mars. Science, 288(5475), 2330-2335.

Mangold N., 2003. Geomorphic analysis of lobate debris aprons on Mars at Mars Orbiter Camera scale: Evidence for ice sublimation initiated by fractures. Journal of Geophysical research. vol. 108, no E4, 8021, doi:10.1029/2002JE001885.

Mangold, N. (2011). Ice sublimation as a geomorphic process: A planetary perspective. Geomorphology, 126(1-2), 1-17.

Mangold, N., and V. Ansan (2006), Detailed study of an hydrological system of valleys, a delta and lakes in the Southwest Thaumasia region, Mars, Icarus, 180(1), 75–87, doi:10.1016/J.Icarus.2005.08.017.

Mangold, N., Gupta, S., Gasnault, O., Dromart, G., Tarnas, J. D., Sholes, S. F., ... & Williford, K. H. (2021). Perseverance rover reveals an ancient delta-lake system and flood deposits at Jezero crater, Mars. Science, 374(6568), 711-717.

Maréchal, C., Boutier, A., Mélières, M. A., Clauzel, T., Betancort, J. F., Lomoschitz, A., ... & Lécuyer, C. (2020). Last Interglacial sea surface warming during the sea-level highstand in the Canary Islands: Implications for the Canary Current and the upwelling off African coast. Quaternary Science Reviews, 234, 106246.

Martian climate with a 3-D global climate model and testing geological predictions. Geophysical Research Letters, 45, 10,249–10,258. https://doi. org/10.1029/2018GL079767

Martin, T. Z. (1995), Mass of dust in the Martian atmosphere, J. Geophys. Res., 100, 7509 – 7512

Martínez-Frías, J., Mederos, E. M., & Lunar, R. (2017). The scientific and educational significance of geoparks as planetary analogues: the example of Lanzarote and Chinijo Islands UNESCO Global Geopark. Episodes Journal of International Geoscience, 40(4), 343-347.

Mauz, B., Bode, T., Mainz, E., Blanchard, H., Hilger, W., Dikau, R., & Zöller, L. (2002). The luminescence dating laboratory at the University of Bonn: equipment and procedures. Ancient TL, 20(2), 53-61.

Mauz, B., Fanelli, F., Elmejdoub, N., & Barbieri, R. (2012). Coastal response to climate change: Mediterranean shorelines during the Last Interglacial (MIS 5). Quaternary Science Reviews, 54, 89-98.

McEwen, A. S., Dundas, C. M., Mattson, S. S., Toigo, A. D., Ojha, L., Wray, J. J., ... & Thomas, N. (2014). Recurring slope lineae in equatorial regions of Mars. Nature geoscience, 7(1), 53-58.

McKeever, S. W. S., Banerjee, D., Blair, M., Clifford, S. M., Clowdsley, M. S., Kim, S. S., ... & Wilson, J. W. (2003). Concepts and approaches to in situ luminescence dating of martian sediments. Radiation Measurements, 37(4-5), 527-534.

McKeever, S. W., Kalchgruber, R., Blair, M. W., & Deo, S. (2006). Development of methods for in situ dating of martian sediments. Radiation Measurements, 41(7-8), 750-754.

McSween, H.Y., Taylor, G.J. and Wyatt, M.B., 2009. Elemental composition of the Martian crust. Science, 324(5928), pp.736-739.

Meco Cabrera, J. F., Sendino, C., Lomoschitz Mora-Figueroa, A., Núñez Ordóñez, A., Huertas, M. J., & Betancort, J. F. (2022). Earth-Moon Barycentre Excursions and Anomalous Quaternary Sea Level Highstands. International Journal of Geosciences.

Meco, J. (1982) : Los bivalvos fósiles de las Canarias Orientales. An. Est. Atlánticos, Las Palmas, 28, pp. 65-125.

Meco, J. (1990). Los fósiles de Los Ajaches/Papagayo y la cronología volcánica de Lanzarote : Un yacimiento a proteger. El Guiniguada.

Meco, J. (1991): La fauna jandiense. (Póster). Casa Museo de Betancuria, Cabildo Insular de Fuerteventura.

Meco, J. (2008). Historia geológica del clima en Canarias.

Meco, J., Guillou, H., Carracedo, J. C., Lomoschitz, A., Ramos, A. J. G., & Rodríguez-Yánez, J. J. (2002). The maximum warmings of the Pleistocene world climate recorded in the Canary Islands. Palaeogeography, palaeoclimatology, palaeoecology, 185(1-2), 197-210.

Meco, J., Muhs, D. R., Fontugne, M., Ramos, A. J., Lomoschitz, A., & Patterson, D. (2011). Late Pliocene and quaternary Eurasian locust infestations in the Canary archipelago. Lethaia, 44(4), 440-454.

Meco, J., Petit-Maire, N., Ballester, J., Betancort, J. F., & Ramos, A. J. (2010). The Acridian plagues, a new Holocene and Pleistocene palaeoclimatic indicator. Global and Planetary Change, 72(4), 318-320.

Meco, J., Petit-Maire, N., Lomoschitz, A., Fontugne, M., Ramos, A. J. G., Carracedo, J. C., ... & Perera, N. (2008). Evolucion eolica. Historia Geologica del clima en Canarias., 153-185.

Meco, J., Pomel, R. S., Aguirre, E., & Stearns, C. (1986). Depósitos marinos del Cuaternario reciente de Canarias.

Meco, J., Scaillet, S., Guillou, H., Lomoschitz, A., Carracedo, J. C., Ballester, J., ... & Cilleros, A. (2007). Evidence for long-term uplift on the Canary Islands from emergent Mio–Pliocene littoral deposits. Global and Planetary Change, 57(3-4), 222-234.

Meco, J., Stearns, C. E. (1981). Emergent littoral deposits in the Eastern Canary Islands. Quaternary Research, 15(2), 199-208.

Meco, J.; Petit-Maire, N.; Fontugne, M.; Shimmield, G.; Ramos, A.J. (1997). The Quaternary deposits in Lanzarote and Fuerteventura (Eastern Canary Islands, Spain): An overview. In Climates of the Past.

Proceeding CLIP Project; Meco, J., Petit-Maire, N., Eds.; Universidad de Las Palmas de Gran Canaria (ULPGC): Las Palmas, Spain, pp. 123–136.

Meresse, S., Costard, F., Mangold, N., Masson, P., & Neukum, G. (2008). Formation and evolution of the chaotic terrains by subsidence and magmatism: Hydraotes Chaos, Mars. Icarus, 194(2), 487-500.

Miall, A. D. (2006). The geology of fluvial deposits: sedimentary facies, basin analysis, and petroleum geology. Springer.

Millar, S. W. S. (2014). Colluvial deposits. Encyclopedia of Planetary Landforms. Springer, New York, 321-328.

Miller, A. Z., Gonzalez-Pimentel, J. L., Stahl, S., Castro-Wallace, S., Sauro, F., Pozzobon, R., ... & Martinez-Frias, J. (2018, April). Exploring possible Mars-like microbial life in a lava tube from Lanzarote: preliminary results of in-situ DNA-based analysis as part of the PANGAEA-X test campaign. In EGU General Assembly Conference Abstracts (p. 1258).

Muhs, D. R., Budahn, J., Skipp, G., Prospero, J. M., Patterson, D., & Bettis III, E. A. (2010). Geochemical and mineralogical evidence for Sahara and Sahel dust additions to Quaternary soils on Lanzarote, eastern Canary Islands, Spain. Terra Nova, 22(6), 399-410.

Murchie, S., Arvidson, R., Bedini, P., Beisser, K., Bibring, J.P., Bishop, J., Boldt, J., Cavender, P., Choo, T., Clancy, R.T. and Darlington, E.H., 2007. Compact reconnaissance imaging spectrometer for Mars (CRISM) on Mars reconnaissance orbiter (MRO). Journal of Geophysical Research: Planets, 112(E5).

Murray, A. S., & Wintle, A. G. (2000). Luminescence dating of quartz using an improved single-aliquot regenerative-dose protocol. Radiation measurements, 32(1), 57-73.

Murray, A. S., & Wintle, A. G. (2003). The single aliquot regenerative dose protocol: potential for improvements in reliability. Radiation measurements, 37(4-5), 377-381.

Nachon, M., Clegg, S. M., Mangold, N., Schröder, S., Kah, L. C., Dromart, G., ... & Wellington, D. (2014). Calcium sulfate veins characterized by ChemCam/Curiosity at Gale crater, Mars. Journal of Geophysical Research: Planets, 119(9), 1991-2016.

NASA. (2024). Mars Sample Return. Retrieved from https://science.nasa.gov/mission/mars-sample-return.

Naughton, F., Goñi, M. S., Kageyama, M., Bard, E., Duprat, J., Cortijo, E., ... & Turon, J. L. (2009). Wet to dry climatic trend in north-western Iberia within Heinrich events. Earth and Planetary Science Letters, 284(3-4), 329-342

Neukum, G., Ivanov, B. A., and Hartmann, W. K., 2001, Cratering records in the inner solar system in relation to the lunar reference system, Chronology and evolution of Mars, Springer, p. 55-86.

Neukum, G., Wise, D.U., 1976. Mars: A standard crater curve and possible new time scale. Science 194, 1381e1387.

Nichols, G. (2009). Sedimentology and stratigraphy. John Wiley & Sons.

Nutz, A., Kwiecien, O., Buylaert, J. P., Guihou, A., Khabouchi, I., Deschamps, P., ... & Bodin, S. (2024). A 60–50 ka African Humid Period modulated by stadial Heinrich events H6 and H5a in northwestern Africa. Palaeogeography, Palaeoclimatology, Palaeoecology, 635, 111952

Orosei R., S. E. Lauro, E. Pettinelli, A. Cicchetti, M. Coradini, B. Cosciotti, F. Di Paolo, E. Flamini, E. Mattei, M. Pajola, F. Soldovieri, M. Cartacci, F. Cassenti, A. Frigeri, S. Giuppi, R. Martufi, A. Masdea, G. Mitri, C. Nenna, R. Noschese, M. Restano, R. Seu, 2018. Radar evidence of subglacial liquid water on Mars, Science, 03 Aug 2018: 490-493

Ortiz, J. E., Torres, T., Yanes, Y., Castillo, C., Nuez, J. D. L., Ibáñez, M., & Alonso, M. R. (2006). Climatic cycles inferred from the aminostratigraphy and aminochronology of Quaternary dunes and palaeosols from the eastern islands of the Canary Archipelago. Journal of Quaternary Science: Published for the Quaternary Research Association, 21(3), 287-306.

Páez, J. D., Ayala, V. A., & Ruiz, C. R. (2000). Unidades geomorfológicas del macizo volcánico antiguo de Famara (Lanzarote, Islas Canarias). Aportaciones a la geomorfología de España en el inicio del tercer milenio: actas de la VI Reunión nacional de Geomorfología, Madrid, 17, 385-394.

Palumbo, A. M., & Head, J. W. (2018). Early Mars climate history: Characterizing a "warm and wet"

Parker, T. J., D. S. Gorsline, R. S. Saunders, D. Pieri, and D. M. Schneeberger, Coastal geomorphology of the Martian northern plains, J. Geophys. Res., 98, 11,061–11,078, 1993.

Pascucci, V., Sechi, D., & Andreucci, S. (2014). Middle pleistocene to holocene coastal evolution of NW sardinia (Mediterranean Sea, Italy). Quaternary International, 328, 3-20.

Perez-Alberti, A., Díaz, M. V., Martini, I. P., Pascucci, V., & Andreucci, S. (2011). Upper Pleistocene glacial valley-junction sediments at Pias, Trevinca Mountains, NW Spain. Geological Society, London, Special Publications, 354(1), 93-110.

Perron J.T., Dietrich W.E., Howard A.D., McKean J.A., Pettinga J.R., 2003. Ice-driven creep on Martian debris slopes. Geophysical research letters, vol. 30, no. 14, 1747, doi:10.1029/2003GL017603.

Phillips R.J., M.T. Zuber, S.E. Smrekar, M.T. Mellon, J.W. Head, K.L. Tanaka, N.E. Putzig, S.M. Milkovich, B.A. Campbell, J.J. Plaut, A. Safaeinili, R. Seu, D. Biccari, L.M. Carter, G. Picardi, R. Orosei, P.S. Mohit, E. Heggy, R.W. Zurek, A.F. Egan, E. Giacomoni, F. Russo, M. Cutigni, E. Pettinelli, J.W. Holt, C.J. Leuschen, L. Marinangeli. 2008. Mars North Polar Deposits: Stratigraphy, Age, and Geodynamical Response, Science, Vol. 320, pp. 1182–1185, DOI: 10.1126/science.1157546Reiss D., Fenton L., Neakrase L., Zimmerman M., Statella T., Whelley P., Rossi A.P., Balme M., 2016. Dust Devil Tracks. Space Science Reviews, 203(1) pp. 143–181.

Picard, M. D., & High, L. R. (1973). Sedimentary structures of ephemeral streams. Elsevier.

Pondrelli, M., Baliva, A., Di Lorenzo, S., Marinangeli, L., & Rossi, A. P. (2005). Complex evolution of paleolacustrine systems on Mars: An example from the Holden crater. Journal of Geophysical Research: Planets, 110(E4)

Pondrelli, M., Rossi, A. P., Le Deit, L., Fueten, F., van Gasselt, S., Glamoclija, M., ... & Pozzobon, R. (2015). Equatorial layered deposits in Arabia Terra, Mars: Facies and process variability. Bulletin, 127(7-8), 1064-1089.

Prescott, J. R., & Hutton, J. T. (1994). Cosmic ray contributions to dose rates for luminescence and ESR dating: large depths and long-term time variations. Radiation measurements, 23(2-3), 497-500.

Preusser, F., May, J. H., Eschbach, D., Trauerstein, M., & Schmitt, L. (2016). Infrared stimulated luminescence dating of 19 th century fluvial deposits from the upper Rhine River. Geochronometria, 43(1), 131-142.

Rahmstorf, S. (2002). Ocean circulation and climate during the past 120,000 years. Nature, 419(6903), 207-214.

Rahmstorf, S. (2003). Timing of abrupt climate change: A precise clock. Geophysical Research Letters, 30(10).

Rapin, W., Dromart, G., Clark, B. C., Schieber, J., Kite, E. S., Kah, L. C., ... & Lanza, N. L. (2023). Sustained wet–dry cycling on early Mars. Nature, 620(7973), 299-302.

Rasmusen, T.L., Thomsen, E., Troelstra, S.R., Kuijpers, A., Prins, M.A., 2003. Millennialscale glacial variability versus Holocene stability: changes in planktic and benthic foraminifera faunas and ocean circulation in the North Atlantic during the last 60000 years. Mar. Micropaleontol. 47, 143–176.

Rasmussen, S. O., Andersen, K. K., Svensson, A. M., Steffensen, J. P., Vinther, B. M., Clausen, H. B., ... & Ruth, U. (2006). A new Greenland ice core chronology for the last glacial termination. Journal of Geophysical Research: Atmospheres, 111(D6).

Rasmussen, S. O., Bigler, M., Blockley, S. P., Blunier, T., Buchardt, S. L., Clausen, H. B., ... & Winstrup, M. (2014). A stratigraphic framework for abrupt climatic changes during the Last Glacial period based on three synchronized Greenland ice-core records: refining and extending the INTIMATE event stratigraphy. Quaternary science reviews, 106, 14-28.

Reineck, H. E., & Singh, I. B. (2012). Depositional sedimentary environments: with reference to terrigenous clastics. Springer Science & Business Media.

Reiss D., Fenton L., Neakrase L., Zimmerman M., Statella T., Whelley P., Rossi A.P., Balme M., 2016. Dust Devil Tracks. Space Science Reviews, 203(1) pp. 143–181.

Reiss, D., Hoekzema, N. M., & Stenzel, O. J. (2014). Dust deflation by dust devils on Mars derived from optical depth measurements using the shadow method in HiRISE images. Planetary and Space Science, 93, 54-64.

Rennó, N. O., Bos, B. J., Catling, D., Clark, B. C., Drube, L., Fisher, D., ... & Young, S. M. (2009). Possible physical and thermodynamical evidence for liquid water at the Phoenix landing site. Journal of Geophysical Research: Planets, 114(E1).

Rhodes, E. J. (2011). Optically stimulated luminescence dating of sediments over the past 200,000 years. Annual Review of Earth and Planetary Sciences, 39(1), 461-488.

Rivoldini, A., Van Hoolst, T., Verhoeven, O., Mocquet, A., and Dehant, V., 2011, Geodesy constraints on the interior structure and composition of Mars: Icarus, v. 213, no. 2, p. 451-472.

Rodríguez Badiola, E., Veintemillas-Verdaguer, S., & Carracedo, J. C. (1994). El edificio isla de Los Ajaches (Lanzarote): episodios eruptivos y su evaluación petrogenética. In memoriam Dr. José Luis Díez Gil, pp. 121-135. ISBN: 84-87021-19-0

Rodriguez, J. A. P., Fairén, A. G., Tanaka, K. L., Zarroca, M., Linares, R., Platz, T., ... & Glines, N. (2016). Tsunami waves extensively resurfaced the shorelines of an early Martian ocean. Scientific reports, 6(1), 25106.

Rodriguez, J. A., Sasaki, S., Kuzmin, R. O., Dohm, J. M., Tanaka, K. L., Miyamoto, H., ... & Ferris, J. C. (2005). Outflow channel sources, reactivation, and chaos formation, Xanthe Terra, Mars. Icarus, 175(1), 36-57.

Roettig, C.B., Kolb, T., Zöller, L., Zech, M., Faust, D., 2020. A detailed chrono-stratigraphical record of Canarian dune archives - interplay of sand supply and volcanism. Journal of Arid Environments 183, 104240.

Roman-Gonzalez, A., Saab, B., Berger, J., Hoyt, J., Urquhart, J., & Guined, J. (2015, October). Mars desert research station: Crew 138. In 66th International Astronautical Congress-IAC 2015 (p. 7).

Romano, E., Sechi, D., Andreucci, S., Bergamin, L., D'Ambrosi, A., De Santis, C., Di Bella, L., Dinelli, E., Frezza, V., Pascucci, V., Pierfranceschi, G., & Provenzani, C. (2024). Paleoecological reconstruction during the Holocene in the Middle Branch of Bue Marino Cave (Sardinia, Italy). The Holocene, 34(1), 74-86. https://doi.org/10.1177/09596836231200435)

Rossi A.P., Gasselt S., 2010. Geology of Mars after the first 40 years of exploration. 10.1088/1674-4527/10/7/003. Research in Astronomy and Astrophysics - RES ASTRON ASTROPHYS.

Ruddiman, W. F., & McIntyre, A. (1981). Oceanic mechanisms for amplification of the 23,000-year ice-volume cycle. Science, 212(4495), 617-627.

Salese, F., Di Achille, G., Neesemann, A., Ori, G. G., & Hauber, E. (2016). Hydrological and sedimentary analyses of well-preserved paleofluvial-paleolacustrine systems at Moa Valles, Mars. Journal of Geophysical Research: Planets, 121(2), 194-232.

Sanchez Guzman, J., & Abad, J. (1986). Sondeo geotérmico Lanzarote-1. Significado geológico y geotérmico. Anales de física. Serie B, Aplicaciones, métodos e instrumentos, 82, 102-109.

Sauro, F., Payler, S. J., Massironi, M., Pozzobon, R., Hiesinger, H., Mangold, N., ... & Bessone, L. (2023). Training astronauts for scientific exploration on planetary surfaces: The ESA PANGAEA programme. Acta Astronautica, 204, 222-238.

Sautter, V., Toplis, M. J., Beck, P., Mangold, N., Wiens, R., Pinet, P., et al. (2016). Magmatic complexity on early Mars as seen through a combination of orbital, in-situ and meteorite data. Lithos, 254–255, 36–52. https://doi.org/10.1016/j.lithos.2016.02.023

Saynor, M. & Erskine, W. (1993). Characteristics and Implications of High-level Slackwater Deposits in the Fairlight Gorge, Nepean River, Australia. Marine and Freshwater Research. 44. 735-47. 10.1071/MF9930735.

Schubert, G., and Spohn, T., (1990). Thermal history of Mars and the sulfur content of its core: Journal of Geophysical Research: Solid Earth, v. 95, no. B9, p. 14095-14104.

Scott, D.H., Carr, M.H., 1978. Geologic map of Mars. US Geological Survey Miscellaneous Investigations Series Map I-1083, scale 1:25,000,000.

Sechi, D., Andreucci, S., Stevens, T., & Pascucci, V. (2020). Age and significance of late Pleistocene Lithophyllum byssoides intertidal algal ridge, NW Sardinia, Italy. Sedimentary Geology, 400, 105618.

Seelos K. D., Arvidson R. E., Jolliff B. L., Chemtob S. M., Morris R. V., Ming D. W., Swayze G. A. Silica in a Mars analog environment: Ka'u Desert, Kilauea Volcano, Hawaii. J. Geophys. Res. Planet., 2010, 115, E00D15, 1-18.

Seidelmann, P. K., Abalakin, V., Bursa, M., Davies, M., De Bergh, C., Lieske, J., Oberst, J., Simon, J.-L., Standish, E., and Stooke, P., 2002, Report of the IAU/IAG working group on cartographic coordinates and rotational elements of the planets and satellites: 2000: Celestial Mechanics and Dynamical Astronomy, v. 82, no. 1, p. 83-111.

Shackleton, S., Menking, J. A., Brook, E., Buizert, C., Dyonisius, M. N., Petrenko, V. V., ... & Severinghaus, J. P. (2021). Evolution of mean ocean temperature in Marine Isotope Stage 4. Climate of the Past, 17(5), 2273-2289.

Shimmield, G., Petit-Maire, N., Meco Cabrera, J., Fontugne, M., & González Ramos, A. J. (1997). The quaternary deposits in Lanzarote and Fuerteventura (eastern Canary Islands, Spain): an overview.

Sholes, S. F., Dickeson, Z. I., Montgomery, D. R., & Catling, D. C. (2021). Where are Mars' hypothesized ocean shorelines? Large lateral and topographic offsets between different versions of paleoshoreline maps. Journal of Geophysical Research: Planets, 126(5), e2020JE006486.

Silvestro, S., Chojnacki, M., Vaz, D. A., Cardinale, M., Yizhaq, H., & Esposito, F. (2020). Megaripple migration on Mars. Journal of Geophysical Research: Planets, 125, e2020JE006446. https://doi.org/10.1029/2020JE006446

Silvestro, S., Fenton L. K., Vaz D.A., Bridges N.T., Ori G.G., (2010). Ripple migration and dune activity on Mars: Evidence for dynamic wind processes. Geophys. Res. Lett., 37, L20203, doi:10.1029/2010GL044743.

Sinha, R. K., Ray, D., De Haas, T., & Conway, S. J. (2020). Global documentation of overlapping lobate deposits in martian gullies. Icarus, 352, 113979.

Slingerland, R., & Smith, N. D. (2004). River avulsions and their deposits. Annu. Rev. Earth Planet. Sci., 32, 257-285.

Smith, D. E., Zuber, M. T., Frey, H. V., Garvin, J. B., Head, J. W., Muhleman, D. O., Pettengill, G. H., Phillips, R. J., Solomon, S. C., and Zwally, H. J., 2001, Mars Orbiter Laser Altimeter: Experiment summary after the first year of global mapping of Mars: Journal of Geophysical Research: Planets, v. 106, no. E10, p. 23689-23722.

Smith, D. E., Zuber, M. T., Solomon, S. C., Phillips, R. J., Head, J. W., Garvin, J. B., Banerdt, W. B., Muhleman, D. O., Pettengill, G. H., and Neumann, G. A., 1999, The global topography of Mars and implications for surface evolution: Science, v. 284, no. 5419, p. 1495-1503.

Soderblom, L.A., Condit, C.D., West, R.A., Herman, B.M., Kriedler, T.J., 1974. Martian planetwide crater distributions: Implications for geologic history and surface processes. Icarus 22, 239-263.

Sohbati, R., Jain, M., and Murray, A. (2012) Surface exposure dating of non-terrestrial bodies using optically stimulated luminescence: a new method. Icarus 221:160–166

Solomon, S. C., Aharonson, O., Aurnou, J. M., Banerdt, W. B., Carr, M. H., Dombard, A. J., Frey, H. V., Golombek, M. P., Hauck, S. A., Head, J. W., Jakosky, B. M., Johnson, C. L., McGovern, P. J., Neumann, G. A., Phillips, R. J., Smith, D. E., and Zuber, M. T., 2005, New perspectives on ancient Mars: Science, v. 307, no. 5713, p. 1214-1220.

Spohn, T., Acuña, M. H., Breuer, D., Golombek, M., Greeley, R., Halliday, A., Hauber, E., Jaumann, R., and Sohl, F., 2001, Geophysical constraints on the evolution of Mars, Chronology and Evolution of Mars, Springer, p. 231-262.

Spooner, N. A. (1994). The Anomalous Fading of Infrared-Stimulated Luminescence from Feldspars. Radiat. Measurements 23, 625–632. doi:10.1016/1350-4487(94)90111-2

Squyres, S. W., & Kasting, J. F. (1994). Early Mars: How warm and how wet? Science, 265(5173), 744-749.

Stevenson, D. J., 2001, Mars' core and magnetism: Nature, v. 412, p. 214.

Stillman D.E., Bue B.D., Wagstaff K.L., Primm K.M., Michaels T.I., Grimm R.E., 2020. Evaluation of wet and dry recurring slope lineae (RSL) formation mechanisms based on quantitative mapping of RSL in Garni Crater, Valles Marineris, Mars. Icarus 335, 113420.

Suchodoletz, H.V., Zöller, L., Hilgers, A., Radtke, U., Faust, D., 2013. Vegas and dune palaeosol-sequences — two different palaeoenvironmental archives on the eastern Canary Islands. In: Fernandez-Palacios (Ed.), Climate change Perspectives from the Atlantic. Past, Present and Future. Servicio de Publicaciones, Universidad de la Laguna de Tenerife, pp. 259–274.

Sullivan R., Thomas P., Veverka J.,2001. Mass movement slope streaks imaged by the Mars Orbiter Camera. J. Geophys. Res., vol. 106, no. El0, PAGES 23,607-23,633

Sullivan, R., Arvidson, R., Bell III, J. F., Gellert, R., Golombek, M., Greeley, R., ... & Wray, J. (2008). Wind-driven particle mobility on Mars: Insights from Mars Exploration Rover observations at "El Dorado" and surroundings at Gusev Crater. Journal of Geophysical Research: Planets, 113(E6).

Sutter B., Dalton J. B., Ewing S. A., Amundson R., Mckay C. P. Terrestrial analogs for interpretation of infrared spectra from the Martian surface and subsurface: Sulfate, nitrate, carbonate, and phyllosilicate-bearing Atacama Desert soils. J. Geophys. Res. Biogeo., 2007, 112, G04S10, 1-19.

Svensson, A., Andersen, K. K., Bigler, M., Clausen, H. B., Dahl-Jensen, D., Davies, S. M., ... & Vinther, B. M. (2006). The Greenland ice core chronology 2005, 15–42 ka. Part 2: comparison to other records. Quaternary Science Reviews, 25(23-24), 3258-3267.

Svensson, A., Andersen, K. K., Bigler, M., Clausen, H. B., Dahl-Jensen, D., Davies, S. M., ... & Vinther, B. M. (2008). A 60 000 year Greenland stratigraphic ice core chronology. Climate of the Past, 4(1), 47-57.

Tanaka K.L., Hartmann W.K., 2016. 2 - Planetary Time Scale. In: J.G. Ogg, G.M. Ogg, F.M. Gradstein (Eds.), A Concise Geologic Time Scale, Elsevier, Pages 9-18, ISBN 9780444637710, https://doi.org/10.1016/B978-0-444-59467-9.00002-9.

Tanaka, K. L., 1986. The stratigraphy of Mars: Journal of Geophysical Research: Solid Earth, v. 91, no. B13, p. E139-E158.

Tanaka, K. L., Skinner Jr, J. A., Dohm, J. M., Irwin III, R. P., Kolb, E. J., Fortezzo, C. M., ... & Hare, T. M. (2014). Geologic map of Mars.

Thiel, C. S., Ehrenfreund, P., Foing, B., Pletser, V., & Ullrich, O. (2011). PCR-based analysis of microbial communities during the EuroGeoMars campaign at Mars Desert Research Station, Utah. International Journal of Astrobiology, 10(3), 177-190.

Thiel, C., Coltorti, M., Tsukamoto, S., & Frechen, M. (2010). Geochronology for some key sites along the coast of Sardinia (Italy). Quaternary International, 222(1-2), 36-47.

Thomas, P., J. Veverka, S. Lee, and A. Bloom (1981), Classification of wind streaks on Mars, Icarus, 45, 124–153.

Thomsen, K. J., Murray, A. S., & Bøtter-Jensen, L. (2005). Sources of variability in OSL dose measurements using single grains of quartz. Radiation measurements, 39(1), 47-61.

Thomsen, K. J., Murray, A. S., Jain, M., and Bøtter-Jensen, L. (2008). Laboratory Fading Rates of Various Luminescence Signals from Feldspar-Rich Sediment Extracts. Radiat. Measurements 43, 1474–1486. doi:10.1016/j.radmeas.2008.06.002

Timmermann, A., Krebs, U., Justino, F., Goosse, H., & Ivanochko, T. (2005). Mechanisms for millennial-scale global synchronization during the last glacial period. Paleoceanography, 20(4).

Tomasi, I., Massironi, M., Meyzen, C. M., Pozzobon, R., Sauro, F., Penasa, L., Santagata, T., Tonello, M., Santana Gomez, G. D., & Martinez-Frìas, J. (2022). Inception and evolution of La Corona Lava Tube System (Lanzarote, Canary Islands, Spain). Journal of Geophysical Research: Solid Earth, 127(6), 6. https://doi. org/10.1029/2022JB024056

Tomasi, I., Tonello, M., Massironi, M., Tesson, P. A., Sauro, F., Meyzen, C. M., ... & Mederos, E. M. (2023). Geology of Lanzarote's northern region (Canary Island, Spain). Journal of Maps, 1-14.

Treiman, A. H. (2003). Geologic settings of Martian gullies: Implications for their origins. Journal of Geophysical Research: Planets, 108(E4).

Treiman, A. H., Bish, D. L., Vaniman, D. T., Chipera, S. J., Blake, D. F., Ming, D. W., ... & Yen, A. S. (2016). Mineralogy, provenance, and diagenesis of a potassic basaltic sandstone on Mars: CheMin

X-ray diffraction of the Windjana sample (Kimberley area, Gale Crater). Journal of Geophysical Research: Planets, 121(1), 75-106.

Trewin, N. H. (1993). Mixed aeolian sandsheet and fluvial deposits in the Tumblagooda Sandstone, Western Australia. Geological Society, London, Special Publications, 73(1), 219-230.

Troll, V. R., & Carracedo, J. C. (2016). The geology of the Canary Islands. Elsevier.

Turon, J. L., Lézine, A. M., & Denèfle, M. (2003). Land–sea correlations for the last glaciation inferred from a pollen and dinocyst record from the Portuguese margin. Quaternary Research, 59(1), 88-96.

Vega, L. L. C. (2010). Sedimentología, estratigrafía, dinámica sedimentaria y evolución de El Jable (Lanzarote). Propuesta de gestión (Doctoral dissertation, Universidad de Las Palmas de Gran Canaria).

Verhoeven, J. W. (1996). Glossary of terms used in photochemistry (IUPAC Recommendations 1996). Pure and Applied Chemistry, 68(12), 2223-2286.

Vinther, B. M., Clausen, H. B., Johnsen, S. J., Rasmussen, S. O., Andersen, K. K., Buchardt, S. L., ... & Heinemeier, J. (2006). A synchronized dating of three Greenland ice cores throughout the Holocene. Journal of Geophysical Research: Atmospheres, 111(D13).

Vlahovljak, M., Paradiso, I., Netti, V., Buono, F., Fallacara, G., Angione, A., & Fuscello, I. (2021, July). HiveMars: Design of a Hybrid-class, scalable Settlement on the martian surface. 50th International Conference on Environmental Systems.

von Suchodoletz, H., Kühn, P., Hambach, U., Dietze, M., Zöller, L., & Faust, D. (2009). Loess-like and palaeosol sediments from Lanzarote (Canary Islands/Spain)—indicators of palaeoenvironmental change during the Late Quaternary. Palaeogeography, Palaeoclimatology, Palaeoecology, 278(1-4), 71-87.

von Suchodoletz, H., Oberhänsli, H., Hambach, U., Zöller, L., Fuchs, M., & Faust, D. (2010). Soil moisture fluctuations recorded in Saharan dust deposits on Lanzarote (Canary Islands) over the last 180 ka. Quaternary Science Reviews, 29(17-18), 2173-2184.

von Suchodoletz, H., Zöller, L., Hilgers, A., Radtke, U., Faust, D., (2013). Vegas and dune-palaeosoil-sequences–two different palaeoenvironmental archives on the Eastern Canary Islands. In: Fernández-Palacios, J.M., de Nascimento, L., Hernández, J.C., Clemente, S., González, A., Diaz-

González, J.P. (Eds.), Climate Change Perspectives from the Atlantic: Past, Present and Future. Servivio de Publicaciones, Universidad de La Laguna, pp. 259–274.

Warren-Rhodes K. A., Lee K. C., Archer S. D. J., Cabrol N., Ng-Boyle L., Wettergreen D., Zacny K., Pointing S. B., . The NASA Life in the Atacama Project Team. Subsurface microbial habitats in an extreme desert Mars-analog environment. Front- Microbiol., 2019, 10, 69, 1-11.

Werner S.C., 2009. The global martian volcanic evolutionary history. Icarus 201 (2009) 44–68.

Werner, S. C., & Tanaka, K. L. (2011). Redefinition of the crater-density and absolute-age boundaries for the chronostratigraphic system of Mars. Icarus, 215(2), 603-607.

Whelley, P. L., & Greeley, R. (2008). The distribution of dust devil activity on Mars. Journal of Geophysical Research: Planets, 113(E7).

Wieczorek, M. A., and Zuber, M. T. (2004). Thickness of the Martian crust: Improved constraints from geoid-to-topography ratios: Journal of Geophysical Research: Planets, v. 109, no. E1.

Williamson, D., Jackson, M., Banerjee, S. K., & Petit-Maire, N. (2004). The magnetism of a glacial aeolianite sequence from Lanzarote (Canary Islands): coupling between luvic calcisol formation and Saharan dust trapping processes during wet deposition events off northwestern Sahara. Geophysical Journal International, 157(3), 1090-1104.

Wilson, S. A., Morgan, A. M., Howard, A. D., & Grant, J. A. (2021). The global distribution of craters with alluvial fans and deltas on Mars. Geophysical Research Letters, 48(4), e2020GL091653.

Wintle, A. G. (1997). Luminescence dating: laboratory procedures and protocols. Radiation measurements, 27(5-6), 769-817.

Wintle, A. G. (2008). Fifty years of luminescence dating. Archaeometry, 50(2), 276-312.

Wintle, A. G., & Murray, A. S. (2006). A review of quartz optically stimulated luminescence characteristics and their relevance in single-aliquot regeneration dating protocols. Radiation measurements, 41(4), 369-391.

Wolff, E. W., Barbante, C., Becagli, S., Bigler, M., Boutron, C. F., Castellano, E., ... & Wegner, A. (2010). Changes in environment over the last 800,000 years from chemical analysis of the EPICA Dome C ice core. Quaternary Science Reviews, 29(1-2), 285-295.

Wright, V.P., Tucker, M.E., 1991. Calcretes: an introduction. In: Wright, V. P., Tucker, M. E. (Eds), Calcretes. IAS Reprint Series, Vol. 2. Blackwell Scientific Publications, Oxford, pp. 1222.

Xiao, L., Huang, J., Kusky, T., Head, J. W., Zhao, J., Wang, J., ... & Xiao, X. (2023). Evidence for marine sedimentary rocks in Utopia Planitia: Zhurong rover observations. National Science Review, nwad137.

Yanes, Y., Kowalewski, M., Ortiz, J. E., Castillo, C., de Torres, T., & de la Nuez, J. (2007). Scale and structure of time-averaging (age mixing) in terrestrial gastropod assemblages from Quaternary eolian deposits of the eastern Canary Islands. Palaeogeography, Palaeoclimatology, Palaeoecology, 251(2), 283-299.

Zazo, C., Goy, J. L., Hillaire-Marcel, C., Gillot, P. Y., Soler, V., González, J. Á., ... & Ghaleb, B. (2002). Raised marine sequences of Lanzarote and Fuerteventura revisited—a reappraisal of relative sea-level changes and vertical movements in the eastern Canary Islands during the Quaternary. Quaternary Science Reviews, 21(18-19), 2019-2046.

Zazo, C., Hillaire-Marcel, C., Goy, J.L., Ghaleb, B. y Hoyos, M. (1997): Cambios del nivel del mar-clima en los últimos 250 Ka: Canarias orientales, España. Boletín Geológico y Minero, 108, 487-497.

Zazo, C.; Hillaire-Marcel, C. L.; Hoyos, M.; Ghaleb, B.; Goy, J. L.; Dabrio, C. J. (1993): The Canary Islands, a stop in the migratory way of strombus bubonios towards the mediterranean around 200 k.a.. Newsletter, n.o 15, pp. 7-15.

Zegers T.E., Oosthoek H.P. J., Rossi A.P., Blom J.K., Schumacher S., 2010. Melt and collapse of buried water ice: An alternative hypothesis for the formation of chaotic terrains on Mars. Earth and Planetary Science Letters 297 (2010) 496–504.

Zeitler, W., Ohlhof, T., and Ebner, H., 2000, Recomputation of the global Mars control-point network: Photogrammetric engineering and remote sensing, v. 66, no. 2, p. 155-162.

Zhang, J., and Li, S.-H. (2020). Review of the Post-IR IRSL Dating Protocols of K-Feldspar. MPs 3, 7. doi:10.3390/mps3010007

Zuber, M. T., (2001). The crust and mantle of Mars: Nature, v. 412, p. 220.

Zuber, M. T., Solomon, S. C., Phillips, R. J., Smith, D. E., Tyler, G. L., Aharonson, O., Balmino, G., Banerdt, W. B., Head, J. W., and Johnson, C. L. (2000). Internal structure   and early thermal

evolution of Mars from Mars Global Surveyor topography and gravity: science, v. 287, no. 5459, p. 1788-1793.

Zucca, C., Sechi, D., Andreucci, S., Shaddad, S. M., Deroma, M., Madrau, S., ... & Kapur, S. (2014). Pedogenic and palaeoclimatic evidence from an Eemian calcrete in north-western Sardinia (Italy). European Journal of Soil Science, 65(4), 420-435.

Zurek, R., 1999. Polar Layered Terrains: Links Between the Martian Volatile and Dust Cycles.

Acknowledgments

I would like to express my deepest gratitude to all the extraordinary people who have supported and encouraged me throughout this important journey.

First and foremost, I sincerely thank **Vincenzo**, my mentor and guide, for imparting not only technical knowledge but also a profound sense of adventure and enthusiasm for science. Thank you for introducing me to the fascinating world of sediments and their captivating stories. Your continuous teachings and unwavering support have transformed my passion for sedimentology into my favorite profession, and for that, I will always be grateful.

A special thanks also goes to my **colleagues**, with whom I've shared unforgettable moments both at sea and on land. Our discussions, laughter, explorations, and coffee breaks have enriched my experience and taught me the value of collaboration and friendship in both the academic and professional worlds.

I extend my heartfelt gratitude to **Laura**, **Ilaria**, and **Simona** for your constant smiles, encouragement, and for always being by my side. Your support and lightheartedness help me through difficult times and keep my motivation high. Thank you, **Daniela**, for guiding me toward embracing and loving who I am.

To my **Mom** and **Francy**, my constant pillars and precious guides through the darkest of nights— thank you. Your love, support, and smiles continually light up my path and inspire me to always give my best.

Finally, I wish to dedicate a special thanks to **Mario**, who gently but profoundly entered my life. Thank you for your support, understanding, and love, which have made my life more beautiful than ever before.

"Fece soffiare un vento dolce e mite. Lieto del vento propizio spiegò le vele il divino Ulisse, e poi seduto al timone con competenza guidava, e il sonno non gli cadde sulle palpebre, nel mentre osservava le Pleiadi e Boote che tardi tramonta e l'Orsa, che chiamano anche col nome di Carro ed è sempre lì compiendo il suo giro e fa la guardia a Orione: è la sola che non tocca mai i lavacri di Oceano"